PRECIPITATION IN SELECTED WROUGHT MAGNESIUM ALLOYS.

by

D.J. STRATFORD, M.Sc.

A thesis submitted for the degree of Doctor of Philosophy of the University of Aston in Birmingham.

March 1969.

"There is something fascinating about science, one gets such wholesale returns of conjecture out of such a trifling investment of fact".

Mark Twain, 1867.

SUMMARY

A study has been made of precipitation in a series of wrought magnesium alloys using hardness, tensile properties and electron microscopy. The use of thin film electron microscopy necessitated the development of a reproducable foil preparation technique and because of the fineness of the structures after ageing at low temperatures, a technique such that this could be determined unambiguously.

The alloys examined were:- Mg-6.0% Zn, Mg-6.0% Zn-0.5% Zr, Mg-6.0% Zn-1.0% Mn, Mg-0.5% Zr and Mg-0.8% Mn, all but the first are commercially available. Precipitation has been previously observed by electron microscopy in all but the two ternary alloys. The results obtained in certain sections of this investigation are at variance with those published and in all but one instance the results presented are conclusive.

The object of this investigation was to explain the excellent ageing response of the Mg-Zn-Mn alloy, the manufacturing and heat treatment of which were determined by the author in a previous investigation (M.Sc.1966, University of Aston).

The effect of various thermal treatments on the strength and microstructure of the first three alloys listed has been examined; in the remainder the effect on microstructure only. The ageing response in the binary Mg-Zn alloy results from the simultaneous precipitation of two precipitate morphologies, both

transforming to a third morphology on continued ageing. The addition of zirconium, whilst producing a very fine grain size, causes the absence of one of these precipitates. This is counterbalanced to a large extent by the precipitation of a ZnZr compound during the normal high temperature solution treatment process.

The addition of manganese to the binary Mg-6.0% Zn alloy causes a dramatic increase in the rate of ageing and in the maximium properties. This ternary alloy responds to a double ageing treatment, but not necessarily by the conventional process of precipitate refinement alone. Due to the precipitation of two morphologies, a change in the ratio of the volume fraction of these also contributes to the strengthening in the alloy. A double ageing response is therefore possible without invoking either the critical temperature or G.P. zone solvus theories.

INDEX

Page No.

CHAPTER 1

Section 1 - Literature Review

Section 2 - Precipitation in Magnesium Alloys

CHAPTER 2.

Theoretical Concepts

CHAPTER 3

Contrast from Second Phase Particles

CHAPTER 4.

Experimental Procedure

Page No.

CHAPTER 5

Results

Magnesium - 6.0% Zn - Z6.

Magnesium - 6.0% Zn - 0.5% Zr - ZW6

Magnesium - 0.5% Zr - ZA.

Magnesium - 6.0% Zn - 1.0% Mn - ZM61.

Magnesium - 0.8% Mn - Mn 80.

Matrix Contrast Effects

CHAPTER 1.

Section 1 - LITERATURE REVIEW

Introduction.

The literature on precipitation hardening is extensive. A comprehensive review of the literature has been published by Kelly and Nicholson[1] and it is interesting to note that this review contains information on face centred and body centred cubic alloys only. This serves to indicate the dearth of research into this subject in alloys which crystallise in the close packed hexagonal structure which is undoubtedly due to the relatively small commercial use of these metals.

The close packed hexagonal structure has a unit cell with axes $a_1 = a_2 \neq c$ and angles $\alpha = \beta = 90^\circ$ and $\gamma = 120^\circ$ with atoms stacked in layers ABABAB. The Miller index system describes a plane in terms of the reciprocals of the distances from the origin at which it cuts the principal axes and with orthonormal axes, similar planes have similar mathematical forms. The cube faces in face and body centred cubic structures have indices (100), (010) and (001). When the axes are not orthogonal similar planes do not have a similar form; the prism planes in Fig. 1.1 are (100), (010) and ($\bar{1}$10).

If a third axis is included in the basal plane a four index notation results which is generally preferred by the metallurgist. The intercepts are then referred to as $\underline{a}_1$, $\underline{a}_2$, $\underline{a}_3$ and $\underline{c}$ and a

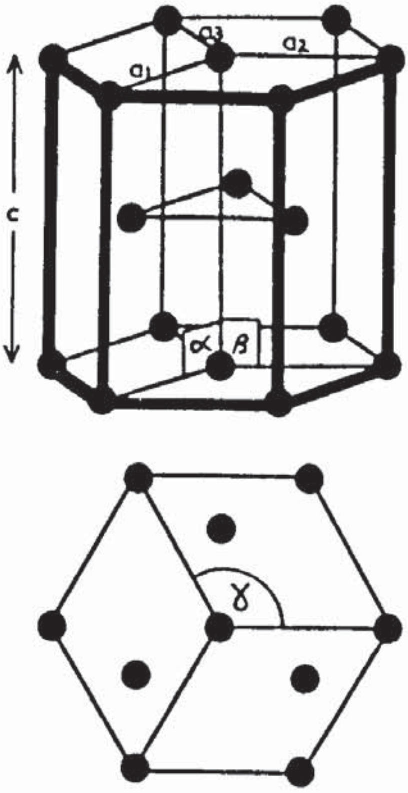

Figure 1.1. The close packed hexagonal unit cell.

random plane as (hkil) where $i = -(h + k)$. The indices of the prism planes then become $(10\bar{1}0)$, $(1\bar{1}00)$, $(0\bar{1}10)$, $(\bar{1}010)$, $(\bar{1}100)$ and $(01\bar{1}0)$ and the system is known as Miller-Bravais indices.

With crystallographic directions Miller indices cannot be converted to Miller-Bravais as simply as with planes. A direction as described with Miller-Bravais has indices such that

$$d = u\underline{a}_1 + v\underline{a}_2 + t\underline{a}_3 + w\underline{c}$$

and these may be converted to Miller indices U V W using the equation[2]:-

$$U = u-t, \quad V = v-t \quad \text{and} \quad W = w$$

To convert Miller to Miller-Bravais indices:-

$$u = \frac{1(2U-V)}{3}, \quad v = \frac{1(2V-U)}{3}, \quad t = -(u + v) \text{ and } w = W$$

This is particularly important when determining the zone axis of a foil with electron diffraction and errors have been made as indicated by Partridge[2]. All planes and directions referred to in this thesis are of the Miller-Bravais form and the results reported by Gallot[3] who used the Miller system have therefore been converted.

Section 2 - Precipitation Hardening in Magnesium Alloys.

Magnesium - Aluminium.

Fisher[4], Fox and Lardner[5] and many others have studied the optical metallography of Mg.-Al alloys after various thermal treatments. Although there is no eutectoid reaction indicated in the equilibrium diagram, the microstructure of these alloys after ageing is remarkably similar to the eutectoid structure of pearlite in carbon steels. The Mg-Al saturated solid solution decomposes discontinuously to form the pearlite type structure composed of $Mg_{17} Al_{12}$ and the solid solution and many of the terms used in ferrous metallography are equally applicable.

Talbot and Norton[6] determined that 50% completion of precipitation was associated with maximum hardness and Leontis and Nelson[7] obtained similar results in alloys with small amounts of zinc. Murakami, Kawano, and Tamura[8] confirmed previous results by using thin film electron microscopy. More recently Clark[9] studied the decomposition of a Mg - 9.0% Al alloy, also by thin film microscopy and found two types of precipitation, a cellular type and a more general precipitation occuring competitively at most ageing temperatures. He found that the spacing between the precipitates, in the form of plates on the (0001)Mg, was too large to harden the matrix significantly and that $(10\bar{1}2)$ twinning was reduced.

'Wavy' slip traces were found on deformed aged samples and considered to be due to cross slip onto $(10\bar{1}0)$ planes and the hardening to be due to dislocation tangles arising from the interaction of the basal and prism dislocations.

Byrne[10] has pointed out a possible error in Clarks conclusions and suggests that the spacing of precipitates in his bulk samples for hardness determination will be less than that of the alloy in the 0.010" thick form used for the thin foil preparation. Byrne reported a change in particle spacing from 2,580 A° to 450 - 700 A° after heat treating a Mg. - 1.33% Mn alloy in .005" thick sheet and bulk form respectively.

The spacing in the former at 2,580 A° was considered to be borderline between a dislocation bowing mechanism, and a particle cutting mechanism for dislocation/precipitate interaction. In the latter case, interaction will take the form of particle cutting.

Magnesium - Manganese.

The equilibrum diagram according to Grogan and Haughton[11] is shown in Fig. 1.2. There is some disagreement about the peritectic point and about the solid solubility. For instance, at 420°C. the solubility in Fig.2 is 0.15% whilst in the diagram from Jones [12] it is 0.4% Mn. Bryne[13] reported precipitation of α Mn as plates or ribbons perpendicular to the (0001)Mg and suggested that they were coherent with these planes and that the

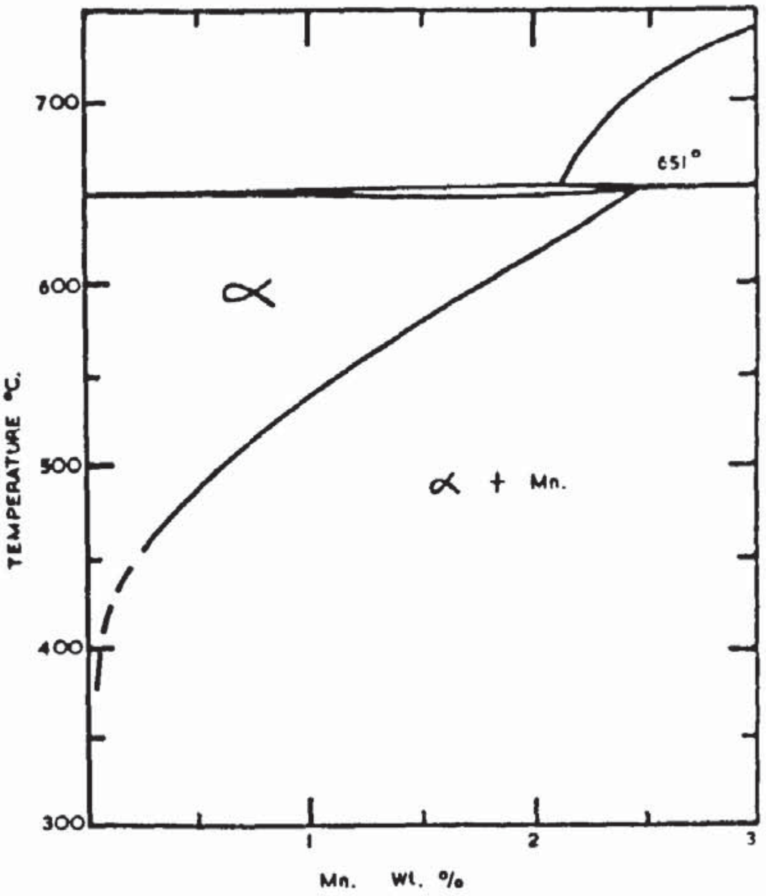

Figure 1.2. Magnesium-Manganese equilibrium diagram.

relationship is

$$(111)\ \alpha\,\mathrm{Mn} \parallel (0001)\mathrm{Mg} \quad \text{and}$$

$$(1\bar{1}0)\ \alpha\,\mathrm{Mn} \parallel (10\bar{1}0)\mathrm{Mg}$$

DeLuca and Byrne[14] observed that the precipitate morphology after ½ hr. at 316°C. was similar to that after ageing for 3 days and that the low temperature work hardening rate increased. Observation of particle shape and distribution led them to believe that the precipitate is sheared and that cross slip was not possible because of the large aspect ratio of the particles.

There is no appreciable hardeneing effect from a precipitation heat treatment in this alloy system and manganese is added in order to confer good corrosion resistence.

Magnesium Zinc

The equilibrium diagram to 90% Zn is shown in Fig. 1.3. The section from 0-85% Zn and from 93-335°C has been studied by Clark and Rhines[15] and the diagram illustrated is according to these authors. The section of the diagram from 0-12% Zn and up to 400°C has been re-plotted and is shown in Fig. 1.4 as this section is pertinant to the present investigation.

Sturkey and Clark[16] examined alloys in the range 4-20% Zn after various thermal treatments using hardness, optical and electron metallography, (with a replica technique) and reflection electron diffraction. They reported a transition phase, $MgZn^1$ forming as rods perpendicular to the (0001)Mg after ageing for

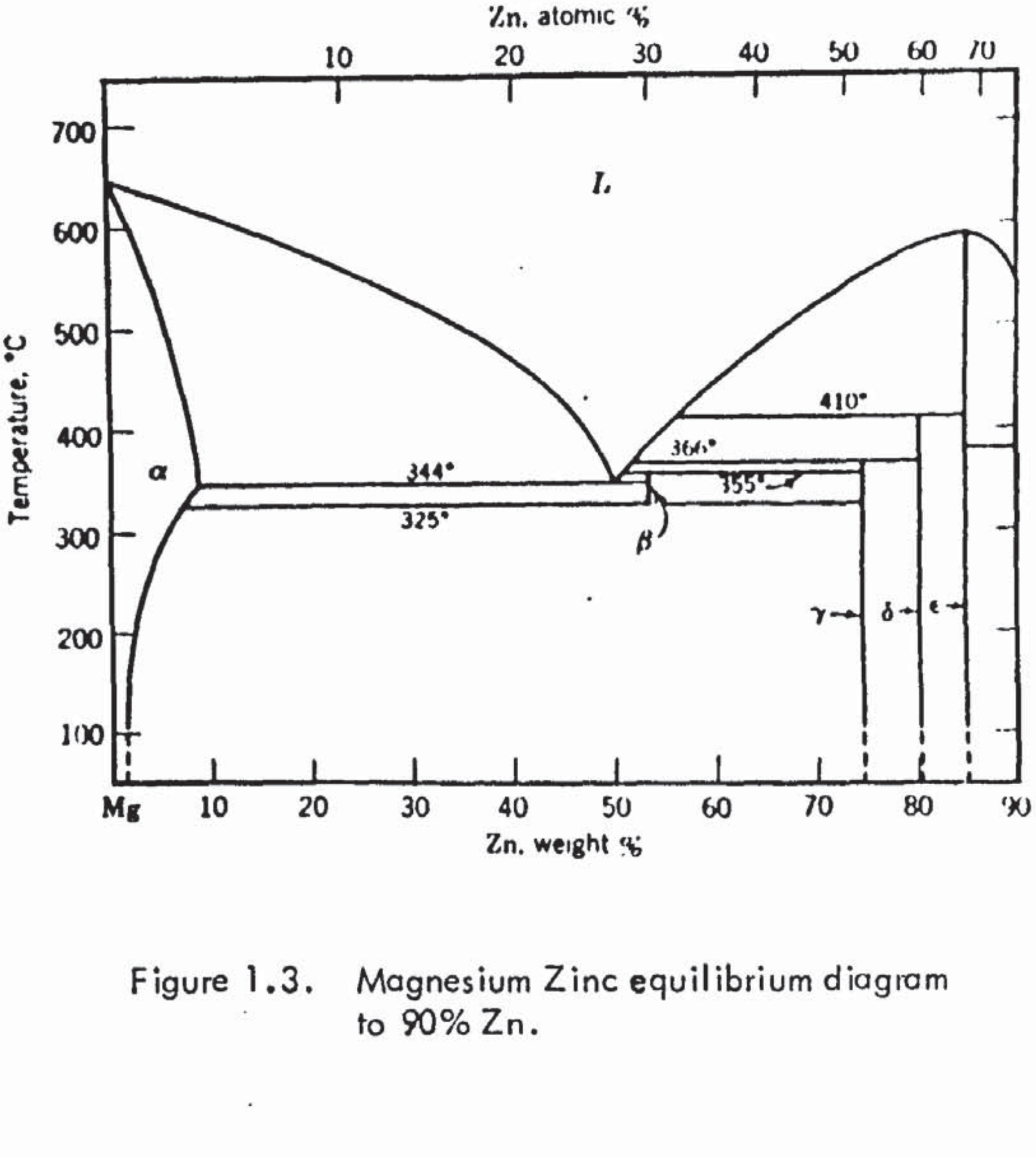

Figure 1.3. Magnesium Zinc equilibrium diagram to 90% Zn.

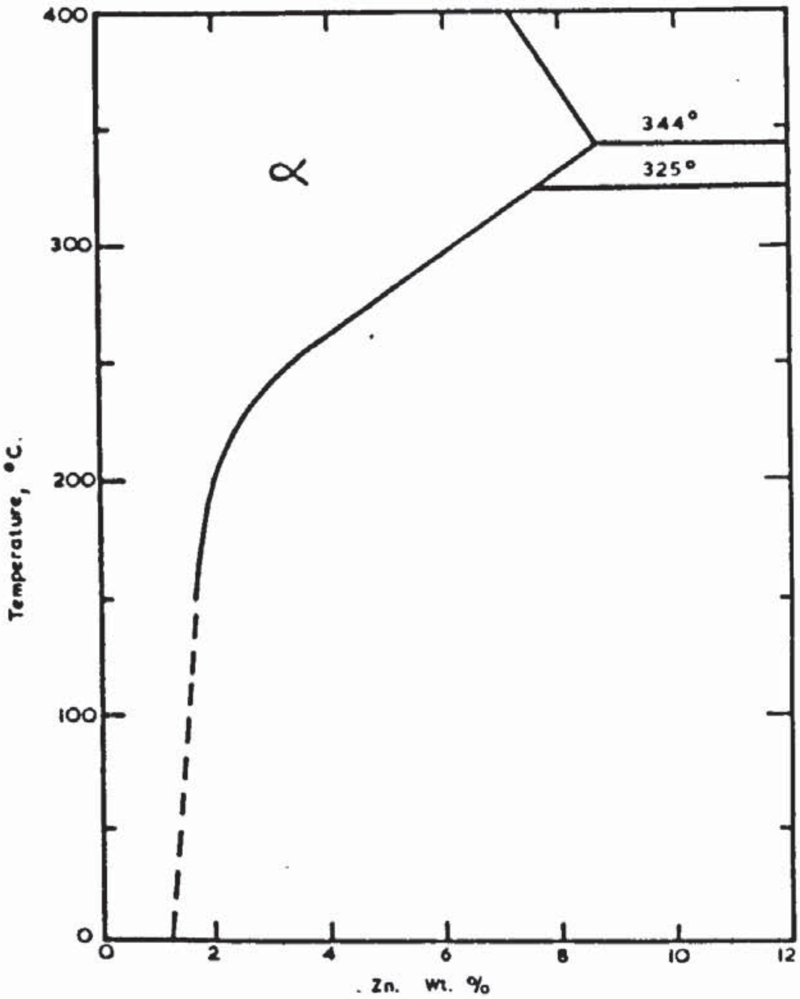

Figure 1.4. Solid solubility of Zinc in Magnesium.

1000 hrs. at 260°C.. Diffraction spots could be indexed on a hexagonal lattice, $a = 5.2A^{o}$ and $c = 8.5A^{o}$. $MgZn_2$ is reported to have a hexagonal structure $a = 5.15\ A^{o}$ and $c = 8.48\ A^{o}$ and was considered not to be the equilibrium phase. From the electron diffraction they concluded that the $MgZn^1$ rods were orientated such that their a axis was parallel to the matrix c axis and the $MgZn^1$ c axis par~~/~~allel to $\langle 11\bar{2}0\rangle$Mg.

Murakami, Kawano and Tamura[17] used X-Rays and thin film microscopy in their examination of precipitation in this alloy system. The X-Ray Laue method employed involved polychromatic radiation thus creating difficulty concerning the origin of diffusion in the diagrams. They reported G.P. zones forming on $(10\bar{1}1)$Mg planes after ageing for short times at low temperatures; 6 hours at 70°C for example. They also illustrated these zones by thin film microscopy at the surprisingly low magnification of 13,500 X. They also concluded that zone formation was hindered and precipitation of $MgZn^1$ accelerated by plastic deformation prior to ageing.

Clark[18] using thin film electron microscopy, again examined precipitation in a Mg-5.0% Zn alloy. He showed by hardness changes that a two stage ageing process was occuring with the first one being due to G.P. zones, which he could not detect. In the fully precipitated condition, complex dislocation tangles around the $MgZn^1$ rods perpendicular to (0001)Mg was considered to be the strengthening mechanism. The $MgZn^1$ transition phase gave d spacings which were only slightly different from those of $MgZn_2$. As the Burgers vectors of all dislocations contributing to plastic deformation in magnesium at room temperature lie in the basal plane, rods perpendicular to the (0001)Mg should be very effective. The comments by Byrne[10] on Clarks previous results from the Mg-9% Al alloy are also applicable to these results on Mg-5%Zn.

Gallot[3] examined precipitation in a Mg-6.0%Zn alloy by the rotating single crsystal method using mono-chromatic X-Rays and thin film electron microscopy. He was unable to prove the existence of G.P. zones by either of these methods. He confirmed Sturky and Clarks[16] results on the orientation relationship of the needles, which he calls $MgZn_2$:-

$$[11\bar{2}0]\ MgZn_2\ //\ [0001]\ Mg \quad \text{and}$$
$$[0001]\ MgZn_2\ //\ \langle 11\bar{2}0\rangle\ Mg$$

He also detected a second precipitate in the form of 'discs' on the (0001)Mg. This he termed $MgZn_2^2$ and the original $MgZn_2$ needles were given the identification $MgZn_2^1$. The orientation relationship between $MgZn_2^2$ and the matrix was determined as:-

$$(0001)\ MgZn_2^2\ //\ (0001)\ Mg \quad \text{and}$$
$$[11\bar{2}0]\ MgZn_2^2\ //\ [10\bar{1}0]\ Mg.$$

Additionally it was shown that the equilibrium precipitate is Mg_2Zn_3 with a triclinic lattice and not MgZn as thought by Clark.

The unit cell of Mg_2Zn_3 is given as:-

$a = 17.24\ A^{\circ}$ $\quad b = 14.45\ A^{\circ}$ $\quad c = 5.20\ A^{\circ}$

$\alpha = 96^{\circ}$ $\quad \beta = 89^{\circ}$ $\quad \gamma = 138^{\circ}$

The orientation relationship is given as:-

$[001]\ Mg_2Zn_3 \ // \ \langle 10\bar{1}0 \rangle Mg$ and the other probably:-

$[100]\ Mg_2Zn_3 \ // \ \langle 4\bar{2}\bar{2}9 \rangle Mg.$

Mg_2Zn_3 is observed after periods of ageing of 1-8 days at 250°C and appears as large irregular plates on the $(10\bar{1}0)$ Mg.

Hall[19] examined precipitation hardening by hardness and thin foil microscopy in Mg-6.0% Zn and Mg-6.0% Zn - 1.0% Au (the second alloy having an enhanced 'single' and 'double' ageing response as shown by Stratford[20], 1966). By employing a direct quenching technique he was able to show that the binary alloy has a G.P. zone solvus of 75-80°C whilst the ternary has a solvus of 110 - 115°C and that both alloys are capable of responding to a 'split' ageing treatment.

Lorimer[21] also examined precipitation in the same Mg-Zn-Au alloy as Hall and obtained a G.P. zone solvus of $110 \pm 5^{\circ}$C, determined by a direct quenching method. Neither Hall nor Lorimer detected G.P. zones in either the Mg-Zn or the Mg-Zn-Au alloys. Lorimer in his Ph.D. thesis has misinterpreted the results presented by Murakami et al [17] by indicating that these authors could be mistaken in concluding that G.P. zones in the Mg-Zn alloy are in the form of plates on $(10\bar{1}0)$Mg. He suggests that the plates are more likely to be needles, perpendicular to (0001)Mg as this would produce an identical streaking effect during diffraction. Murakami et al in fact reported G.P. zones as plates on $(10\bar{1}1)$Mg which is at 62° to (0001)Mg and could not be mistaken for needles perpendicular to (0001)Mg..

Additionally the enhanced response of the Mg-Zn-Au alloy was explained on the basis that the gold addition served to raise the G.P. zone solvus from 75-80°C. to 110°C. It was suggested that the addition of manganese would have a similar effect and therefore both those elements were analogous to silver when alloyed with the Al-Zn-Mg alloys in that the zone solvus was raised. It was proposed that the nucleation and growth of precipitates in these three magnesium alloys could be explained on the nucleation theory for precipitates in aluminium alloys.

Neither Hall nor Lorimer indicate foil orientation in their results. It will be shown that this is a most important factor when examining, by transmission electron microscopy a close packed hexagonal alloy in which the precipitate is in the form of needles with an aspect ratio that can be a large as 180:1.

Stratford[20] using tensile properties, examined the ageing response of a Mg - 6.0%Zn - 1.0% Mn alloy. It was demonstrated that the ageing response in this alloy was such that the 0.1% P.S. as solution treated could be more than doubled, from 12.0 t.s.i. to 25.0 t.s.i.. The elastic properties achieved were considerably better than those obtained in any other wrought magnesium alloy.

The ageing response was shown to be related to the manganese content and this was considered to be due to the formation of a ternary compound. X-Ray powder diffraction of this phase gave inter planer spacings which could be indexed on a hexagonal unit cell of a = 5.1 Kx c = 16.7 Kx and $^c/a$ = 3.26. It was also shown that the ageing response is related to the delay between solution treatment and ageing and that an increasing delay increases the maximum properties and the rate of artificial ageing.

Of practical importance is that the new alloy is capable of manufacture on an industrial scale into a wide range of extrusion shapes and sizes.

Magnesium Zirconium.

The Mg-Zr equilibrium diagram according to Schaum and Burnett[22] is shown in Fig. 1.5. and is a peritectic system with a steeply falling solid solubility with temperature, althouth there is no published evidence of precipitation of α Zr. A limit of about 0.6 - 0.8% Zr is encountered when manufacturing this alloy by normal alloying procedures. In the solid state, there is a strong tendency for the zirconium to form a hydride during thermal treatment in air circulating furnaces, due to the presence of water vapour in the atmosphere.

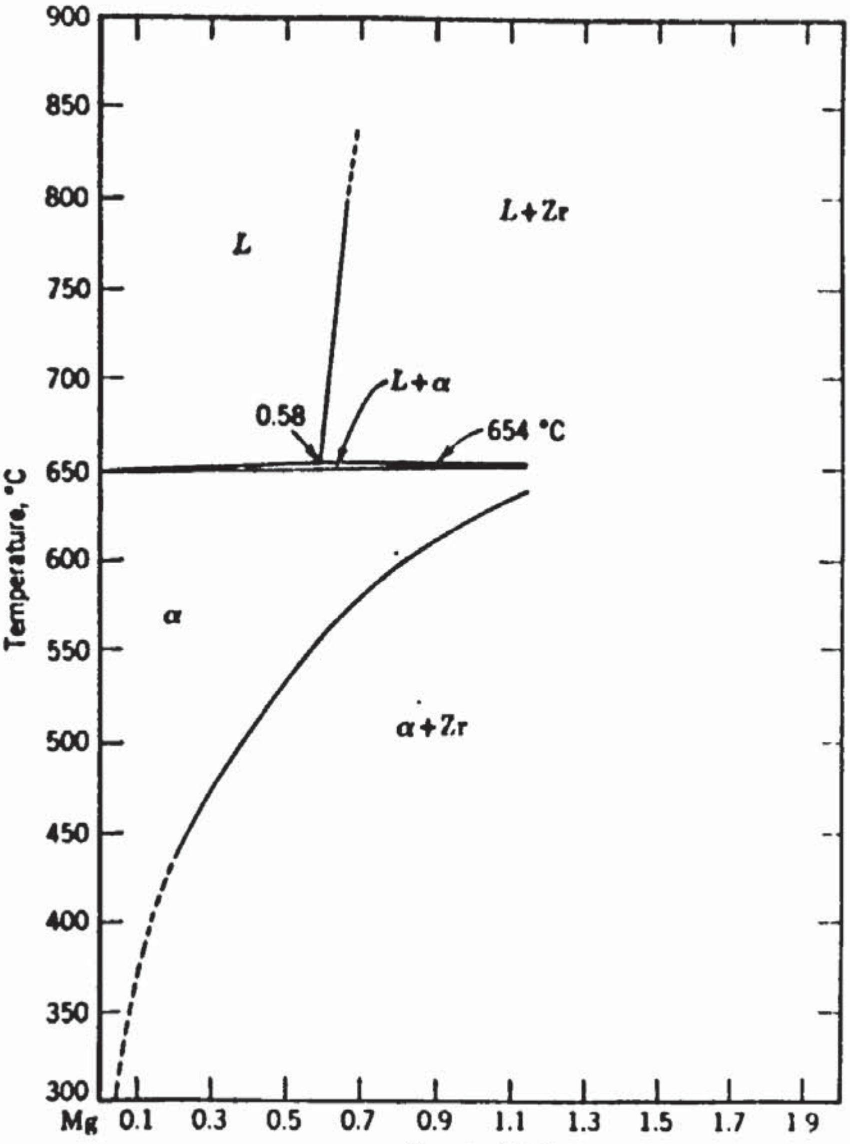

Figure 1.5. Magnesium Zirconium equilibrium diagram to 1.1% Zr.

Examination of the Mg - 0.5% Zr alloy has been directed toward creep and high temperature deformation studies and Greenfield, Smith and Taylor[23] have shown an increase in creep resistance when this alloy is heat treated in moist CO_2 at 600°C.. This was considered to be due to the formation of zirconium hydride and the grain coarsening that occurs at 600°C..

Harris, Partridge, Eeles and Rickards[24] studied the structure of zirconium hydride and showed that it was the ϵ form and face centred tetragonal with a = 4.97 and c = 4.46A°. Two morphologies were found, hexagonal discs or rectangular platelets with the major faces of the hexagonal discs parallel to $\langle 11\bar{2}0 \rangle$ Mg.

Harris and Partridge[25] concluded that zirconium hydride forms preferentially at grain boundries and on dislocations during hydriding a homogenised Mg - 0.6% Zr. alloy. They determined that precipitation also occurs during creep in a moist atmosphere and that the precipitate distribution has a marked effect on the rupture ductility. They showed a loss of rupture ductility from 50 to 3% when creep testing alloys at 400°C. which had been hydrided in the as extruded and the as homogenised condition respectively.

Mushovic[27] examined hydrided Mg - 0.6% Zr using tensile properties at various temperatures and thin film microscopy.

He detected small spherical particles apparently coherent with the matrix which had not been previously reported.

Magnesium - Thorium.

This alloy system has received considerable attention because of the good creep resistance of magnesium thorium alloys. Yamamoto and Rostoker[28] have studied this binary system and also the Mg-Th-Zr ternary system. They showed that the addition of zirconium slightly reduces the thorium content of the eutectic. Sturkey[29] using electron diffraction in the reflection geometry identified a metastable Laves phase, this preceeds the equilibrum phase which he identified as Mg_4Th. The metastable phase is reported as face centred cubic as is the equilibrium phase Mg_4Th, a = 14.3A°.

Electrical resistivity and transmission electron microscopy were used by Murakami et al[30] in a study of a Mg-4%Th alloy. They concluded that G.P. zones were formed in this alloy although the micrographs showing this are not conclusive, as with the previous results published by these authors on the Mg-Zn[17] system. The results on these two alloy systems by these authors are the only reported observation of G.P. zones in a hexagonal close packed alloy.

Magnesium - Thorium - Zirconium.

Mushovic[27] examined the ageing process in this alloy system using tensile properties at various temperatures and with thin film microscopy. There is no effect of zirconium on the precipitation mechanism and the alloy can be considered as a binary magnesium thorium alloy. He reported that thorium atoms segregated to certain lattice planes and that the first precipitate to form at 325°C. has an ordered hexagonal close packed structure with a probable composition of Mg_3Th. At longer ageing times the metastable Laves phase Mg_2Th is formed and has face centred cubic symmetry and grows as plates at right angles to (0001)Mg in a direction parallel to $\langle 11\bar{2}0 \rangle$ Mg. This is contrary to the results of Sturkey[29] who reported these plates as being on the (0001)Mg, but the evidence presented by Mushovic is conclusive.

The evidence demonstrating the initial diffusion is not conclusive as it is from an image formed using a $(10\bar{1}1)$Mg diffracted beam. The "streaking" perporting to show a perturbance of the matrix lattice by thorium atoms can also be explained by the presence of magnesium oxide on the surfaces of the foil. Using a $(10\bar{1}1)$Mg diffracted beam (d $(10\bar{1}1)$ Mg = 2.44 A°) to form an image from a foil with an oxide present (d (111) MgO = 2.43 A°) could result in the imaging of the oxide. The 'streaking' would result if the diffracted beam image was formed by displacing the objective aperture thereby causing severe astigmatism.

The orientation of the semi-coherent Laves phase was reported to be:-

$$(111)\ Mg_2Th.\ //\ (0001)\ Mg.\quad \text{and}$$
$$\langle 220\rangle Mg_2Th.\ //\ \langle 11\bar{2}0\rangle\ Mg.$$

The electron diffraction pattern from which this was determined is remarkably similar to one published by Hales, Dobson and Smallman[31]. These authors examined oxidation of pure magnesium by beam heating in an electron microscope and showed a preferential oxide/metal orientation relationship of:-

$$(111)\ MgO\ //\ (0001)\ Mg.\quad \text{and}$$
$$\langle 220\rangle MgO\ //\ \langle 11\bar{2}0\rangle\ Mg.$$

In a second publication by Mushovic and Stoloff[32] the original diffraction pattern is again presented but printed slightly differently. This clearly shows two continuous rings, the inner arising from a spacing of 2.1 A°, the outer from 1.48 A° and the outer one shows intensity maxima close to the $(11\bar{2}0)$Mg diffraction spots as reported by Hales et al.

$d\ (100)\ MgO = 2.106\ A^o \quad I/I_1 = 100$ and

$d\ (220)\ MgO = 1.489 \quad I/I_1 = 52$, A.S.T.M. index.

Intermetallic Compounds.

Before presenting the results of this investigation it is prudent to examine the published results with regard to the intermetallic compounds in the MgZn alloy system. A general outline has been given in the literature review but it is proposed to examine the compounds in more detail, particularly $MgZn_2$. Included in this examination is the ternary Mg-Zn-Mn intermetallic identified by the author in a previous investigation[20]. The intermetallic compounds in question are Mg_7Zn_3, Mg_2Zn_3; MgZn, $MgZn_2$ and the ternary Zn_4Mg_3Mn. The data for the first three are from Clark and Rhines[15] and for $MgZn_2$ from the A.S.T.M. index.

The spacings of the ternary compound from previous work, have been redetermined with chromium radiation instead of copper to enable the large d spacings to be measured with increased accuracy. The interplanar spacings are illustrated graphically in Fig.1.6(a) and (b).

Spacings calculated for two hexagonal unit cells based on a = 5.2. c = 8.48 A° and a = 5.24 c = 17.1 A° are also included. The former is the supposed unit cell for $MgZn_2$ and the latter, the unit cell giving the best fit on a Hull-Davy chart for hexagonal symmetry for the ternary compound.

$MgZn_2$.

Referring to Fig.1.6(a) and (b), the important fact to note is that the measured inter-planar spacings cannot be completely accounted for by the calculated spacings, additionly an interplanar spacing as large as 5.2 A° is not possible with the unit cell

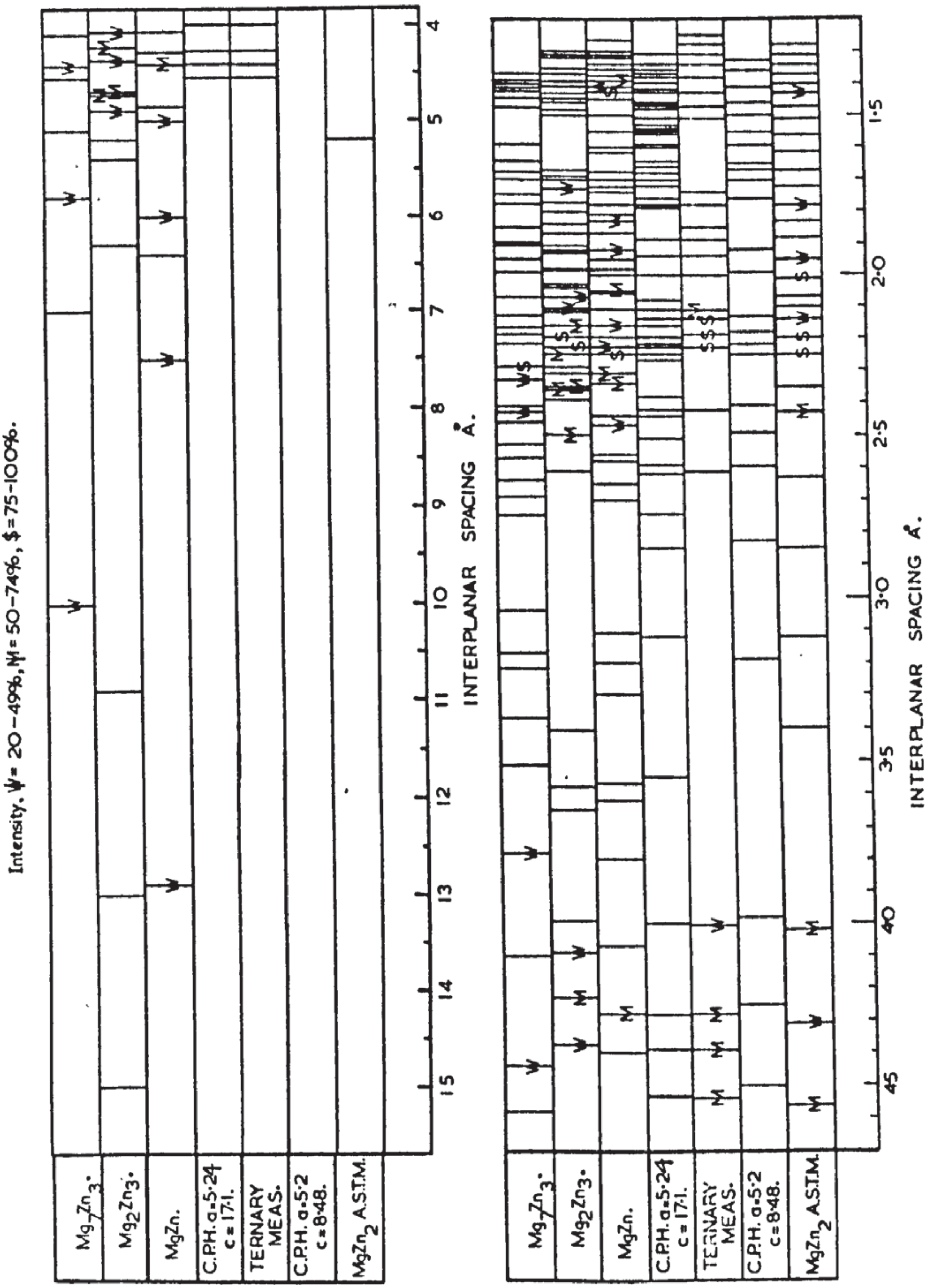

Figure 1.6. Interplanar Spacings of relevant compounds.

indicated.

The spacings used for this phase in the present investigation are based on the calculated values. Gallot[3] determined the structure of $MgZn_2^1$ (needles) as hexagonal a = 5.2 c = 8.5 A° and $MgZn_2^2$ (discs) also hexagonal a = 5.2 and c = 8.48 A°. He concludes from similarities in intensities that these are both $MgZn_2$ as given in the A.S.T.M. index although he does not mention the serious discrepency between the calculated d spacings from such a unit cell and those from the index.

MgZn.

This according to Clark and Rhines[15], is the equilibrium phase, although more recent work by Gallot[3] has shown that the equilibrium phase is Mg_2Zn_3. MgZn is reported to be hexagonal with a = 5.33 and c = 8.58 A° although certain weak reflections indicate that this cell should be doubled.

McKeehan[42] suggests the structure is better described as an orthorhombic structure with

$$a_1 = \sqrt{3}\,a \quad (10\bar{1}0) \quad = \quad 9.23\ A^o$$
$$b = a \perp (11\bar{2}0) \quad = \quad 5.33\ A^o$$
$$c = 17.16\ A^o$$

Mg_2Zn_3 and Mg_7Zn_3

Gallot[3] determined the unit cell of Mg_2Zn_3 as tri-clinic. with

$a = 17.24$ A° $\alpha = 96°$

$b = 14.45$ A° $\beta = 89°$

$c = 5.2$ A° $\gamma = 138°$

Mg_7Zn_3 is not stable below 325°C and has therefore not been encountered in investigations into the low temperature ageing of the dilute alloys.

Ternary Phase.

The spacings of this phase are such that a hexagonal unit cell a = 5.2 A° c = 17.1 A° can account for nearly all the observed spacings. The spacings not accounted for with this unit cell can be indexed by doubling the c spacing to 34 A°. No attempt has been made to solve this structure uniquely but the measured d spacings have been used in the present examination of the ternary alloy.

CHAPTER 2.

Theoretical Concepts.

Section 1 - Homogeneous Nucleation.

The reaction

$$\alpha_1 \rightarrow \alpha_2 + \beta$$

where α_1 is a saturated solution, α_2 the solution at equilibrium with β the equilibrium phase between two metals is perhaps the most widely used and investigated and possibly the least understood in the field of metallurgy. There are numerous complexities encountered in attempting to completely explain this reaction and many theories have been postulated. In condensed systems the major difficulty is related to the accommodation of the β phase by the α_2 phase as there are almost invariably dilatation effects accompanying the process. The elastic properties of the matrix will constrain or perhaps modify any process demanding a deviation from normal. There is an added complication in that initially the precipitate is generally coherent with the matrix. A coherent interface by definition has no strain surface energy and this situation is approached with small interfaces. With increasing area the misfit can be accommodated by elastic strain in both the matrix and precipitate. The strain energy can be removed by the presence of an interface dislocation[1] and if the number of dislocations/unit area is small then large parts of the interface can remain coherent and the whole interface termed semi-coherent.

A large number of dislocations/unit area results in a complete loss of coherency and gives an incoherent interface. Any anisotropy of elastic moduli of the matrix can have a significant effect on precipitate orientation and coherency with the matrix. Any change in anisotropy with temperature will be important as most reactions are carried out at relatively elevated temperatures.

Nicholson[33] has discussed some recent ideas on precipitate nucleation in alloys, distinguishing between a thermally activated nucleation process and one where the alloy is unstable to small fluctuations in composition and decomposes spontaneously. The former is termed a nucleation and growth transformation the latter spinodal decomposition. This is illustraded in Fig. 2.1 which is an hypothetical free energy/composition diagram.

The composition of the supersaturated alloy is represented by C_I with a free energy F. The composition of the matrix and precipitate at the reaction temperature is represented by Cm and Cp and free energies Fm and Fp. initial composition C_I free energy F decomposes to Cm and Cp and free energies Fm and Fp, the free energy of the system falls from F to an average free energy shown by F_1. At earlier stages the average free energy is lowered, as illustraded by the line connecting C^1m to C^1p with an average free energy of F_2. There is therefore a continuous lowering of the energy in the system accompanying transformation, and this process represents spinodal decomposition.

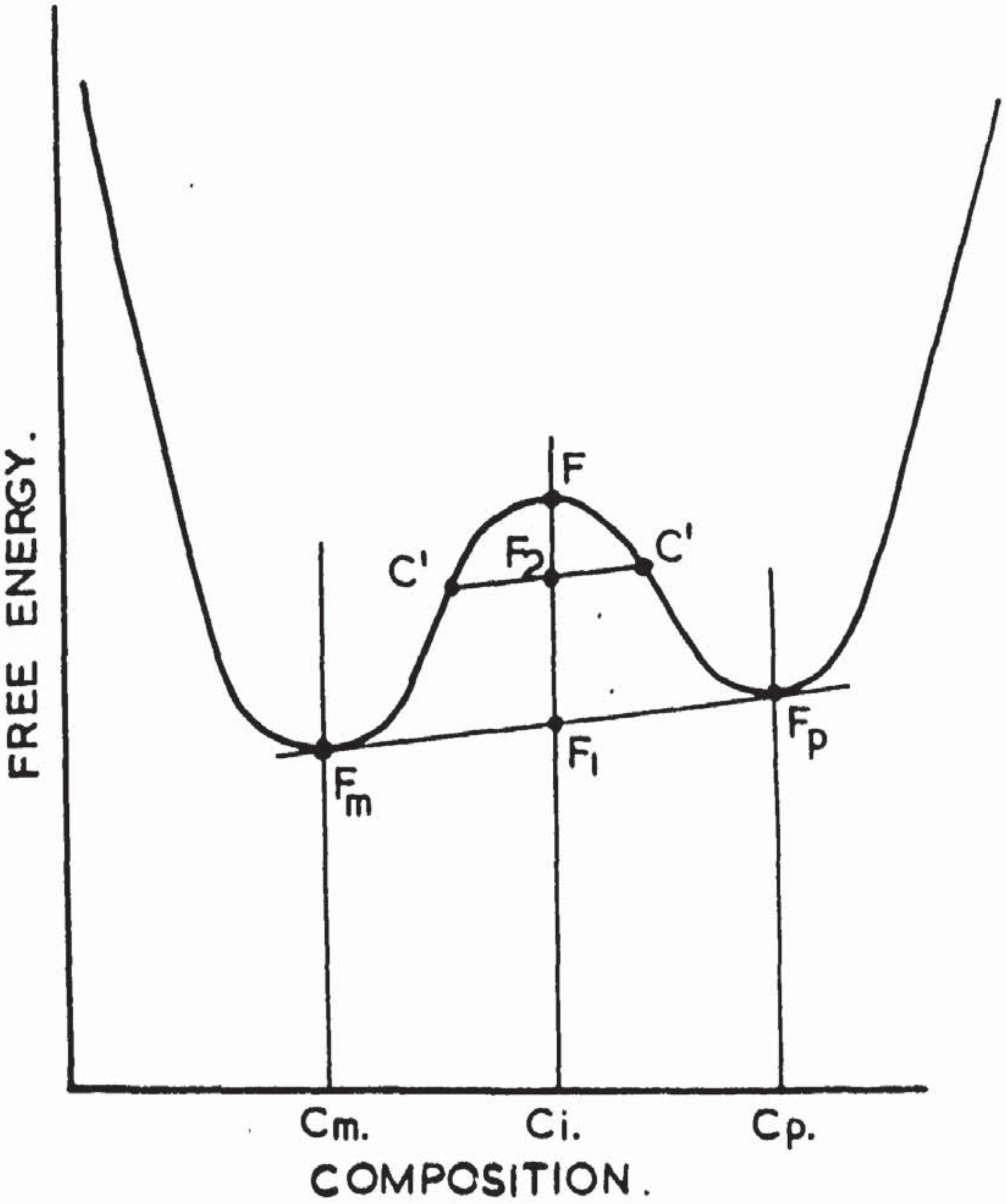

Figure 2.1. Hypothetical free energy/composition diagram illustrating spinodal decomposition.

A second example is shown in Fig. 2.2 but in this instance the initial composition C_I is displaced towards Cm. C_I will decompose as before to Cm, Fm and Cp, Fp with an average free energy F_1. It is evident that at the very early stages of transformation a situation is reached where a rise in the average free energy is demanded. This is illustrated by the line joining an intermediate stage C^1m to C^1p with free energy F_2. It can be seen that F_2 is greater than F and F1 and a thermally activated nucleation step is required. This is in contrast to the situation illustrated in Fig. 2.1 where there is no thermodynamic barrier to transformation. The transition between these two processes depends on the point of inflexion on the free energy curves with respect to the initial composition of the alloy. The increase in free energy is required when C_I is between Cm and $\frac{d^2F}{dc^2} = 0$ the point of inflexion on the curve. The transition between the two processes is therefore not precise.

The composition profiles for the initial decomposition in each process is shown in Fig. 2.3. Fig. 2.3 (a) shows the spinodal decomposition profile and it is typified by a diffuse interface and continued decomposition by diffusion of solute from solute poor to solute rich regions. With the nucleation and growth process the interface is sharp and continued growth takes place by solute diffusion down the solute concentration gradient as shown in Fig. 2.3 (b).

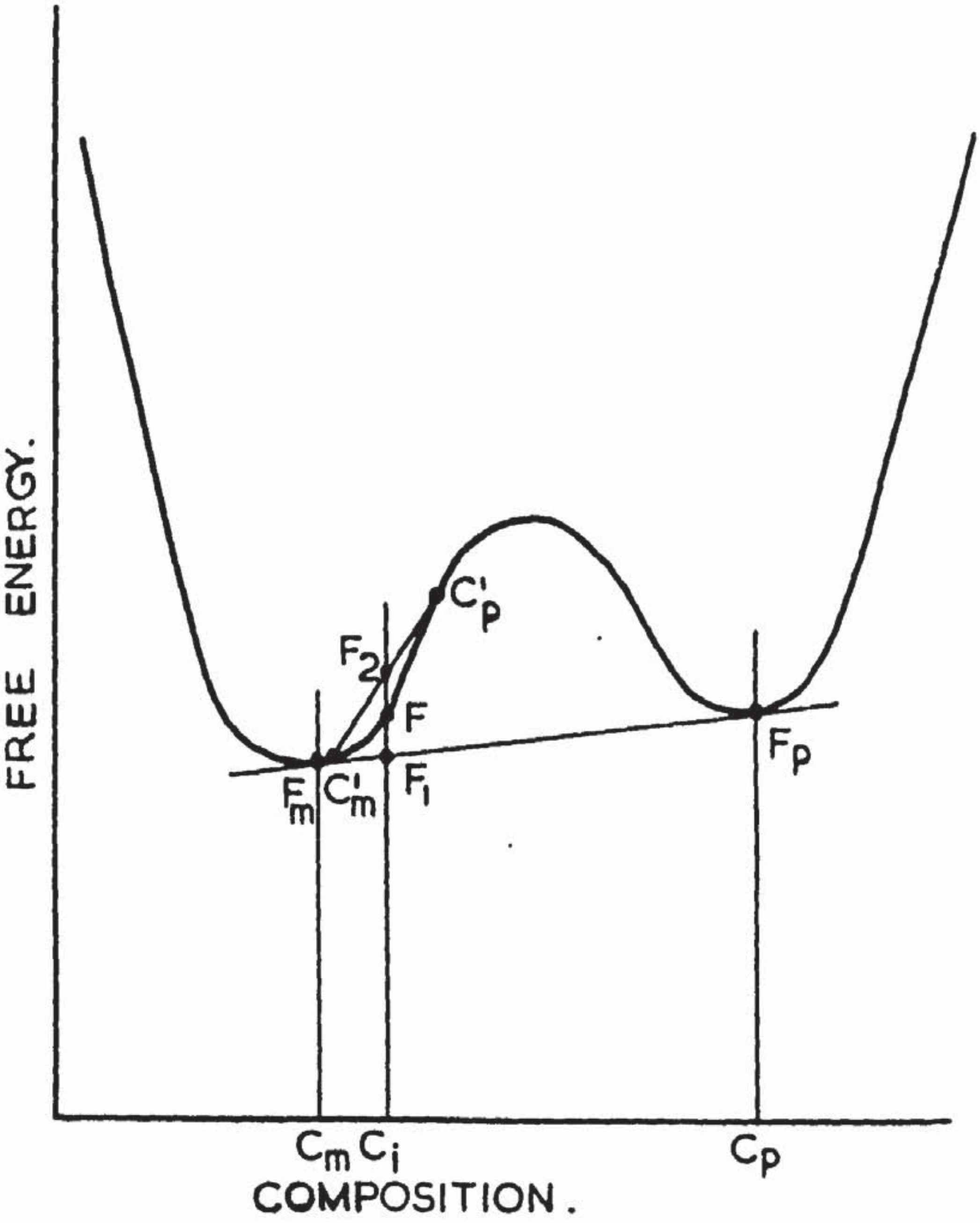

Figure 2.2. As Fig.2.1. illustrating a nucleation and growth transformation.

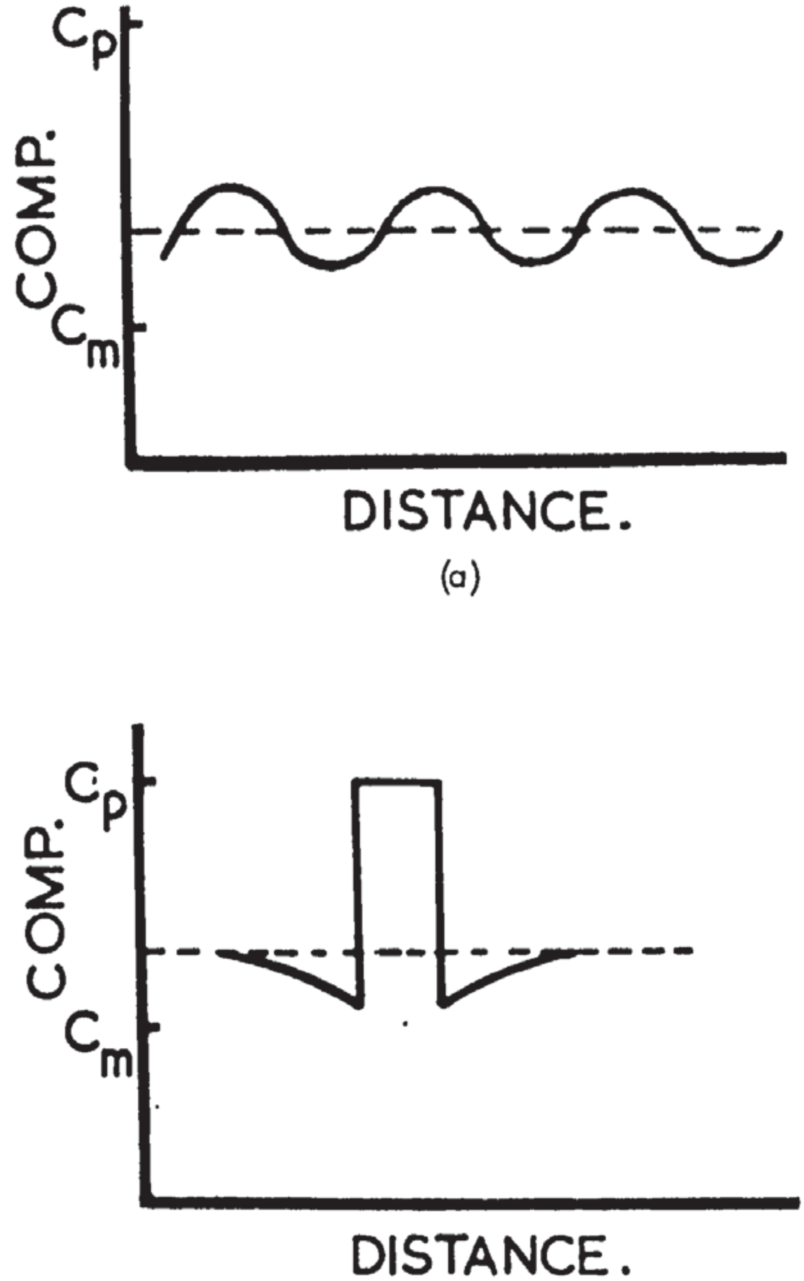

(a)

(b)

Figure 2.3. Concentration profile for
(a) spinodal decomposition, and
(b) classical nucleation and growth.

An additional important feature illustrated in Fig. 2.2. is that during the very early stages of decomposition the initial precipitate can be in equilibrium with a more concentrated solid solution than indicated by the equilibrium diagram.

The loci of the points of inflexion at different temperatures and compositions results in a further line on the equilibrium diagram, the spinodal line. This line is also a solvus and in the above case would be termed the G.P. zone solvus. This is illustrated for a general case in Fig. 2.4. Consider an alloy, composition C which intersects the two solvus lines at T_1 and T_2 °C.. If the alloy is heated above T_1 and then cooled rapidly to room temperature to produce a saturated solid solution and then heated to the $\alpha + \beta$ range between T1 and T2 only the equilibrium phase will form and below T_2 the metastable phase will form. This does not necessarily mean that the equilibrium phase will not precipitate below T_2, it means that the activation energy for zone formation is lower than for the stable phase. Fig. 2.4 can represent a particular case by adjusting the room temperature position with respect to T1 and T2. The three possible positions for room temperature are (a) below T_2 (b) between T_2 and T_1 (c) above T_1 and as (c) represents complete solubility at room temperature it will not be considered further.

If T_A, the artificial ageing temperature and RT are both below T_2 or both between T_1 and T_2 then the decomposition will

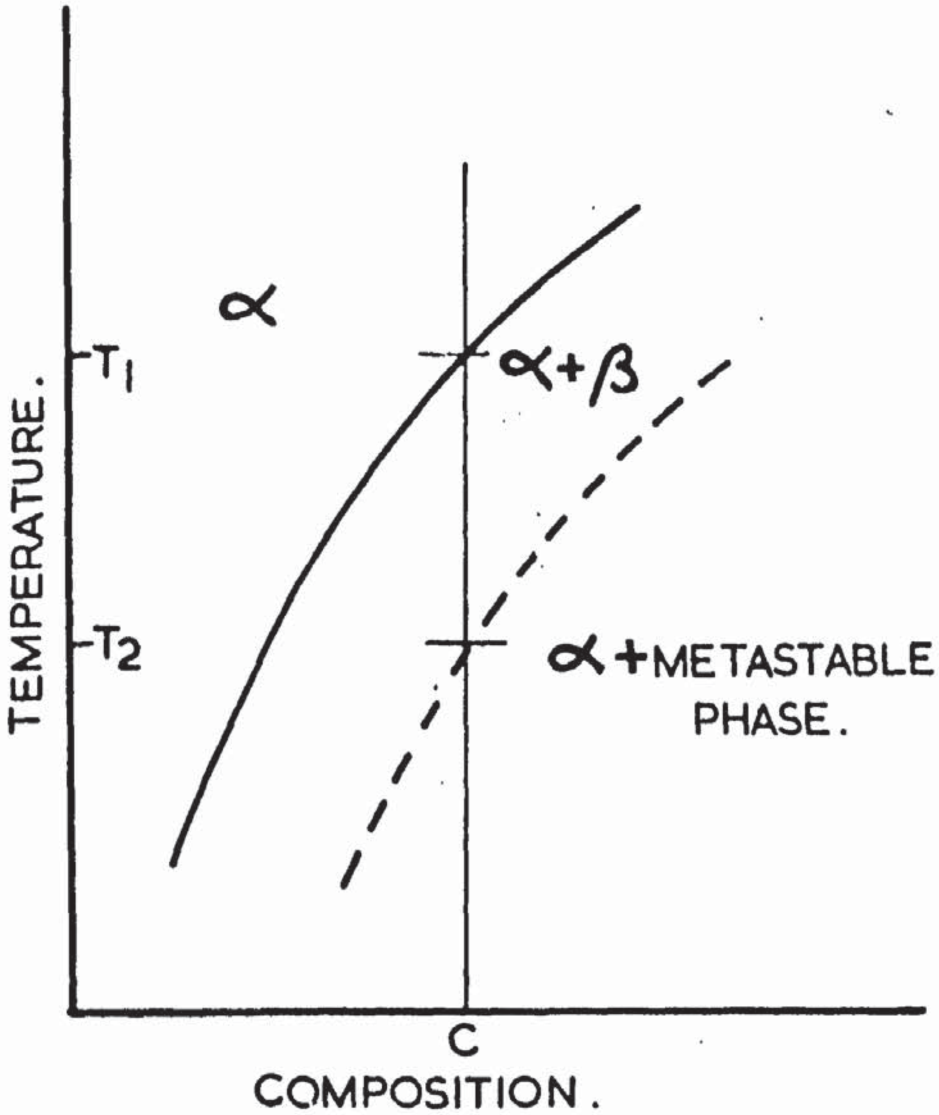

Figure 2.4. The metastable phase boundary formed by the loci of the points of inflexion in the free energy/composition diagrams.

proceed according to the equilibrium diagram. If RT is below T_2 and T_A above T_2 then dramatic changes in the transformation are possible if the metastable phase can nucleate the equilibrium phase. (It is assumed that the temperature of the quenching medium is room temperature). The metastable phase can act as a nucleus if it has reached a size d_{crit} which is stable to the rise in temperature from room temperature to the higher ageing temperature

Two theories have been proposed to explain the changes resulting from "two stage" ageing, these are the "Thermodynamic" and "kinetic" theories. The former is due to Nicholson and his co-workers and the latter to Pashley and his co-workers. This distinction is probably artificial in that any transformation process must involve both kinetics and thermodynamics. Nicholson refers to T_2 (Fig. 2.4) as the G.P. zone solvus temperature and Pashley as the temperature above which homogeneous self nucleation of clusters will not occur. Once the alloy is below T_2 (T.G.P. or Tcrit.) the two theories diverge and the "thermodynamic" approach requires that all the excess solute is out of solution in the form of clusters or zones whilst the "Kinetic" approach requires a saturated solution.

The driving force for growth in the former instance is the reduction of total surface area of the interface by a 'ripening' process, the initial clusters having formed during the quench or immediately afterwards. The kinetic theory, on the other hand, demands that zones will form and grow after the quench, due to the solute super-saturation. Both theories recognise the existence of a critical zone size which can nucleate the equilibrium phase as outlined above. In terms of zone growth these two theories are illustrated schematically in Fig. 2.5., which shows the change in number at a size with size. It is not intended that the scales on the number at size axes in Fig. 2.5 (a) and (b) are identical but it is intended that d_{crit} is the same. Fig. 2.5 (a) shows the predicted distribution curves with increasing time below T_2 for the thermodynamic and 2.5 (b) for the kinetic theory. The difference between the two theories is evident as is their similarity. They are similar in that increasing time displaces the distribution curve to the right thereby increasing the number of zones above the critical size d_{crit}, defined previously giving a progressively increasing number of zones which will nucleate the equilibrium phase. The essential difference between the two theories is in the manner in which these distribution curves change with time. The coarsening theory demands a large number of small zones growing to a decreasing number of larger zones. The kinetic theory depends on the increasing size of a constant number of zones, although there is an increase in number initially to attain this constant value.

Experiments to demonstrate this change have been performed and the effect of increasing time (t_1 to t_4) demonstrated. Because of the fineness of the structures involved, examination by thin film electron microscopy has been limited to observing the structure after ageing at a second higher temperature. Any change in structure in terms of precipitate size and distribution can be interpreted as a change in the number of zones above $d_{crit.}$ and as indicated previously both theories coincide when the zone size is greater than this value. It is therefore not surprising that the observed changes can be explained satisfactorily by both theories.

Conclusive proof will involve examining zone formation with time at a constant temperature and there are two difficulties encountered when attempting to carry out this experiment with thin film electron microscopy. Firstly there is the visibility of the zones themselves and secondly the very significant effect of foil thickness at these small particle sizes in attempting to determine the number of particles. The only satisfactory method is to examine a constant area of a solution treated and quenched sample in the form of a foil, after various intervals of natural ageing. This technique will introduce other difficulties. The foil surfaces and any vacancy effect from the surface oxide, for instance. The proximity of the zones to the surface should be dectectable by asymmetrical strain fields. If the "thermodynamic" theory is correct, zones should become visible (or be visible) then increase in size and decrease in number wheras with the "kinetic" theory an increase in size at a constant number would occur, although size should stabilize as dictated by the temperature of ageing.

A second critical size can be included in Figs. 2.5(a) and (b), that is the resolution of the microscope. It can be seen then, that both theories will predict an increase in the number visible. It is only by examining the change in the shape of the distribution curve and comparing this with the change expected from a ripening process that an indication of the correct theory will be obtained.

Section 2 - Determination of the Metastable Phase Boundary.

There are two basic techniques for locating the meta stable phase boundary these are:-

(a) Direct quenching

(b) Reversion heat treatment.

To determine the complete solvus line the experiments are repeated with a number of alloy compositions.

Direct Quenching.

The sample is heated in the single phase region and quenched to a lower temperature and maintained at this temperature for the time required to give maximum properties at that temperature normally. This is repeated for a lower quenchant and ageing temperature until a dramatic change in the quantity and size of the precipitate occurs and a refinement of about 1000:1 in precipitation occurs over a small temperature range.[34] It has been shown that quenching rate effects this temperature[35] significantly in that rapid quenching with its associated excess vacancies increases the apparent metastable phase boundary. In Al - 17.5%Zn an increase of 5°C. is observed when changing from oil to salt quenching but with Al - 1.2%Mg_2Si this difference is 30°C..[35]

Section 3 - Reversion Heat Treatments.

In this instance the sample is solution treated and quenched to room temperature and allowed to naturally age to give a sensible increase in hardness. The sample is then re-heated to various temperatures for various times and any re-solution of zones will result in a loss of hardness. Maximum loss will occur when all the zones are dissolved i.e. at temperatures above the solvus. The temperature at which the loss reaches a maximum is defined at the meta stable phase boundary temperature for that alloy composition. This technique is that developed by Beton and Rollason.[36]

Differences between the critical temperature as determined by both methods have been shown[35] and for an Al - 17.5%Zn $T_{crit.}$ by direct quenching is 160°C. and by reversion 170°C..

Section 4 - Heterogeneous Nucleation.

It has long been recognised[37,38,39] that the rate of formation and growth of zones in aluminium copper alloys is many orders of magnitude greater than that indicated by the calculated diffusion of copper, measured at high temperatures and interpolated to the ageing temperature. It is considered that an excess of thermal vacancies retained during the quench after a high temperature solution treatment is responsible for this discrepancy.

The supersaturation of vacancies on quenching is related to the solution treatment temperature T°C by

$$C_v = A \exp \left(-\frac{Ef}{KT}\right)$$

A = Constant

Ef = Energy of formation of a vacancy.

K = Boltzmann's constant.

At high temperatures C_v is considered to be about 10^{-4}/cc i.e. every 10,000th atom site is a vacancy, giving 10^{19} vacancies/cc.. At room temperature the equilibrium concentration is around 10^{-20} i.e. about 100/cc so that a loss of vacancies by nuclection of vacancy clusters or migration to vacancy sinks must occur during or immediately after the quench.

In an Al - 4% Cu alloy (approximately 2 atomic % Cu) there are 2×10^{21} atoms of copper/cc., giving a ratio of 200:1 Cu atoms : vacancies. The dramatic effect of vacancies is possibly related to the repeated transfer of solute/vacancy pairs until the vacancy is lost to a sink. Many solute atoms can therefore experience an enchanced diffusion rate from a single very mobile vacancy and the zone growth will be abnormally high.

As nucleation requires the formation of an interface within the system any location in the matrix where the surface energy is low will enable the activation energy to be decreased such that an equilibrium phase can form without the formation of a transition phase. Local areas satisfying this condition are grain boundaries dislocation lines and stacking faults. It is well known that precipitation of an equilibrium phase can occur at a grain boundary whilst precipitation is absent or at an early stage within the grain.

Dislocations can be introduced by cold work, stresses arising from quenching, and by condensation of excess vacancies. Precipitation on dislocations as with grain boundaries leads to a decrease in the surface energy term since any misfit of the precipitate can be accommodated by a decrease in the line tension of the dislocation. If the precipitate is partially coherent and its misfit vector is parallel to the Burgers Vector of the dislocation the growth rate will be enhanced and the larger the misfit between solute and solvent the greater will be the effect of dislocations. A dislocation will have little effect on the growth of a coherent precipitate.

Nucleation of precipitates on stacking faults is related to the layer of matrix with a different crystal structure and to the presense of partial dislocations and the change in activation energy.

CHAPTER 3.

Section 1 - Contrast from Second Phase Particles.

Second phase particles are primarily detected in thin films by two contrast mechanisms[40], these are:-

(a) Matrix contrast.

(b) Particle contrast.

Matrix Contrast.

Matrix contrast results from a perturbance in an otherwise geometrically perfect lattice and the ability to detect this peturbance by an alteration of the diffraction conditions. As there is a marked similarity between dislocation contrast and contrast from any strain field associated with a precipitate the contrast mechanism for a dislocation will be described and the relevance indicated.

If $\underline{g}$, the reciprocal lattice vector for a crystalline matrix is such that S, the displacement vector is not on the sphere of reflection then diffraction will not occur. If the perturbance causes local areas of the matrix lattice to rotate then g can be changed to a condition where S = 0 and strong diffraction occurs. The perturbance can then be imaged. This is illustrated in Fig. 3.1. The reciprocal lattice from the undistorted matrix is represented by $\underline{g}$, displacement vector S_2 and

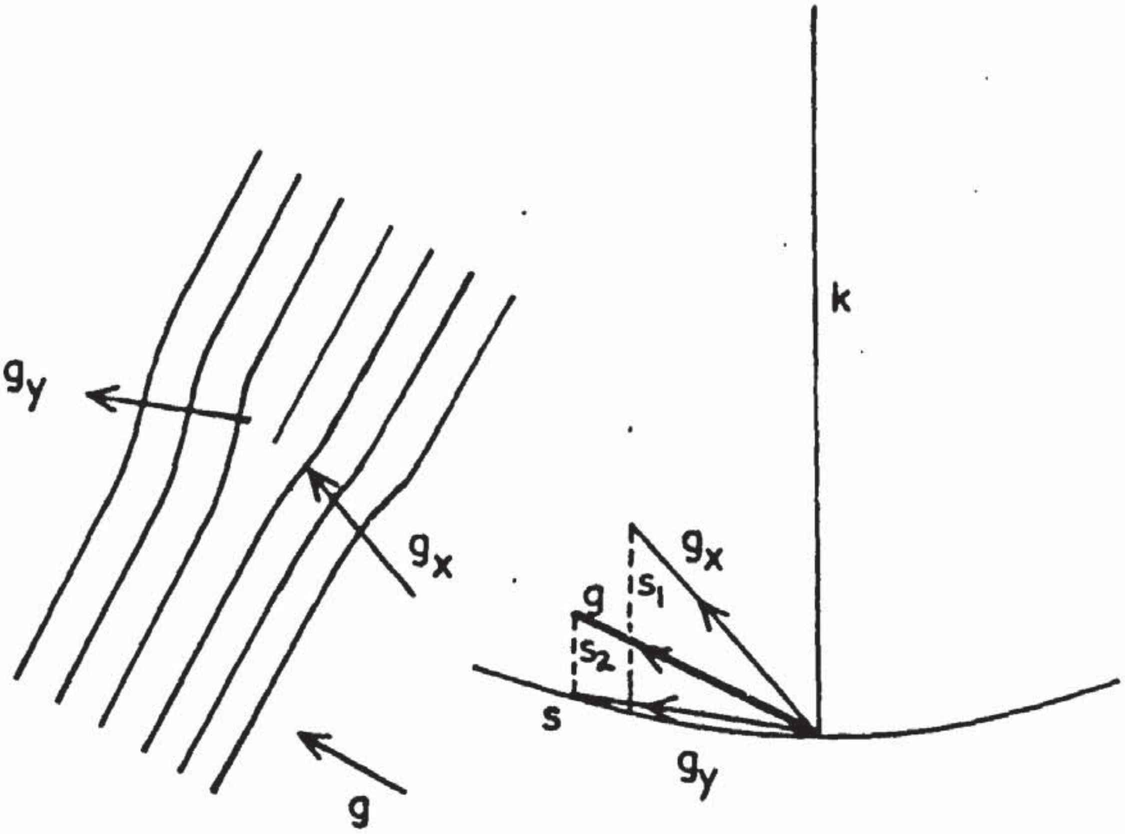

Figure 3.1. Schematic representation of the imaging of a dislocation.

as $S_2 \neq 0$ there is no diffraction. The vectors for the affected planes are gy and gx. With gx, $s_1 \neq 0$ but with gy $S = 0$ and hence gy will give strong diffraction and therefore be visible. If the specimen it tilted such that $S_2 = 0$ i.e. a bend contour, the dislocation will be invisible.

If on one side of the bend contour S_2 is below the sphere of reflection and $S_1 = 0$ and on the other side S_2 is above and $S = 0$, each half of the dislocation will be imaged on opposite sides of the contour.

The visibility of the dislocation is best understood by considering the planes parallel to the surface of Fig. 3.1. These are not affected by the presence of the dislocation and g is at right angles to the surface: g and b (the Burgers vector of the dislocation) are at right angles. The scaler product between g and. b is $/g/ \times /b/ \times \cos\theta = 0$ as $\cos 90^\circ = 0$
Dislocations are therefore not visible when $g.b = 0$

Partridge[2] gives a table of values for g.b for the first seven reflections and for $\frac{1}{3}\langle 11\bar{2}0\rangle$ $\frac{1}{3}\langle 11\bar{2}3\rangle$ and $\langle 0001\rangle$ type Burgers vectors for the close packed hexagonal structure.

Considering a second phase:- if it is not coherent or is coherent and not causing strain, no contrast will result. These two conditions are represented in Fig. 3.2 (a) and 3.2(b) respectively.

Fig.3.3(a) and 3.3(b) illustrate the case with a coherent

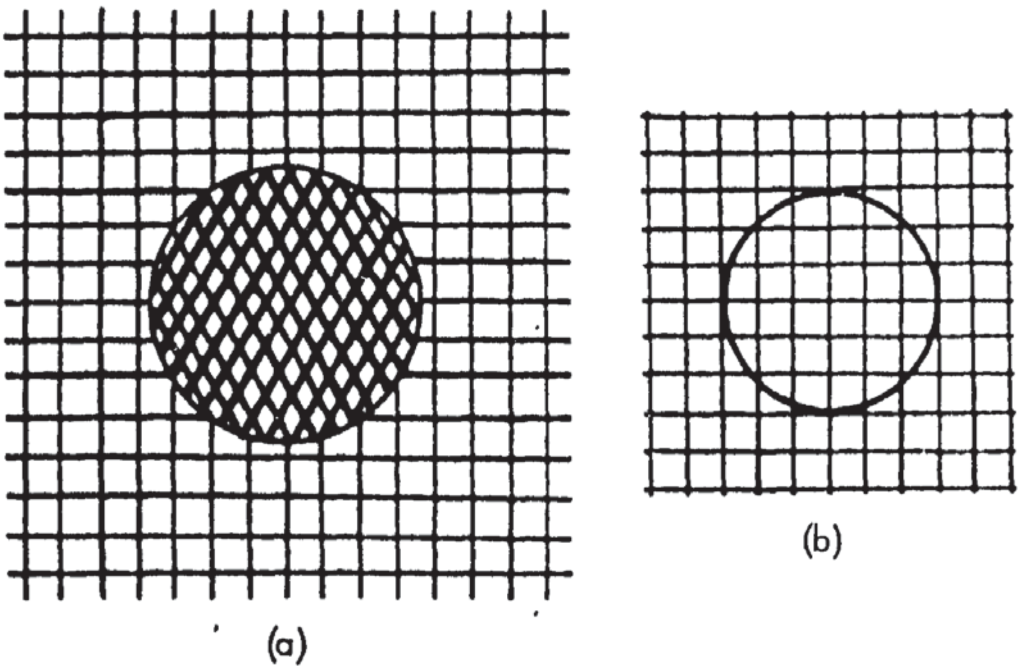
(a)

(b)

Figure 3.2. Cross section of two particles
(a) incoherent, and
(b) coherent.

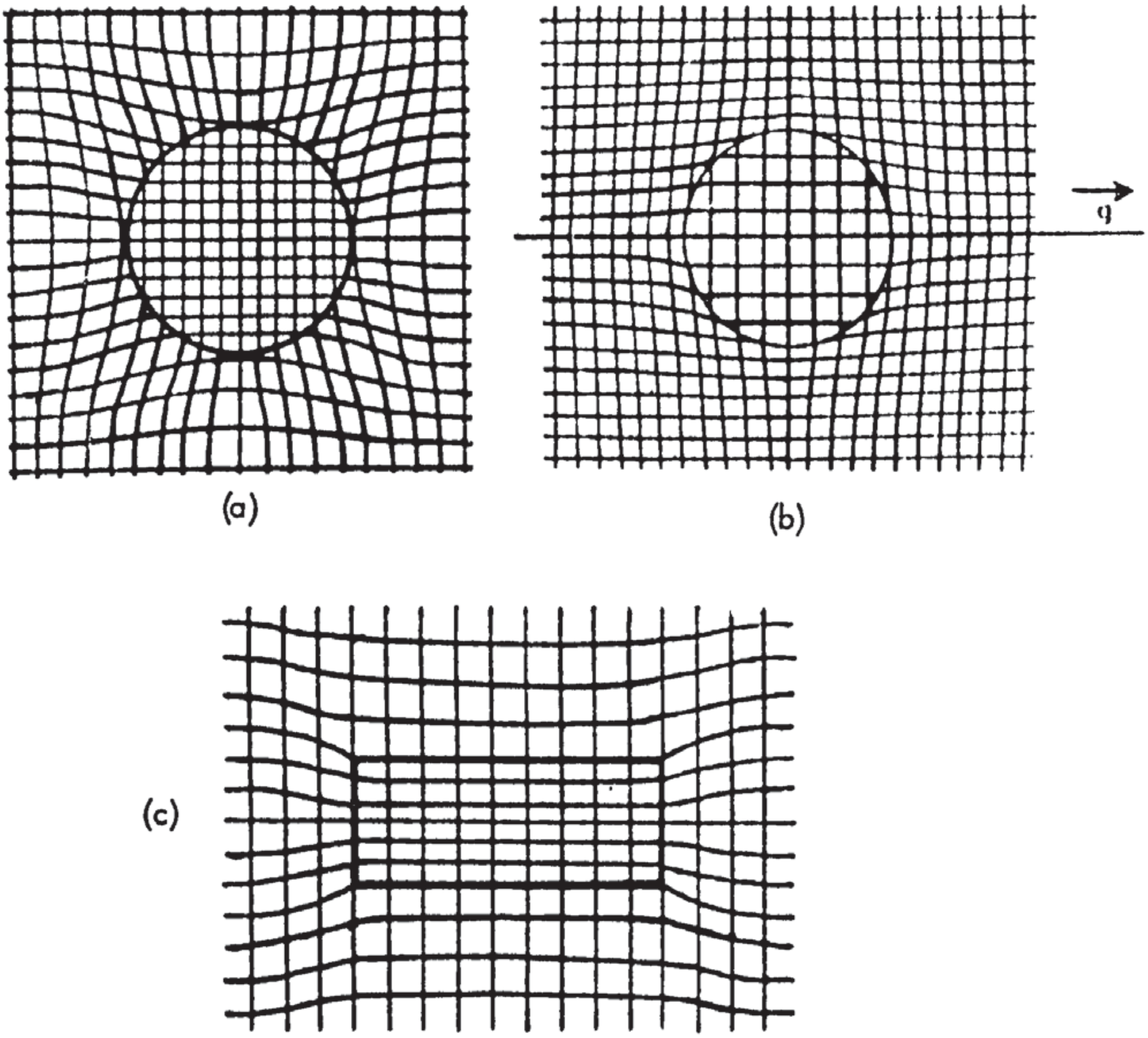

Figure 3.3. Cross section of three coherent particles with
(a) spherical particle with a negative misfit,
(b) with a positive misfit and
(c) a disc shaped particle with a negative misfit.

particle causing strain. In Fig. 3.3(a) by a negative misfit and 3.3(b) with a positive misfit. The associated matrix perturbance can be seen and therefore as with the dislocation, will be detected under certain diffracting conditions.

A 'line of no contrast' will occur and with the operating g as indicated it will be vertical through the undeviated lattice. Fig. 3.3(c) illustrates the case of a disc which is coherent on its faces and its rim. With the operating g as in 3.3(a) and 3.3.(b) ~~and~~ the "no contrast" will be vertical and widened to form a circle. The resulting appearance will be of a 'ring'.

The predicted contrast from a spherically symetrical strained particle in an isotropic matrix is shown in Fig. 3.4. after Ashby and Brown.[41] Fig. 3.5 shows the predicted variation of the image width in Fig. 3.4 as a function of $\frac{\epsilon g r_o^3}{\xi_g^2}$

ϵ = In 'situ' strain.
ξ = Extinction distance of the operating reflection
ro = Radius of the particle.

This function is analogous to the parameter g.b in dislocation contrast theory. The only unknown in the above expression is ϵ. By comparing measurements of strain fields from 30 particles of Cobalt in a Cu-Co alloy with the calculated values, good agreement was achieved. The strain is calculated from:-

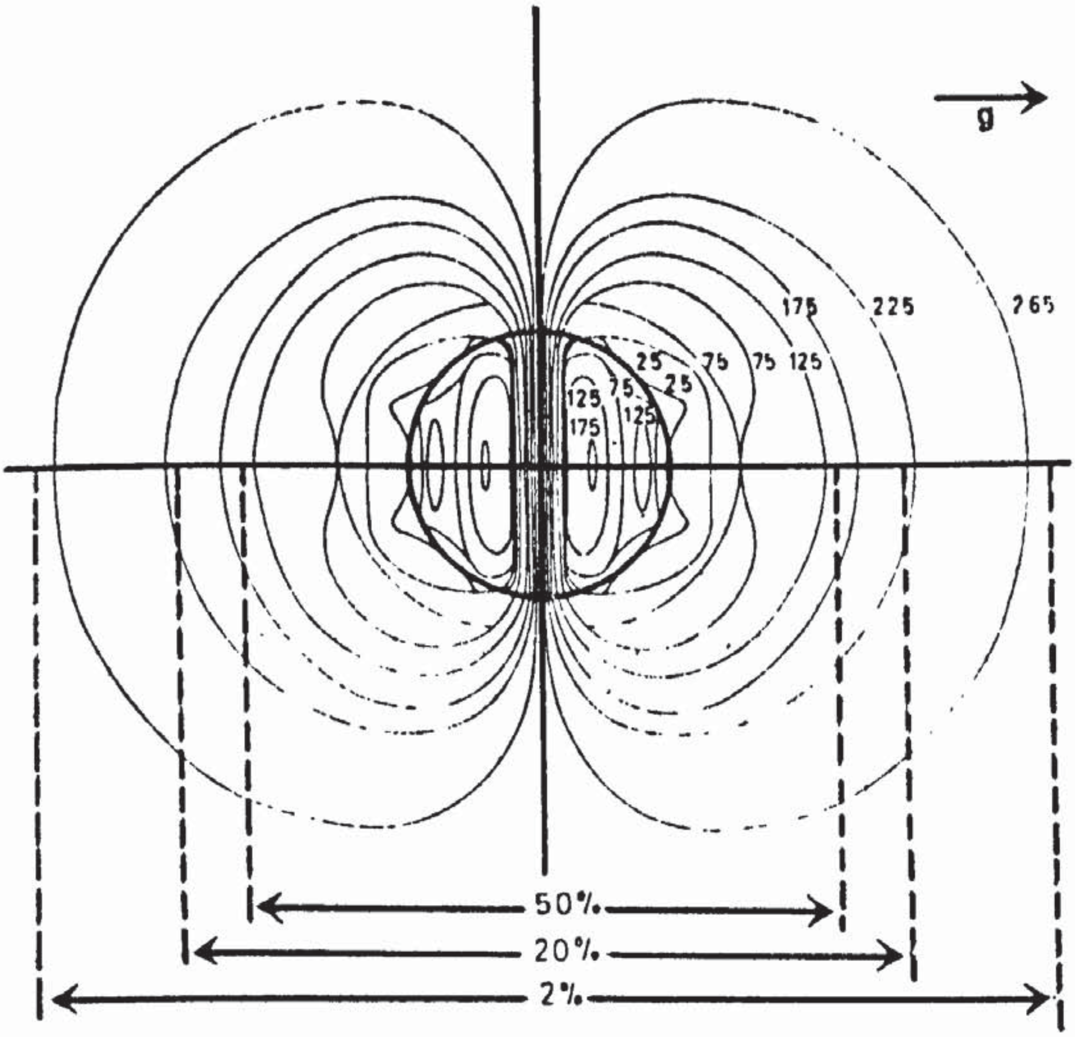

Figure 3.4. Predicted strain field image around a spherically symmetrical precipitate.

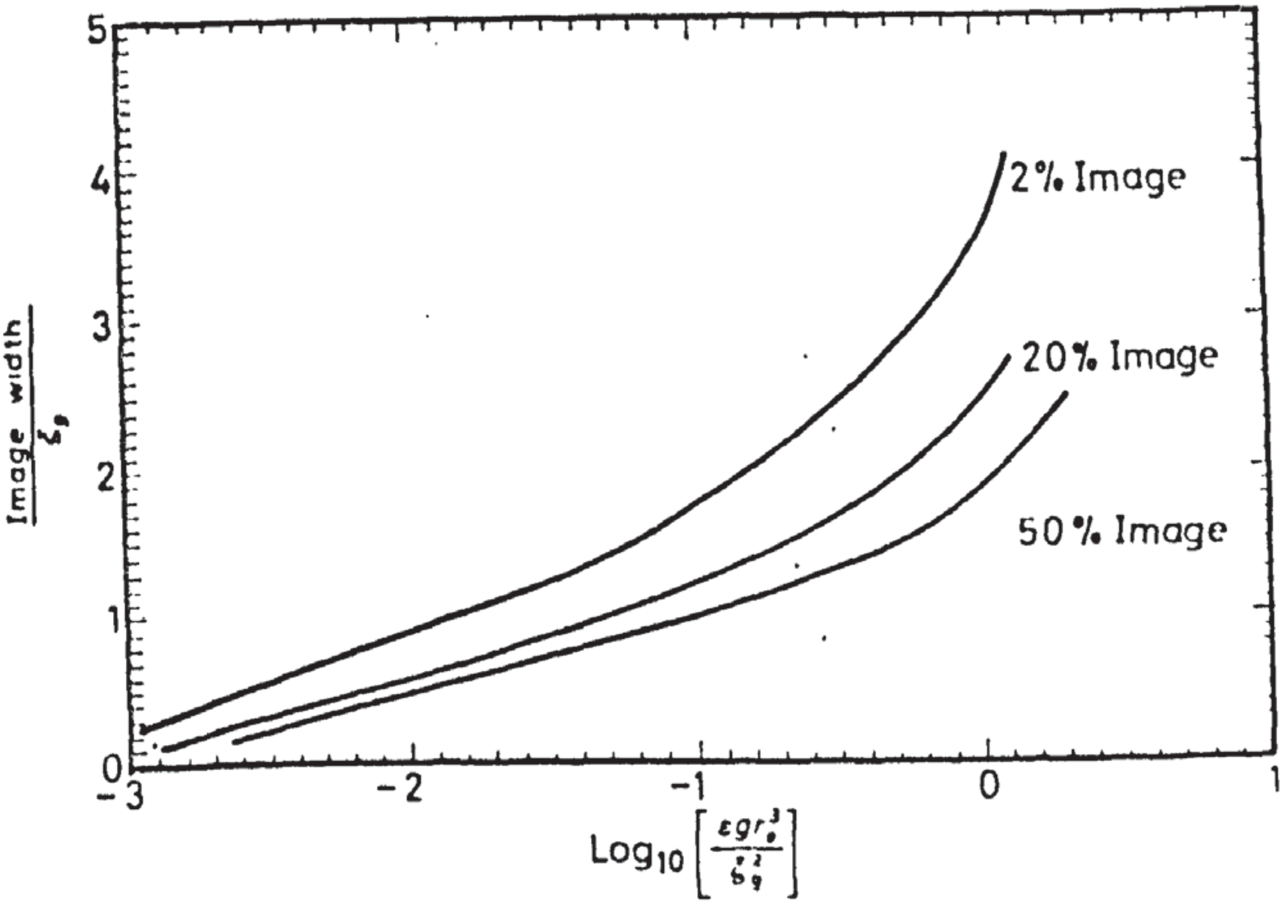

Figure 3.5. Predicted variation of strain field image width for a spherical particle as a function of the diffracting conditions, particle size and strain.

$$= \frac{3k\bar{\delta}}{3k + \frac{2E}{1+\nu}}$$

where k = Bulk modulus of the precipitate

E = Youngs Modulus of the matrix

ν = Poissons ratio of the matrix

$\bar{\delta}$ = Misfit $= \frac{2(a1 - a2)}{a_1 + a_2}$

The above technique has been extended to examine the contrast from a disc precipitate, but the whole technique is considerably more difficult. Assuming that the greatest misfit occurs normal to the plane of the disc and that the ratio radius:thickness is high a series of relationships as shown in Fig. 3.6 is obtained. In the function $\frac{R^2}{\xi^2_g}$ g.bp Cos θ

bp is related to the misfit, analogous to a dislocation loop with a perturbance of a fraction of a Burgers vector, $\bar{\delta}$ is the misfit, and strain given by $bp = \Delta t\,\bar{\delta}$ where Δt is the thickness of the disc. θ is the angle between g and the direction normal to the disc or its projected direction in the plane of the foil. The function is similar to the previous one for the spherical case with pure dilation.

There are many problems associated with these relationships and difficulties are considerable when calculating the "in situ" strain, for instance anisotropy of moduli of matrix and precipitate are complicating factors.

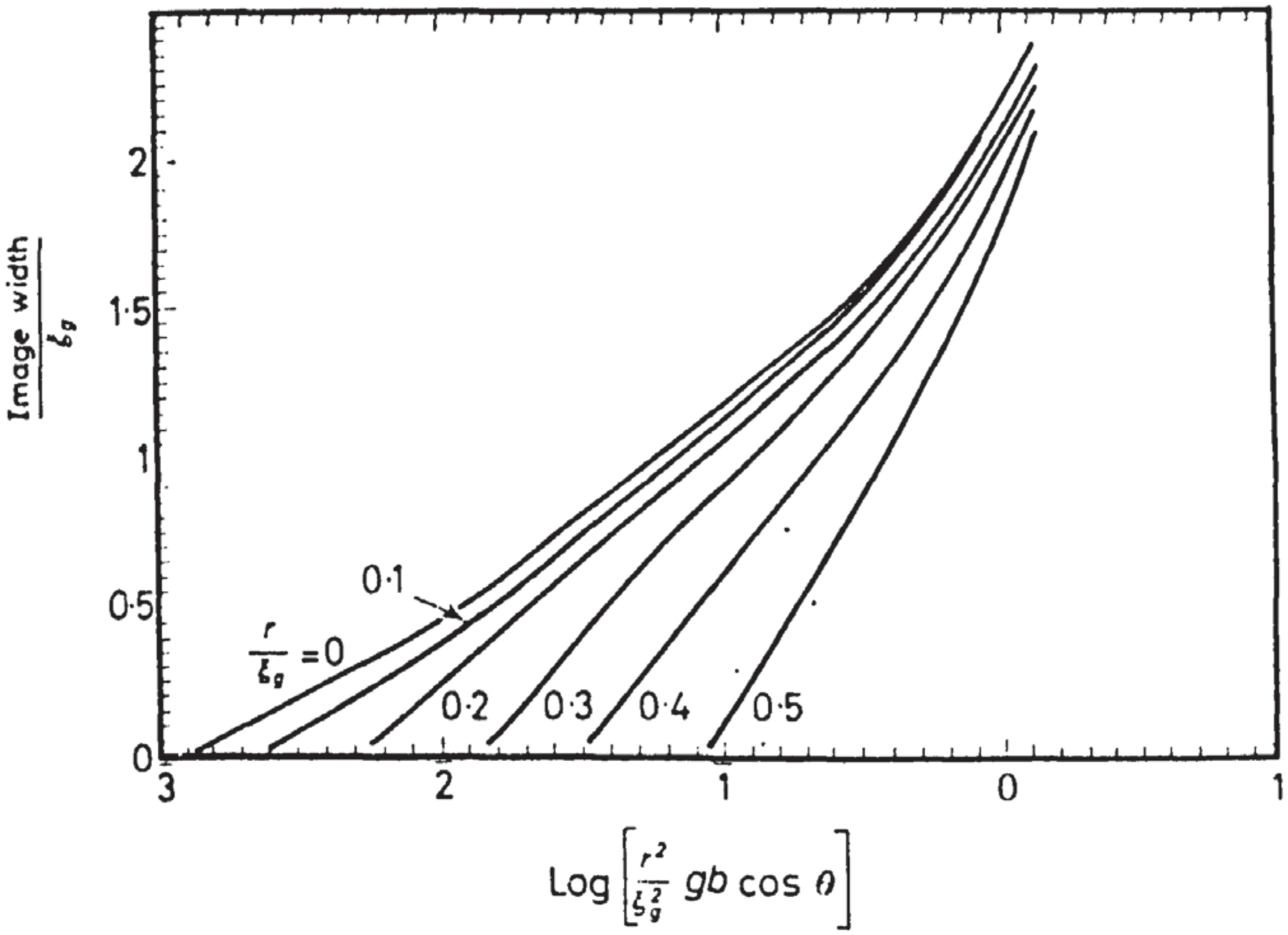

Figure 3.6. Predicted variation of coherency strain field image width for a disc shaped particle.

It is possible to use the strain field contrast to determine the sense of the strain, this is considerably easier. It is possible to determine whether the strain is negative or positive i.e. the situation shown in Figs. 3.3(a) and 3.3(b) respectively.

If the particle is within $\xi/2$ of either surface of the foil, large asymmetrical strain fields are predicted due to a surface relaxation effect. This is illustrated in Fig. 3.7 along with the analysis required to determine the sense of the strain.

Dislocation Ring Contrast.

This arises from the perturbance of the matrix and/or precipitate planes and causes contrast as for the case of a dislocation. It can arise from a coherent or partially coherent precipitate but it is generally stronger for the partially coherent condition since b is effectively large. In the case of thin disc type precipitates perpendicular to the electron beam this can be an important contrast process as other contrast mechanisms are inoperative in this condition. This has been illustrated in Fig. 3.3(c).

Section 2 - Precipitate Contrast

The second phase itself can produce contrast through four effects listed below:-

(i) Structure factor.

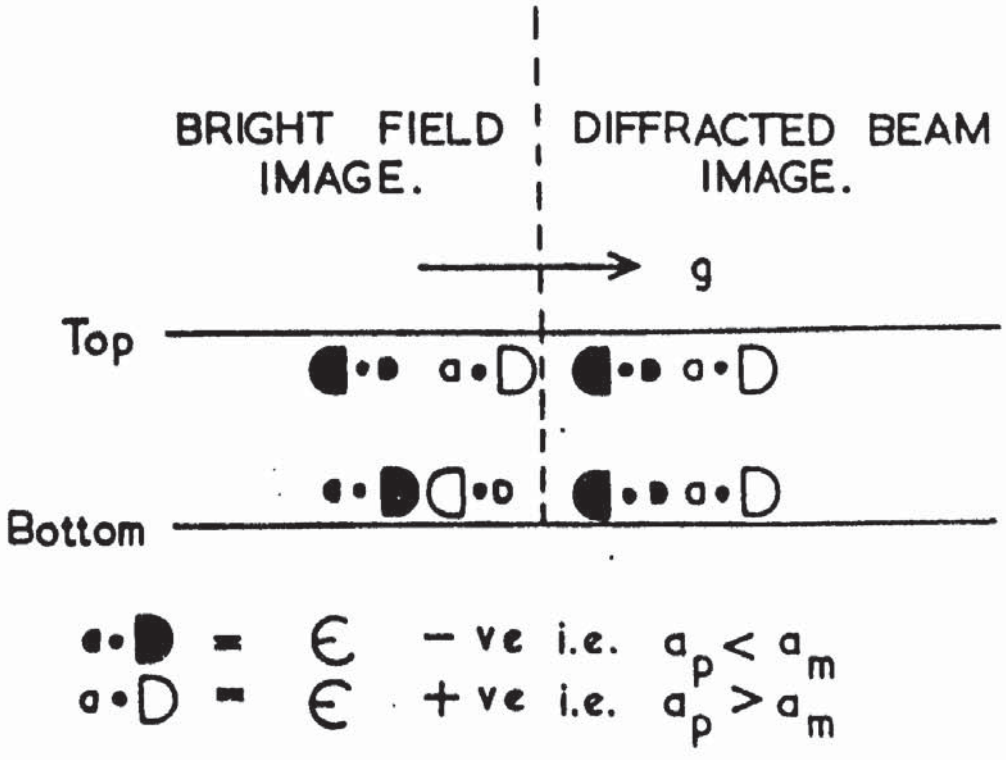

Figure 3.7. Analysis to determine the sense of strain from a precipitate.

(ii) Orientation.

(iii) Displacement fringes.

(iv) Moiré fringes

Structure Factor Contrast

This arises from the difference in extinction distance brought about by the localised presence of solute atoms and gives an apparent increase in foil thickness and contrast is possible.

Orientation Contrast

Orientation contrast results if the particle is of a size and suitable orientation to produce its own diffraction pattern. If the matrix is strongly diffracting and the precipitate is not or vice versa strong contrast results. If the precipitate is diffracting strongly Sp = 0, then conditions for diffracted beam microscopy of the precipitate are ideal. This results in simple sharp images of the precipitate if the beam can be tilted into the optical axis of the microscope.

This is the most common form of contrast encountered in crystalline solids.

Displacement Fringe Contrast

This occurs where there is a translation of a set of matrix planes which causes a change in the phase of the incident and diffracted waves. This can be caused by a semi-coherent particle, stacking fault or a grain boundary and the fringes define regions of constant depth in the foil. On a planer precipitate they run parallel to the line of intersection of the precipitate disc and the foil surface.

Moiré Fringe Contrast

Moiré fringes result when two crystals overlap. The lattice parameters can be different and the lattice planes parallel or the parameters equal but not parallel. The optical anologue of these two conditions is shown in Fig. 3.8. Fig. 3.8(a) is for dissimilar planes and Fig. 3.8.(b) for identical planes.

Additionally a perturbance in one of the lattices is effectively magnified thus allowing resolution of structures below the resolution of the microscope. The optical anologue is shown in Fig. 3.9. Fig. 3.9(a) respresents a dislocation in a parallel moiré pattern from equal lattice spacings, Fig. 3.9(b) from different spacings. The situations illustrated by Fig. 3.8(a) and 3.9(b) are to be expected from a precipitate/matrix interaction due to the dissimilar lattices.

The moiré spacing from different lattice spacings and parallel is:-

$$D = \frac{d_1 d_2}{|d_1 - d_2|}$$

d_1 = d spacing matrix

d_2 = d spacing ppte

and with equal lattice spacing but rotated

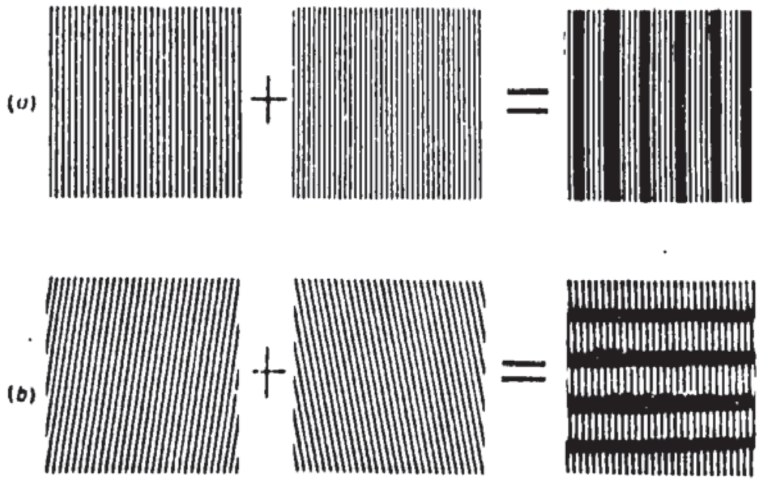

Figure 3.8. Moire patterns from
(a) dissimilar parallel planes, and
(b) similar planes not parallel.

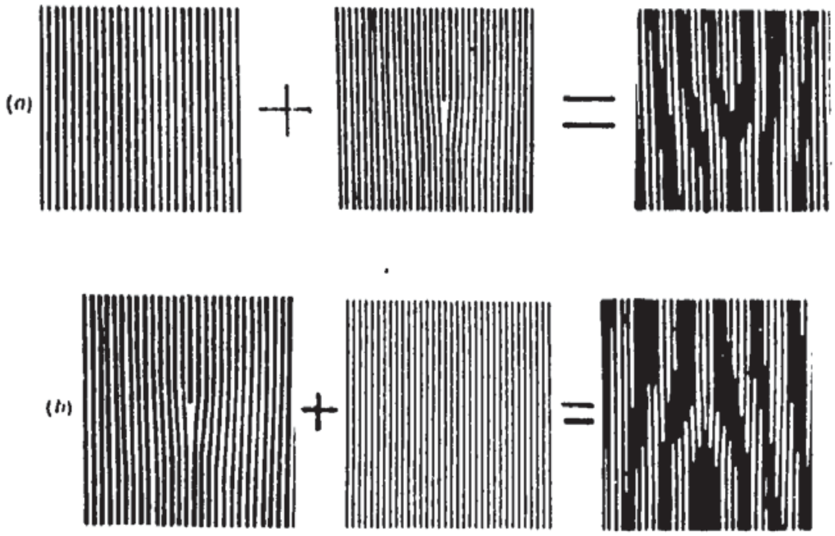

Figure 3.9. Moire patterns from planes with
(a) similar spacing with a defect in one set of planes, and
(b) dissimilar spacing with a defect in the wider spaced planes.

$$D = \frac{d}{2\sin\frac{\alpha}{2}} \qquad \alpha = \text{angle between gratings}$$

This is generally expressed as $D = \frac{d}{\alpha}$ for small angles.

With different spacings and a small rotation the moiré spacing is given by:-

$$D \simeq \frac{d_1 \, d_2}{\left[(d_1 - d_2)^2 + d_1 d_2 \alpha^2\right]^{1/2}}$$

Moiré fringes do not involve an electron wavelength function, therefore the spacing is not dependant on the accelerating voltage. Additionally as they occur when lattice planes of both matrix and precipitate are parallel, (even with a rotation pattern in the orthogonal direction) the direction of the pattern is determined by the operating reflections only.

These two factors enable the origin of any fringe pattern contrast to be established as the two conditions for moiré formation are strict and easily checked.

The alloy systems examined in this investigation have produced precipitate/matrix relationships such that all of these contrast mechanisms have been observed.

CHAPTER 4.

Section 1 - Experimental Procedure.

Preparation and Fabrication of Materials.

The alloys were manufactured from commercial purity materials by the usual industrial processes for magnesium alloys. The alloys examined were nominally:- Mg.-6.0% Zn.-1.0%Mn., Mg.-6.0%Zn., and Mg.-6.0%Zn.-0.5%Zr.; these will be referred to as ZM61, Z6 and ZW6. During the investigation it was found necessary to examine two further alloys, Mg.-0.8%Mn. and Mg.-0.5%Zr.; referred to as MN80 and ZA respectively. The composition of the alloys in the wrought condition is shown in Table I.

Table I.

Alloy	% Zn.	% Mn.	% Al.	% Fe.	% Si.	% Zr.	Grain Size*
ZM61(A)	6.14	.80	-	.010	.004	-	.005"
ZM61(B)	6.32	1.18	-	.011	.003	-	.002"
ZW6	5.92	.01	-	.005	.001	-	.001"
Z6	5.94	.01	-	.008	.010	-	.002"
MN80	-	0.82	-	.007	-	-	.060"
ZA	-	-	-	.006	.001	0.55	.080"

* Grain size after solution treatment.

The alloys were semi-continuously cast into 7 feet long billets at 2 inches per minute, the ZM61, Z6 and ZW6 into 12 inch diameter and the MN80 and ZA into $8\frac{1}{2}$ inch diameter billets. The billets were machined and cut to a suitable length for extrusion. The ZM61 and ZW6 were extruded at 400°C at 2 feet per minute and the Z6 at 330°C and 2 feet per minute. The MN80 and ZA were extruded at 420°C. at 20 feet per minute. The Z6 and ZW6 were extruded into 3 inch diameter, the ZM61 into 2 inch diameter and the MN80 into $1\frac{1}{2}$ inch diameter bar. The ZA was extruded into $\frac{1}{8}$" x 1" flat strip.

The profound effect of position in the extrusion length on tensile properties in the solution treated condition after extrusion at temperatures around 300°C. has been demonstrated.[20]

The 3 inch diameter bar was therefore chosen to enable the ageing response to be determined over the shortest possible length of extrusion. Eight 0.75 inch diameter x 9 inch long bars could be removed from a 9 inch length of this extrusion. The tensile properties of the Z6 and ZW6 are from an 8 feet length removed from the middle of the 50 feet long extrusion. The tensile properties at the front and back positions of this eight feet length were checked; the difference was insignificant.

Heat Treatment.

Samples used in the direct quenching experiment were solution treated in a fluidised bed controlled to ± 2°C. as 0.5 inch diameter x 0.025 inch thick discs and quenched and aged in an oil bath maintained to ± 0.2°C. of the required temperature. Samples for the hardness and tensile property measurement were solution treated in an air circulating furnace controlled to ± 5°C.. The specimens were solution treated as 0.75 inch diameter x 9 inch long machined bars and to obtain a constant cooling rate during quenching into water at 20°C. the bar was kept horizontal. A 0.75 inch long piece was removed from each bar for the hardness specimens. The delay at room temperature was kept constant at 2-3 minutes for all the hardness samples in Z6, ZW6 and ZM61. The tensile bars in Z6 and ZW6 were delayed for 8 days prior to ageing to compare with the results on ZM61 previously published by the author[20]. Ageing at 120°C and above was in an air furnace and below in an oil bath. This excludes the reversion experiment in which all samples were aged in the oil bath.

The ZA was homogenised after extrusion, for 96 hrs. at 600°C. in CO_2 with a moisture content of less than 30 p.p.m. at Birmetals Ltd. The hydriding was carried out in pure hydrogen.

Mechanical Properties

Hardness tests were done on duplicate samples, with three impressions per sample, using the Vickers and Rockwell machines. The Vickers machine 5 kg. Load 2/3 inch objective, was employed for detecting any reversion phenomenon in naturally aged specimens, which were 0.5 inch diameter and .0625 inch thick. All other hardness tests were done on a Rockwell machine using either the E Scale, 100 Kg. .125 inch diameter ball or the H scale, 60 Kg also .125 inch ball. In this instance samples were generally not less than 0.5 inches thick in order to avoid any interfering effect from the machines anvil, (although one experiment involved the use of 0.125" thick strip).

A discrepancy between the published results on Z6 and those obtained in this investigation was encountered, thus necessitating the use of other Rockwell machines to elminate any possible machine error. Tensile properties were determined in duplicate using 0.564 inch diameter standard test pieces with a 3 inch parallel length and elongation measured over 2 inches ($4\sqrt{A}$). The Proof Stress values were determined from load elongation curves plotted manually with an extension scale such that 0.5 inch represented an extension of .001 inch.

The tensile properties of ZM61 are those previously reported by the author[20], but the hardness values are of specimens heat treated with Z6 and ZW6 samples.

Section 2 - Preparation of Thin Foils.

A 0.125 inch thick disc was removed from the freshly sawn end of the tensile bar blanks. They were then ground to 0.015 inch thick on No.220 papers in a jig constructed for this purpose. Samples for the direct quenching experiment were ground to 0.015

inch thick prior to heat treatment. The discs were then gripped in a crocodile clip and laquered, for thinning by the 'window' method.

The published methods for preparing thin foils were tried and found to be relatively successful in that many transparent areas were always produced. Although chemical polishing only, has been employed by Clark[9], the quickest and most reproducible method for all the alloys in all conditions examined was found to be electro-polishing. This produces very large transparent areas with little tendency toward "wedge" formation; Fig. 4.1 (613) shows a typical area with at least 10,000 square microns thin enough for examination at the highest available magnification. Irrespective of the method of thinning, alloy composition and thermal history, all foils had a surface defect which precluded observation of any fine structure. The severity of this defect generally increased with solute concentration and solution treated or 'under aged' samples were particularly affected. Fig. 4.2 (969) shows the defect which is circular 'patches' relatively evenly distributed over the surfaces. These 'patches' which are 100-1500 A° in diameter are crystalline and can therefore be made to go in and out of contrast, as shown in Fig. 4.2. A second defect is also evident in Fig. 4.2 which closely resembles the structure of a polished and etched cored solid solution.

Various methods were tried to eliminate these two defects.

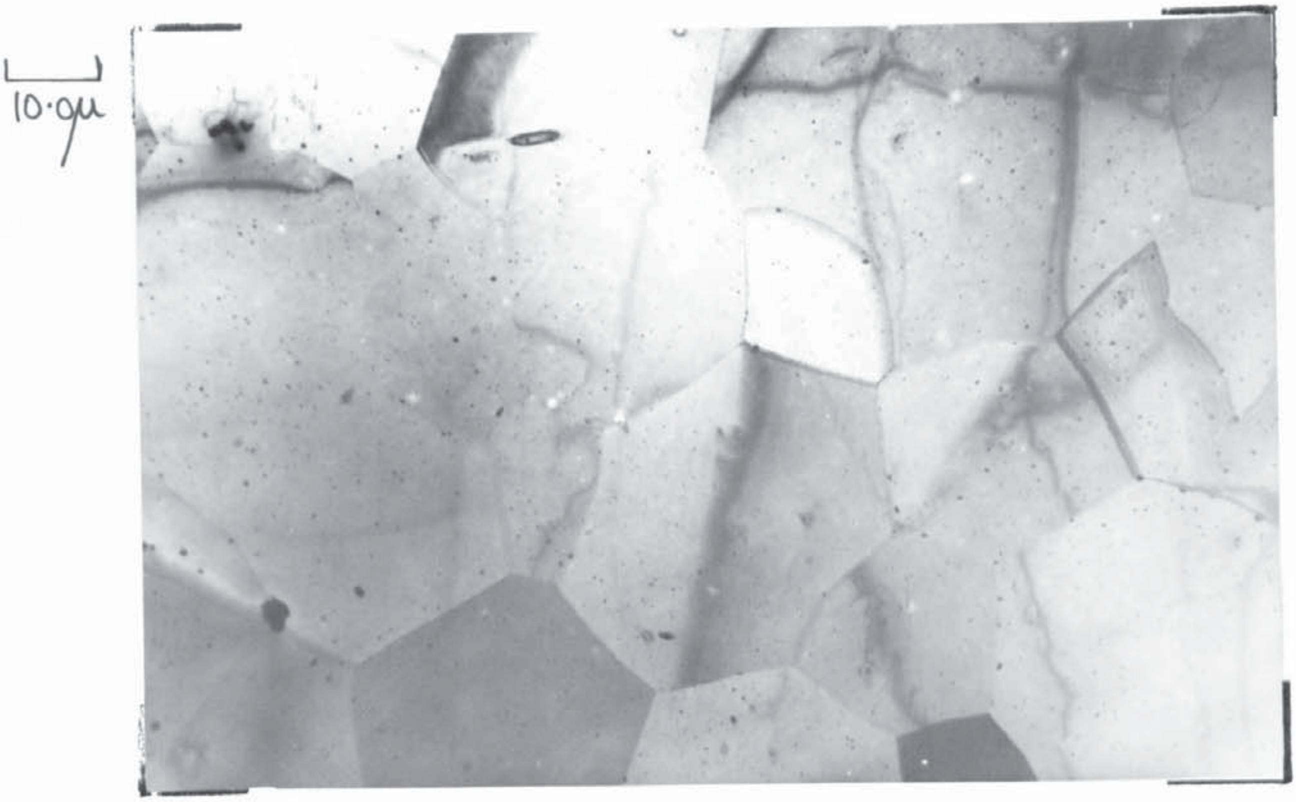

Figure 4.1. Showing a typical area produced by electro-thinning.

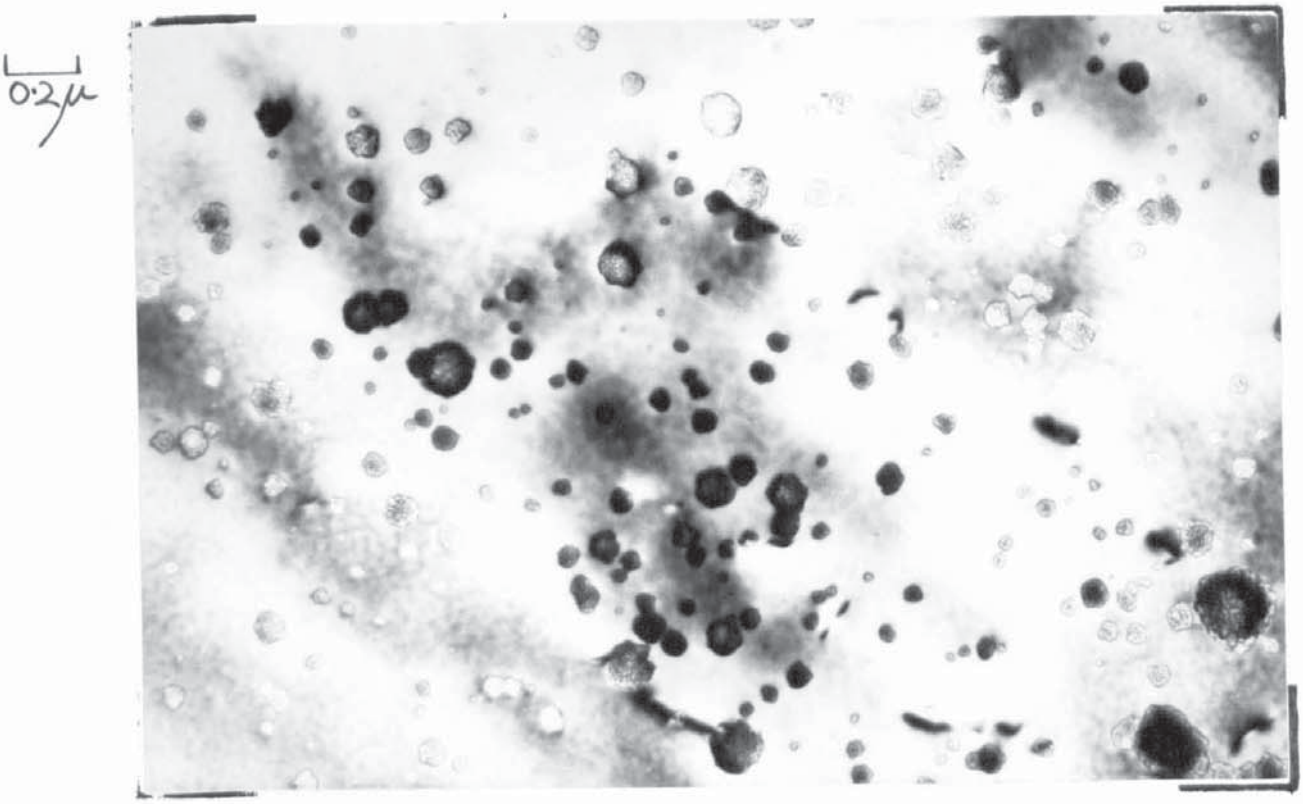

Figure 4.2. Surface defect on the as electro-thinned specimens.

The concentration and temperature of the electrolyte, nitric acid in methyl alcohol, were altered but no improvement resulted. Ethyl alcohol was used instead of methyl alcohol, and produced an improvement in surface quality. A more significant result of this charge was that the plateau on the Jaquet curve was easily detected by continuously increasing the voltage and observing the change in current. This facilitated thinning a wide range of samples with differing areas.

It was considered unlikely that an electro thinning technique would produce a good surface, therefore chemical polishing or cleaning was examined. Many solutions were tried and it was found that consistently good results were obtained with ortho-phosphoric acid. This almost eliminated the severe 'patch' defect and cleaned the surface such that the 'coring' type defect could be clearly seen, as shown in Fig. 4.3 (1281). Fig. 4.4 (1580) shows this in detail on a Z6 sample solution treated and naturally aged for 8 months. The 'patch' defect is just evident but a third defect is now apparent within the "branches" of the second defect. This takes the form of dark spots about 100 A$^{\circ}$ diameter. These three defects have no orientation relationship with the matrix as indicated by the two orientations shown in Fig. 4.4, but the size of the third defect is such that it could be mistaken for G.P. zones, particularly in this naturally aged sample.

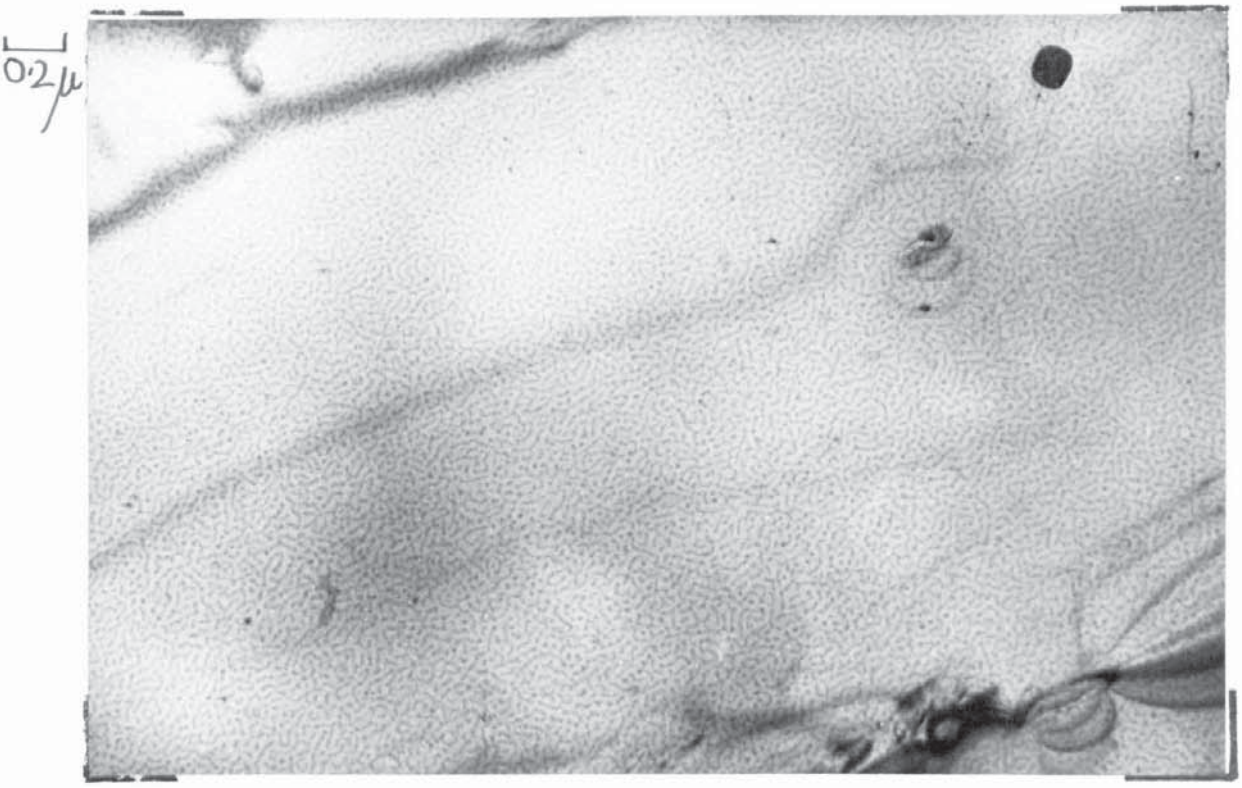

Figure 4.3. A second surface defect, resembling 'coring'.

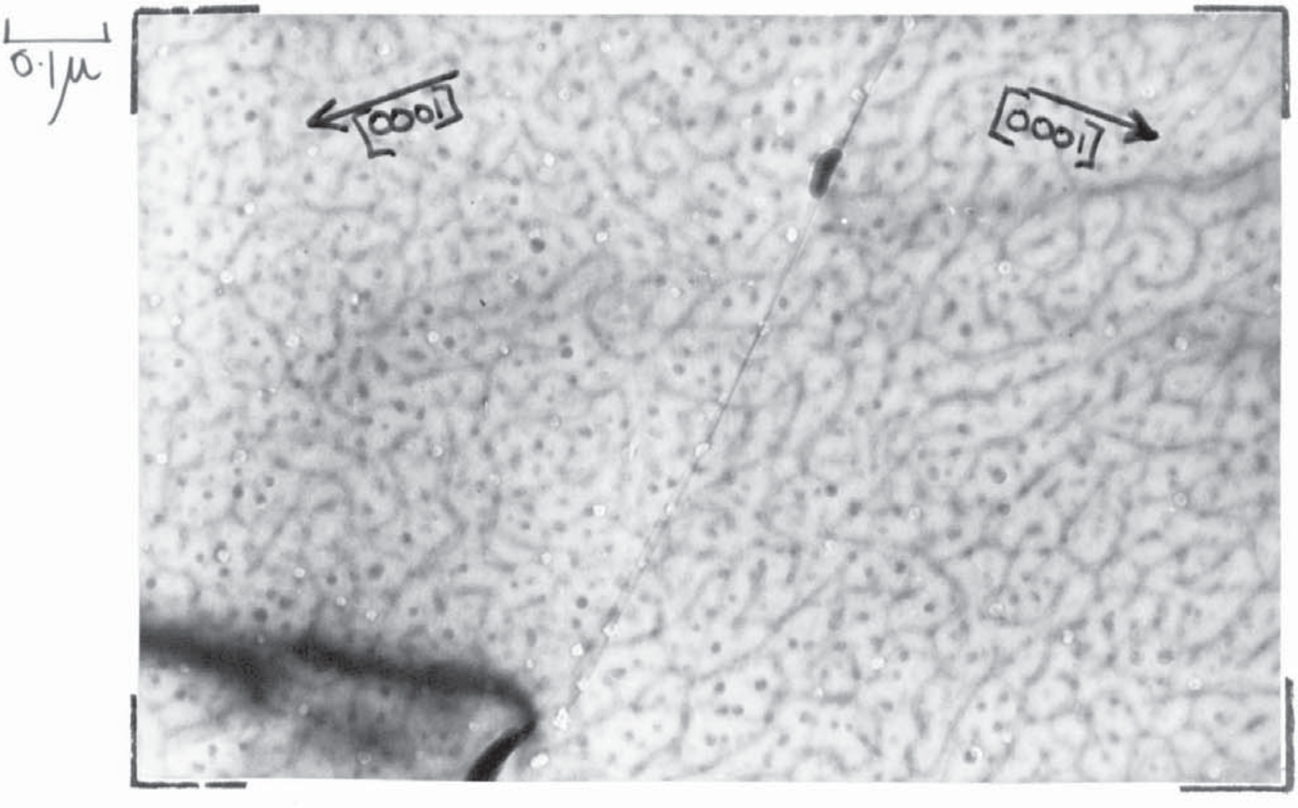

Figure 4.4. Defect as in Fig. 4.3 at a higher magnification.

It was found that on cooling the ortho-phosphoric acid to between -5 and -15°C. a clean surface was obtained. Very infrequently a fourth defect was encountered which is crystalographically related to the matrix. This is illustrated in Fig. 4.5 (385) in a sample of ZW6 solution treated and aged. This defect can be seen as large 'bands' which lie on the Mg(0001) and to a lesser extent on Mg $(01\bar{1}0)$. In this form it cannot be mistaken as a genuine structure but it sometimes takes on a more subtle form. This is shown in Fig. 4.6 (1576). In this case the defect is smaller, and not continuous as in Fig. 4.5 but it has caused large, generally symmetrical strain fields which could be mistaken for strain fields associated with precipitation.

The technique developed for producing thin foils by the "window" method and avoiding the artifacts illustrated is as follows:-

(1) Electro-polish in 33% HNO_3 in ethyl alcohol at 15-25°C., continuously agitating the sample to avoid corrugation by rising gas bubbles, until perforation.

(2) Wash the sample in absolute alcohol, and dry between filter papers.

(3) Remove a specimen for examination and insert in a folding 'oyster shell' type grid.

(4) Immerse specimen and grid into ortho-phosphoric acid, at -5 to 15°C. using the lowest temperatures for 'under aged' samples.

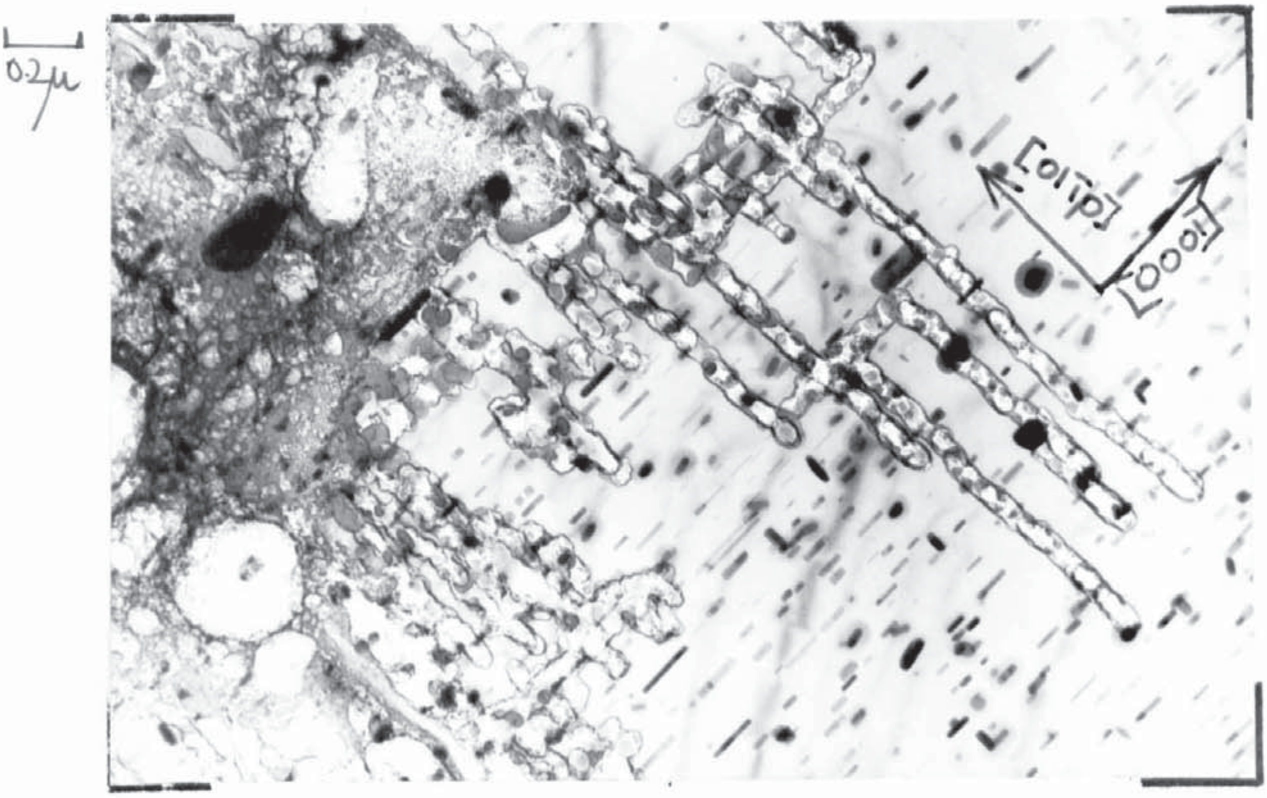

Figure 4.5. Showing a defect with an orientation relationship with the matrix.

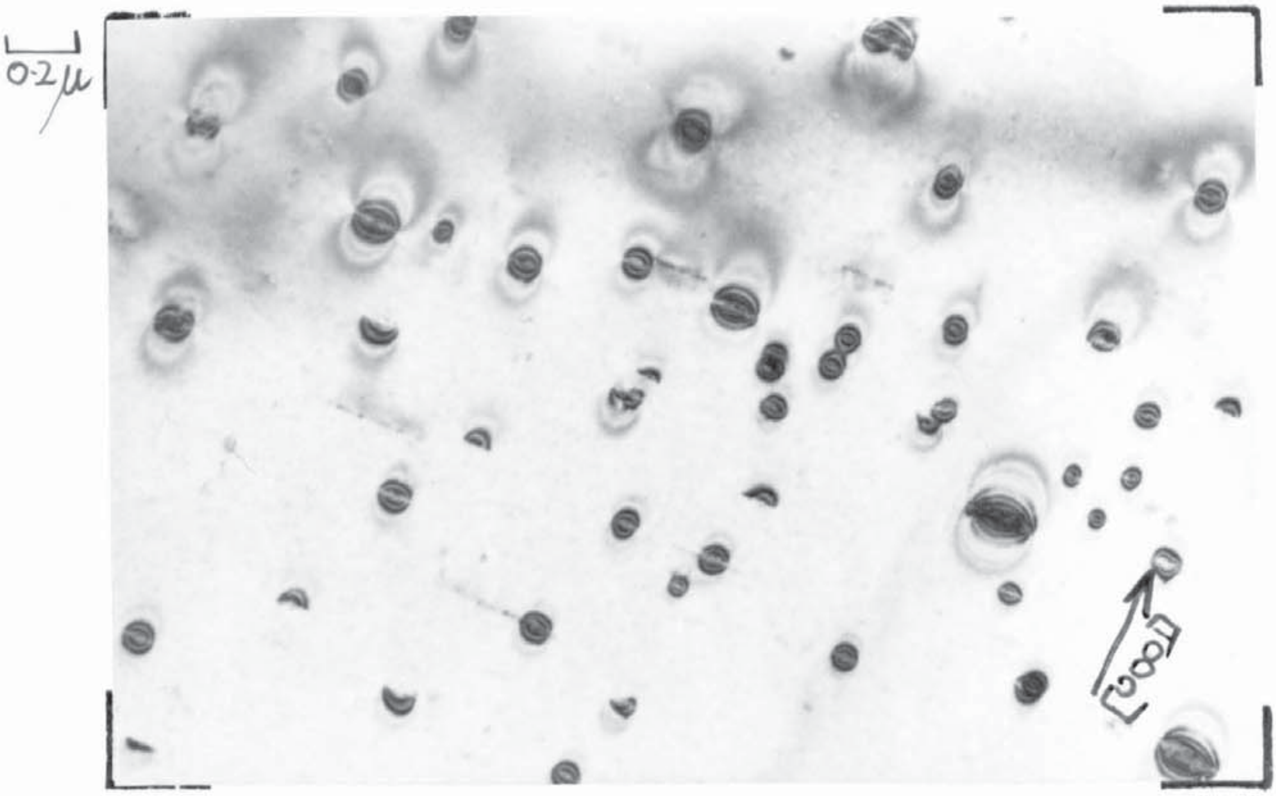

Figure 4.6. Defect as shown in Fig. 4.5. but on a very fine scale.

On immersion a delay of about 5-10 seconds occurs before the specimen and grid are hidden in a cloud of bubbles. They are agitated for 5-10 seconds, quickly removed and violently washed on both sides by a jet of absolute alcohol for 5-10 seconds and finally dried between filter papers.

It should be mentioned that on cooling the ortho-phosphoric acid a transformation, such that a temperature rise from about -20°C (its approximate freezing point) to +24°C occurs when 50cc's are cooled. The co-exsistance of a solid and liquid phase does not mean that the liquid is at its freezing point. It should be disregarded and a fresh quantity cooled.

Section (4) of this technique is extremly useful in that the sample can be re-immersed in the ortho-phosphoric acid after examination in the microscope. Two advantages result, firstly other areas of the sample are thinned sufficiently for further examination and secondly the previously thin areas are dissolved and the carbon contamination film is left behind and acts as an extraction replica. This was found particularly useful with the ZW6 alloy. Furthermore, diffraction patterns of an extract could be standardised by a matrix pattern simply by moving the specimen slightly, thereby calibrating the microscope.

Foil Orientation.

It is worth indicating the effect of foil orientation on the appearance of precipitates in an alloy with a close packed hexagonal structure. Lorimer[21] and Hall[19] make no mention of foil orientation and with a precipitate in the form of needles, foil orientation has a dramatic effect. The crystallography of the C.P.H. lattice is such that there is not the plane multiplicity as with cubic structures. With cubic symmetry for instance there are three (100) planes orthogonally disposed, whereas with C.P.H. there is only one (0001) plane. In a foil of an alloy with a cubic structure with a disc shaped precipitate on the (100) planes there are three orientations of the discs and their shape andsize can be easily detected. On the other hand with a disc precipitate parallel or perpendicular to the (0001) plane in a C.P.H. structure severe truncation can hinder an assesment of size and shape. If the foil is prepared from material with a preferred orientation i.e. thin rolled sheet, the (0001) planes in magnesium will be in or near to the plane of the sheet and foil and unless some twinning has been retained with its associated crystallographic rotation of almost 90°, the appearance in an orthogonal direction will not be appreciated. With extrusions in magnesium there is a tendency for the (0001) planes to lie parallel to the extrusion axis. A transverse sample will therefore have the $(10\bar{1}0)$ or $(11\bar{2}0)$ planes parallel to the foil surface. Hall[19] encountered preferred orientation when he mistook the discs of $MgZn_2^2$ on the (0001) planes for needles.

His foils were generally of the $\{10\bar{1}0\}$ or $\{11\bar{2}0\}$ type and this precluded an examination with the (0001) planes perpendicular to the beam and even with the (0001) planes at an angle of 20-30° it is difficult to image a disc unambiguously.

Fig. 4.7 illustrates eleven commonly occuring electron diffraction patterns for close packed metals and is taken from Partridge[2]. The crystallographic directions parallel to the beam are in square brackets and the plane perpendicular to the beam in round brackets. The spots appearing as X are forbidden reflections which can occur due to double diffraction.

It should be noted that a direction is not perpendicular to a plane of the same indices except for directions of the type $\langle 0001 \rangle$ and $\langle hki0 \rangle$. The indices of the normal to a plane (hkil) are given by

$$\left[h, k, i, \frac{3}{2}\left(\frac{a}{c}\right)^{2} l\right]$$

A foil preparation technique was developed such that samples could be removed from bulk material at various angles to the extrusion axis to enable orthogonal directions to be observed. Additionally the criticism by Byrne[10] does not apply to the results of this research. Particle spacing is from the actual bars used in determining the tensile and hardness values.

Electron Microscopy.

An A.E.I. E.M.6G. with a ± 5° tilting goniometer stage and

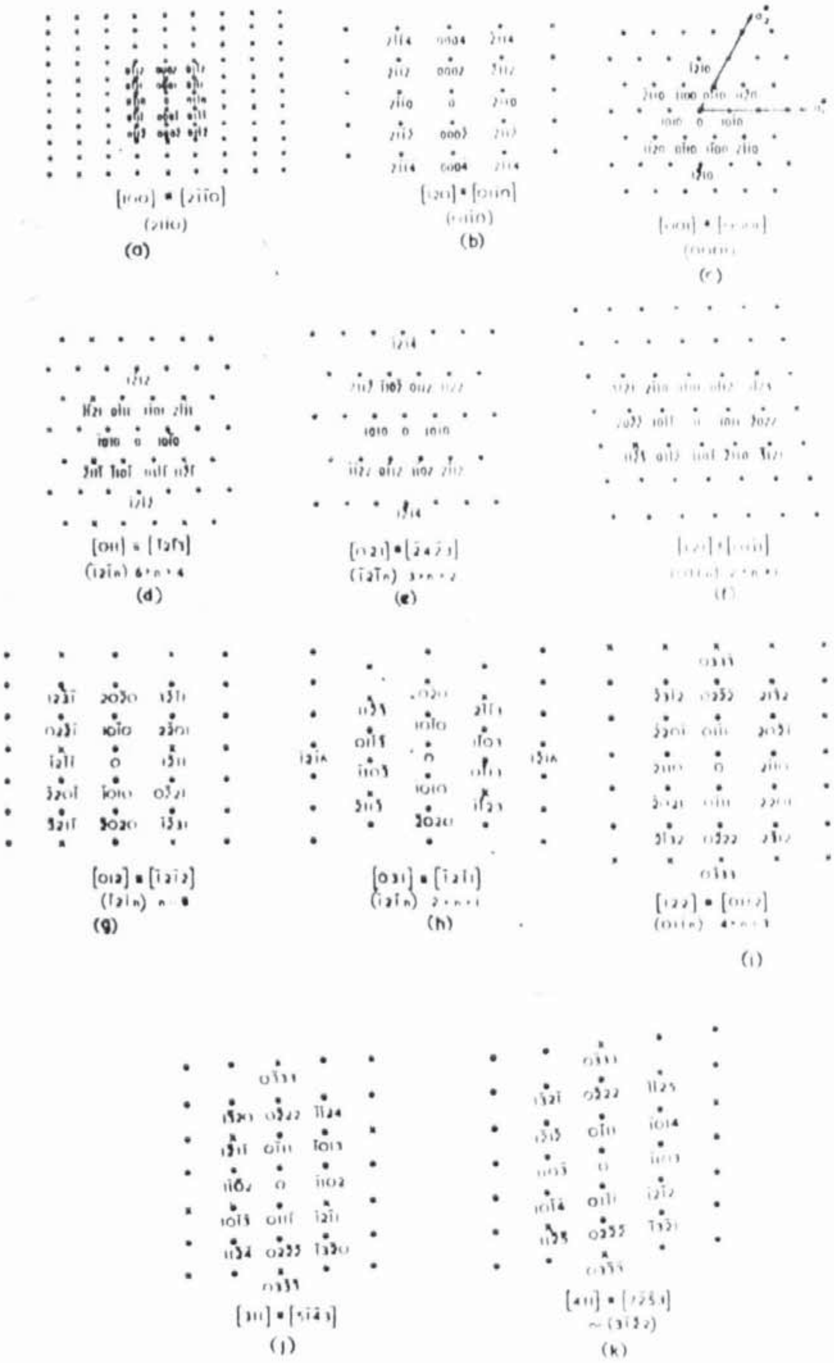

Figure 4.7. Electron diffraction patterns frequently obtained from H.C.P. metals. (after Partridge, (2)).

electrostatic beam tilting device was used for this investigation. All micrographs and diffraction patterns presented were taken at 100 Kv. unless otherwise indicated.

CHAPTER 5.

Results.

Introduction.

This investigation has been primarily concerned with alloys based on Mg -6.0% Zn, (Z6). The effect of an addition of 1.0% Mn to this alloy (designated ZM61) on the mechanical properties and electron microstructure has been determined. An alloy in the Mg-Zn-Zr system (designated ZW6) has also been examined as it has been commercially available for a number of years and because it does not significantly respond to an age hardening sequence.

The object of the investigation therefore was to explain the enhanced ageing response, in terms of ageing rate and maximum properties, caused by the addition of 1.0% Mn and the loss of a response by the addition of 0.5% Zr, to a binary Mg - 6.0% Zn alloy.

Section 1 - Magnesium - 6.0% Zinc - Z6.

It was intended to solution treat the Z6 at 420°C. in order to directly compare the results with those of ZM61 and ZW6, but cracking occurred on quenching. This was only apparent when the alloy was tensile tested. The solution treatment temperature was lowered to 380°C.; although 300°C would have sufficed according to the diagram, it was considered advisable to keep the temperature as close to 420°C as possible.

Mechanical Properties.

The discrepancy between the published hardness results and those obtained in this investigation is indicated in Fig. 5.1. The results from the present work were obtained by determining the hardness on both the E and H scales on the Rockwell machine. Clark[18] obtained an increase of 27 points on the E scale at 149°C, the present work has given 18 points. The rate of ageing and the time to maximum hardness are similar but the absolute values are such that the hardness of the aged Z6 is only just superior to the solution treated values of Clark. His hardness values were obtained for $\frac{1}{8}$" x 1" bar stock and therefore most likely done on a longitudinal face. The results of the present work shown in Fig. 5.1 are from a transverse face.

Hardness determinations therefore were carried out on a longitudinal face, and these results are shown in Fig. 5.2. Results from the transverse face are repeated for comparison. The results obtained with the other two alloys examined are also included. Generally the three alloys have transverse values slightly higher than the longitudinal ones. The difference in ZW6 after 4 hours ageing is small, but the difference in Z6 increases to give a difference of nearly 4 points on an ageing

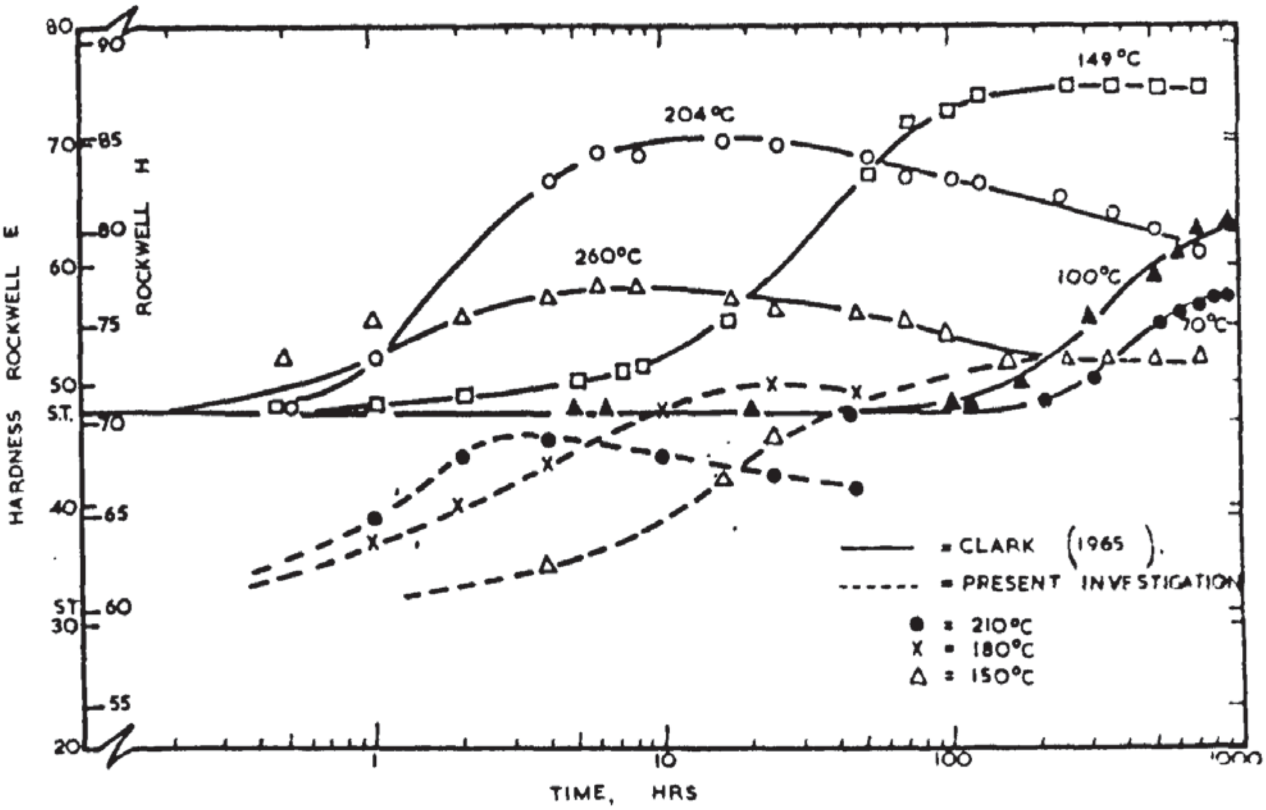

Figure 5.1. Age hardening of Mg-Zn alloy, according to Clark and the present investigation.

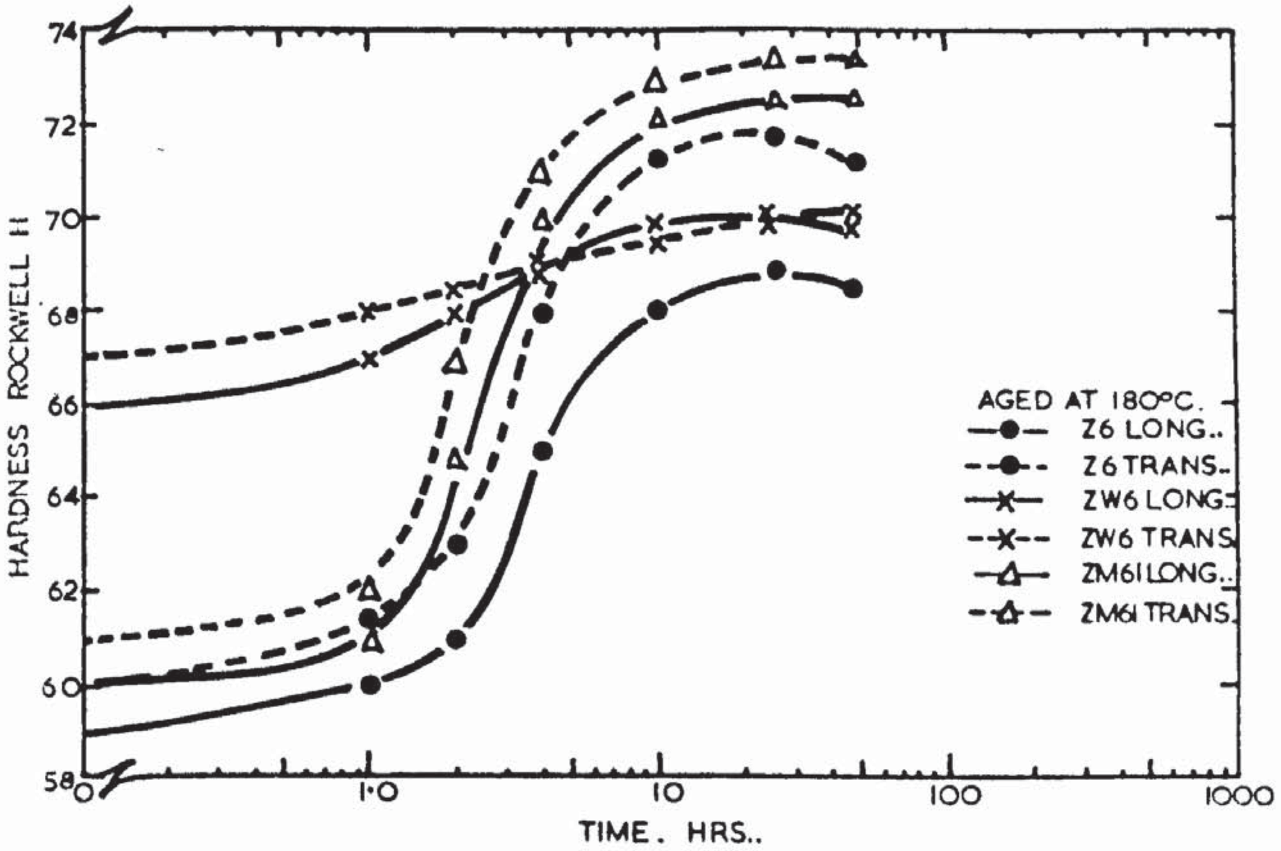

Figure 5.2.

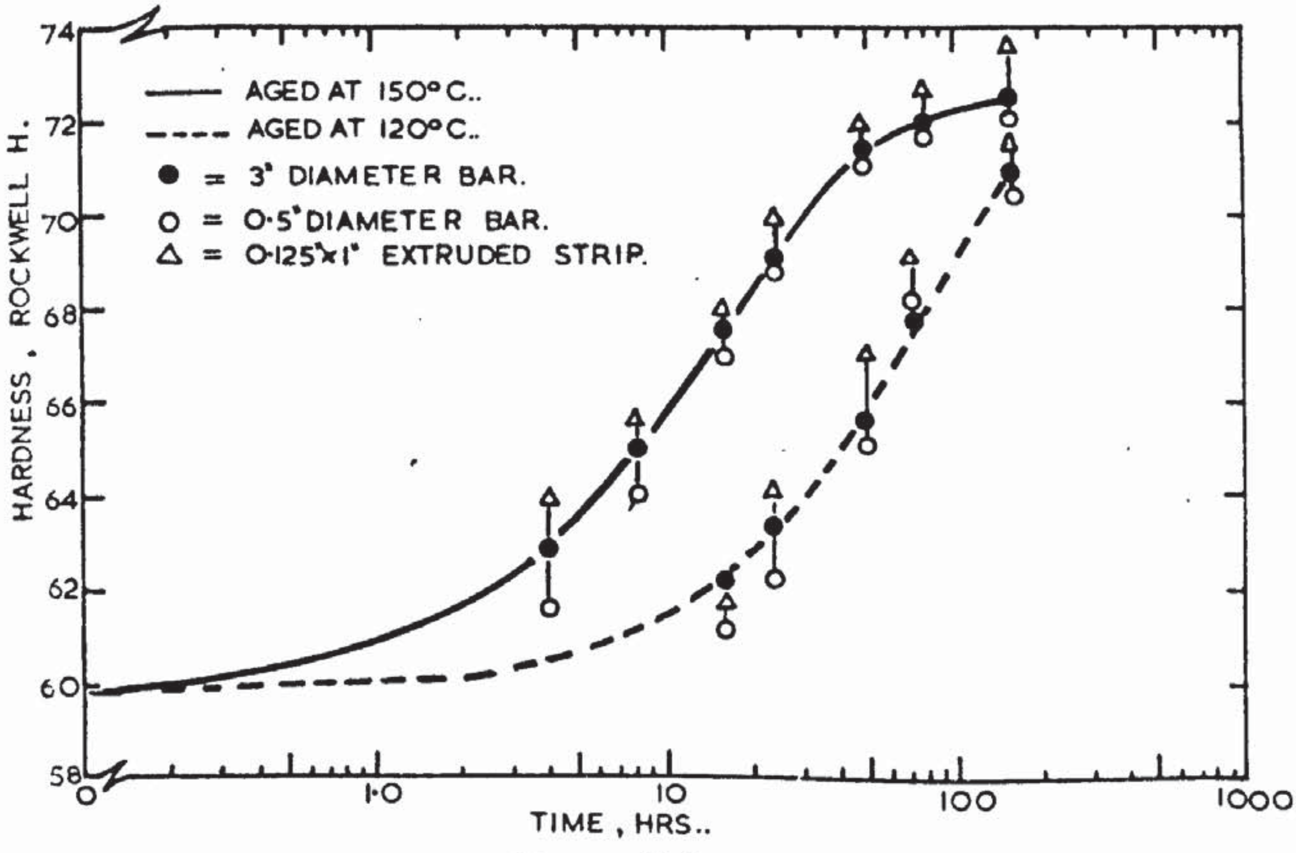

Figure 5.3.

response of 13 points. The transverse hardness is greater than the longitudinal. The ageing response of ZW6 and ZM61 will be examined in detail later but the similarity between the hardness on longitudinal and transverse surfaces should be noted.

The Z6 results are from specimens cut from the ends of tensile bars which were removed from the mid-radial position of the 3" diameter extrusion. This 3" diameter extrusion was re-extruded into $\frac{1}{2}$" diameter bar and $\frac{1}{8}$" x 1" flat strip. This provided a range of sample sizes at different extrusion ratios in order to determine any sample effect. The ageing response at 120 and 150°C of the 3" and $\frac{1}{2}$" diameter bar and the strip is shown in Fig.5.3 and the results from the 3" and $\frac{1}{2}$" diameter bar apply to a transverse face. The overall difference between the three extrusions is small.

The ageing response at temperatures from 60 to 210°C in 30°C increments is shown in Fig. 5.4 which illustrates the change in hardness and Fig. 5.5 illustrating the increase in the 0.1% Proof Stress. The complete tensile properties are shown in the Appendix so as to be comparable with those on ZM61 presented previously by the author[20]. Comparing the hardness and 0.1% proof stress ageing curves, the increase in the proof stress precedes that of the hardness and the maximum is therefore reached slightly sooner. This could possibly be related to the different delays prior to ageing, 8 days for the samples for

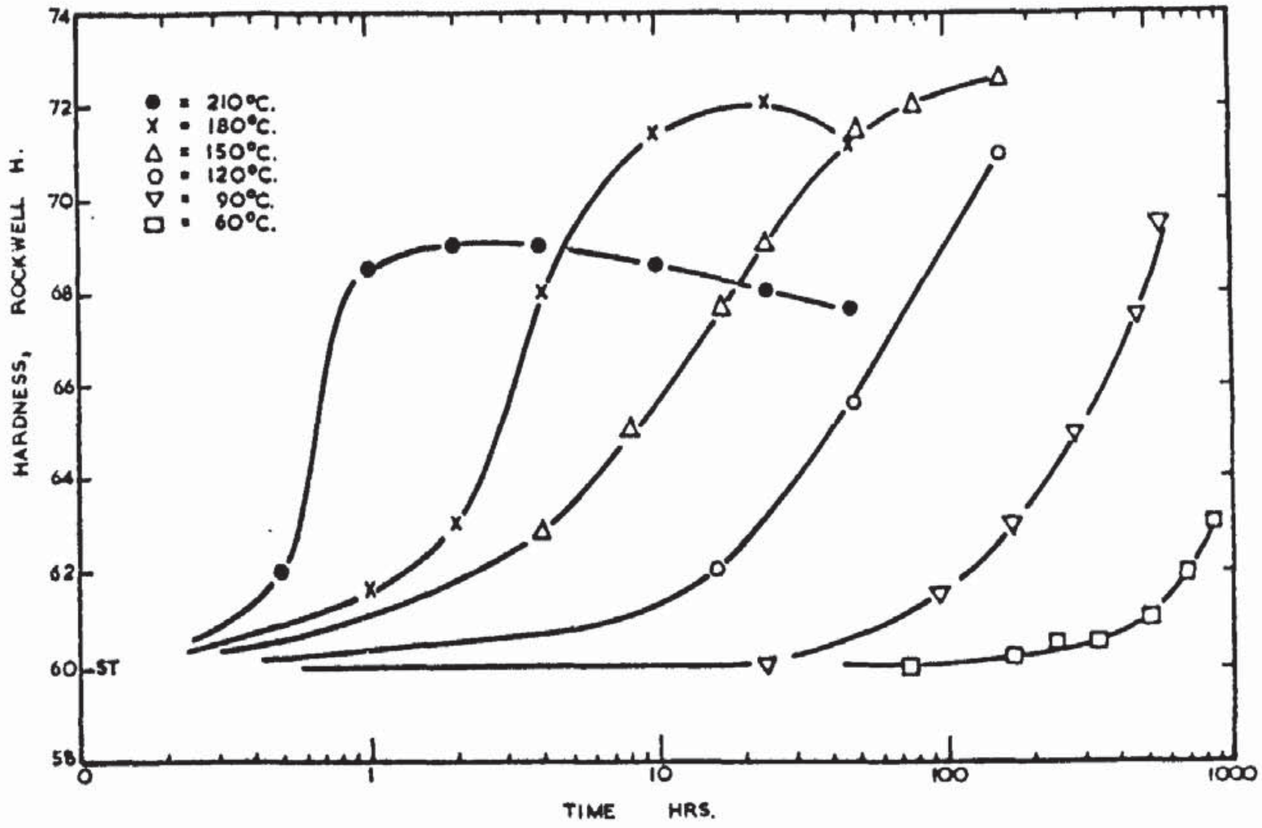

Figure 5.4.

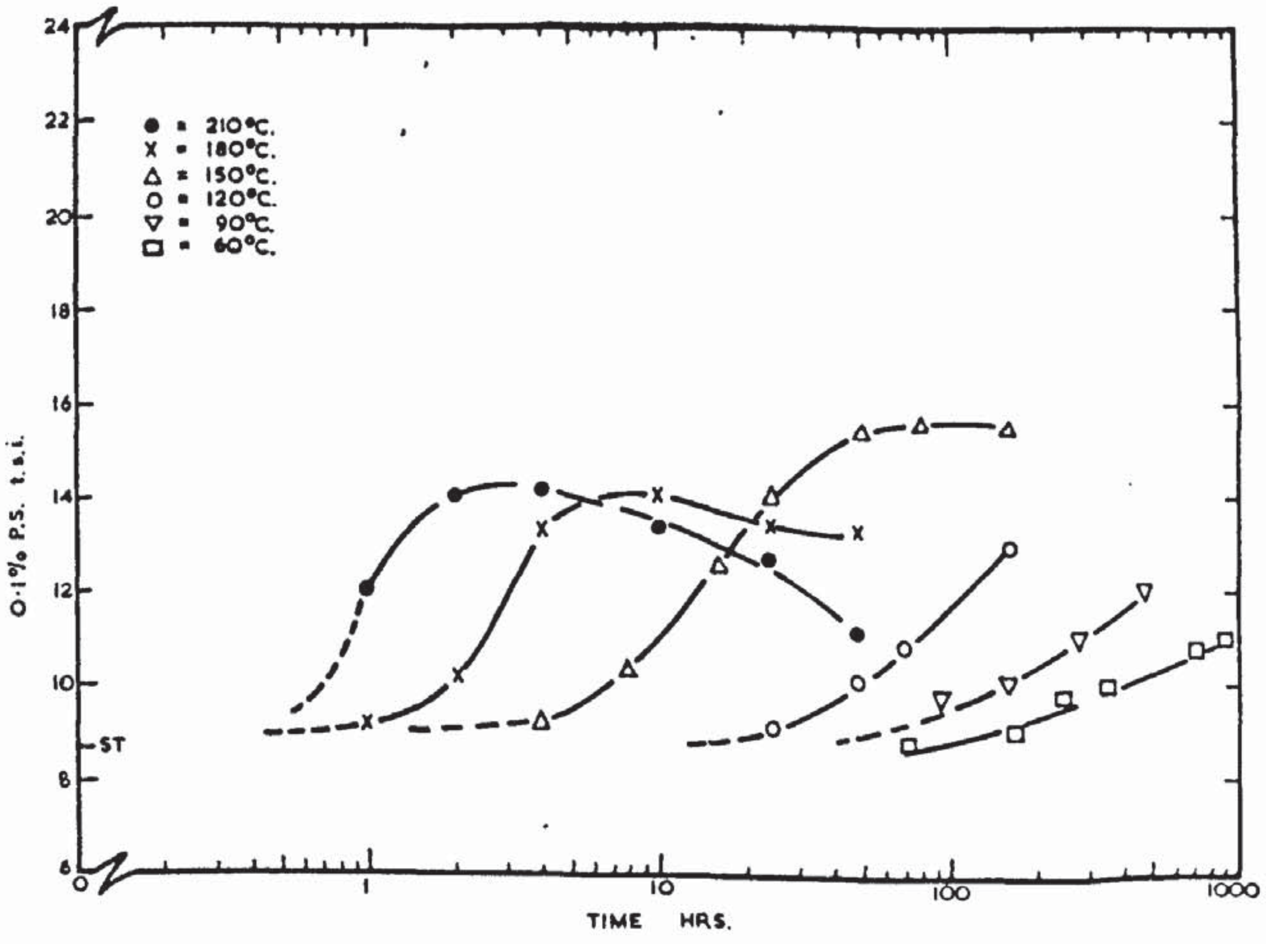

Figure 5.5.

tensile testing and only 2-3 minutes for the hardness samples. At 180°C an increase in hardness from 60 to 72 (Rockwell H) and in 0.1% P.S. from 8.6 to 14 t.s.i. is achieved. This represents an increase of 20% and 62% respectively. Referring to Fig. 5.2 the response on the Rockwell E scale is 63%. Interpolating Clarks results, the increase in hardness, from the solution treated hardness value is, on the E scale, 50% and the H scale, 21%. It is therefore evident that care is required when referring to any property change in terms of a per centage change on the original property.

Electron Microstructure.

The results will be presented in order of increasing ageing temperature.

Room Temperature.

Only one period of natural ageing was examined, this was 9 months, during which the hardness (Vickers 5 Kg. 2/3" objective) increased from 47.8 to 51. The structure is illustrated in Fig. 5.6 (1572). The precipitate is detectable due to matrix contrast which takes the form illustrated in Fig. 3.4 from which it should also be noted that the diameter of the particle is approximately half the length of the line of 'no contrast'.

Fig. 5.7 (1578) is an image formed from an (0002) Mg. diffracted beam, the matrix strain is now more easily seen. The

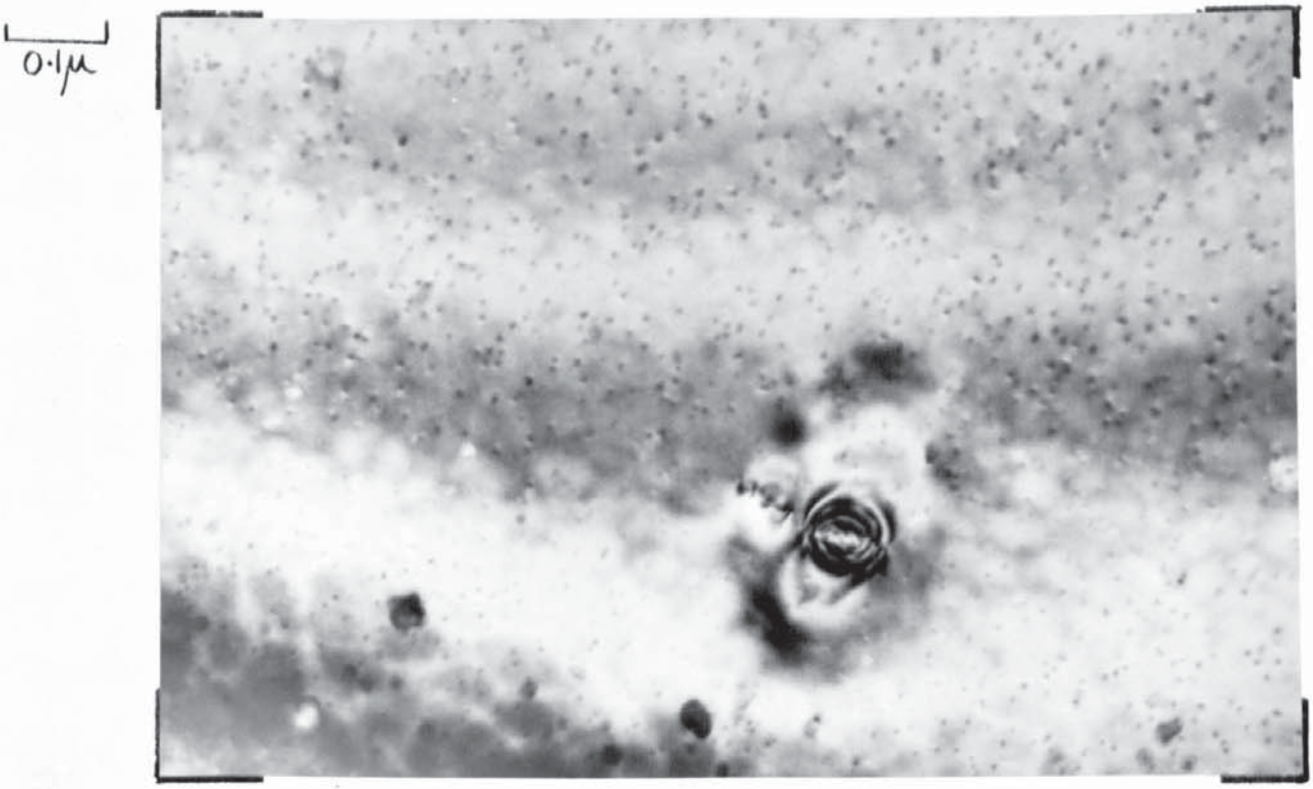

Figure 5.6. Z6 aged for 9 months at room temperature.

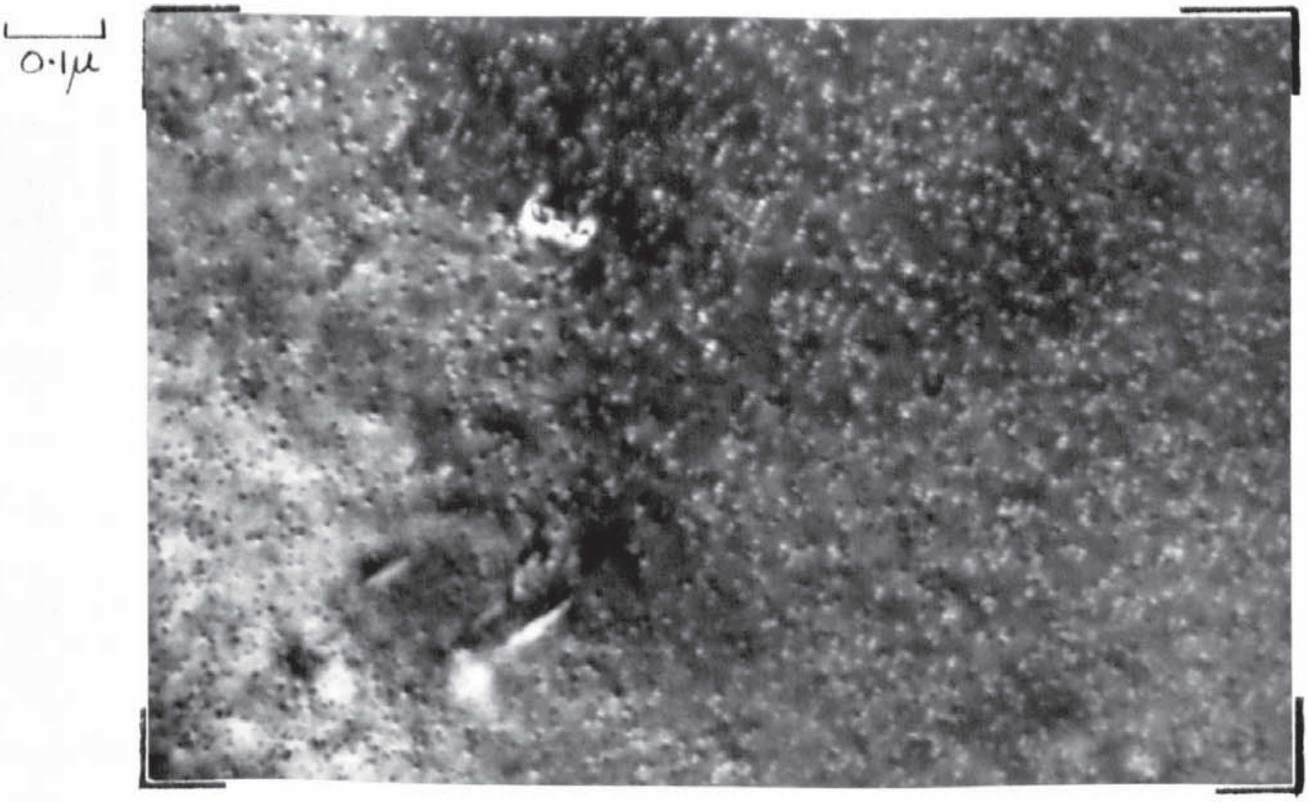

Figure 5.7. Image formed using an (0002)Mg diffracted beam.

line of 'no contrast' is parallel to the basal planes and could arise from a spherical particle about $30A^{o}$ diameter or from a disc $60A^{o}$ diameter and perhaps 15 A^{o} thick. If the particle were spherical (ref. Fig. 3.3(a) and (b)) then the line of 'no contrast' should be visible under two beam conditions with the $(10\bar{1}0)$ Mg vector operating. These diffracting conditions were used many times but the contrast was not resolved into the two components. Fig. 5.6 and Fig. 5.7 are from foils of the type $(10\bar{1}0)$ Mg foil plane; a strong (0002)Mg reflection is required to image the two components. The precipitates are therefore discs on the basal planes.

Fig. 5.6 and Fig. 5.7 also serve to illustrate the effect of foil thickness on the apparent quantity and distribution of precipitate, particularly at these very small sizes. Although these two illustrations are at equal magnifications it is clear that the area shown in Fig. 5.7 is thicker than that in Fig. 5.6 making it difficult to obtain any accurate number versus size of precipitate diagrams in order to differentiate between the 'thermodynamic' and 'kinetic' theories of nucleation.

The structures presented represent the very early stages of transformation and the structure causing this contrast phenomenon will be referred to as G.P. zones. Specimens of the alloy in this condition were used for the reversion experiments described later, to determine the critical temperature.

Ageing at 60°C..

Fig. 5.8 (1452) shows the structure after 96 hours and as the foil plane is not quite of the $(10\bar{1}0)$ Mg type the two components of the strain contrast are not resolved.

Fig. 5.9 (732) illustrates the structure after 330 hours. The foil orientation is $(10\bar{1}0)$ Mg with an (0002) vector operating. G.P. zones and the $MgZn_2^1$ needle precipitates perpendicular to (0001)Mg are evident. The length of the line of 'no contrast' is 75-100A°; slightly longer than in the sample naturally aged for 9 months. Fig. 5.10 (728) is a similar structure with a $(10\bar{1}2)$ Mg operating vector in a $(10\bar{1}0)$ Mg foil. The zones are still evident but the line of no contrast is absent as in Fig. 5.8. The matrix contrast is 60-70A° across and the $MgZn_2^1$ needles 60-400A° long. There are between 1500-2000 precipitates per square micron. This structure is very similar to the structure after ageing for 696 hours which is illustrated in Fig. 5.11 (1155) and indicates that the 'matrix contrast' is arising from a particle of a constant size characteristic of the ageing temperature. The increase in hardness and tensile strength with this fairly extensive precipitation is surprisingly small.

Ageing at 90°C..

The structure after 48 hours at 90°C is shown in Figs. 5.12 and 5.13 (596 and 588) and both are from a $(11\bar{2}0)$ foil. The

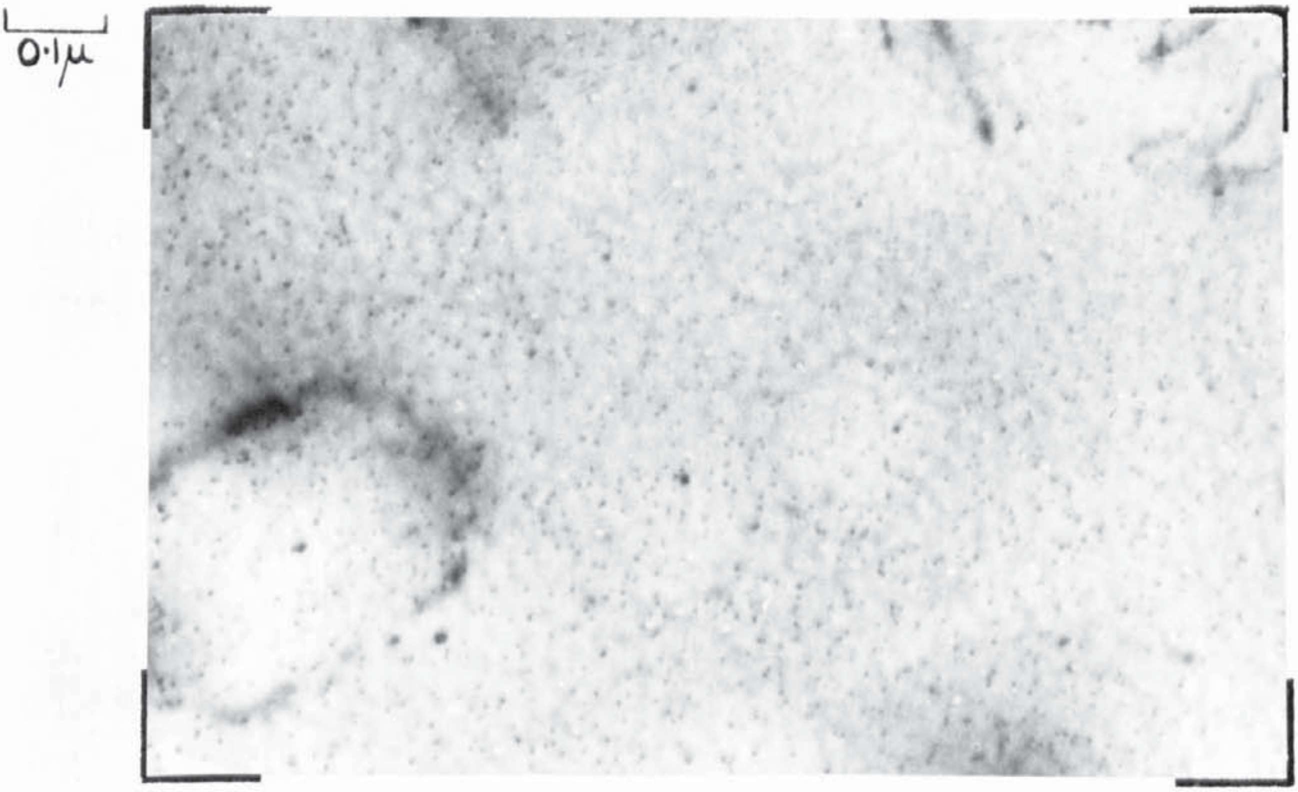

Figure 5.8. Structure after 96 hours at 60^{o}C..

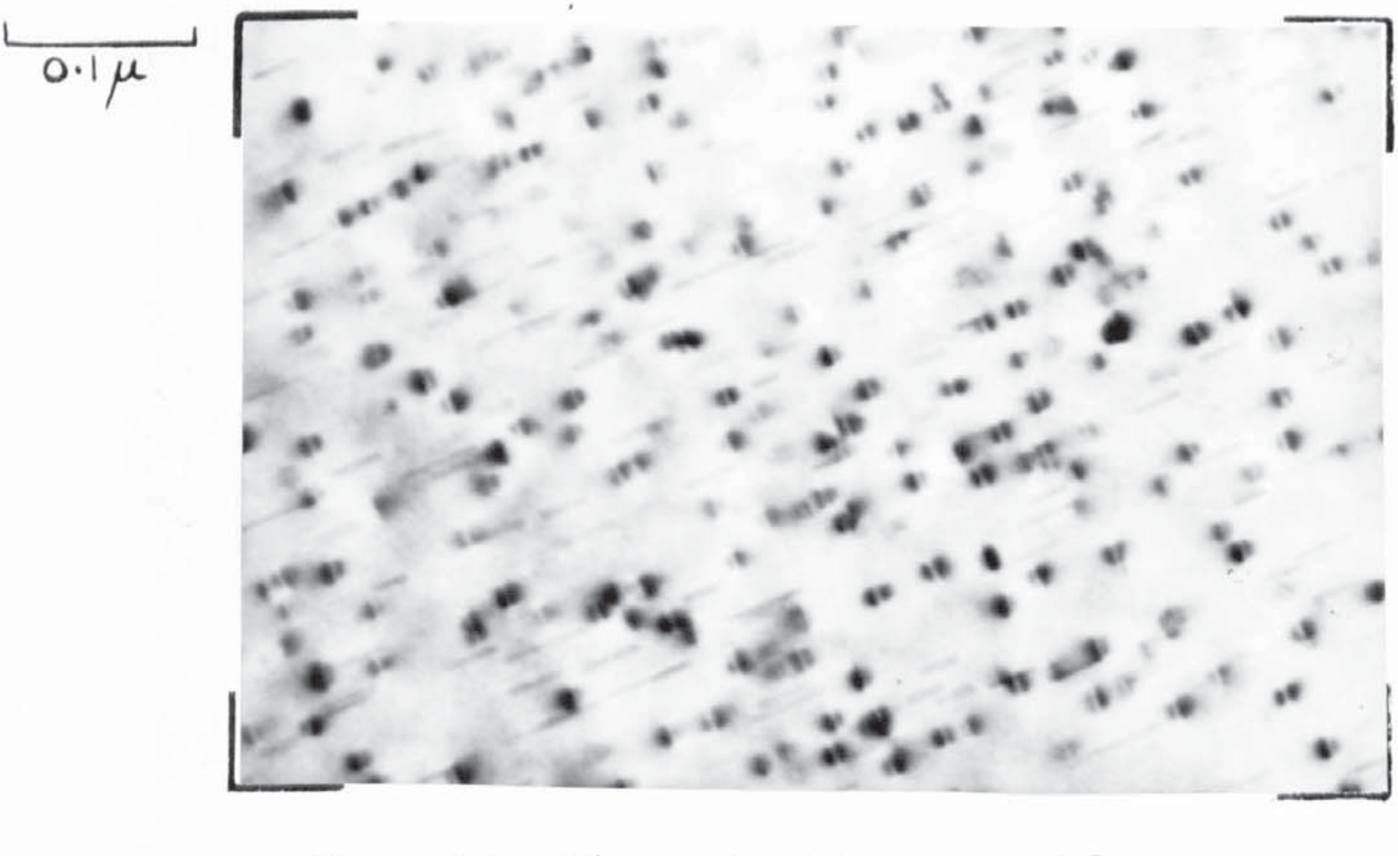

Figure 5.9. Z6 aged for 330 hours at 60^{o}C..

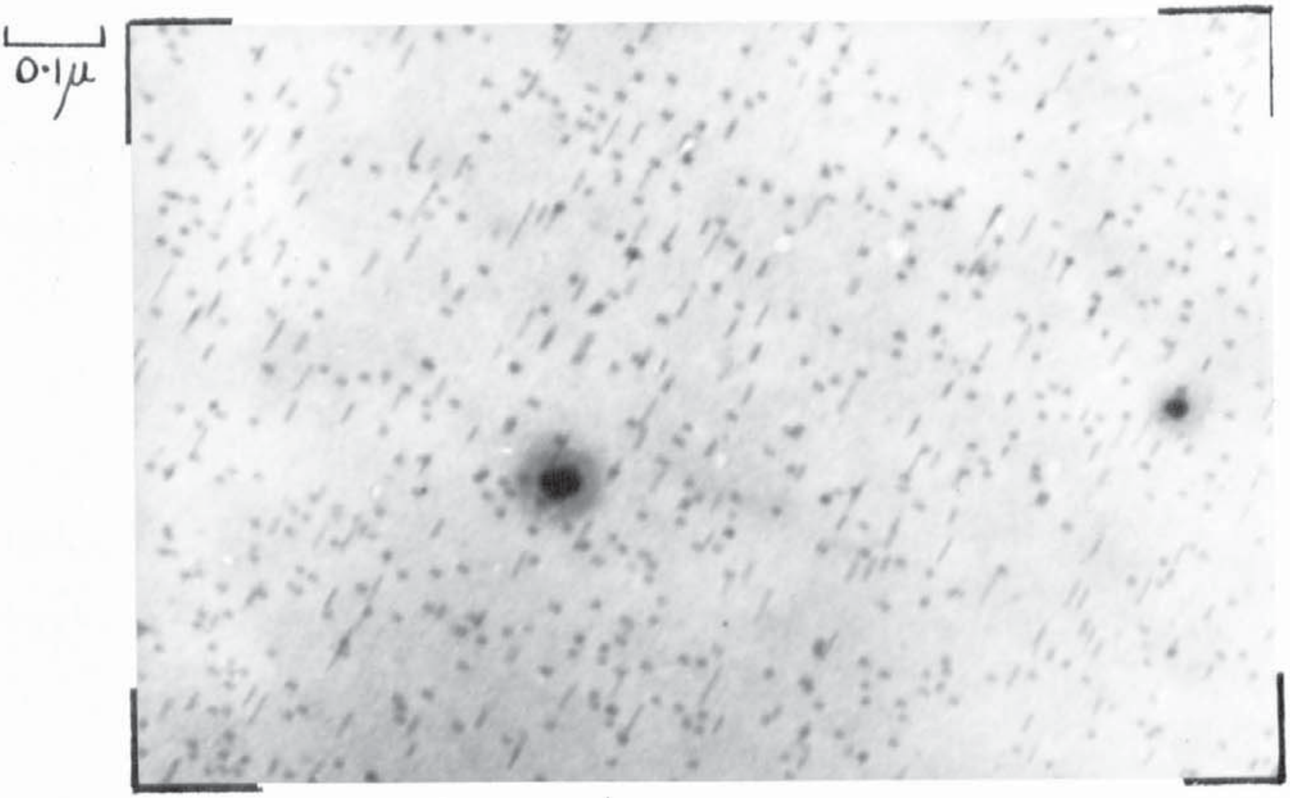

Figure 5.10. Sample as Fig. 5.9. but with a (10$\bar{1}$2) vector operating.

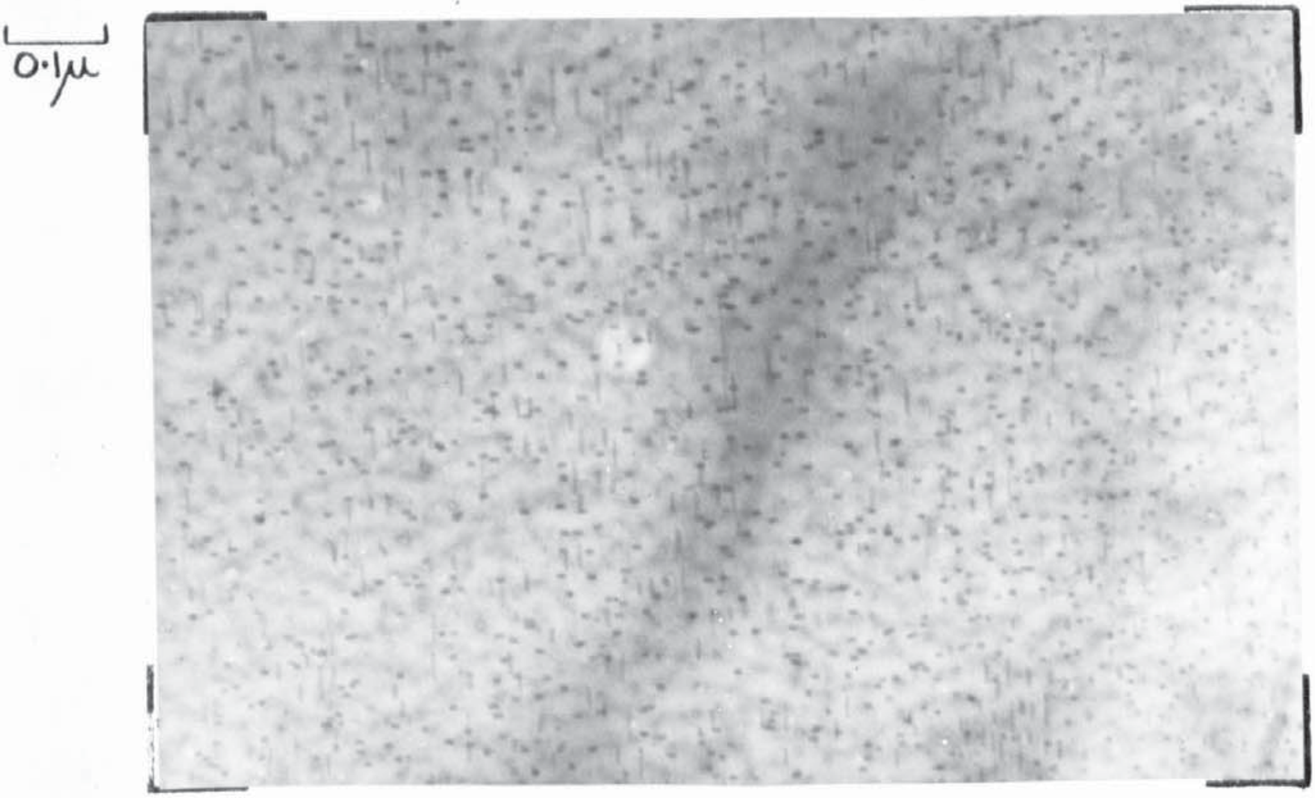

Figure 5.11. Alloy Z6 after 696 hours at 60°C..

presence of zones is evident in Fig. 5.12 with the line of no contrast and Fig. 5.13 shows that extensive precipitation has occurred and also the presence of the artifacts causing the large matrix strain contrast. The increase in the ratio $MgZn_2^1$ needles: zones at $90^{\circ}C$ when compared with the structure after ageing at $60^{\circ}C$ should be noted. The needle length, from Fig. 5.12 varies between 150-600A°, spacing between 100-2000A° and there are 200-300 precipitates per square micron.

After ageing for 96 hrs. at $90^{\circ}C$ discs of $MgZn_2^2$ on the (0001)Mg are formed as shown in Fig. 5.14 (1000) in a $(10\bar{1}0)$ foil. The light patches are a preparation defect. The similarity between the disc precipitate and the 'matrix contrast' is apparent, but the confusion is eliminated when this structure is observed in an (0001)Mg foil. This is shown in Fig. 5.15 (998) which is also at the same magnification as Fig. 5.14. The $MgZn_2^2$ discs are lighter than the needles due to their shorter diffracting length, and the diameter of the discs is about two to three times that of the $MgZn_2^1$ needles.

In Fig. 5.14 the needle length is between 150-2000 A° there are 300-450 per square micron and in Fig. 5.15 there are 500-650 per square micron with a spacing of 100-2000A°. Figs 5.16 and 5.17 (999 and 997) show two further features; Fig. 5.16 illustrates heterogeneous nucleation on a dislocation and it takes the form of a "string of pearls" effect. Fig. 5.17 shows

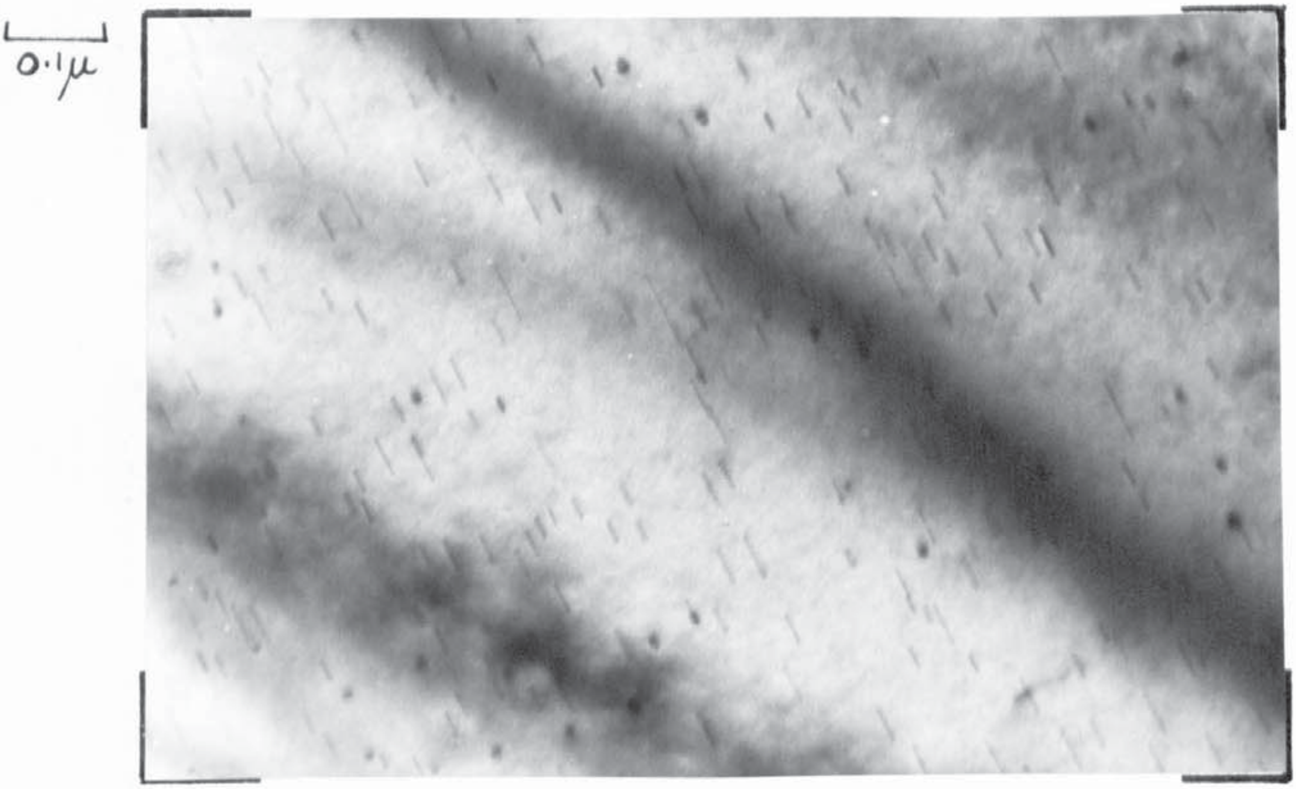

Figure 5.12. Showing the structure after 48 hours at 90°C.,

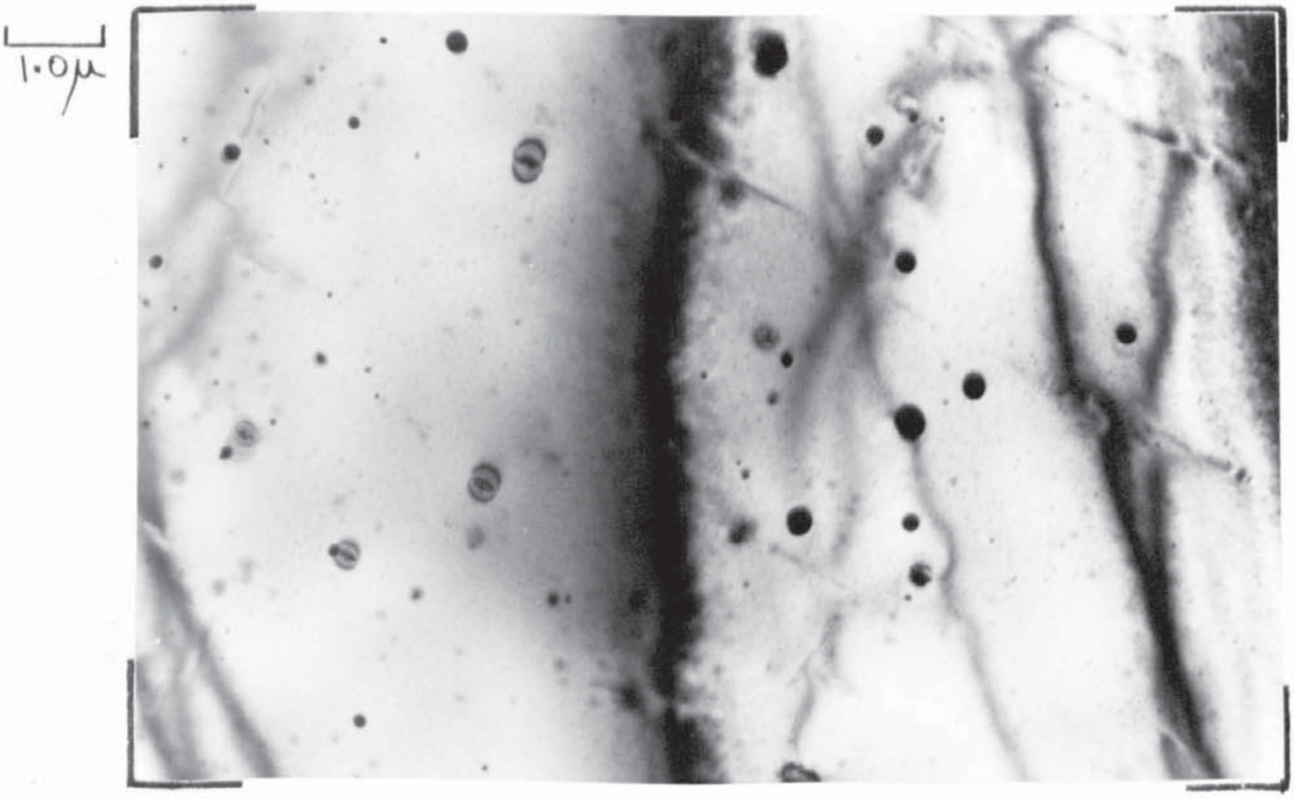

Figure 5.13. As Fig.5.12. showing extensive precipitation.

Figure 5.14. Z6 aged for 96 hours at 90°C..

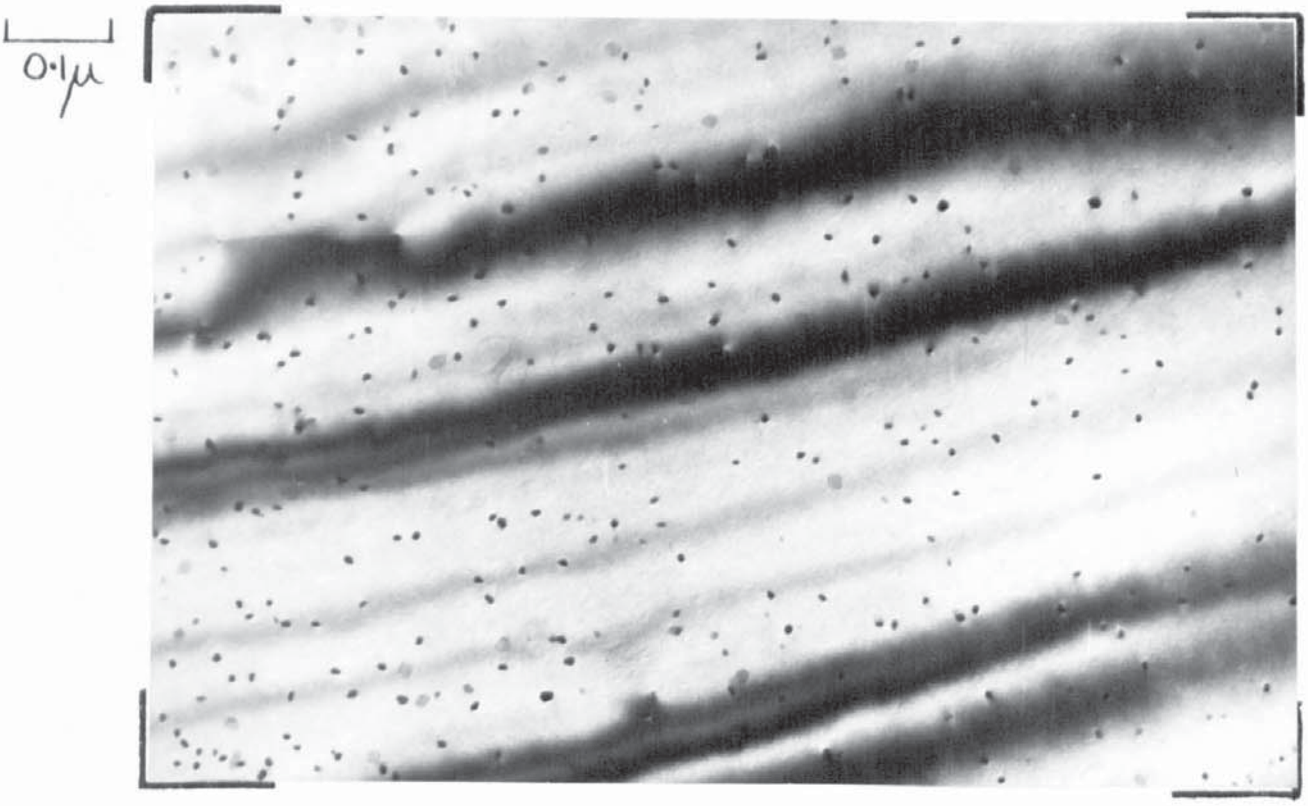

Figure 5.15. As Fig. 5.14. showing structure in an (0001) Mg foil.

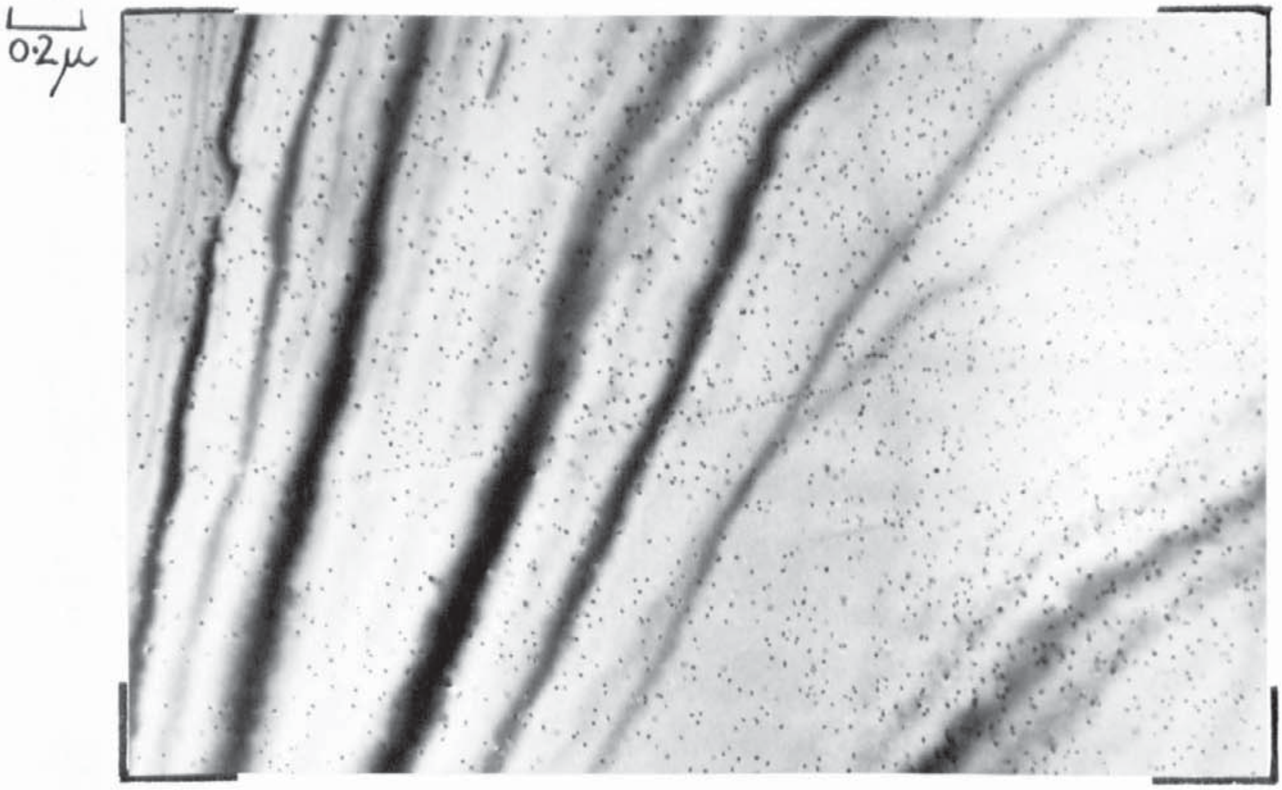

Figure 5.16. Showing heterogeneous nucleation in sample aged for 96 hours at 90°C..

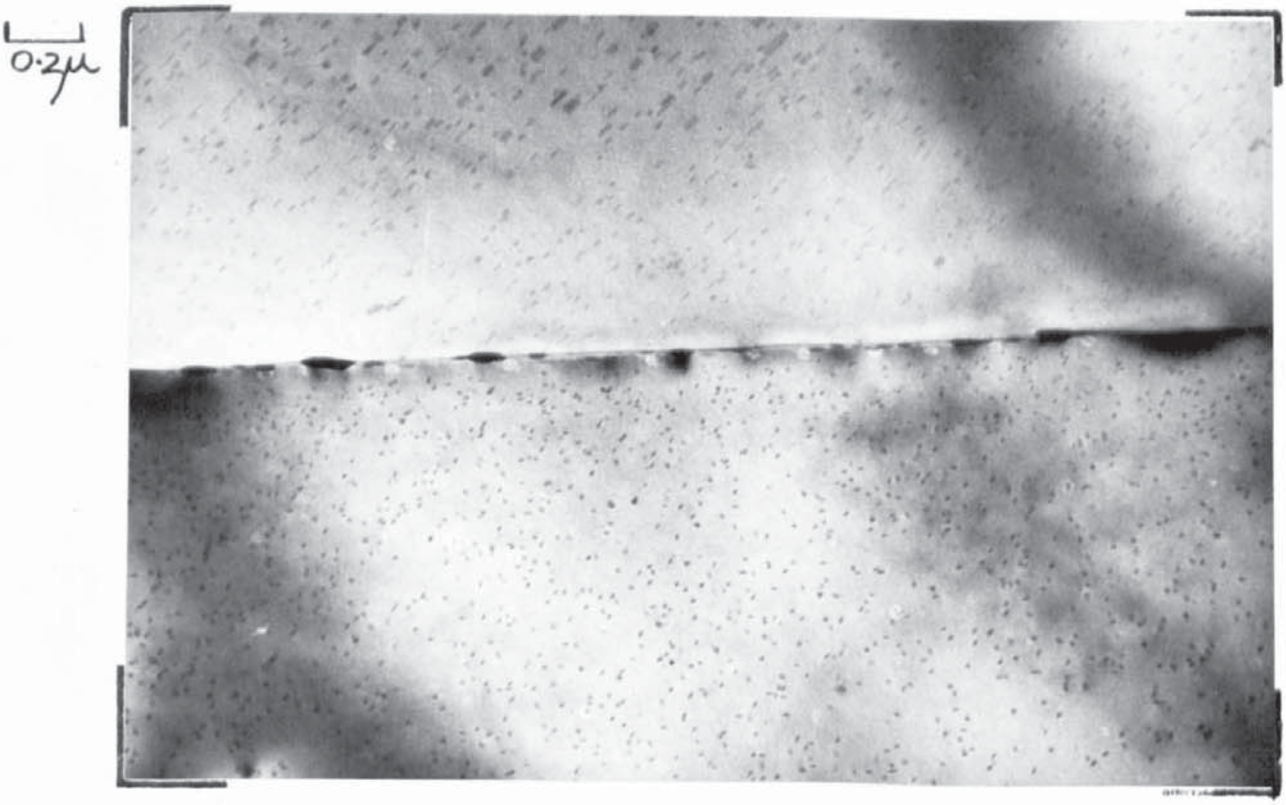

Figure 5.17. Illustrating grain boundary precipitation and a small precipitate free zone.

precipitation at a grain boundary and there is no precipitate free zone resulting from any vacancy migration to the grain boundary.

With a precipitate in the form of needles it is possible that the needle can be nucleated away from any vacancy denuded zone and grow into it, until solute denudation is encountered. In Fig. 5.17 the grain boundary is parallel to the electron beam; the lower grain is in an (0001) Mg orientation and the upper one is close to this orientation. The needles close to the grain boundary, since they are parallel to it, must have been nucleated there and are growing parallel to the boundary.

After 456 hours at 90°C. the needle length is 100-5000 A^{o} as illustrated in Fig. 5.18 (1104) which is from a $(10\bar{1}0)$ Mg foil and the needles are therefore not truncated. The selected area diffraction pattern of this structure is shown in Fig. 5.19 (1105).

The matrix pattern is a $(10\bar{1}0)$ type and the precipitate spots arise from interplanar spacings as shown below, along with the relevant 'd' spacing from Fig. 1.6.

Spot	dA^{o}	Nearest, A.S.T.M.	Nearest, Calc.	Reflection (hkil)
1	2.22	2.20	2.218	$(11\bar{2}2)$
2	2.12	2.10/2.14	2.125	(0004)
3	2.36	2.43	2.41/2.48	$(10\bar{1}3)/(11\bar{2}1)$

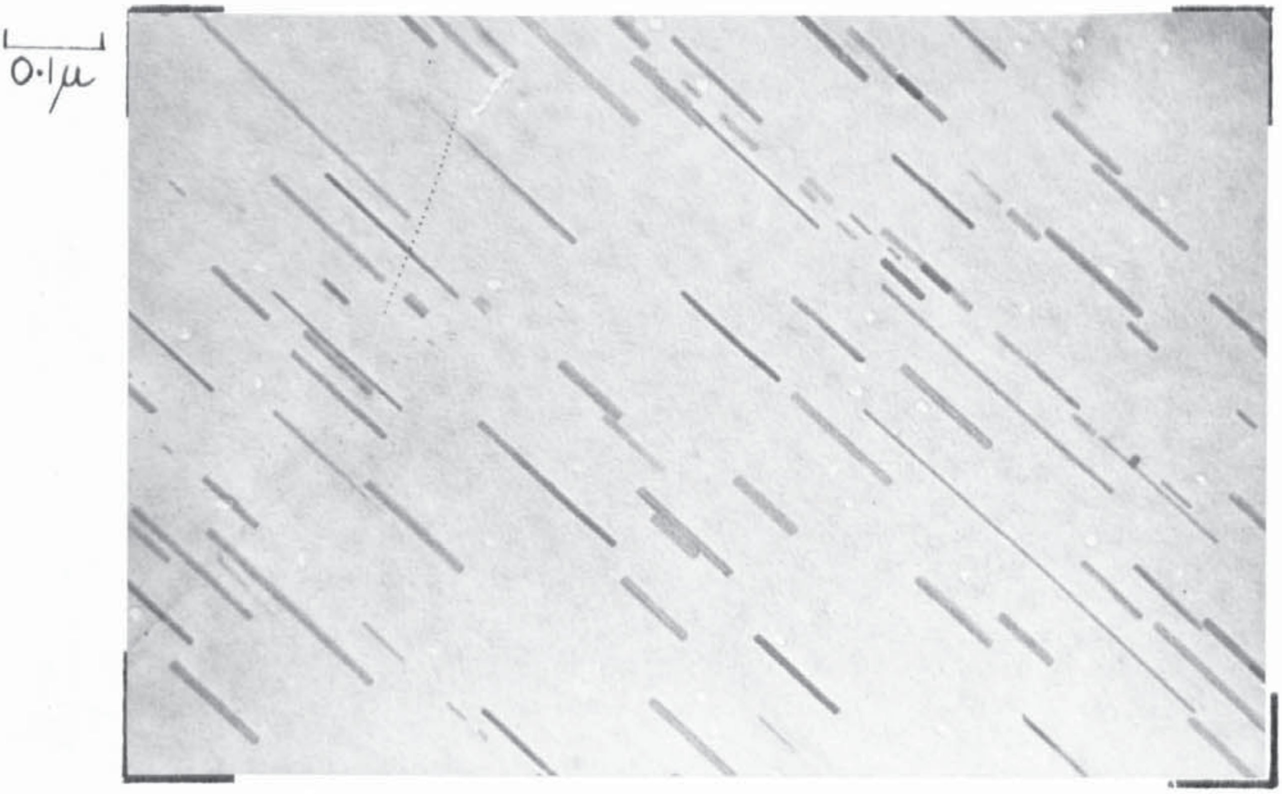

Figure 5.18. Z6 aged for 456 hours at 90°C..

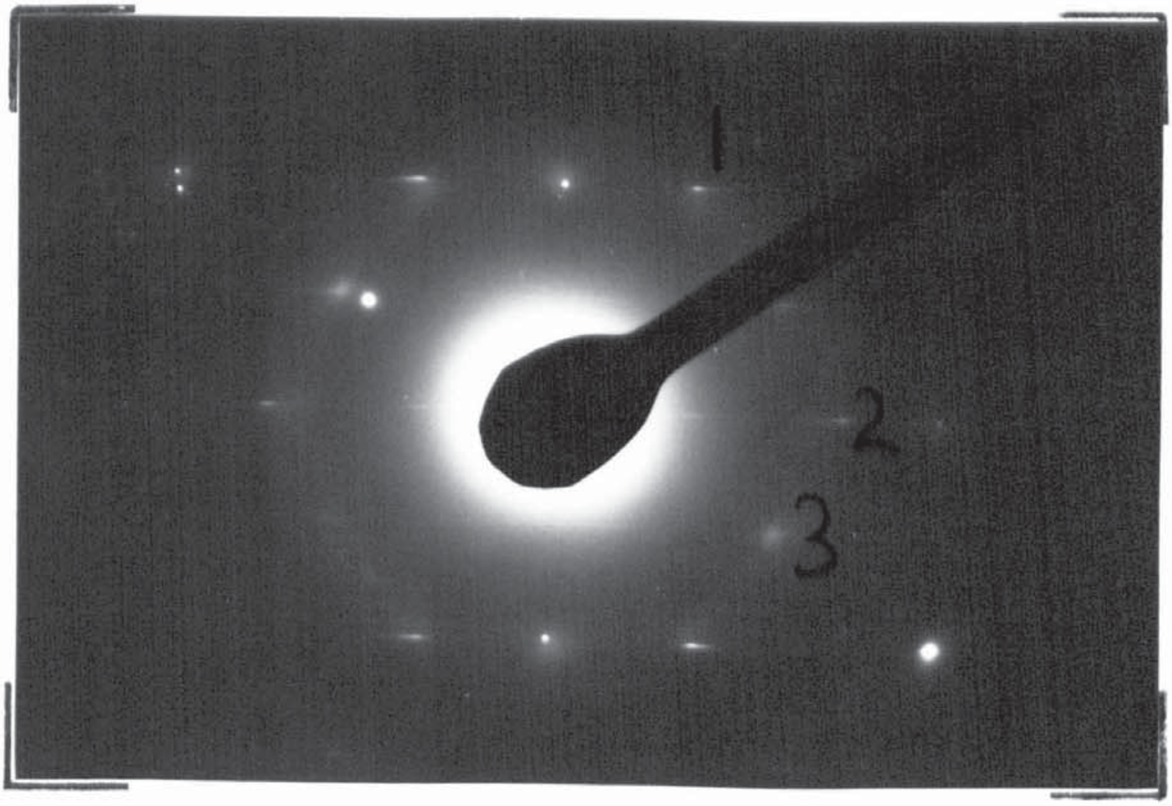

Figure 5.19. Selected area diffraction pattern of Fig.5.18.

Diffraction spots numbered 1 and 2 are from a $(10\bar{1}0)$ precipitate zone axis, confirming the relationship reported by Gallot[3]. Diffraction spot numbered 3 must also be from the needles as no discs of $MgZn_2^2$ are present in Fig. 5.18. It must **arise** from needles in the other two $[11\bar{2}0]$ Mg directions.

The geometry of the relationship indicates that the planes giving rise to the 2.36A° value should be of the same type and at an angle of 55° to each other. Of the two possibilities shown in the table, $(10\bar{1}3)$ and $(11\bar{2}1)$ type planes the angle between $(10\bar{1}3)$ and $(1\bar{1}03)$ is 55° 36' and between $(11\bar{2}1)$ and $(2\bar{1}\bar{1}1)$ 57° 12'. The diffracted beam forming spot number three therefore comes from the $(10\bar{1}3)$ type planes in the precipitates obeying the other two orientation relationships.

Severe truncation of the needles is shown in Fig.5.20 (1110) which is from the same foil as Fig. 5.18 but from a grain with a $(10\bar{1}n)$ Mg orientation where $4 > n > 3$. The angle of the needles to the beam is therefore about 60°.

Direct quenching experiments were carried out on this alloy and samples were quenched to 90°C.. This temperature was selected for the first direct quenching experiment. The results of Hall[19] indicated a G.P. zone solvus of 75-80°C, it was therefore anticipated that the very dramatic change in precipitate distribtuion, would be encountered. It is usual to age a direct

Figure 5.20. As Fig. 5.18. but with the (0001)Mg at about 60° to the electron beam.

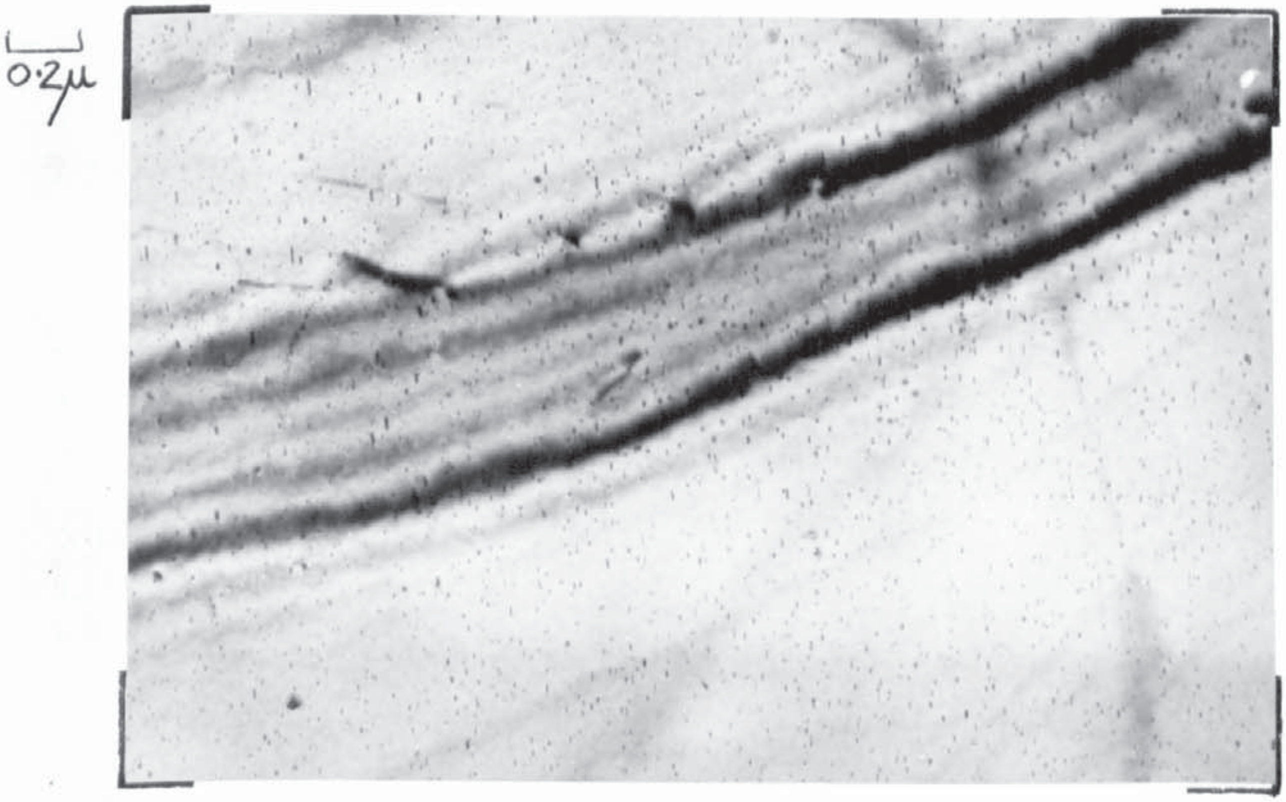

Figure 5.21. Structure after 96 hours at 90°C. in a sample directly quenched to the ageing temperature.

quenched sample for a time that would result in maximum properties if the alloy were quenched to room temperature and then aged. In this alloy, the time involved would be in excess of 500 hours.

It was considered not worthwhile to extend the time at 90°C. to longer than 96 hours, as it has been demonstrated that extensive precipitation could be observed after this time in the samples quenched to room temperature. It was therefore decided to age the direct quenched samples for 96 hours.

Fig. 5.21 (1038) shows the structure after ageing for 96 hours at 90°C after direct quenching to this temperature. The foil is close to an (0001) Mg type and the structure is very similar to that shown in Fig. 5.16 which is of the sample quenched to room temperature. G.P. zones were also detected in the direct quenched sample as illustrated in Fig. 5.22 (1054) with a (10$\bar{1}$0) Mg foil orientation and again the similarity with Fig. 5.14 is evident. The G.P. zone solvus from this experiment is above 90°C. for the Mg-6.0% Zn alloy. Fig. 5.23 (1054) shows a thin dark line in and parallel to the line of no contrast and it is considered that this is a disc approximately 9A$^{\circ}$ thick and 70A$^{\circ}$ diameter.

This evidence and the inability to show a line of no contrast with either a (11$\bar{2}$0)Mg or (10$\bar{1}$0)Mg reciprocal lattice vector operating demonstrate that the zones are discs on the basal planes of the matrix.

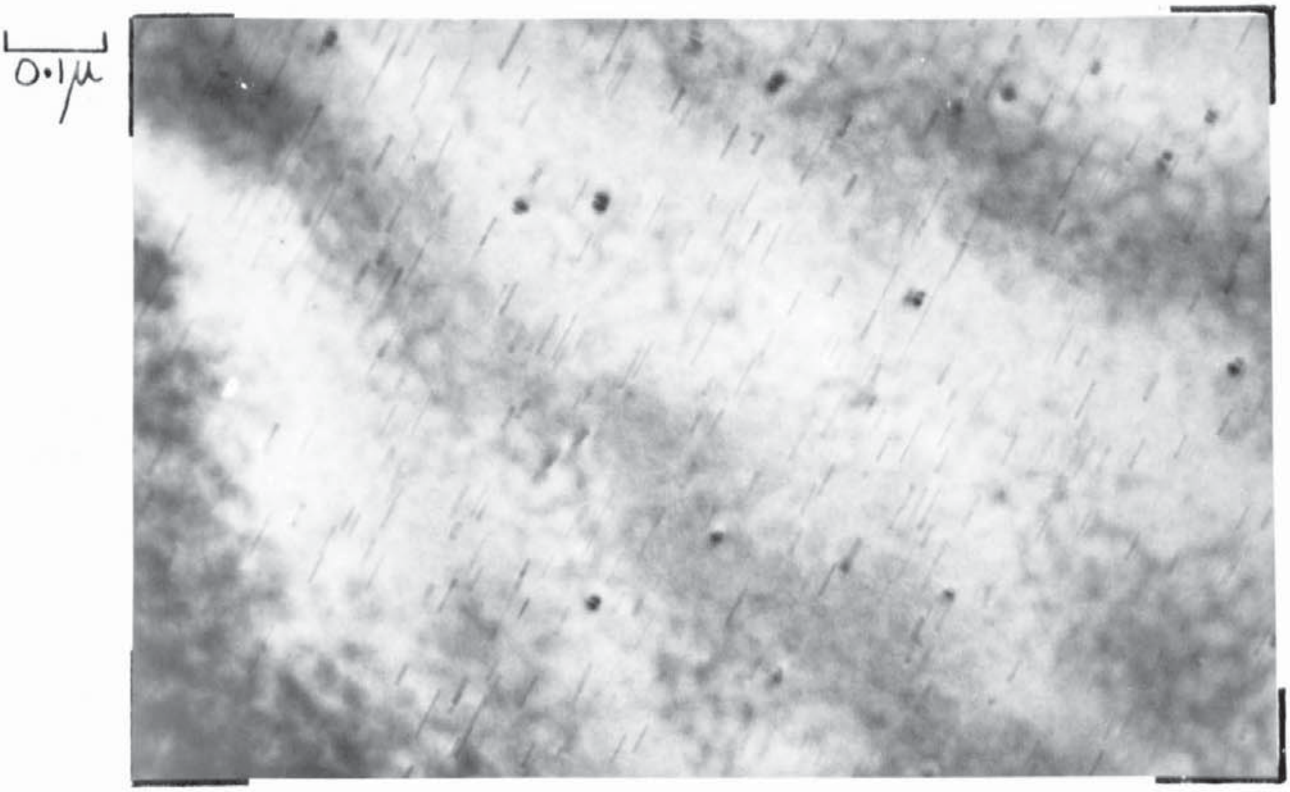

Figure 5.22. As Fig. 5.21 but showing matrix contrast from G.P. zones.

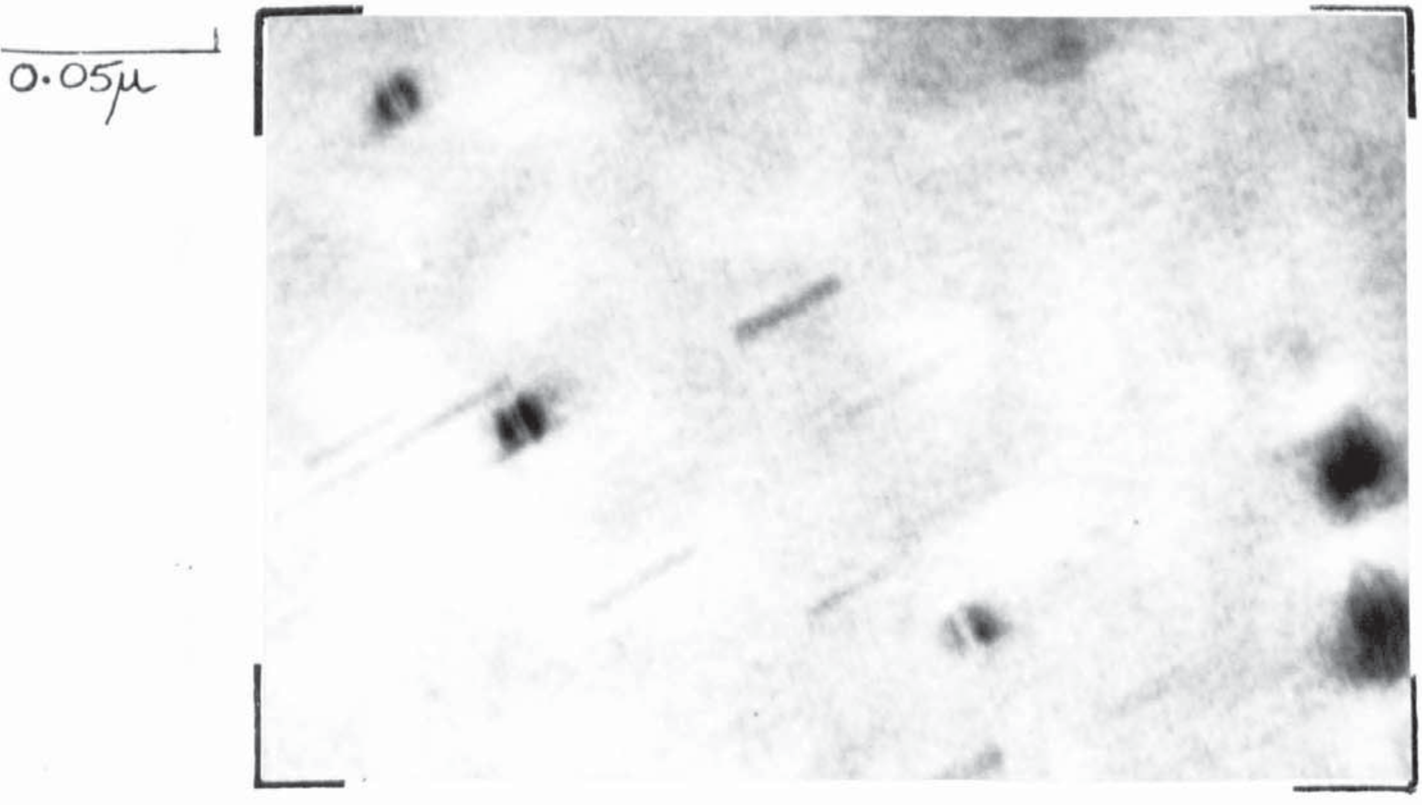

Figure 5.23. As Fig. 5.22 showing a thin dark line between the two components of the matrix contrast.

Ageing at 120°C..

Fig. 5.24 (1278) shows the structure in an (0001) foil after 16 hours at 120°C. and is very similar to the previous illustrations. Heterogeneous nucleation was also detected and Fig. 5.25 (1275) shows a small intermetallic particle that has "pumped out" dislocations during the quenching due to the differential thermal contraction. These dislocations have caused preferred nucleation of the needles of $MgZn^{1}_{2}$ and Fig. 5.26 (1279) is similar but the particle is absent and also serves to illustrate a consistent precipitate spacing on the dislocation lines of between 250 and $400A^{\circ}$.

Ageing for 264 hours results in the structure shown in Fig. 5.27 (1230) and is of a $(11\bar{2}0)$Mg foil and Fig. 5.28 (1229) which is near to an(0001)Mg foil, both at the same magnification. The futility of attempting to relate the number of precipitates per unit area to the number per unit volume particular with a C.P.H. matrix, is clearly demonstrated by these two illustrations.

Fig. 5.29 (1233) shows an image formed using a diffracted beam from the precipitate. The pattern and the diffracted beam used are shown in Fig. 5.30 (1234 or 5) and the matrix pattern is a combination of a $(10\bar{1}0)$Mg foil and an (0001)Mg foil as would be expected from the area shown in Fig. 5.29. The $MgZn^{1}_{2}$ needle length is between 500 and 6000 A° and the spacing is around 500 A°. Extensive precipitation at the grain boundary is also apparent in

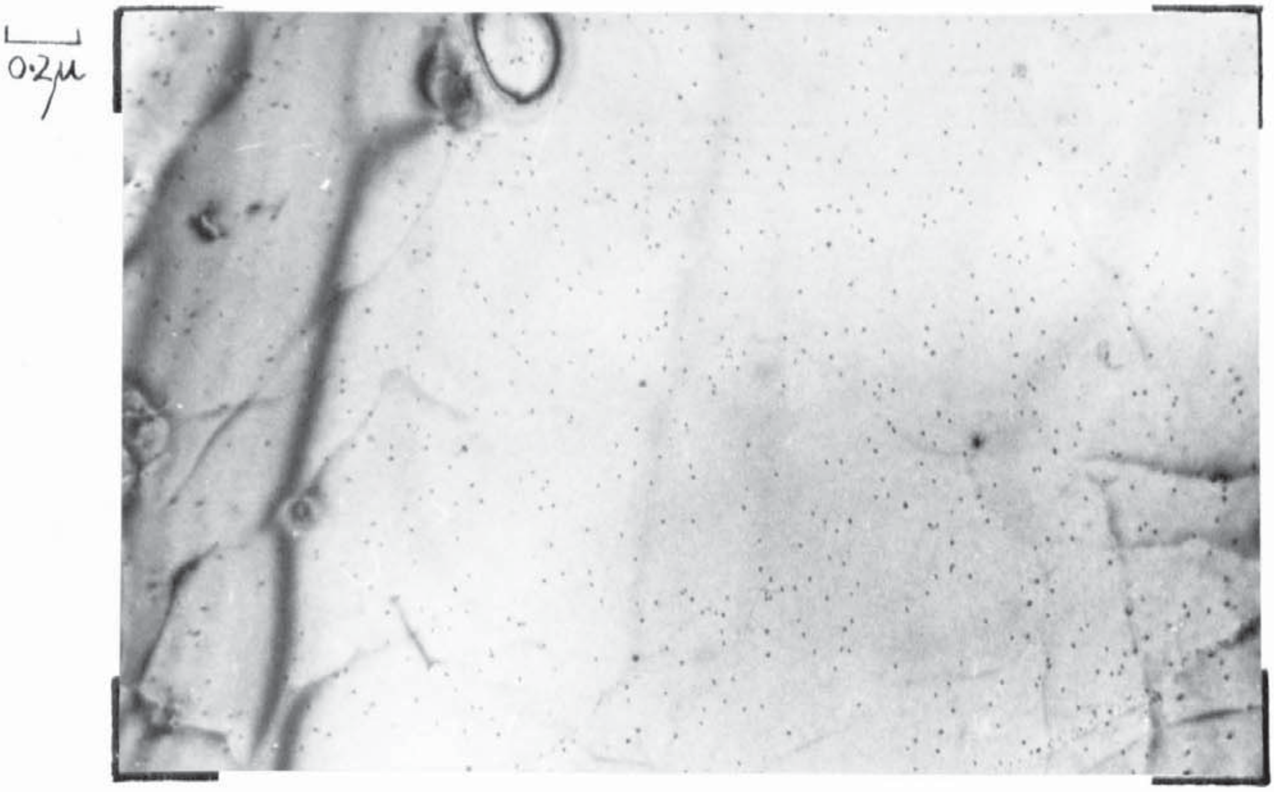

Figure 5.24. Z6 aged for 16 hours at 120°C.. Foil orientation is (0001) Mg.

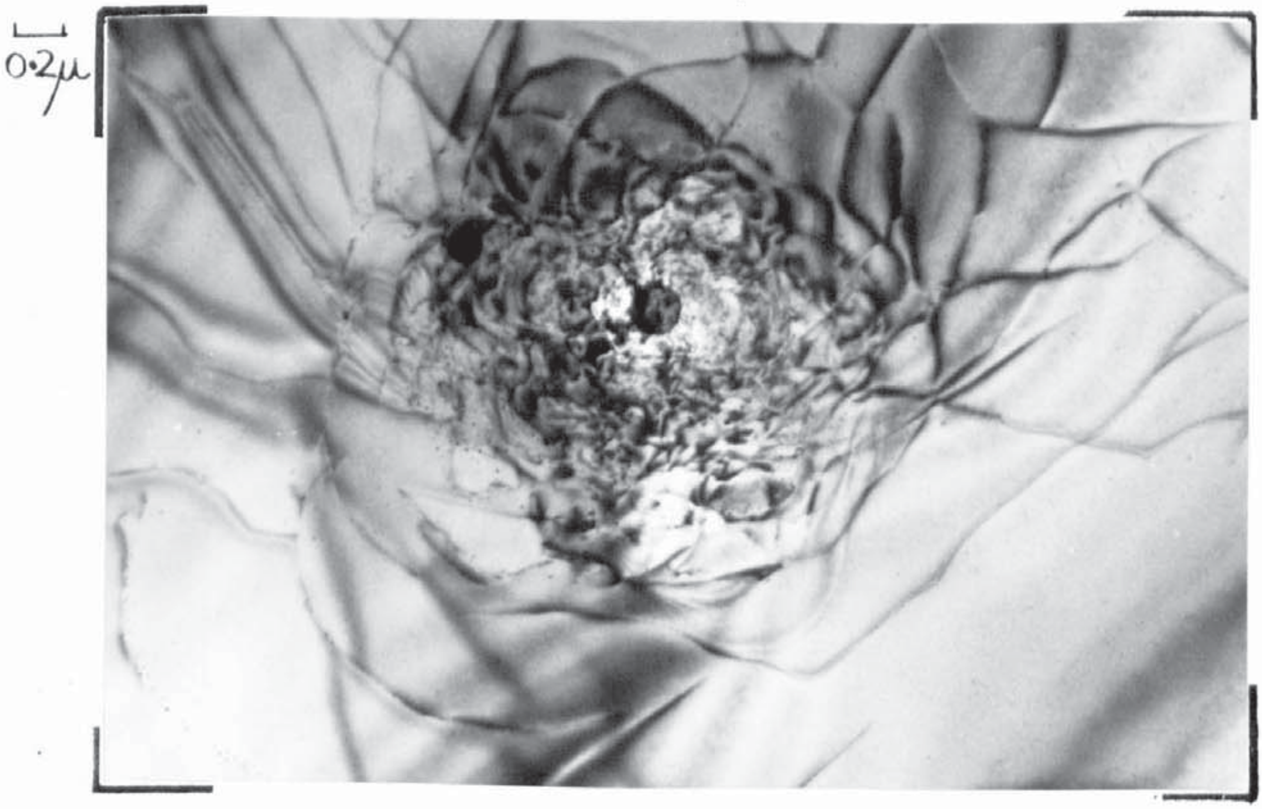

Figure 5.25. As Fig. 5.24 showing heterogeneous nucleation.

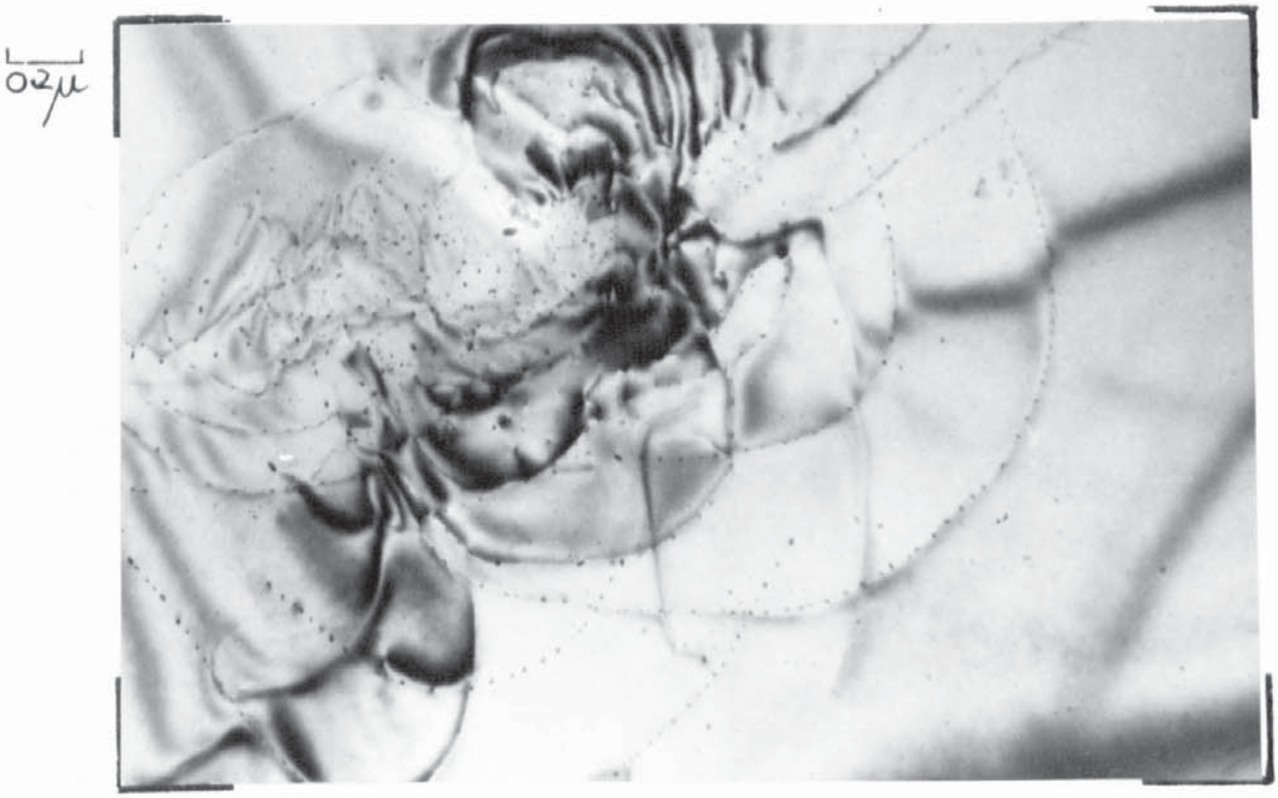

Figure 5.26. As Fig. 5.25. but illustrating a fairly constant precipitate spacing on the dislocations.

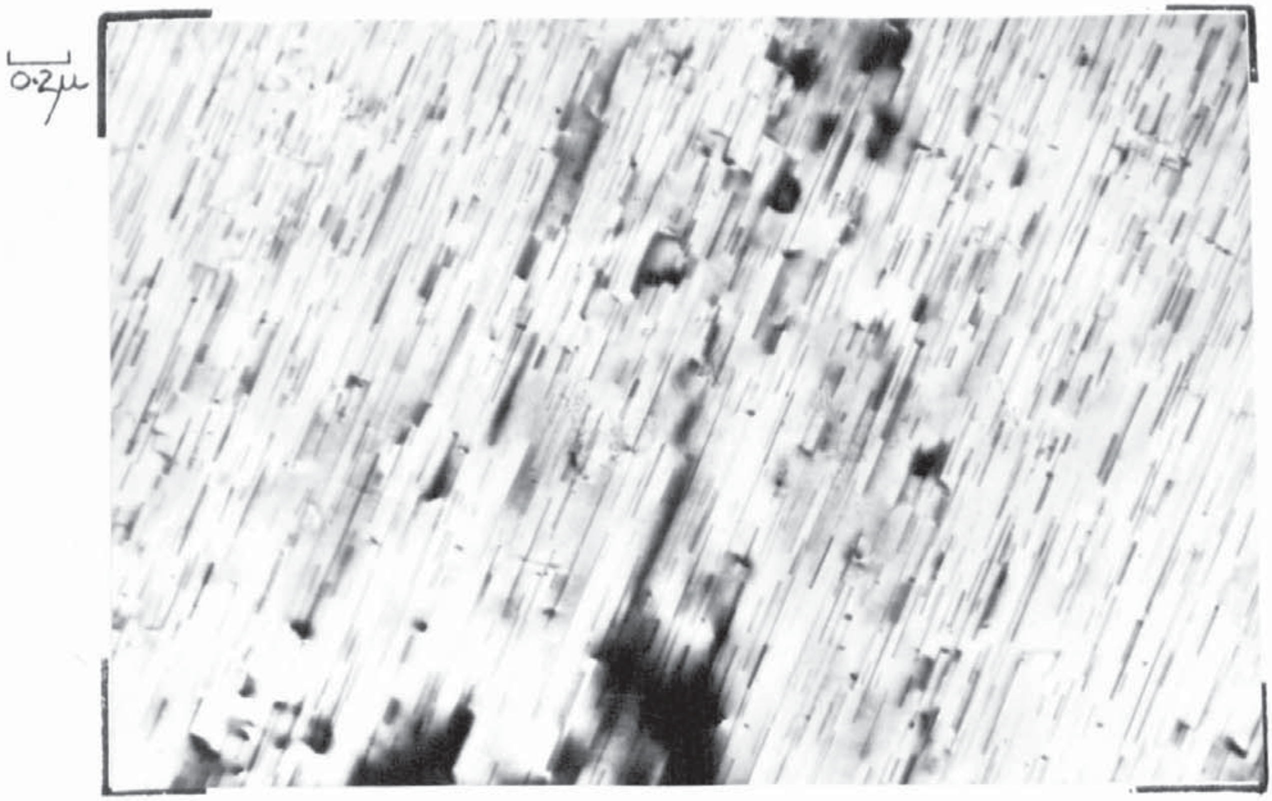

Figure 5.27. Structure of Z6 aged for 264 hours at 120°C..

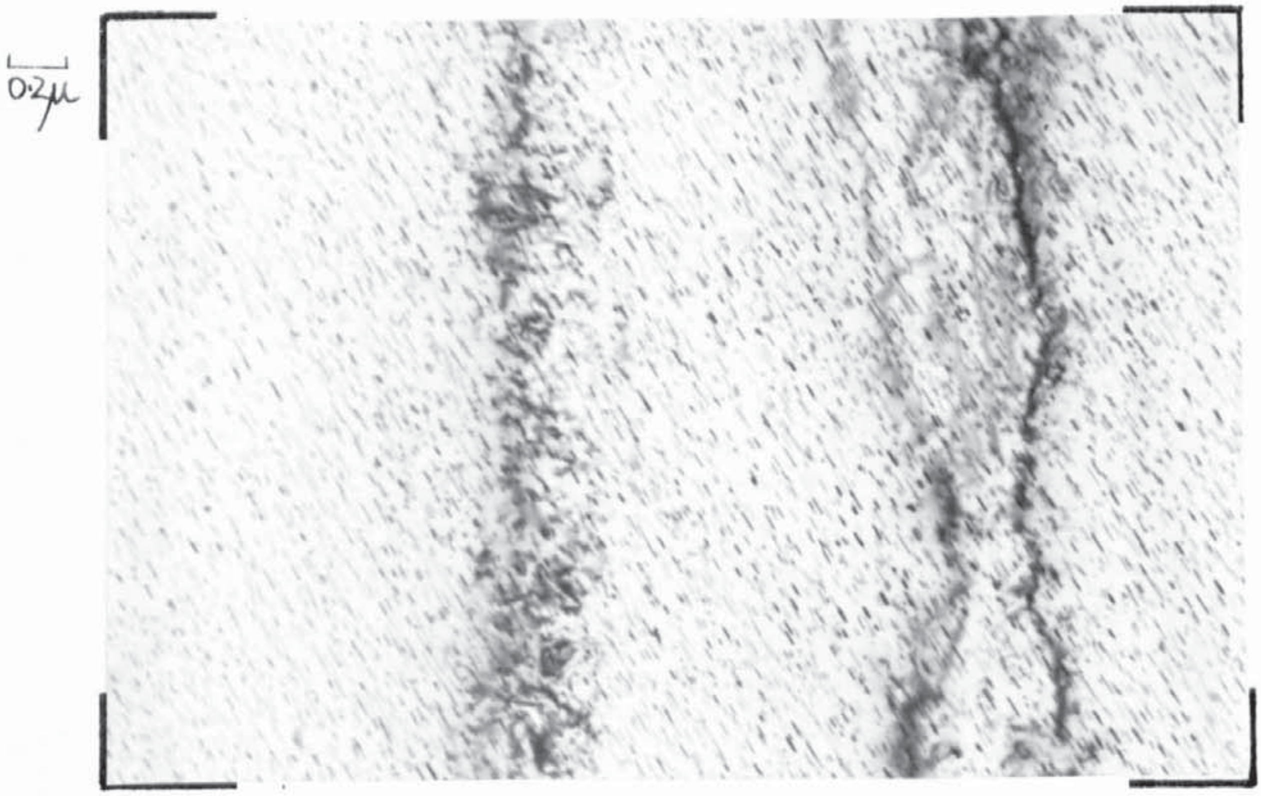

Figure 5.28. As Fig. 5.27 but the foil orientation is close to (0001) Mg.

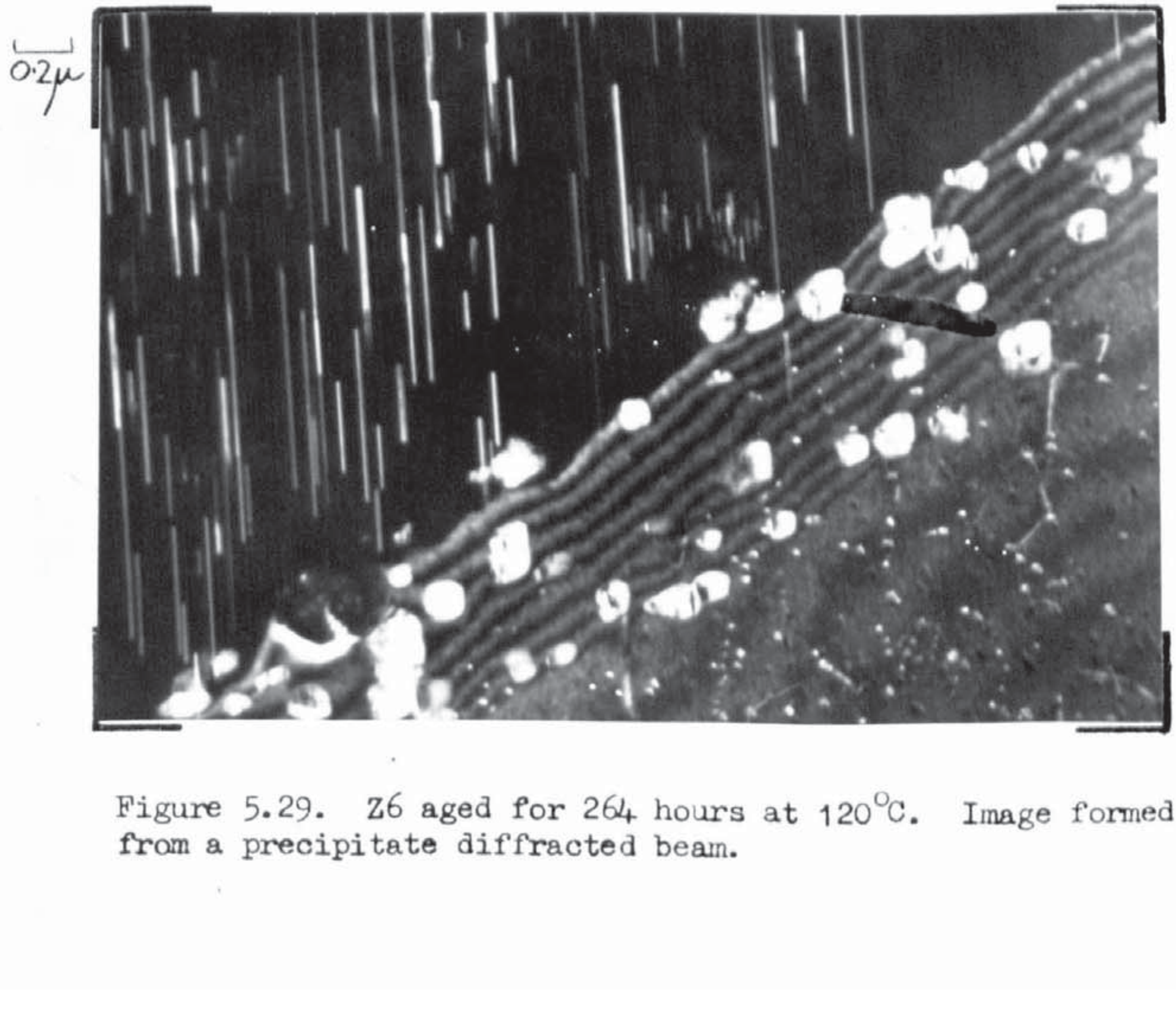

Figure 5.29. Z6 aged for 264 hours at 120°C. Image formed from a precipitate diffracted beam.

Fig. 5.29 and all three orientations are visible due to the coincidence that they have each produced a diffracted beam which has been accepted by the objective aperture. The diffraction spot used to form the structure shown in Fig. 5.29 is labelled. The precipitate pattern is as previously shown in Fig. 5.19.

Fig. 5.31 (1221) shows the structure after quenching directly to 120°C. and ageing for 264 hours. There is no significant difference between precipitate densities in samples direct quenched or quenched to room temperature prior to ageing.

The results of these direct quenching experiments and subsequent precipitation are in conflict with those of Hall[19]. He reported a G.P. zone solvus of 75-80°C. This should result in sparse precipitation generally heterogeneously nucleated when the alloy is quenched directly to temperatures above this. A refinement in the dispersion of the precipitate by a factor of 1000 has been quoted by Lorimer and Nicholson[34] for an Al-Zn-Mg alloy quenched to below its G.P. zone solvus temperature when compared with one quenched above this temperature prior to ageing.

This phenomenon has not been observed in this alloy in this investigation when it is quenched directly to a temperature as high as 120°C.. The G.P. zone solvus is therefore above 120°C..

Ageing at 180°C..

Fig. 5.32 (1424) illustrates the structure after 1 hour at

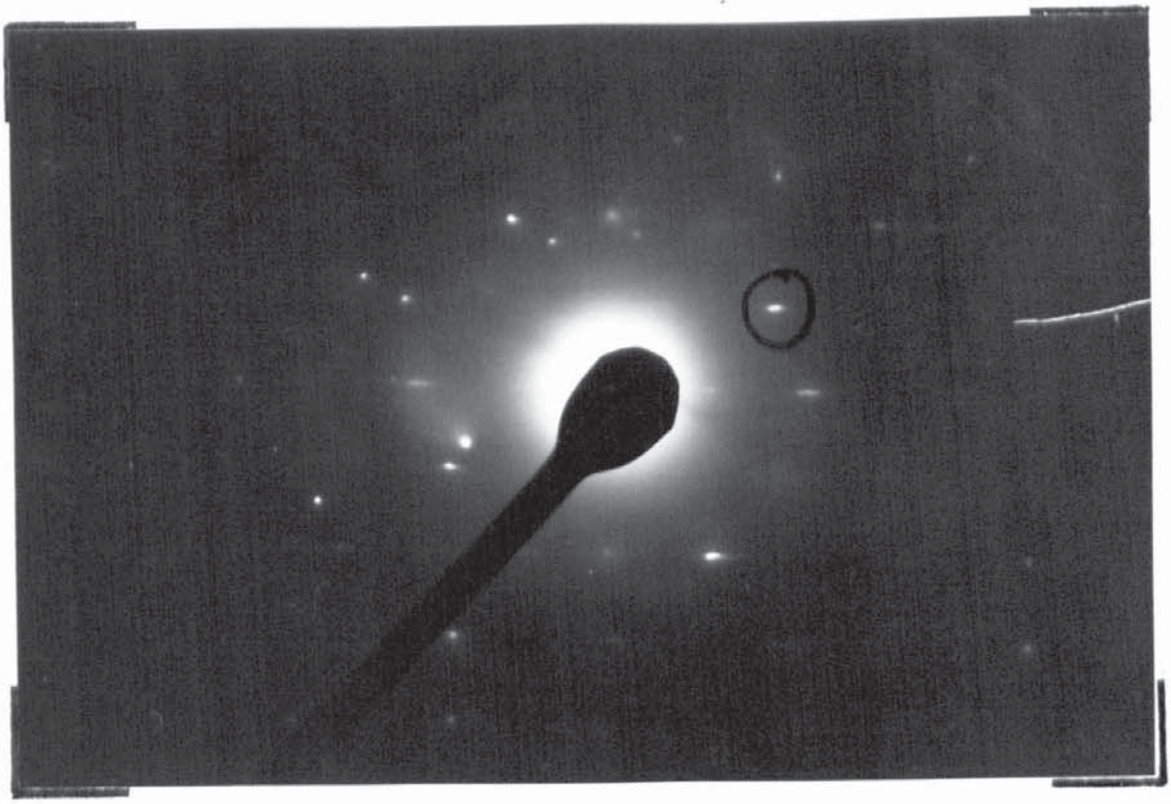

Figure 5.30. Selected area diffraction pattern, showing spot used for Fig. 5.29.

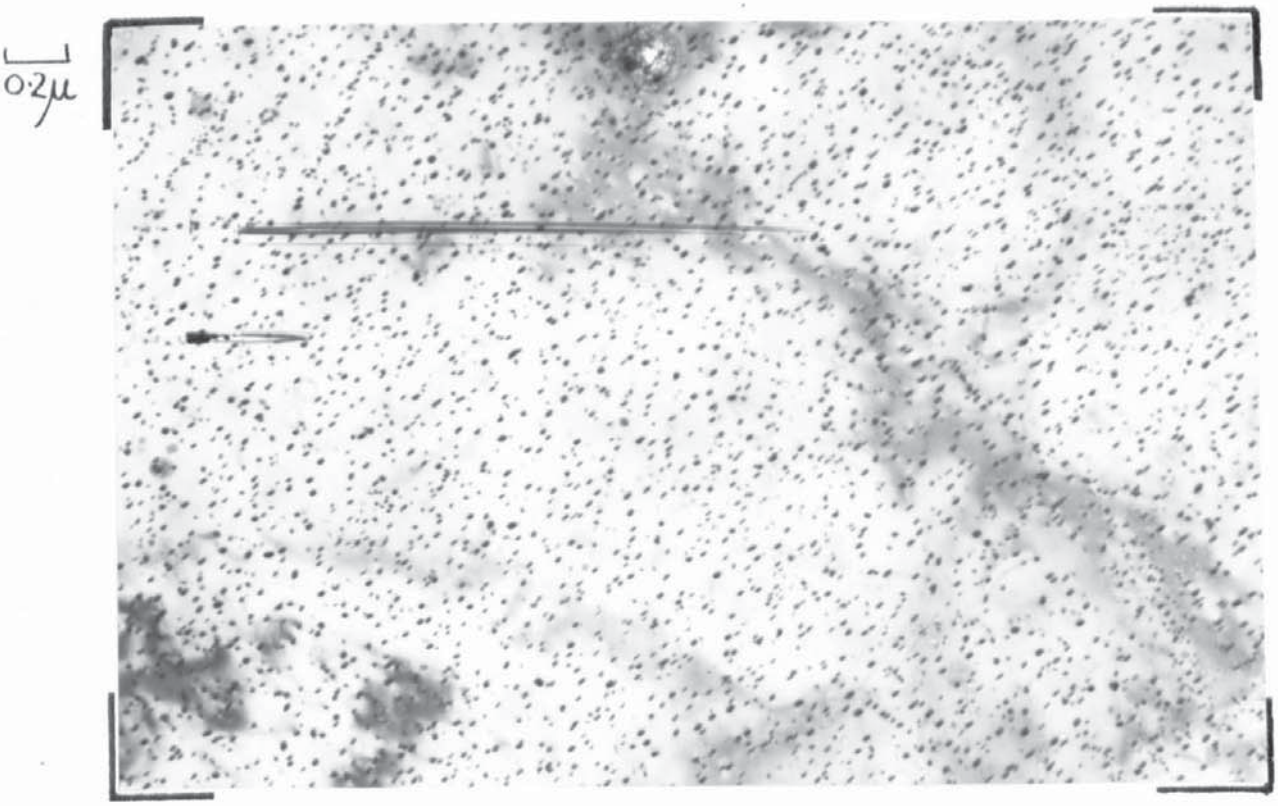

Figure 5.31. Structure of sample aged for 264 hours at 120°C. after directly quenching to the ageing temperature.

180°C. in an (0001)Mg foil; heterogeneous nucleation is apparent and the precipitate spacing is 800-10,000 A$^{\circ}$. Fig. 5.33 (1433) is a diffracted beam image from a (10$\bar{1}$0) Mg beam and the matrix strainassociated with some of the needles is evident. Some precipitates are not showing strain fields in reversed contrast: this is due to there being three precipitate orientations and only one (10$\bar{1}$0)Mg beam being used to form the image.

The structure after 10 hours which corresponds to peak hardness and slightly overaged on the 0.1% P.S, is illustrated in Fig. 5.34 (561) at a relatively low magnification. Extensive precipitation within the grains and large precipitates at the boundaries is evident. The photograph also serves to demonstrate a preferred thinning at the grain boundaries which could be misinterpreted as a precipitate free zone, as at A for instance in Fig. 5.34. Fig. 5.35 (569) also illustrates a wide precipitate free zone between grains and in this instance is due to the boundary being at a large angle to the electron beam and not oriented to show displacement fringes.

Fig. 5.36 (503) and Fig. 5.37 (550) are of (10$\bar{1}$0)Mg and (0001)Mg foils respectively. The three precipitates are evident in these illustrations. The equilibrium phase Mg_2Zn_3 is clearly seen in Fig. 5.36 as discs perpendicular to the electron beam. The $MgZn_2^1$ needle length is 200-12,000 A$^{\circ}$ and the spacing 200-5000 A$^{\circ}$ although the average spacing is closer to 750-1000 A$^{\circ}$. There are

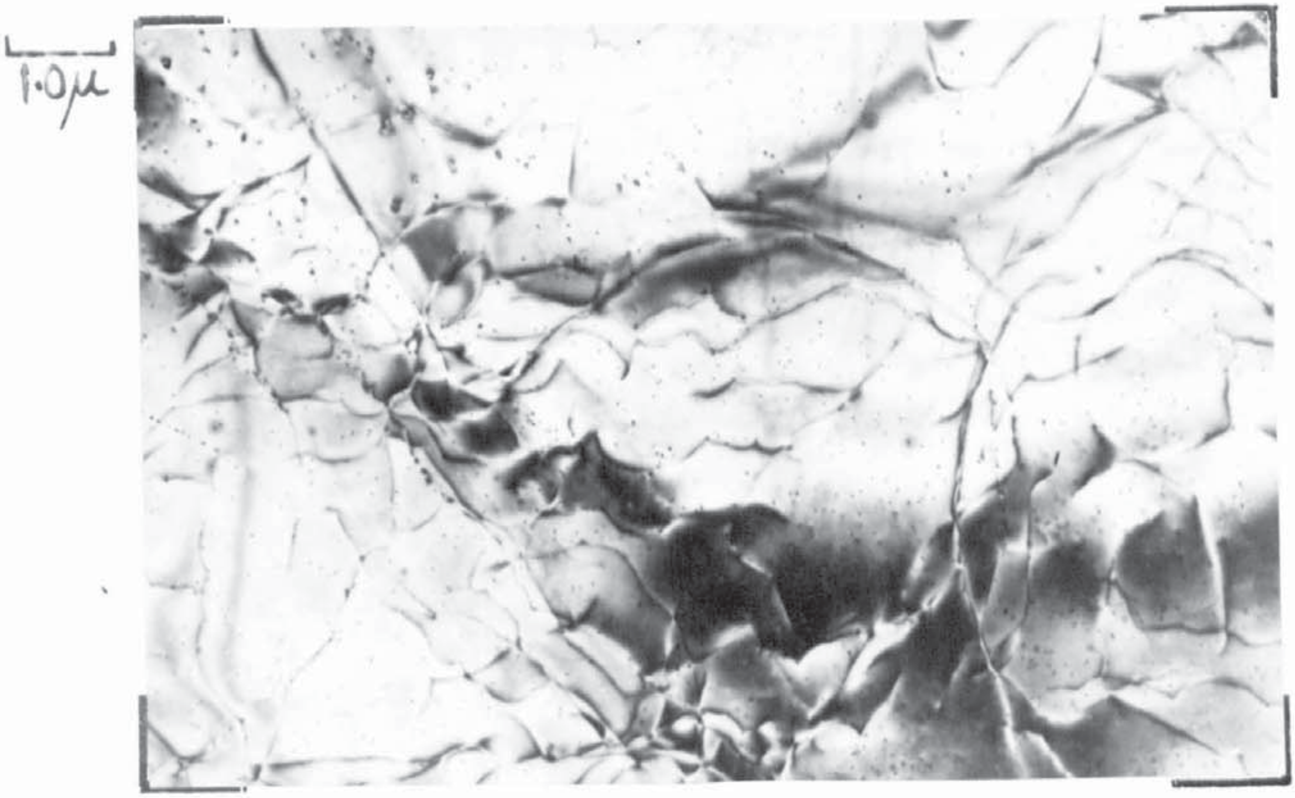

Figure 5.32. Z6 aged for 1 hour at 180°C..

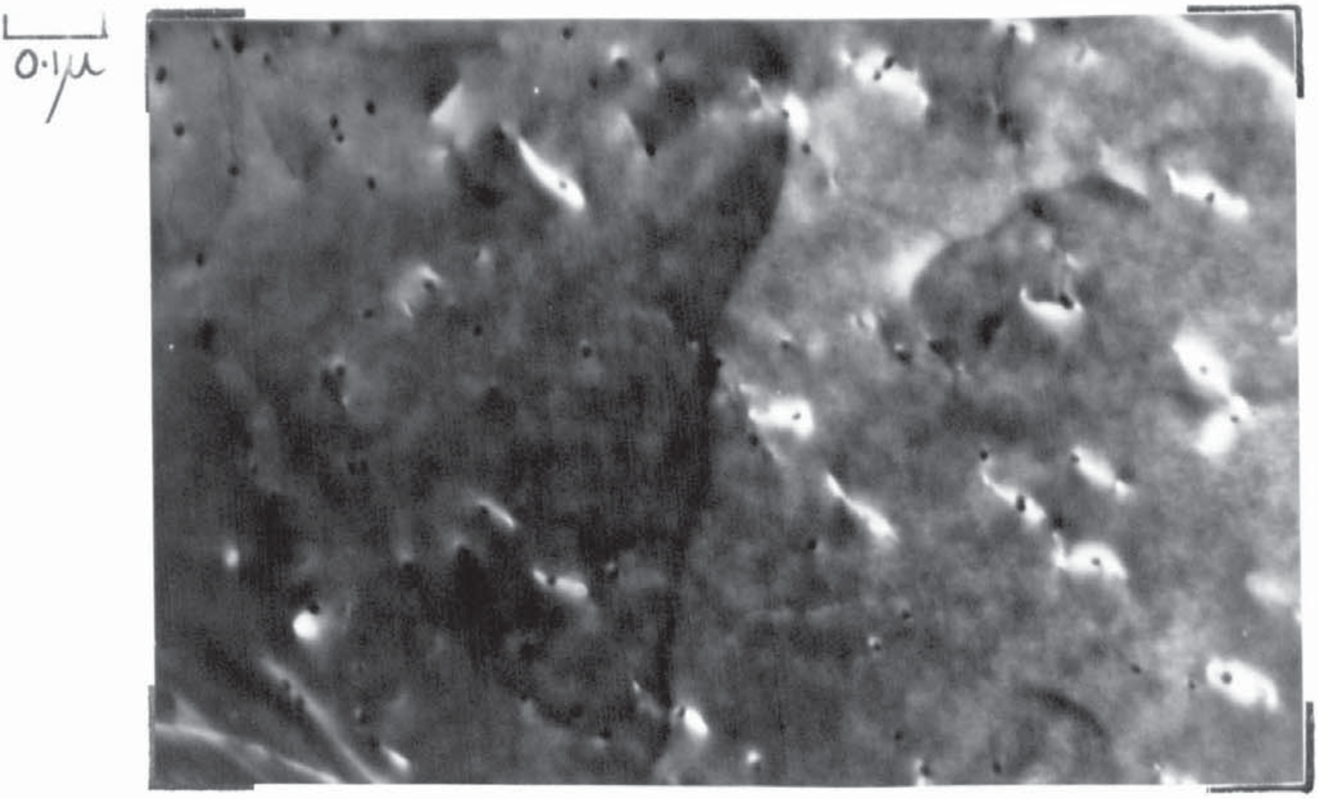

Figure 5.33. Diffracted beam image using a $(10\bar{1}0)$Mg beam. Sample as in Fig. 5.32.

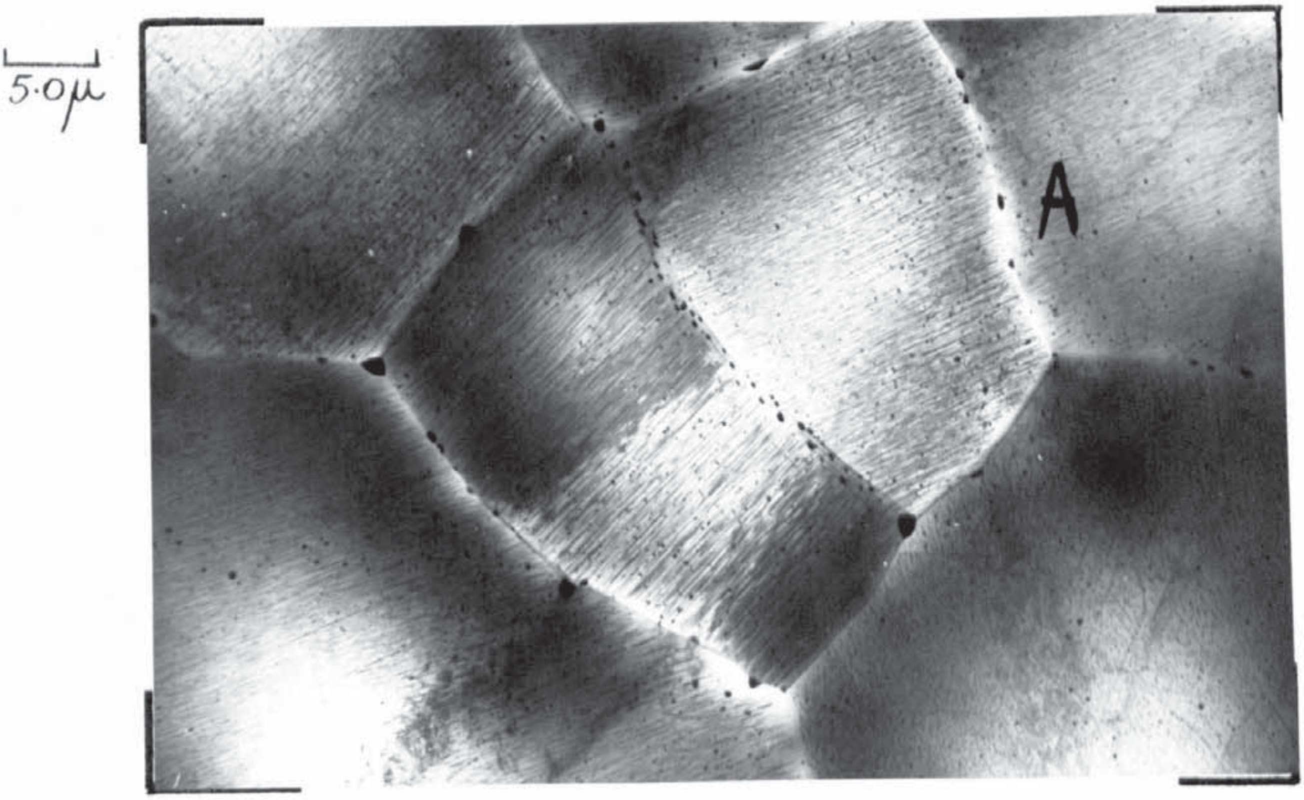

Figure 5.34. Structure after 10 hours at 180°C. showing extensive grain boundary precipitation.

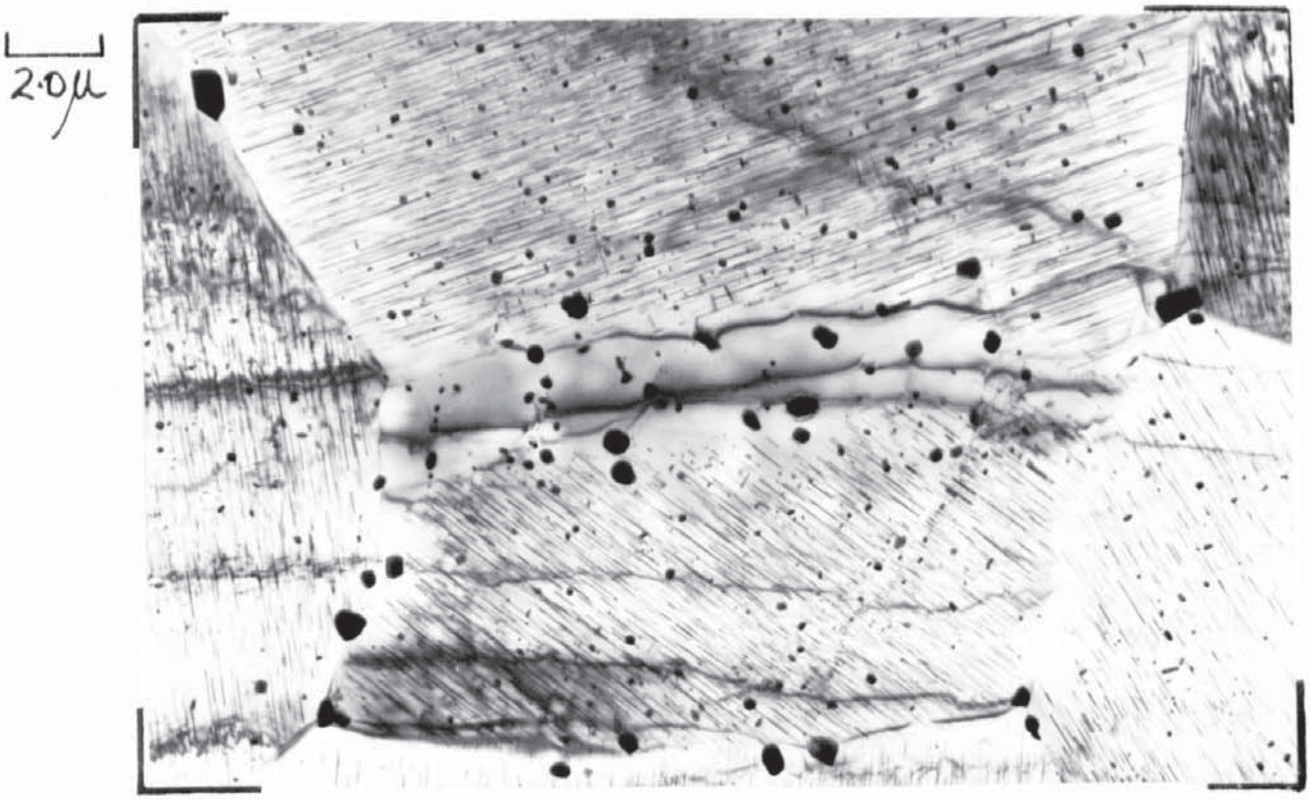

Figure 5.35. Z6 aged for 10 hours at 180°C..

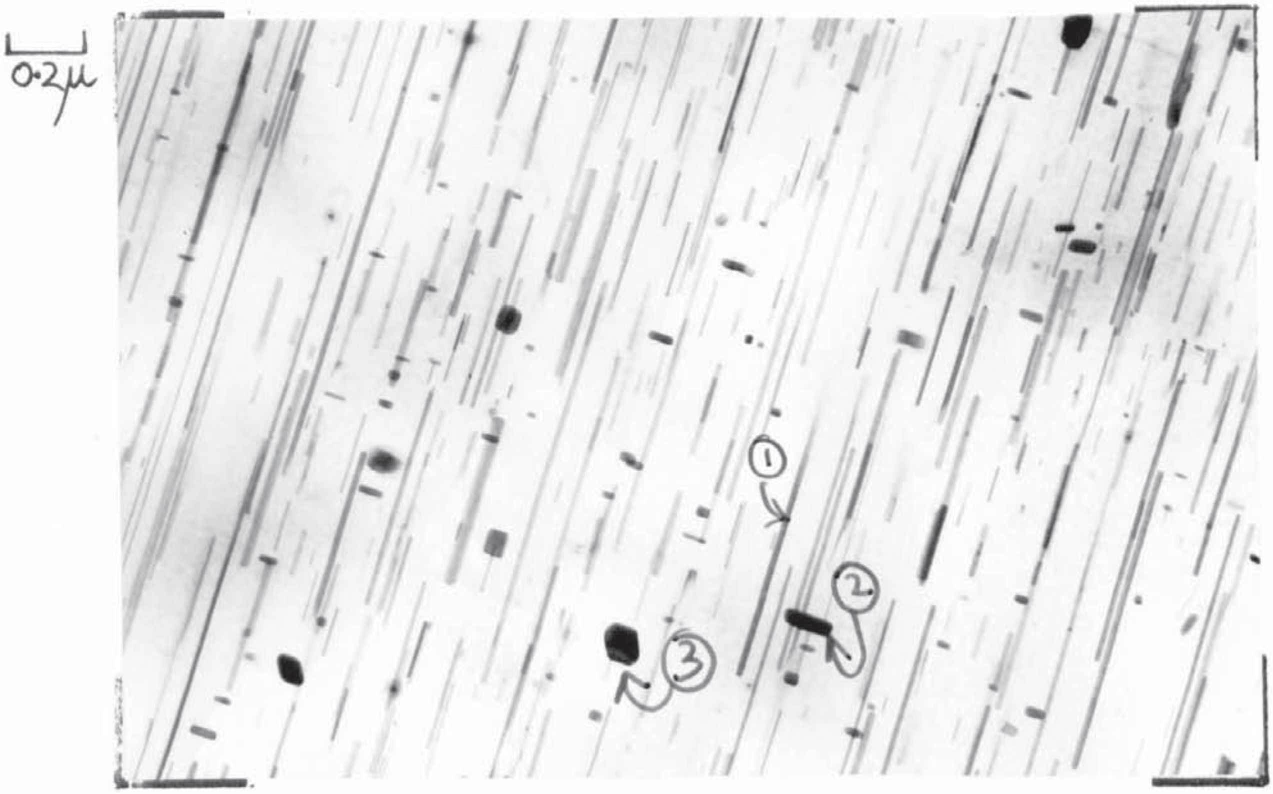

Figure 5.36. As Fig. 5.35 showing the three precipitates, formed in this alloy, (1) $MgZn_2^{1}$ (2) $MgZn_2^{2}$ and (3) Mg_2Zn_3.

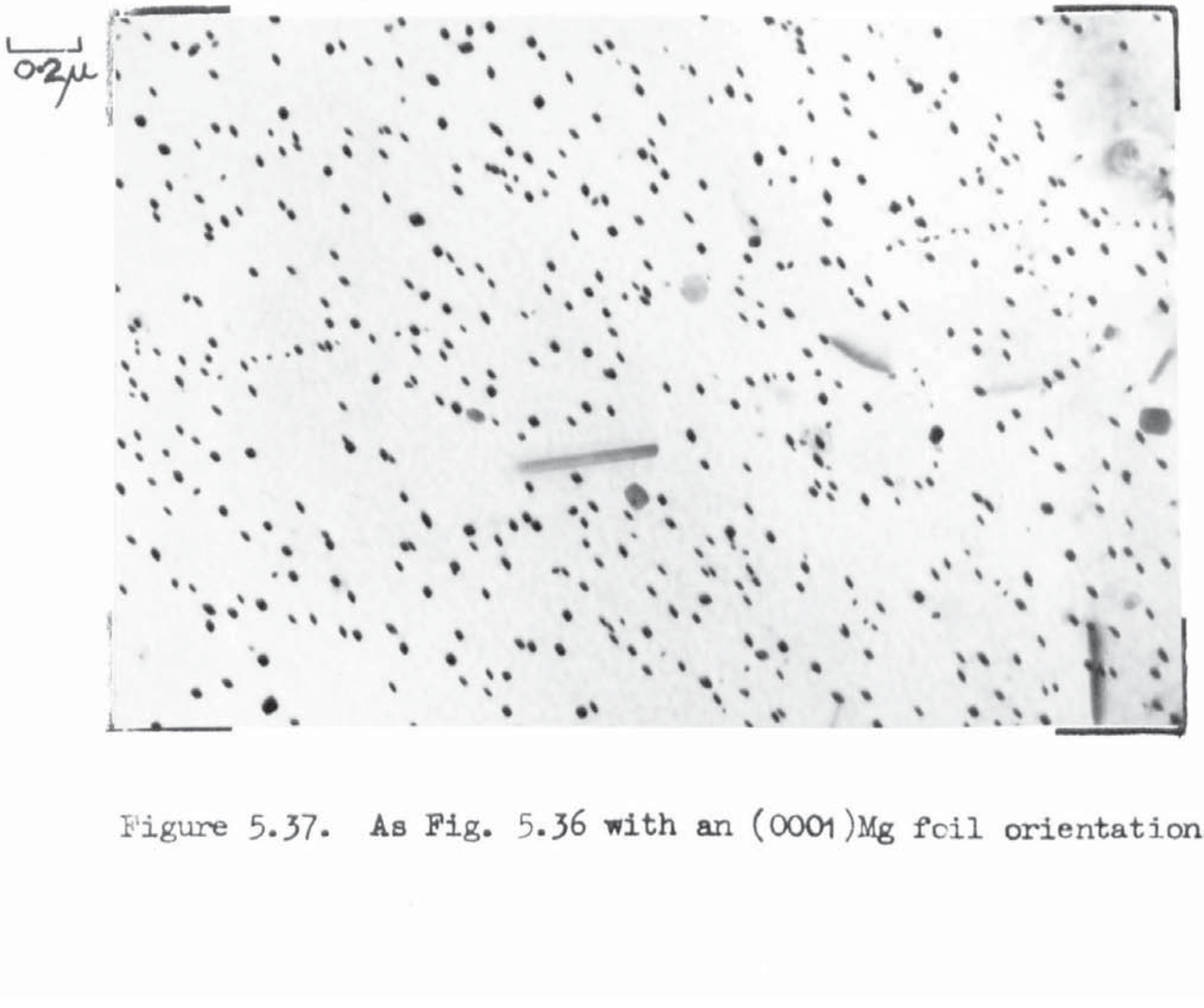

Figure 5.37. As Fig. 5.36 with an (0001)Mg foil orientation.

100-130 needles per square micron.

The diffraction pattern for Fig. 5.36 is shown in Fig. 5.38 (560) and is of the (10$\bar{1}$0)Mg type. The precipitate pattern is as Fig. 5.19 but with additional spots from the $MgZn_2^2$ discs and possibly the Mg_2Zn_3.

Ageing at 210^{o}C..

Fig. 5.39 (624) shows the structure after 8 hours ageing in an (0001)Mg foil. The $MgZn_2^1$ needle spacing is between 2,000-12,000 A^o and the $MgZn_2^2$ discs have reached 1000 - 2,500 A^o in diameter. Fig. 5.40 (633) illustrates a grain boundary almost parallel to the electron beam with a 2,400-6,000 A^o wide precipitate free zone on one side and only 600-1000 A^o on the other. Comparing this with published precipitate free zones it is immediately evident that the existence and extent of the zone is not as distinct as those in the Al-Zn-Mg alloy system[34]. The distribution of the coarse precipitate and its shape hinder any quantitative assessment of a P.F.Z in this alloy. An exact (10$\bar{1}$0)Mg or (11$\bar{2}$0)Mg oriented foil was not obtained on samples aged for 8 hours at 210^{o}C, therefore measurement of the true needle length was not possible.

Fig. 5.41 (1127) is of a (11$\bar{2}$0) Mg foil but in a sample aged for 48 hours at 210^{o}C. and needle lengths of 60-15,000 A^o were observed but the range was generally limited to 1,500 - 7,500 A^o.

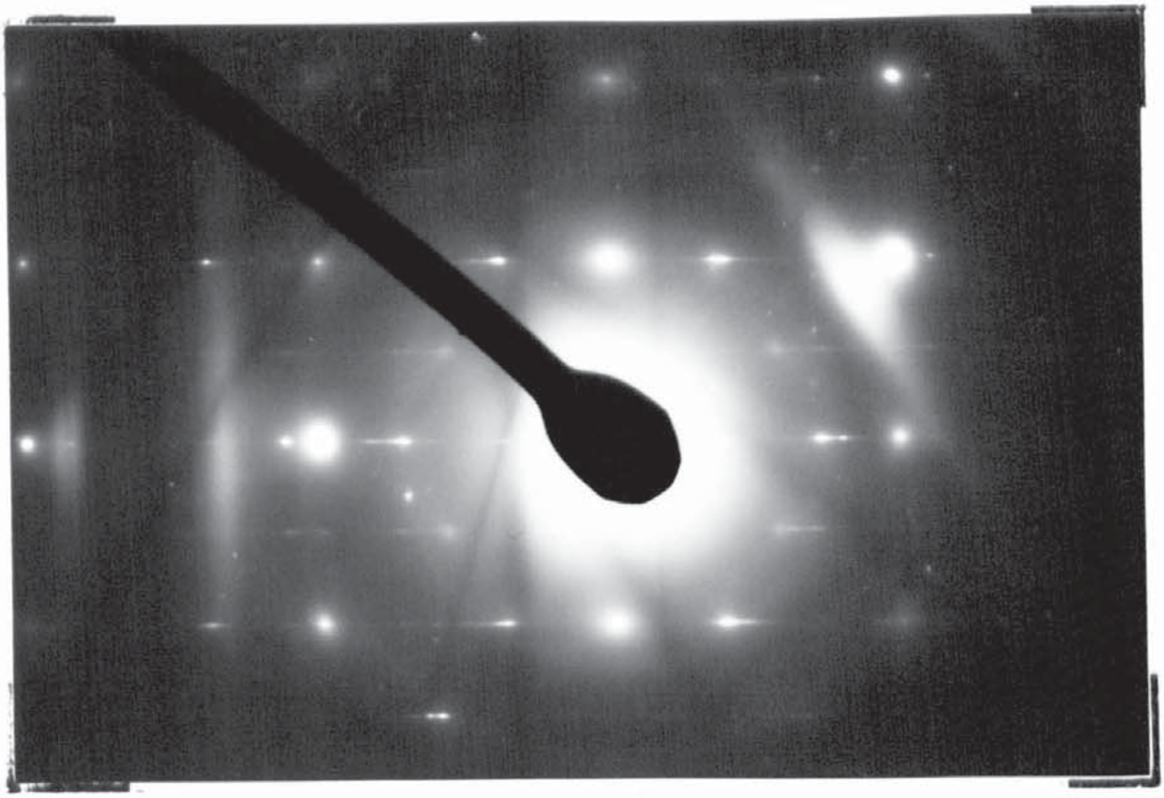

Figure 5.38. Selected area diffraction pattern of area shown in Fig. 5.36.

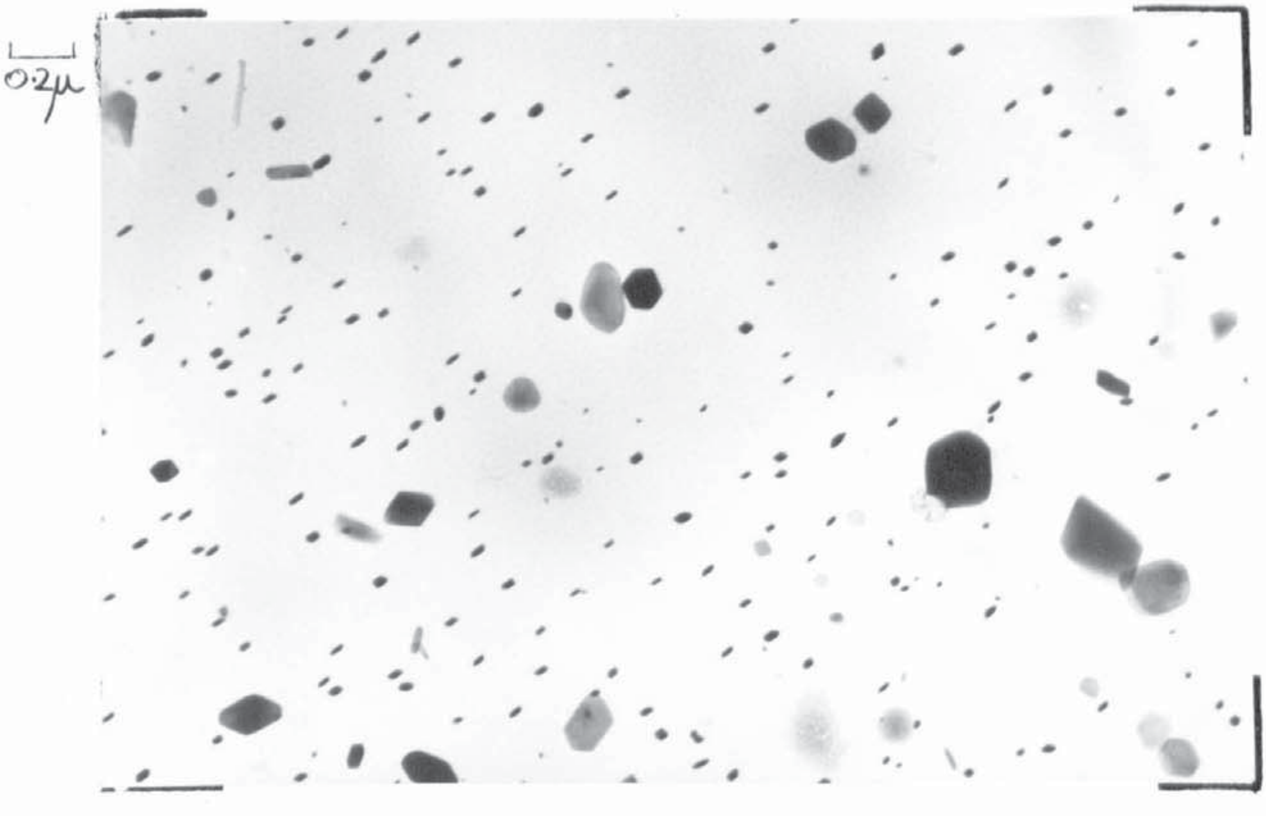

Figure 5.39. Z6 aged for 8 hours at 210°C..

Figure 5.40. As Fig. 5.39 showing an asymmetrical precipitate free zone.

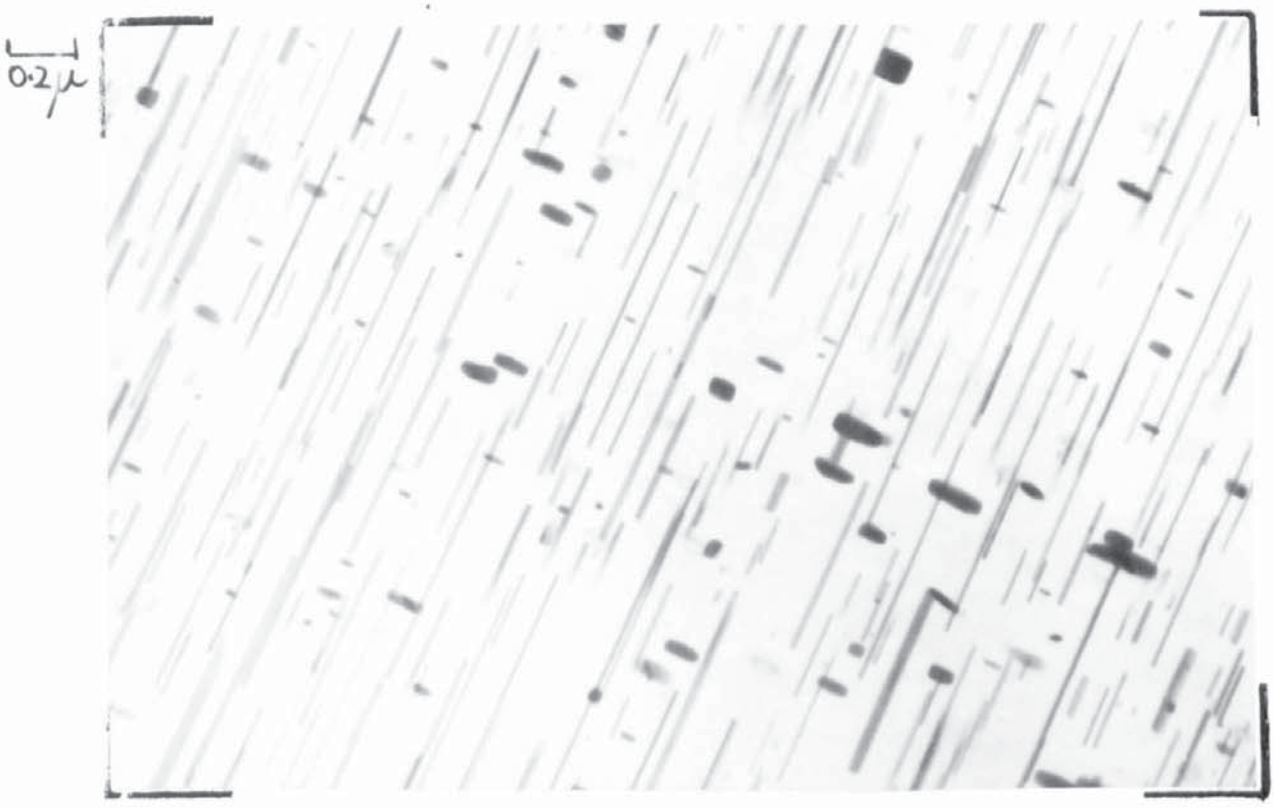

Figure 5.41. Structure after ageing for 48 hours at 210°C.

Fig. 5.42 (1124) is of an almost (0001)Mg foil and the equilibrium Mg_2Zn_3 is evident as a needle like precipitate at 60° to each other. The $MgZn_2^2$ discs have reached a size of 750-2000 A$^{\circ}$ in diameter and the $MgZn_2^1$ needle spacing is 500-2000 A$^{\circ}$.

Ageing at 240°C..

Hardness and tensile property changes were not determined at this temperature but the electron metallography was examined. Fig. 5.43 (821) shows three grain orientations, (0001)Mg, (11$\bar{2}$0) and one at a slight angle to (0001)Mg. One needle in the (11$\bar{2}$0) Mg grain has reached a length of 27,000 A$^{\circ}$. The needle spacing from the (0001)Mg grain is 600-2,000 A$^{\circ}$ and this sample was aged for 8 hours.

Double Ageing.

The results reported by Hall[19] indicating an enhanced response when the alloy is "split aged" were considered to result from bracketing the G.P. zone solvus by the two ageing temperatures. A similar treatment was given to samples in this investigation. A 9 inch length of the 3 inch diameter bar was sectioned to give six ¾ inch diameter bars from the mid-radial position. These were randomised and heat treated in pairs to give duplicate tensile bars: the results are shown overleaf.

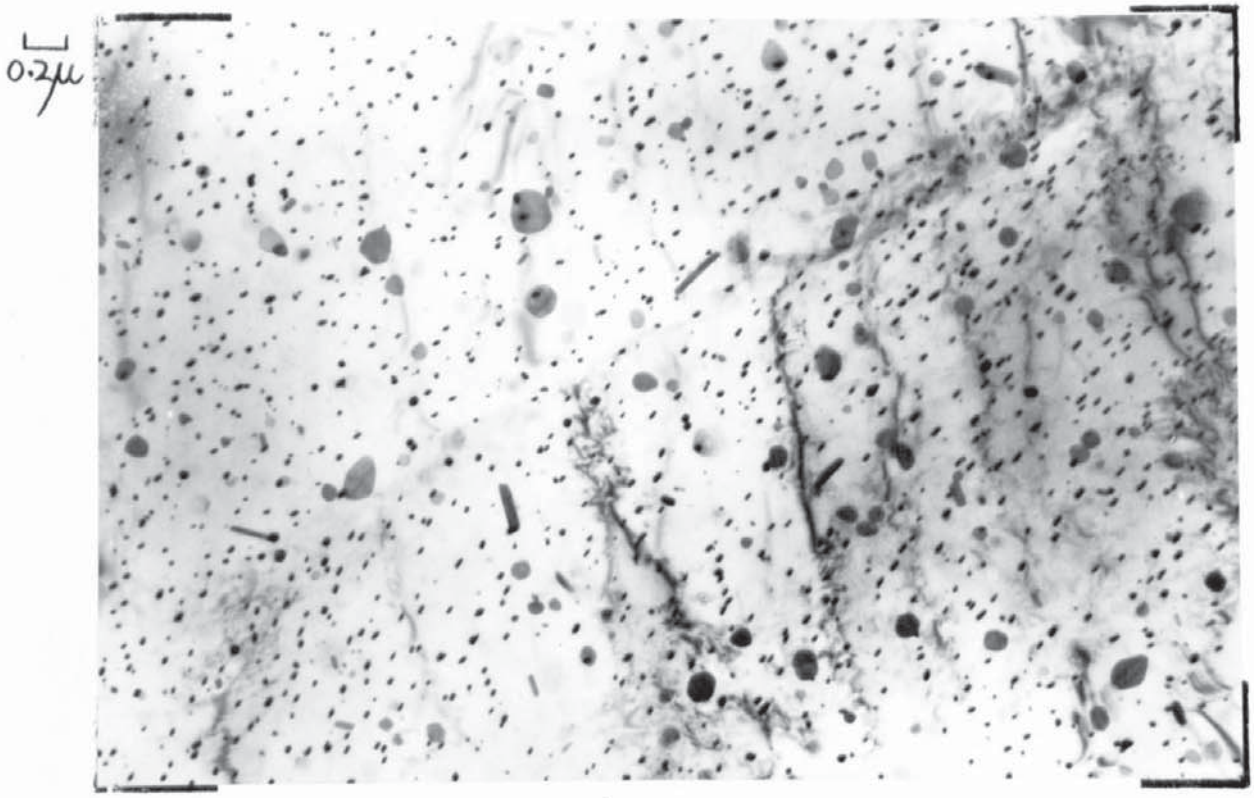

Figure 5.42. As Fig. 5.41 showing the structure in an (0001)Mg foil.

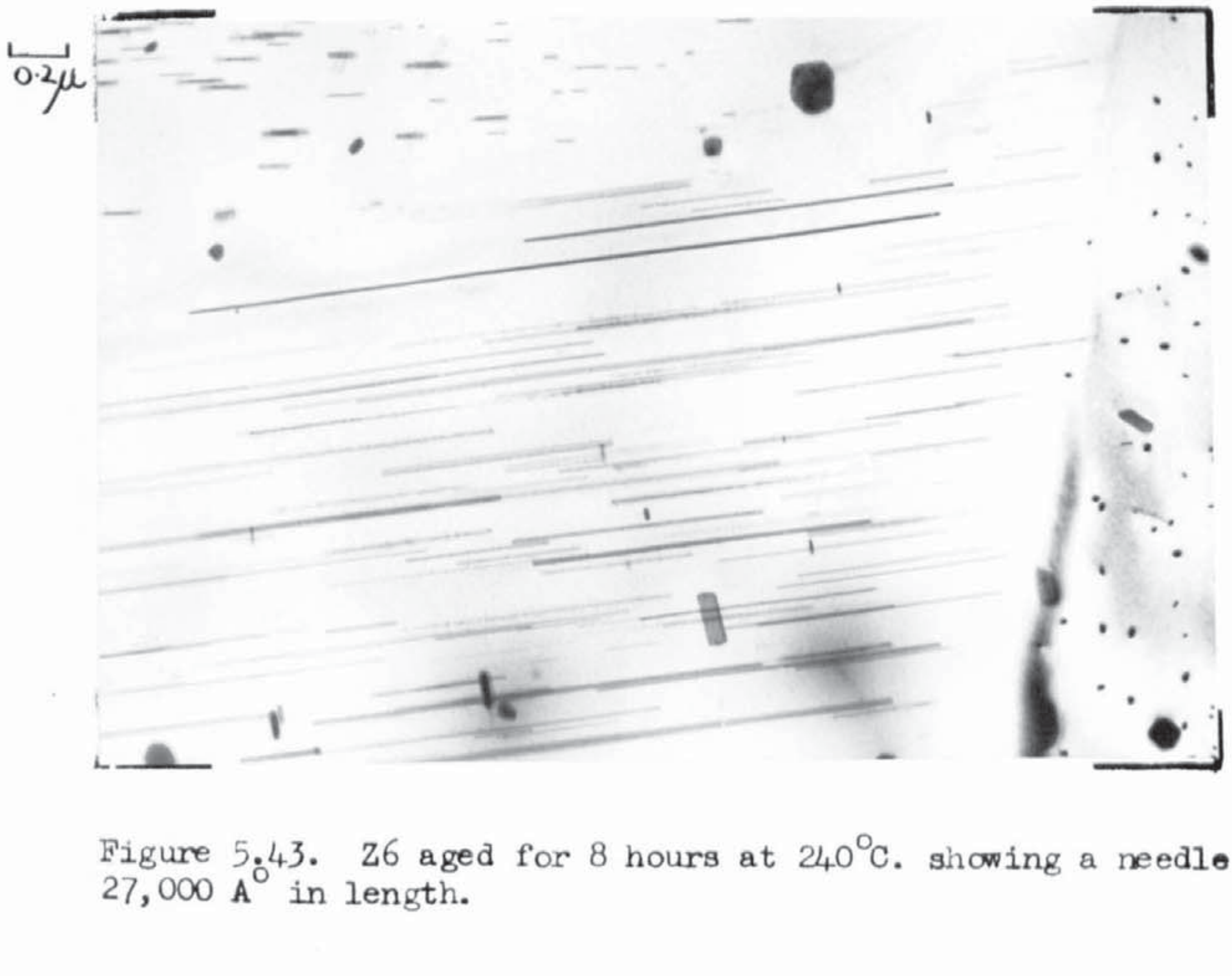

Figure 5.43. Z6 aged for 8 hours at 240°C. showing a needle 27,000 A° in length.

CONDITION	0.1% P.S. t.s.i.	0.2% P.S. t.s.i.	T.S. t.s.i.	El% on $\sqrt{4}$ A
16/170°C	14.3	16.2	21.3	12
16/170°C	15.0	17.0	21.5	9
48/65°C + 16/170°C	15.2	17.2	21.5	8
48/65°C + 16/170°C	15.9	17.8	21.3	10
96/65°C + 16/170°C	15.9	17.9	21.6	8
96/65°C + 16/170°C	16.1	18.0	21.4	8

The second ageing temperature of 170°C was chosen to enable a direct comparison to be made with the results reported by Hall[19].

Electron Microstructure

Fig. 5.44 (1553) shows the structure after ageing for 16 hrs. at 170°C, in a $(10\bar{1}0)$ Mg foil and the only reliable parameter available is that of needle length which is between 150-1,700 A°. Fig. 5.45 (1564) shows the structure after ageing for 96 hrs./65°C and 16 hrs./170°C and it is also from a $(10\bar{1}0)$ Mg foil. There is a slight difference in magnification between Fig. 5.44 and Fig. 5.45. The needle length is 90-3000 A° but generally between 90-1100 A°. Fig. 5.46 (1568) is of an (0001) Mg foil after the double ageing treatment and the precipitate spacing is 70-500 A°.

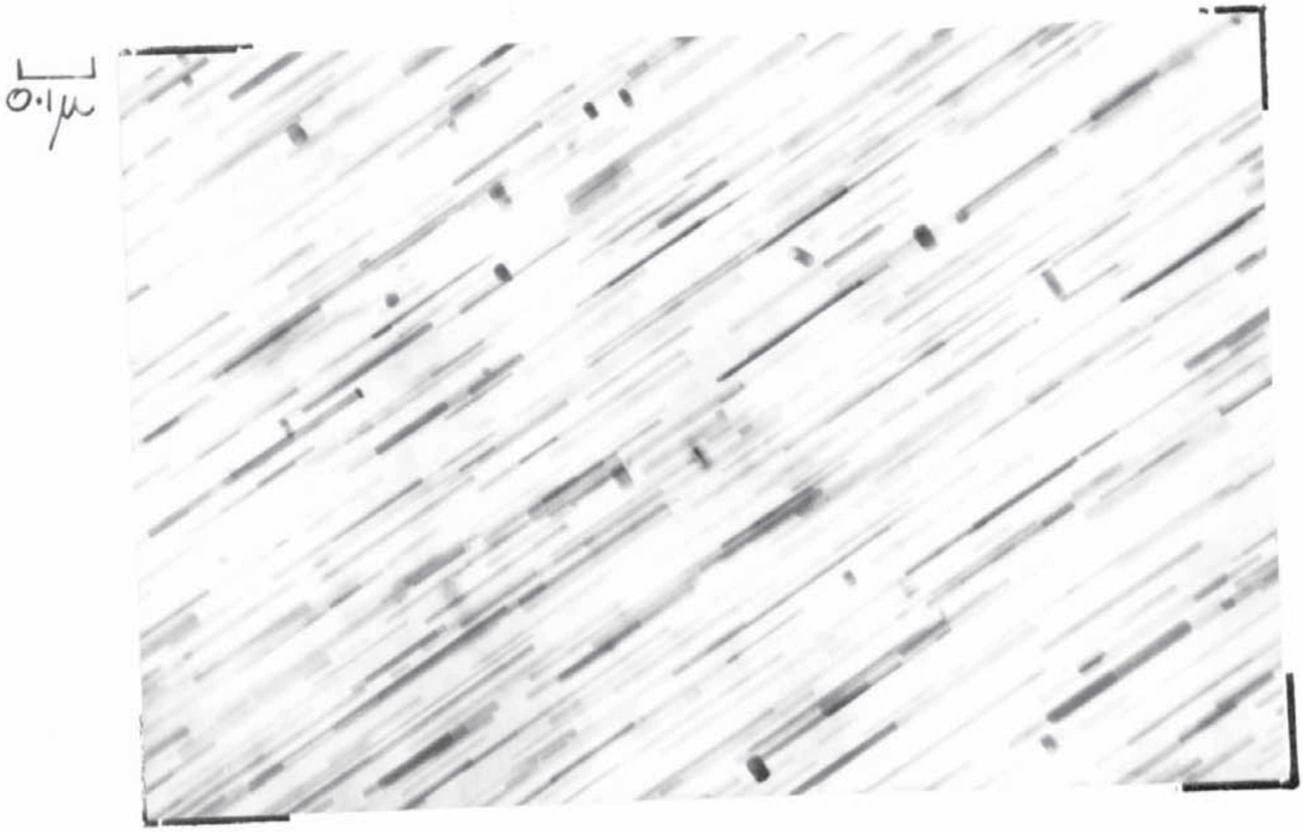

Figure 5.44. Structure after 16 hours at 170°C.

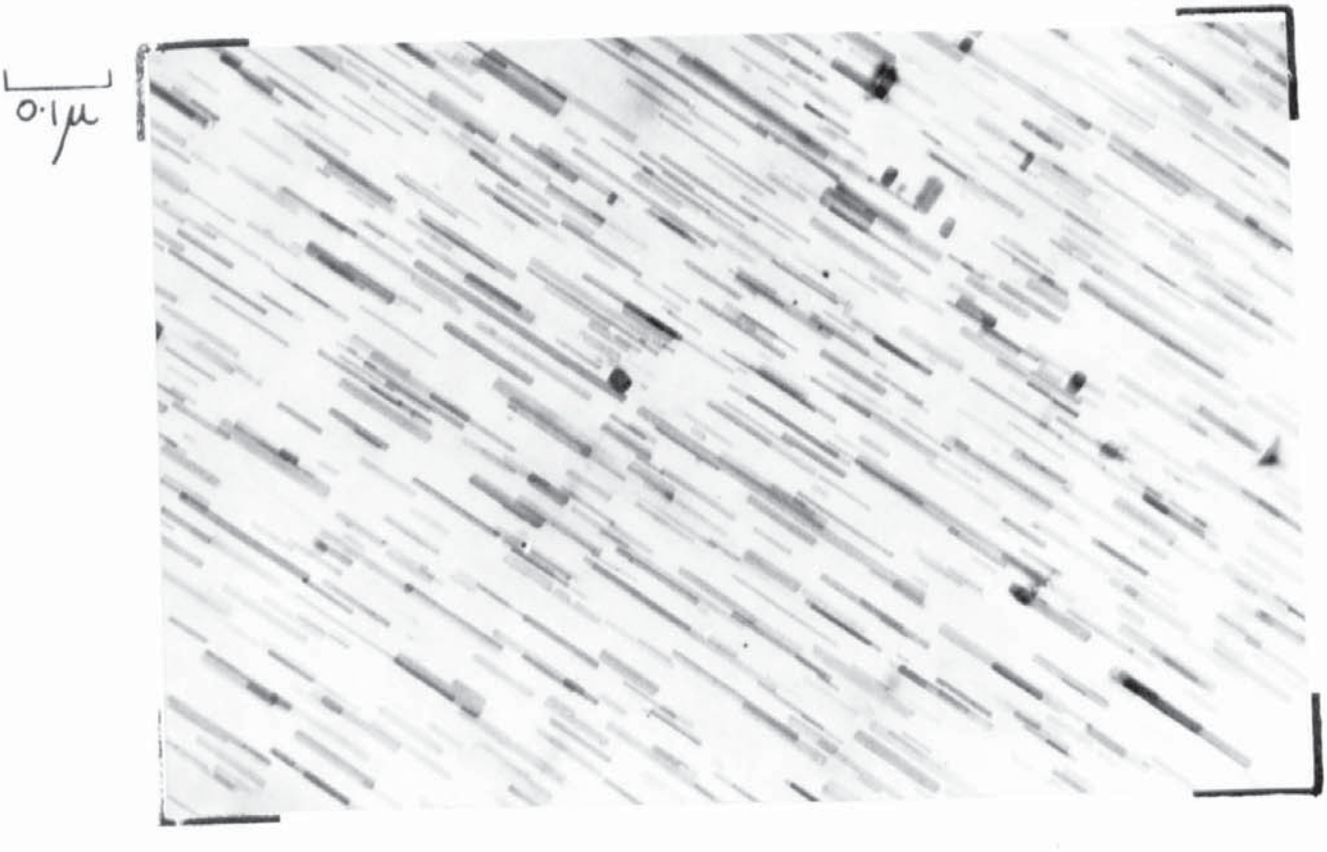

Figure 5.45. Structure after ageing for 96 hours at 65°C. followed by 16 hours at 170°C.

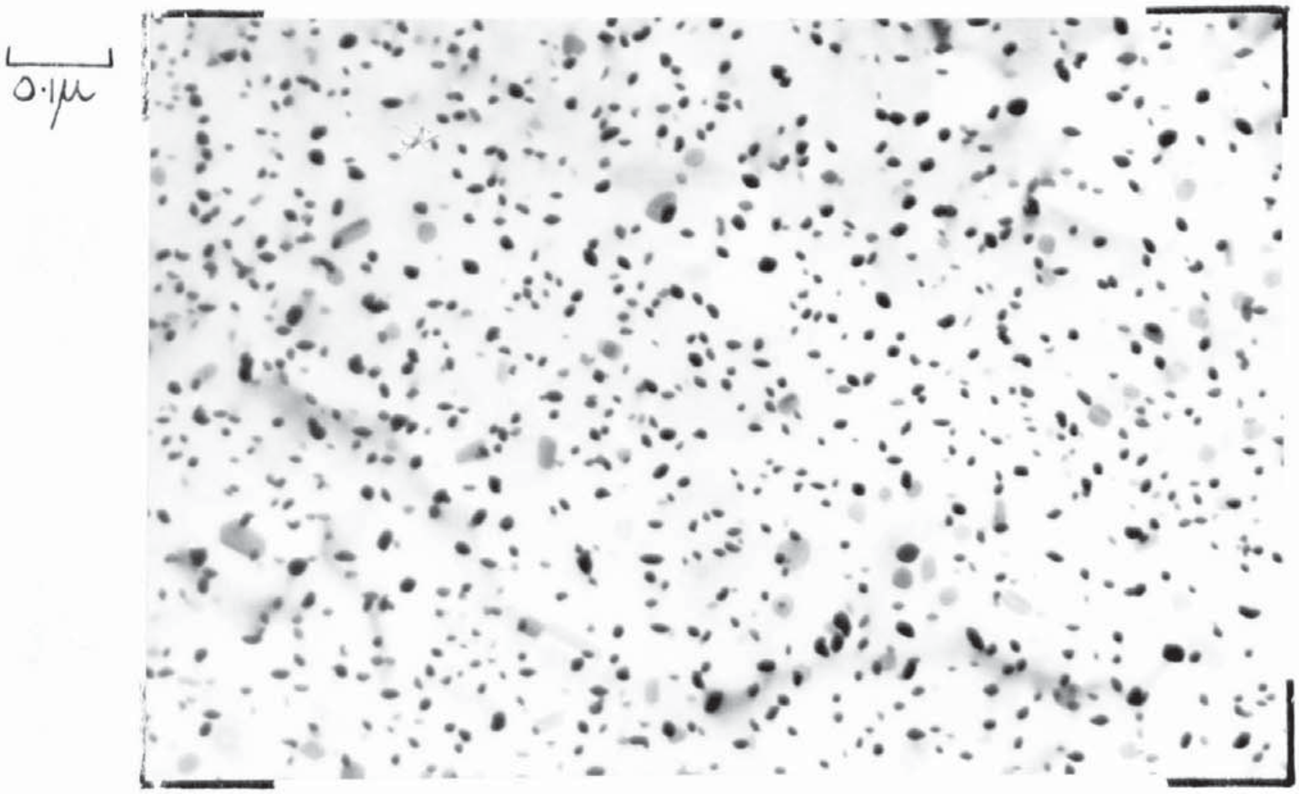

Figure 5.46. As 5.45 showing structure in an (0001)Mg foil.

The $MgZn_2^2$ has grown to about 4000 A° in diameter. Overall, a decrease in the precipitate length of about 25% has resulted from the double ageing process, which is reflected in the slight increase in tensile properties shown in the table.

Fig. 5.46 should be compared with Fig.5.37 which is of the alloy after 10 hrs. at 180°C. only. There are between 300 and 360 precipitates per square micron shown in Fig. 5.46 compared to 100-130 in the sample shown in Fig. 5.37. The slight difference in ageing temperature has also contributed to this refinement and also the shorter ageing time at 180°C..

Analysis of the G.P. zone strain fields.

The technique to determine the magnitude and sense of the strain has been described in the section dealing with contrast from second phase particles. The very small size of the zones, the difficulty of obtaining a zone axis such that the line of no contrast could be observed before carbon contamination caused any deterioration in image quality, precluded the determination of the magnitude of the in situ strain. As illustrated in Fig.3.7 the contrast effects from the zones when imaged with the undeviated beam and then with a diffracted beam from the matrix can provide a method of determining the sense of the strain. This was possible and Fig. 5.47 and 5.48 (1070,1069) are from the same area of a $(10\bar{1}0)$Mg foil.

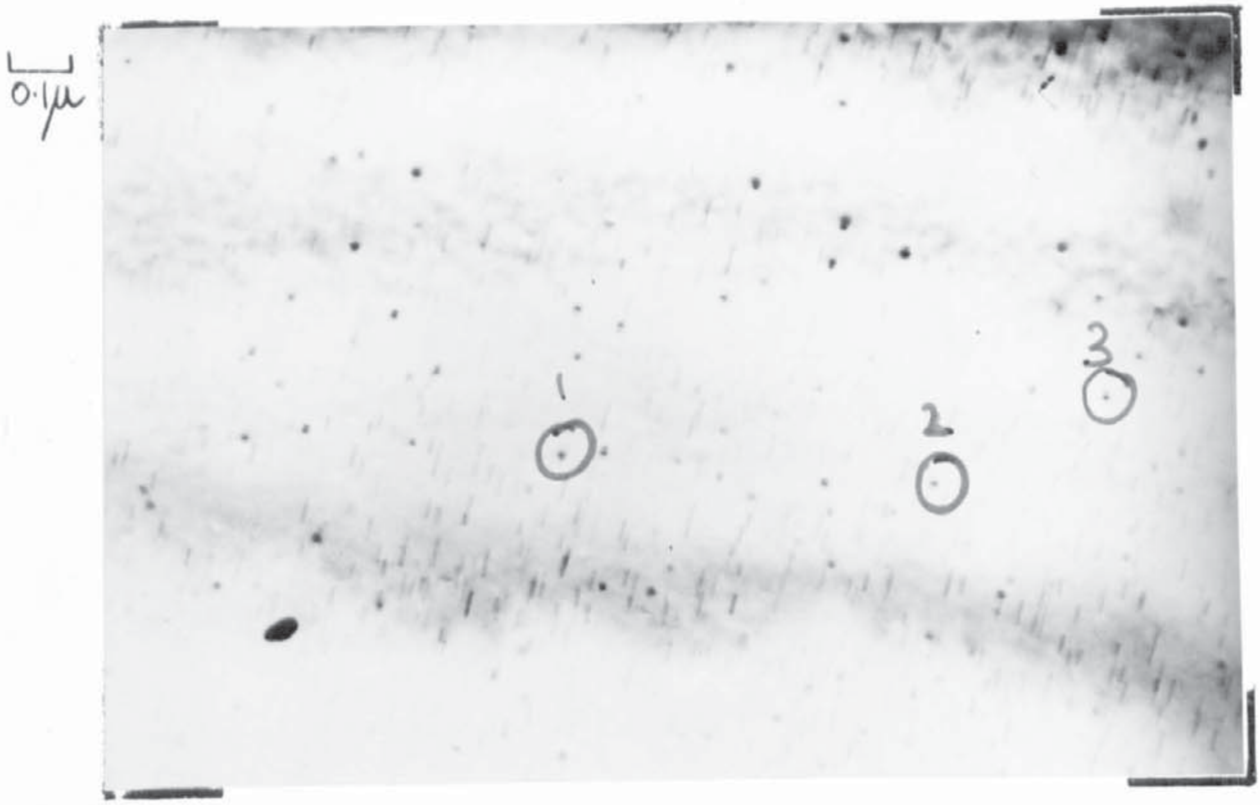

Figure 5.47. Structure used to determine the sense of the in situ strain.

Figure 5.48. Area as shown in Fig. 5.47 but imaged with an (0002) Mg. diffracted beam.

Fig. 5.47 is the normal image from the undeviated beam and Fig. 5.48 is formed using an (0002)Mg beam. The direction of the (0002)Mg operating vector is indicated. Three asymmetrical strain fields are circled and numbered. Numbers 1 and 2 in Fig. 5.47 are similar and the larger strain field is such that its curvature is concave to g and as they are identical to the images in Fig. 5.48 they are close to the top of the foil and the strain is positive. Number 3 is at the bottom of the foil as the asymmetry is reversed. This also indicates a positive in situ strain.

Determination of the Metastable Solvus.

The direct quenching experiments did not confirm Halls[19] results and as G.P. zones have been detected visually in the naturally aged alloy it was decided to use the reversion method to determine the zone solvus.

The alloy was solution treated at 380°C. water quenched and naturally aged for 9 months. The structure after this ageing sequence has been illustrated in Fig. 5.6 and Fig. 5.7, and the particles were considered to be discs about 60 A° diameter and 15 A° thick on the magnesium basal planes. This is to be compared with the zone size of 80-90A° reported by Carpenter and Garwood[44] for an Al-22.5%Zn Alloy.

Fig. 5.49 shows the change in hardness on artificial ageing

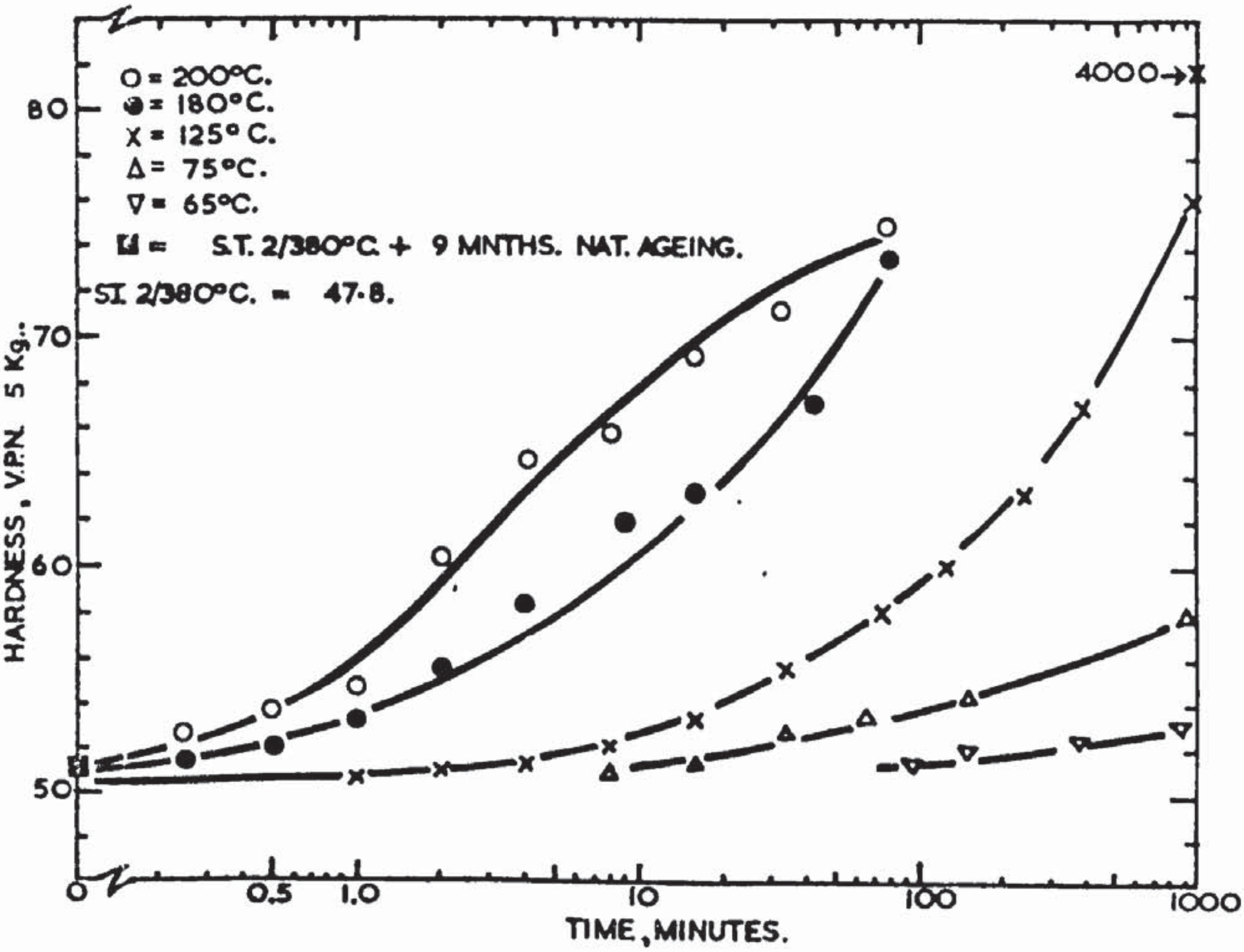

Figure 5.49. Change in hardness on artificially ageing samples naturally aged for 9 months.

of the naturally aged samples. At 180 and 200°C. there is an almost immediate response, and the hardness increases. Although the 90 and 60°C curves are not continued to times of less than 8 and 90 minutes respectively, hardness determinations at shorter times were examined and since they gave no change, they were omitted from Fig. 5.49 for clarity.

Section 2 - Magnesium 6.0% Zinc 0.5% Zirconium ZW6.

The samples were solution treated in the form of 0.75 inch diameter and 9 inch long bars. The solution treatment temperature was 420°C thus providing a direct comparison with the Mg-Zn-Mn alloy.

Mechanical Properties.

The longitudinal and transverse hardness values after ageing at 180°C. have been illustrated in Fig. 5.2 and the similarity between the hardness on a longitudinal and transverse face demonstrated. The increase in hardness and 0.1% P.S. on ageing at various temperatures is shown in Fig. 6.1 and 6.2. The complete tensile data is to be found in the Appendix plotted on a linear scale to compare with those previously published by the author[20] on the Mg-Zn-Mn alloy.

The hardness and proof stress curves are almost identical in that the rate of ageing and time to the maximum is practically coincident in spite of the significant difference in delay periods prior to ageing. The ageing response at 180°C is 3.2 points on the hardness and 3.6 t.s.i. on the 0.1% P.S..

The most significant points about the ageing, considering the 0.1% P.S. values, are the high solution treated value and the ability of the alloy to reach proof stresses greater than 18.0 t.s.i. by thermal treatment alone. The ageing times required

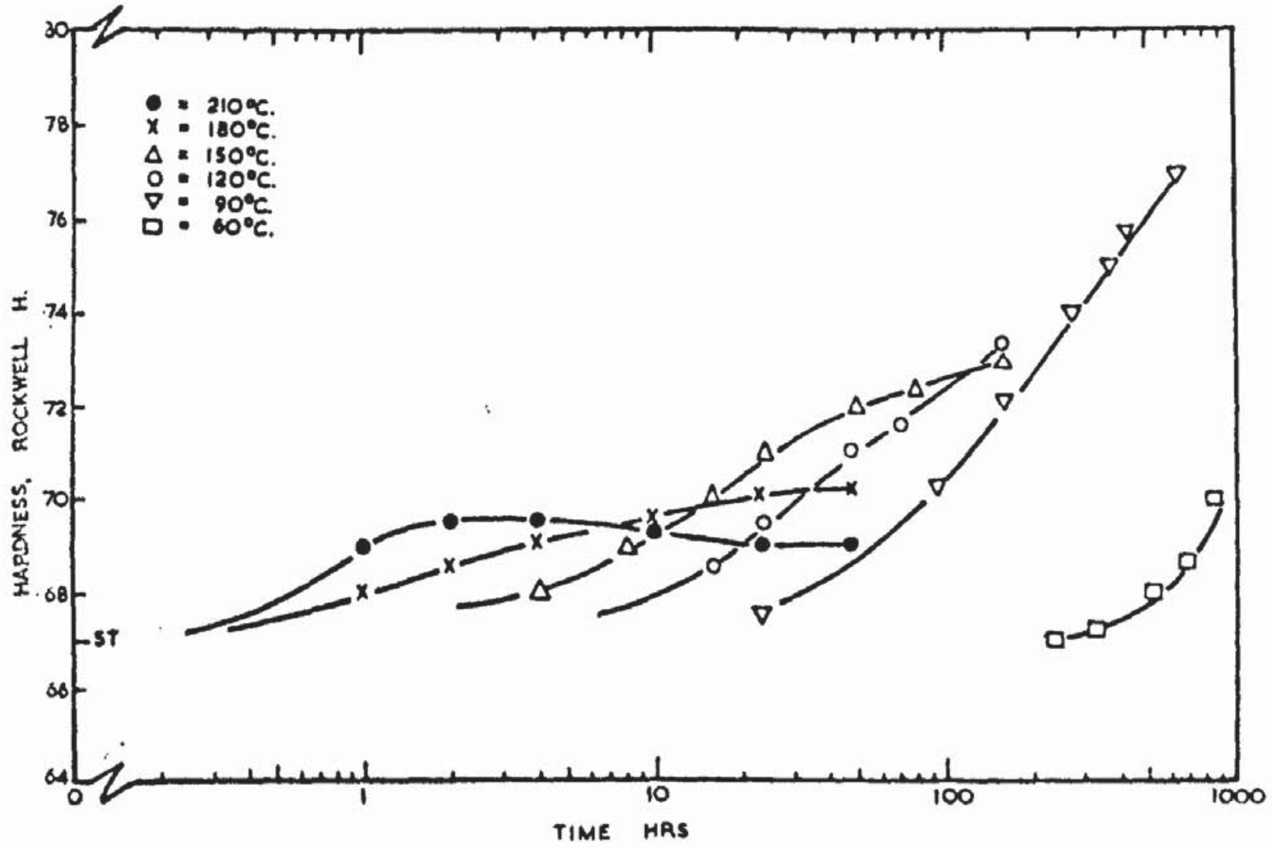

Figure 6.1.

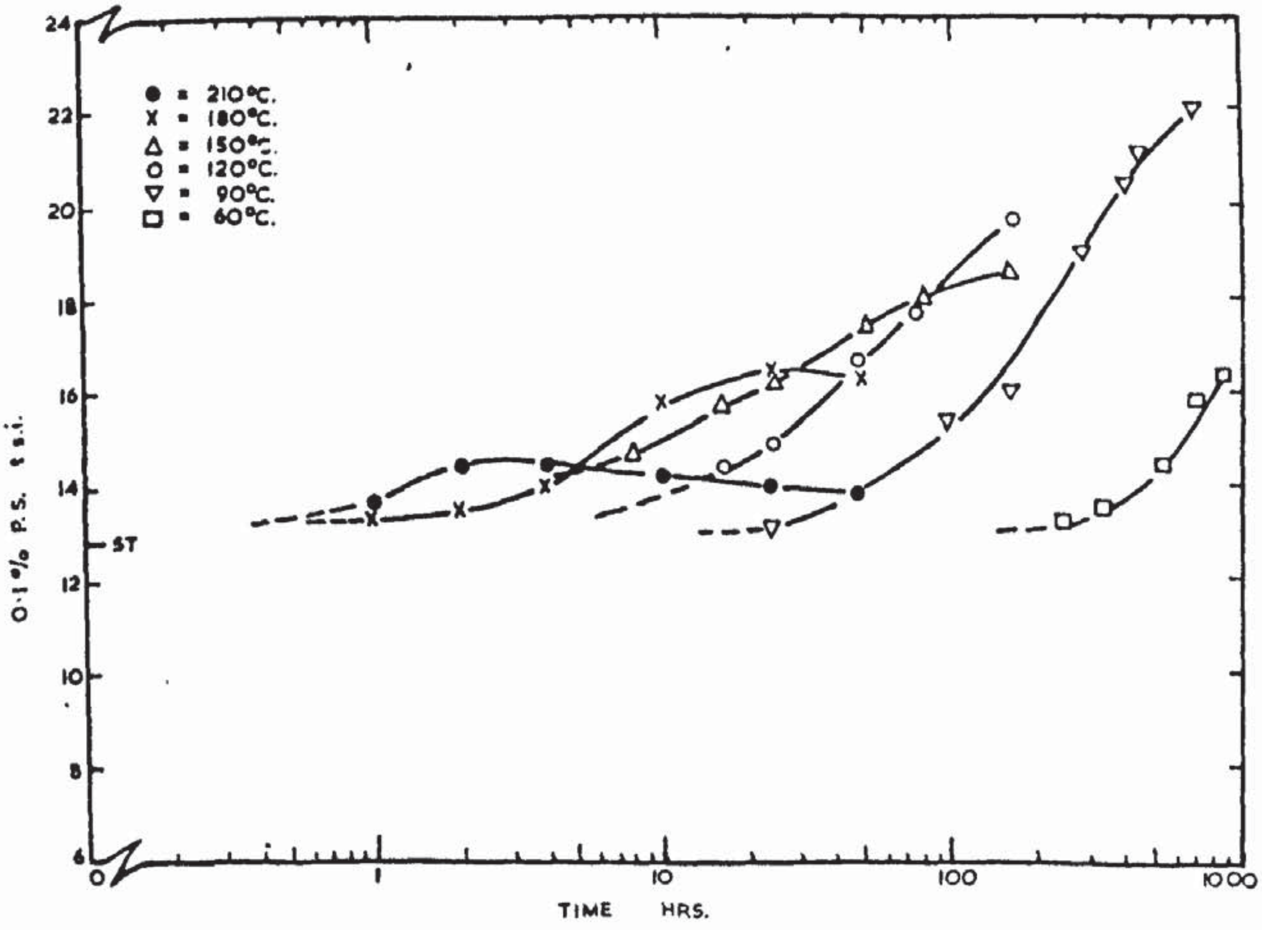

Figure 6.2.

are rather long, about 80 hours at 120°C and 250 hours at 90°C.. The time to maximum 0.1% P.S. is equal to that of Z6 at 210°C. but at the lower temperatures ZW6 responds more rapidly than Z6.

Electron Microstructure.

The structure of the alloy after solution treatment for 2 hours at 420°C, followed by water quenching, is shown in Fig.6.3 (313). Copious precipitation and a very fine grain size are clearly evident. The precipitate clearly has no orientation relationship with individual grains and due to the "stringer" formation was obviously present during the working process. This structure is therefore responsible for the high strength of this alloy in the solution treated condition.

The structure in the as extruded condition was examined and found to be very similar to the solution treated microstructure. Fig. 6.4 (968) is the as extruded structure and the area is from a 'stringer' of intermetallics. Some particles have a 'halo' of carbon contamination which indicates that they are on a surface and they have probably deposited on the surface during removal of the foil from the electrolyte and the orientation will therefore be random.

This alloy was the only one of those examined which caused a marked darkening of the polishing solution indicating an extraction process occurring. The extract was separated from

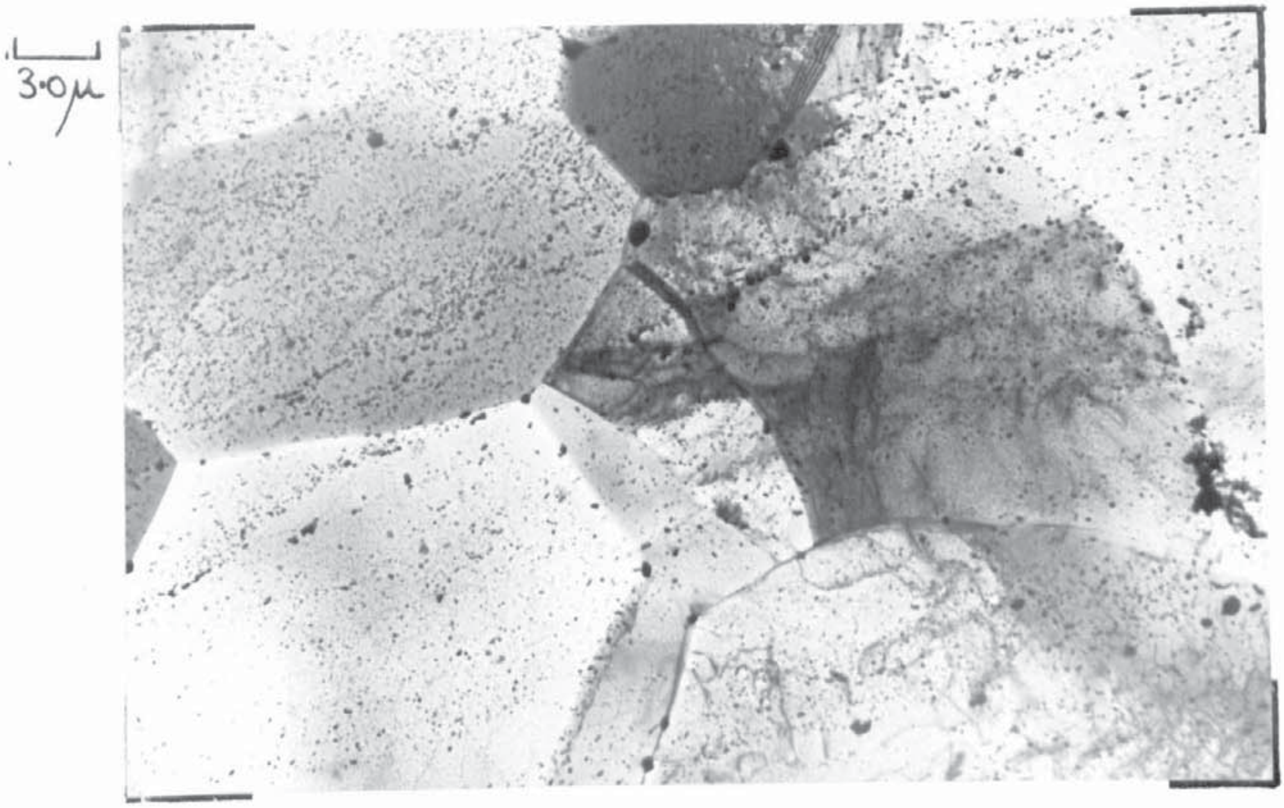

Figure 6.3. ZW6. solution treated for 2 hours 420°C. W.Q.

Figure 6.4. ZW6. in the as extruded condition.

the electrolyte by centrifuging and examined by the powder X-Ray diffraction technique.

The pattern obtained was complex with a very large number of lines, undoubtedly due to a mixture of two patterns. The structures were not solved.

Fig. 6.5 (392) is of the alloy in the solution treated condition and from a $(11\bar{2}0)$Mg zone. In this instance a large proportion of the precipitates are oriented with respect to the matrix, these needles are generally perpendicular to the (0001)Mg. One or two particles have formed a Moiré pattern and the pattern is perpendicular to the operating $(10\bar{1}0)$Mg vector. These particles were precipitated either on cooling after extrusion or during subsequent solution treatment or more probably a combination of these two. The particles are possibly a binary Zn-Zr compound, a ternary Mg-Zn-Zr compound or zirconium hydride. It was because of this third possibility that the Mg-Zr alloy system was examined, although it was considered unlikely that the precipitate was a hydride as it is reported to occur as discs on the (0001)Mg and not perpendicular to (0001)Mg.

The possibility of using the foil surface cleaning process and the carbon contamination film deposited in the microscope as an extraction replica has been outlined. Fig. 6.6 (416) shows this on this alloy in the solution treated condition. A U shape is apparent, with the remaining thin foil on the outside

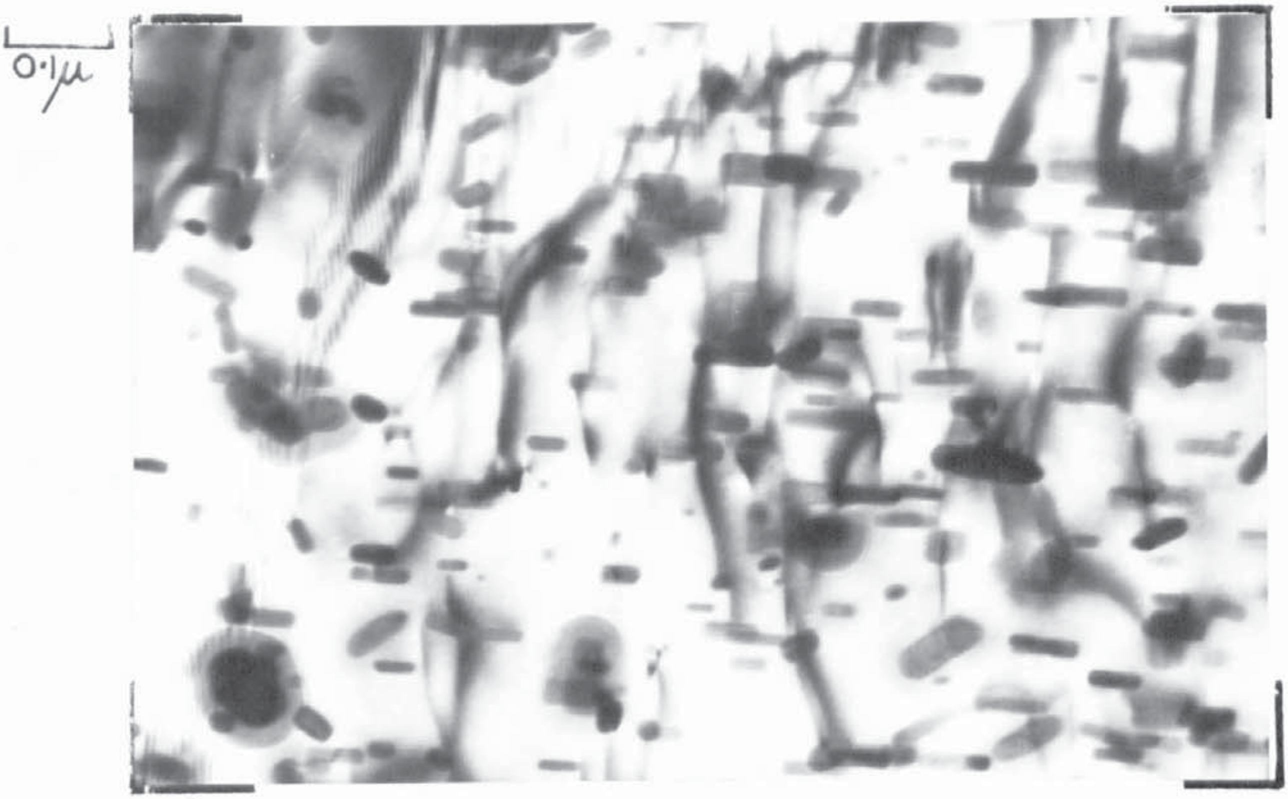

Figure 6.5. Structure in the solution treated condition.

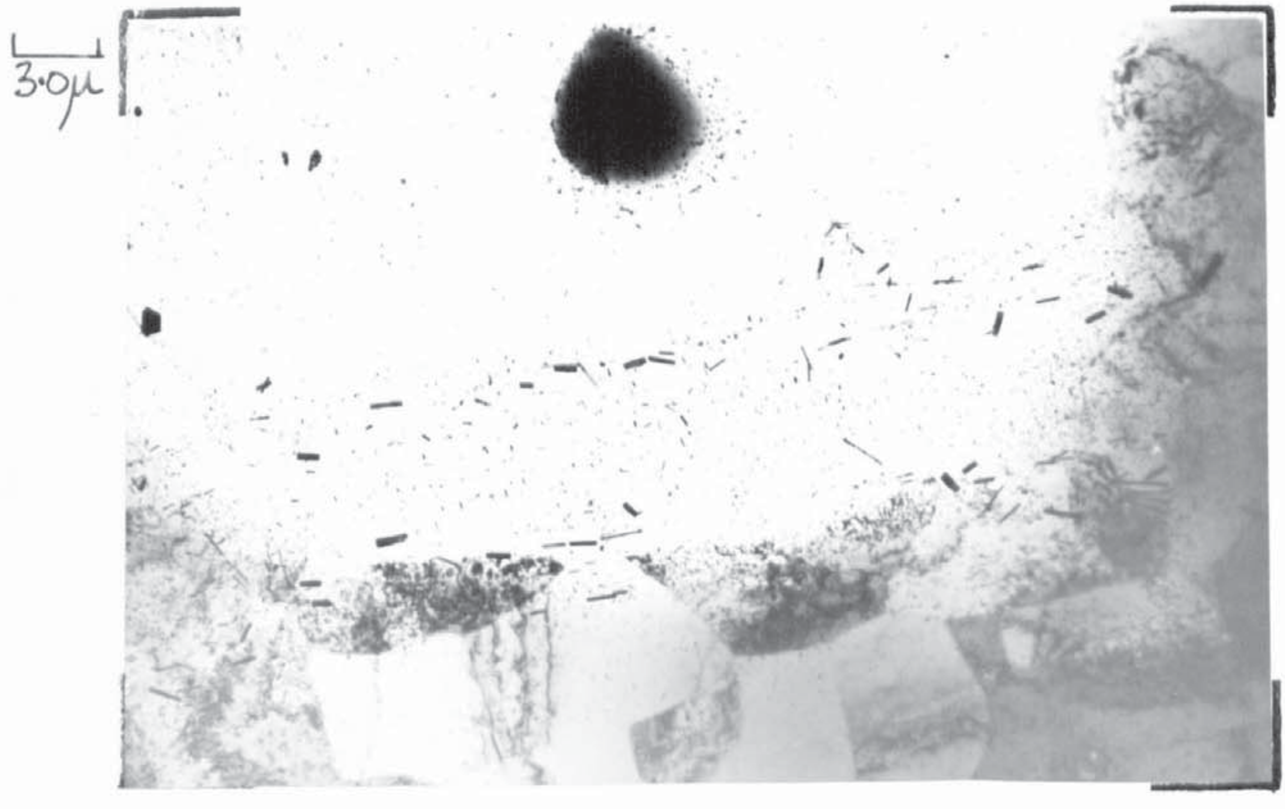

Figure 6.6. Showing a stringer of intermetallic particles held in the contamination layer.

and the carbon film within the U. A stringer of regularly shaped intermetallic particles crosses the bottom of the U and it can be seen to go from the foil into the carbon into the foil. Due to the very large difference in thickness and diffraction contrast between the carbon and the matrix, it is an effect difficult to illustrate. A "stringer" of particles has been retained in the carbon, and the continuation of the stringer into the matrix is evident.

Fig. 6.7 (417) shows the particle and the matrix/carbon boundary at a higher magnification. The precipitate size is very variable from 500-1000 A$^{\circ}$ in Fig. 6.5 to 1000-5000 A$^{\circ}$ in Fig. 6.6. Fig. 6.8 (419) is a diffraction pattern of this extract. The pattern was subsequently standardised from the matrix by slightly moving the specimen. No useful information was obtained from this pattern due to the multiplicity of diffraction spots.

Ageing at 90°C..

The alloy was examined after various times at 90°C. and the structures obtained were essentially as those of Z6. Fig. 6.9 (1029) shows the structure after ageing for 96 hours after direct quenching to the ageing temperature. The massive precipitate previously referred to is evident and the grain boundary precipitate and fine precipitation within the grains from the ageing treatment is

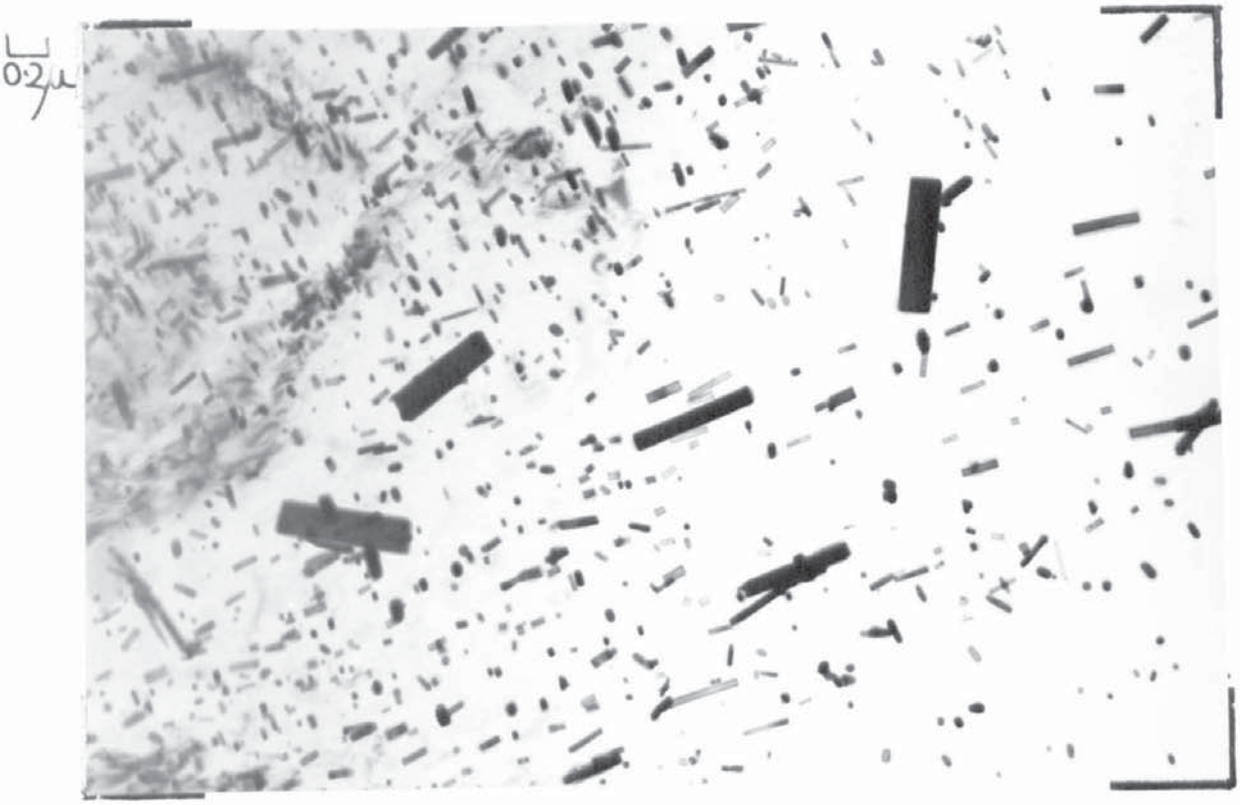

Figure 6.7. As Fig. 6.6. showing contamination/thin foil interface.

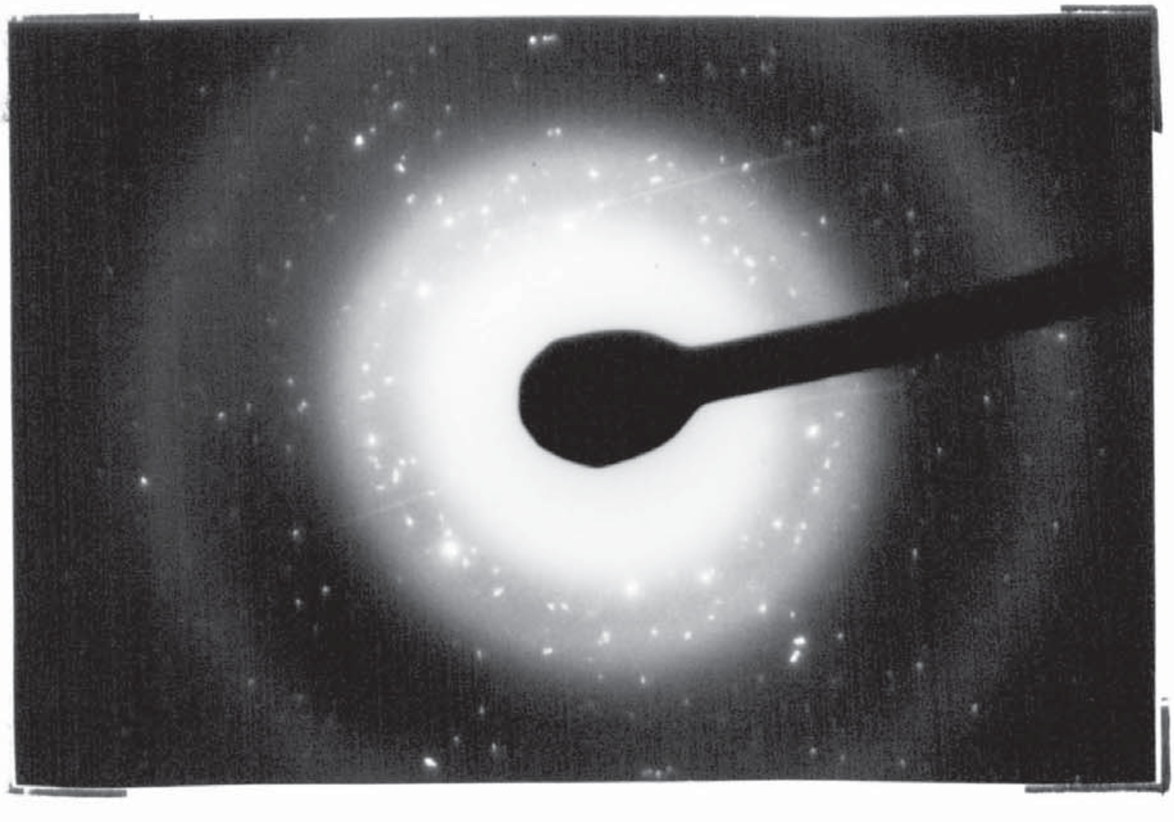

Figure 6.8. Selected area diffraction pattern of the area shown in Fig. 6.7.

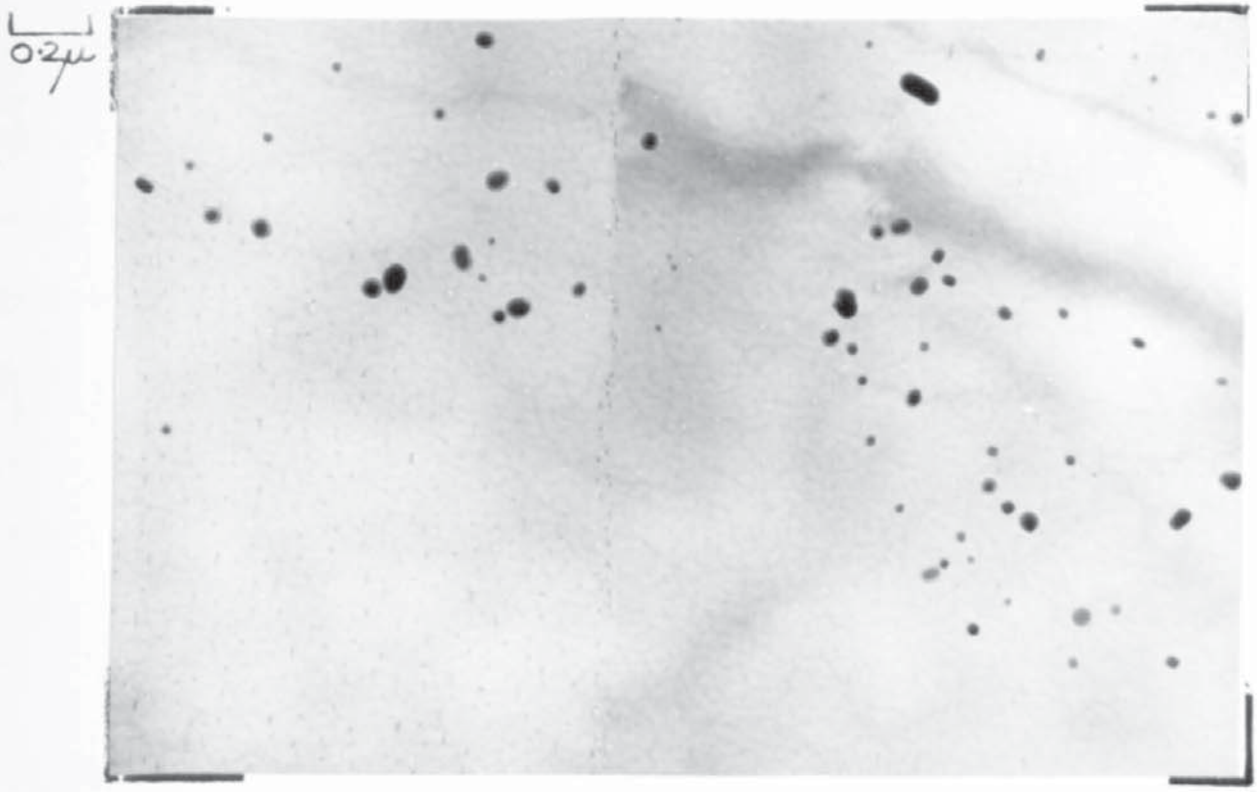

Figure 6.9. ZW6 aged for 96 hours at 90°C. after quenching directly to the ageing temperature.

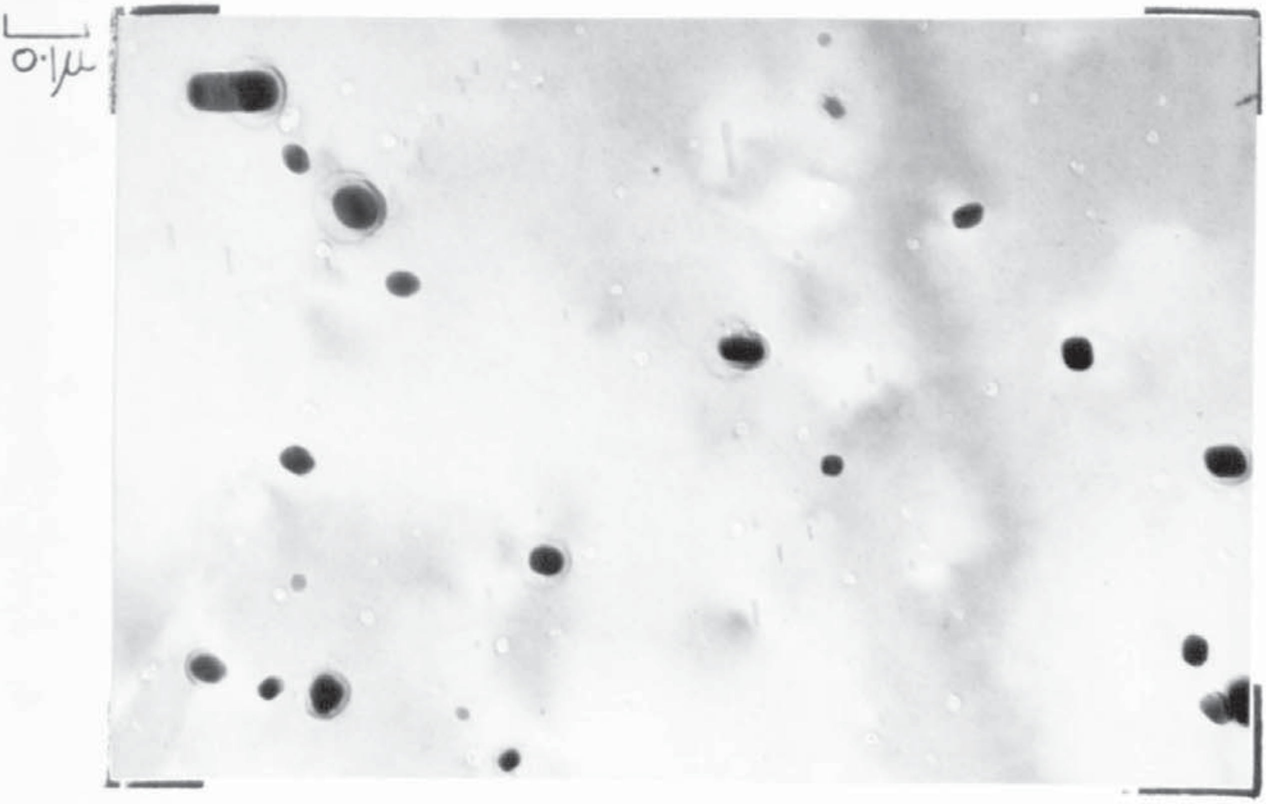

Figure 6.10. As Fig. 6.9.

apparent. Fig. 6.10 (1031) illustrates the fine homogeneously nucleated precipitate in a (11$\bar{2}$0)Mg foil. Some needle precipitate has grown to 100-500 A$^{\circ}$ in length. The fine precipitate has been imaged due to matrix and/or structure factor contrast.

There was no essential difference between this sample and one quenched to room temperature prior to ageing at 90°C.. The G.P. zone solvus is therefore above 90°C. for this alloy.

The structure after ageing for 456 hours at 90°C. is shown in Fig. 6.11 (1116) in a (10$\bar{1}$0)Mg foil. The matrix contrast from the G.P. zones has been resolved into its two components and the needles have grown to 50-500 A$^{\circ}$ in length. Fig. 6.12 (1117) illustrates a triple point and a precipitate free zone between 100-500 A$^{\circ}$ wide. There is a small amount of coarse precipitate at the grain boundaries. The randomly oriented and distributed intermetallic particles present prior to ageing are evident.

Fig. 6.13 (1151) shows that some of these intermetallic particles are oriented with respect to the matrix. Neglecting the particles with the carbon 'halo' the long axis of the precipitates are disposed at three angles to the (0001)Mg. These are . 90°, 0° and 37° and in a (11$\bar{2}$0)Mg foil the 37° inclination is close to that of (20$\bar{2}$5)Mg with (0001)Mg at 36° 51'.

From these results it is evident that when the aged precipitate approaches the size of the precipitate formed during extrusion or solution treatment the difficulty of relating the

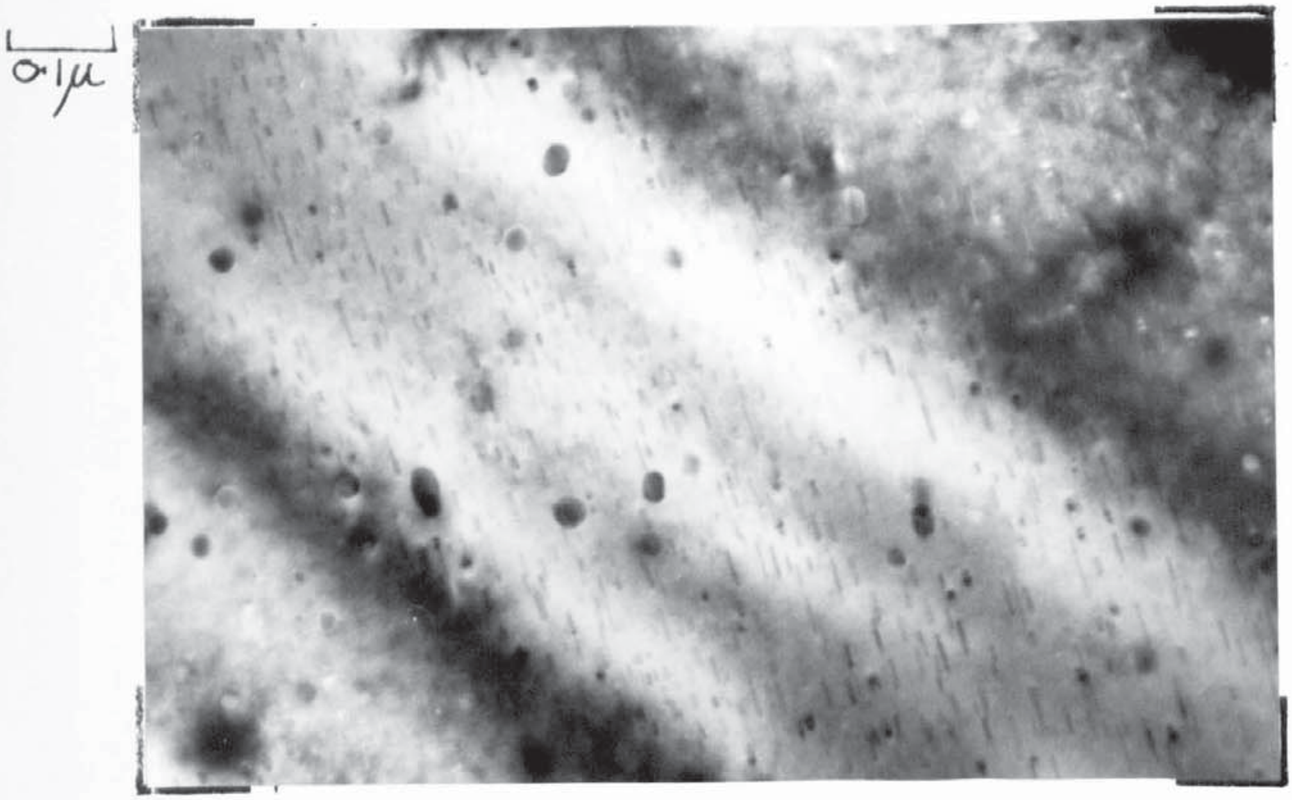

Figure 6.11. Structure after ageing for 456 hours at 90°C..

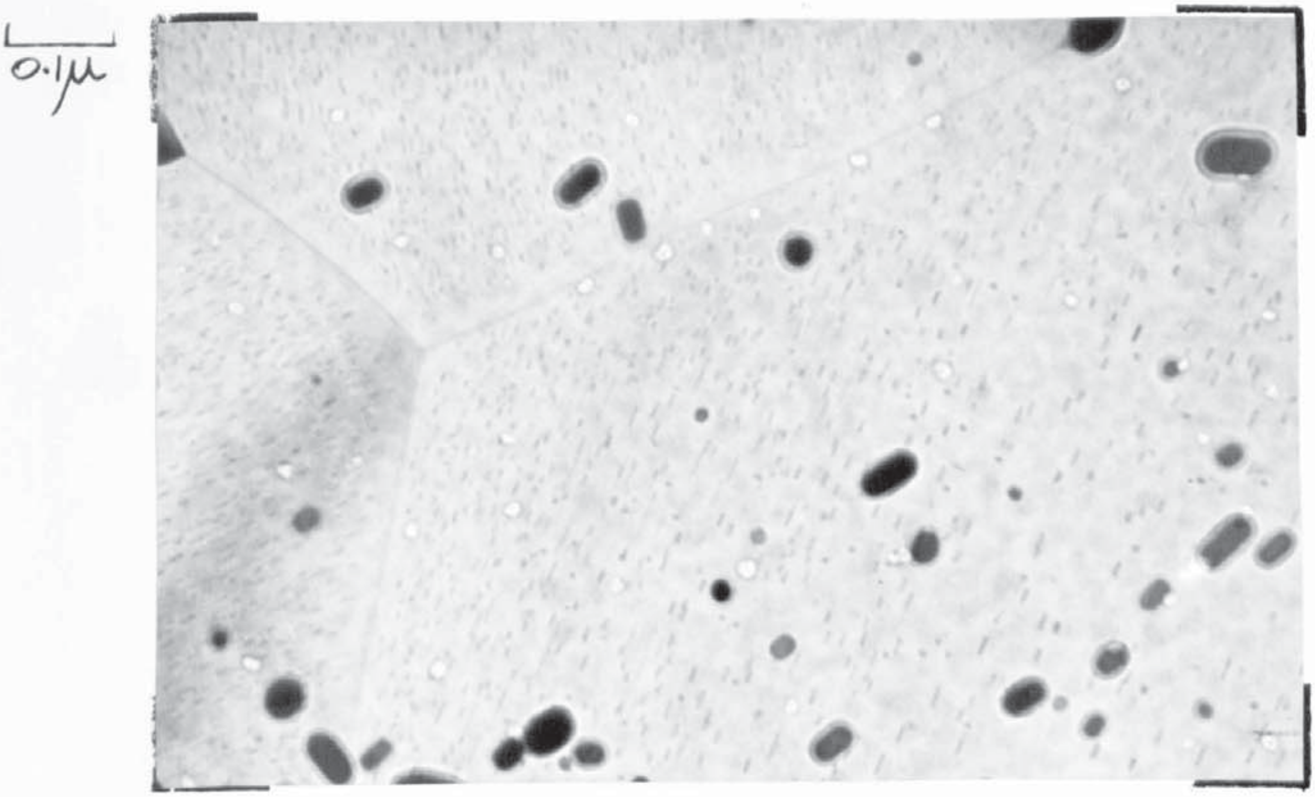

Figure 6.12. ZW6 aged for 456 hours at 90°C..

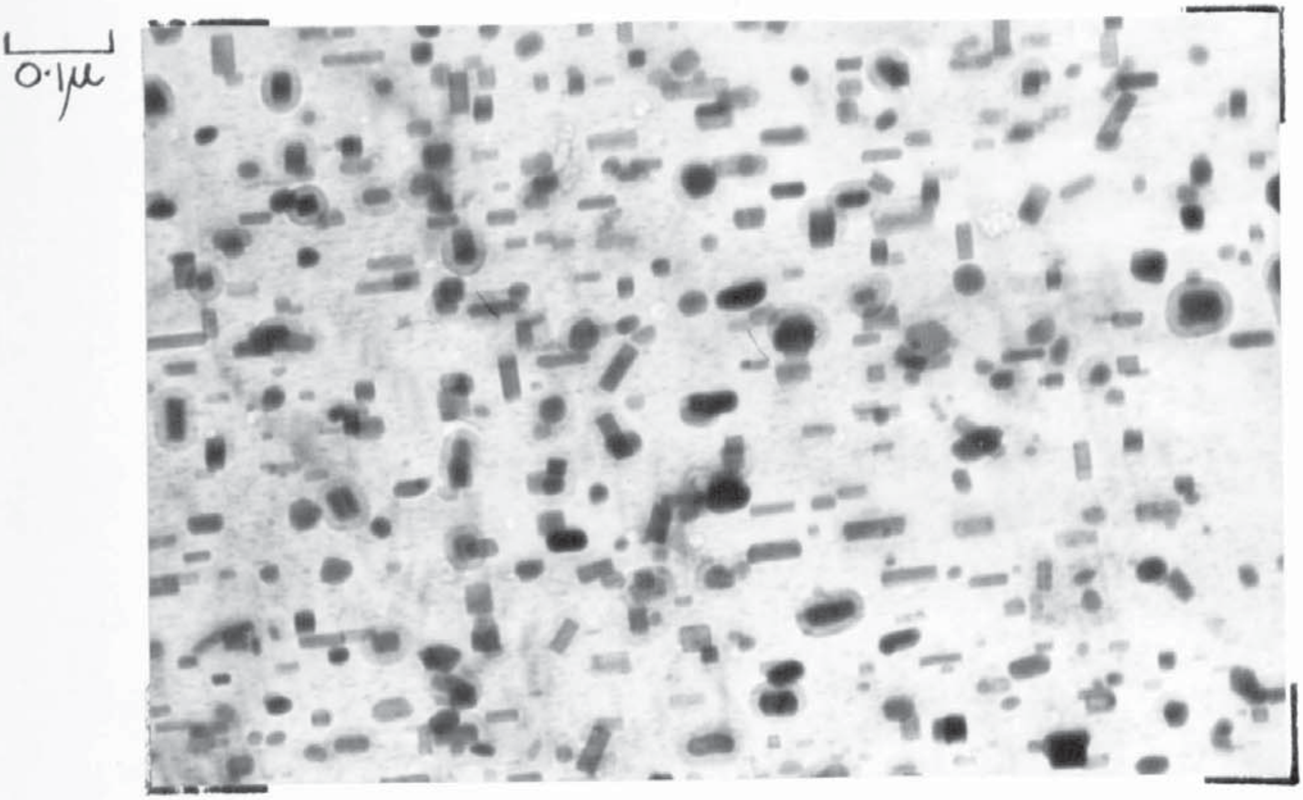

Figure 6.13. Showing the fine precipitate from ageing at 90°C. for 456 hours and the coarse precipitate from solution treatment.

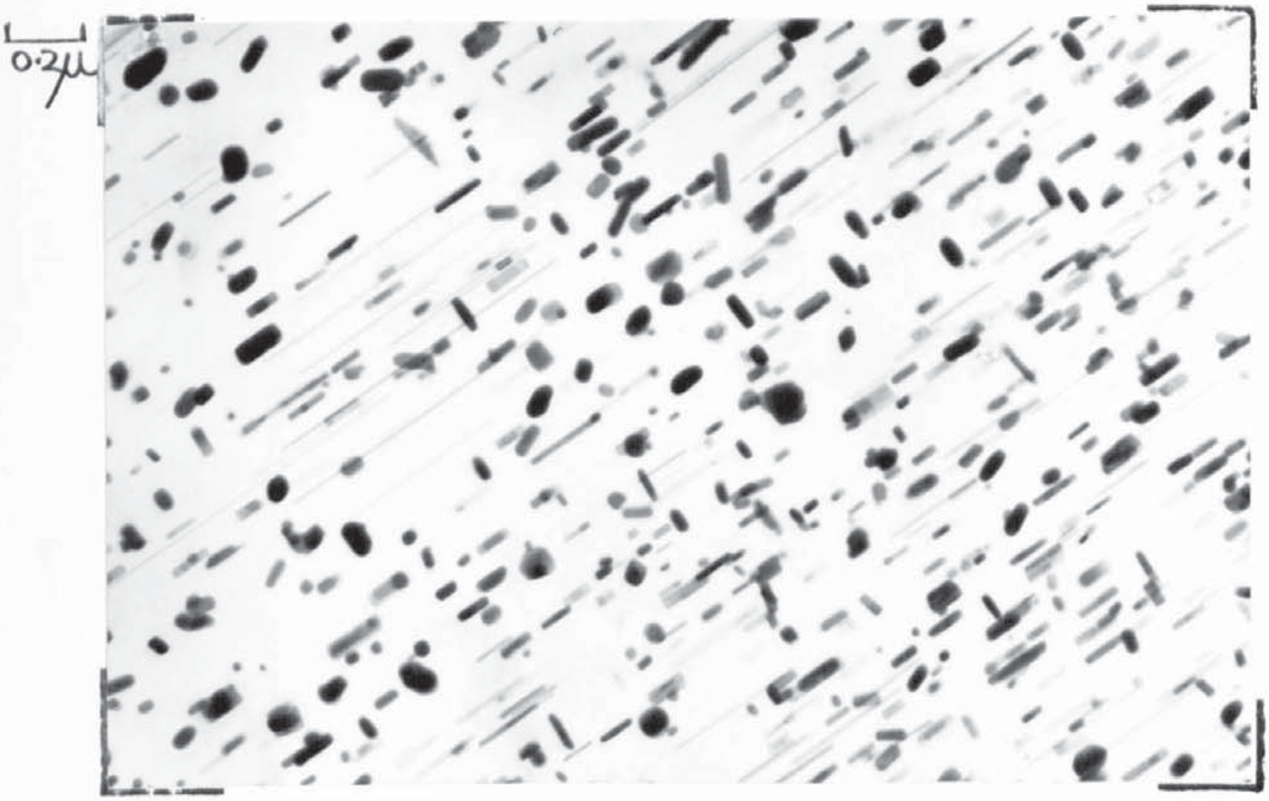

Figure 6.14. ZW6 aged for 16 hours at 180°C.

microstructure to mechanical properties is increased. The solution heat treatment will cause additional precipitation to occur, and solution treatment time will be important.

Ageing at 180°C..

Fig. 6.14 (786) shows the structure after 16 hours ageing. The precipitate at this temperature is the long thin generally less contrasting needles which are between 250-7,500 A° in length. Fig. 6.15 (785) illustrates an extreme variation in needle length over a very small area of the sample. The needle length varies from 250-500 A° with some growing to 7,500 A°. There are also large areas free from precipitation which could be related to a solute denudation resulting from the loss of zinc to the massive precipitates, but it could also indicate a super-saturation driving force for nucleation.

Fig. 6.16 (782) illustrates the sparse precipitation during this 180°C treatment within areas containing precipitate from the solution treatment process. There is no significant difference in the needle length between these two areas.

Figs. 6.17 and 6.18 (778 and 729) show the structure formed with the undeviated beam and that from a diffracted beam from the needle precipitate. The diffraction pattern and the spot used for Fig. 6.18 is shown in Fig. 6.19 (780). The pattern is a $(10\bar{1}0)$Mg type and the precipate spots as in Fig. 5.19.

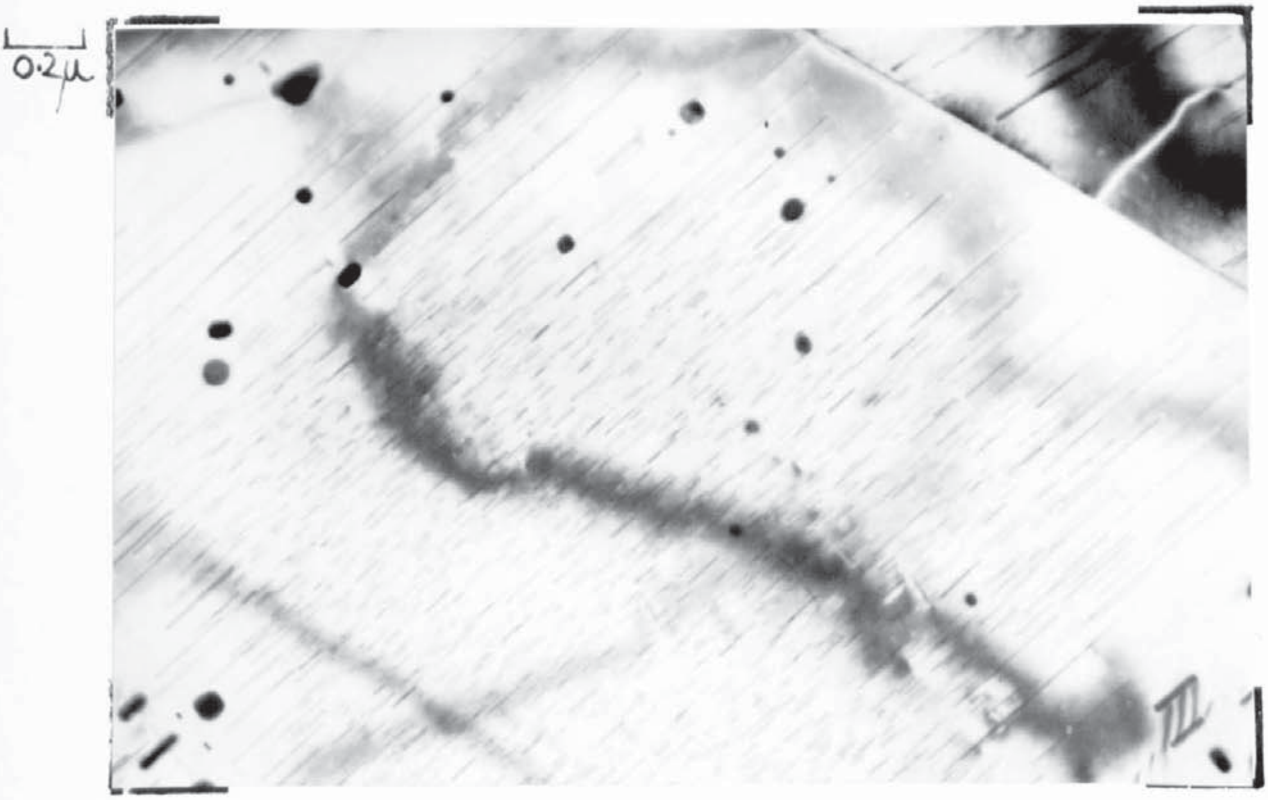

Figure 6.15. Structure after 16 hours at 180°C..

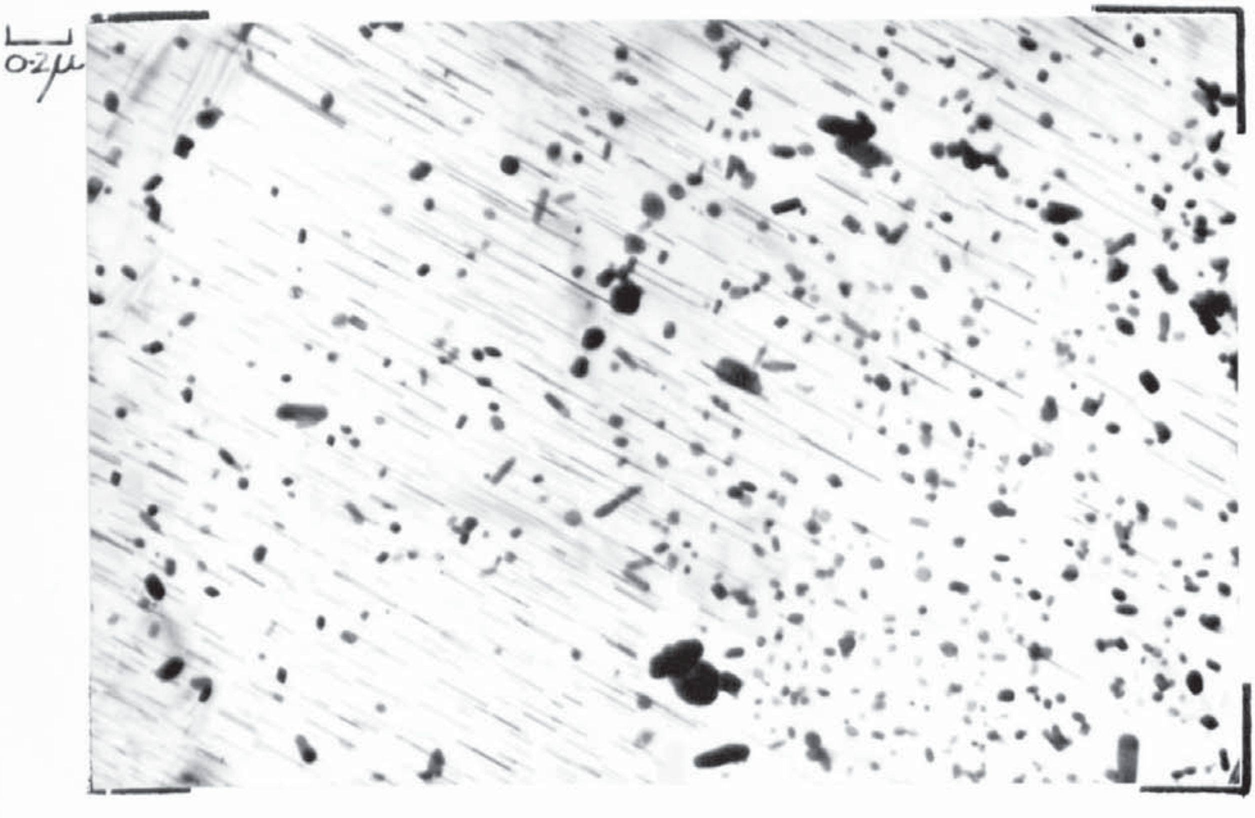

Figure 6.16. As Figs. 6.14 and 6.15.

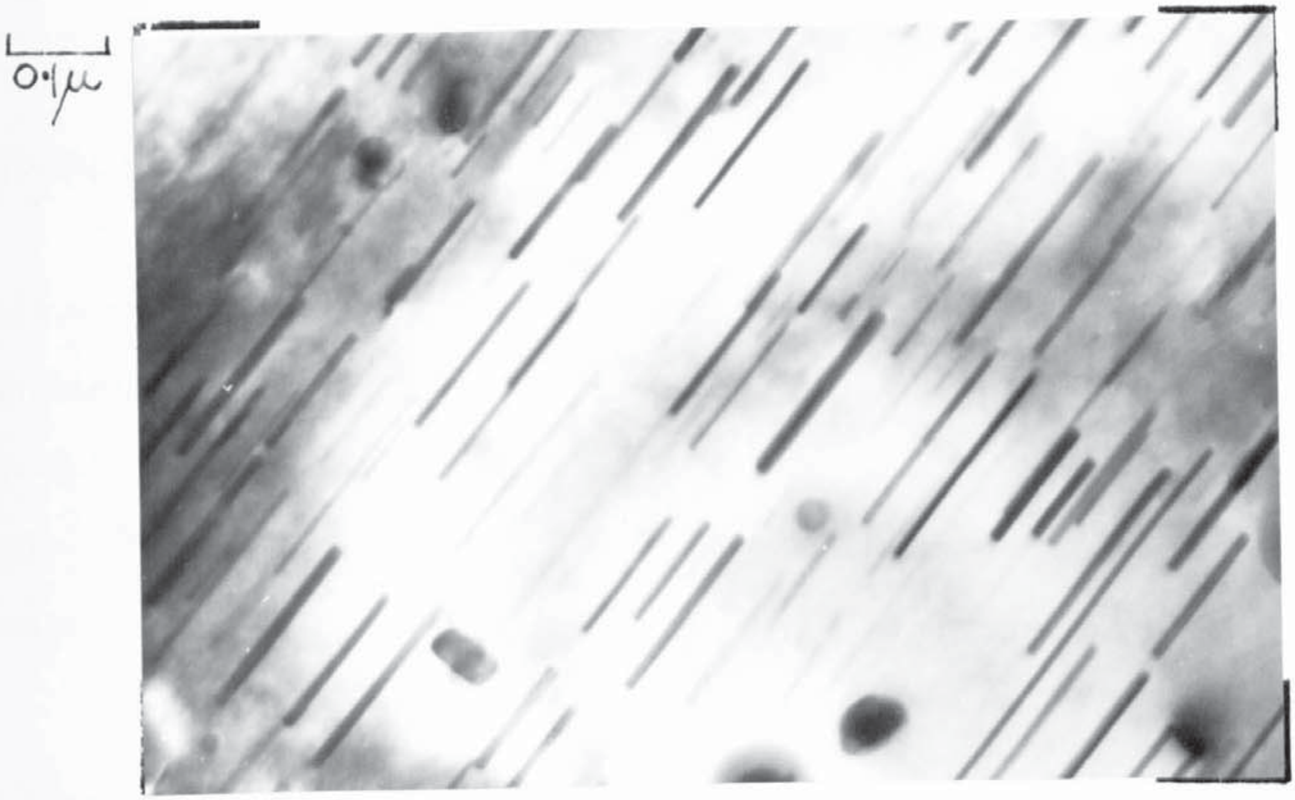

Figure 6.17. Showing precipitation after 16 hours at 180°C..

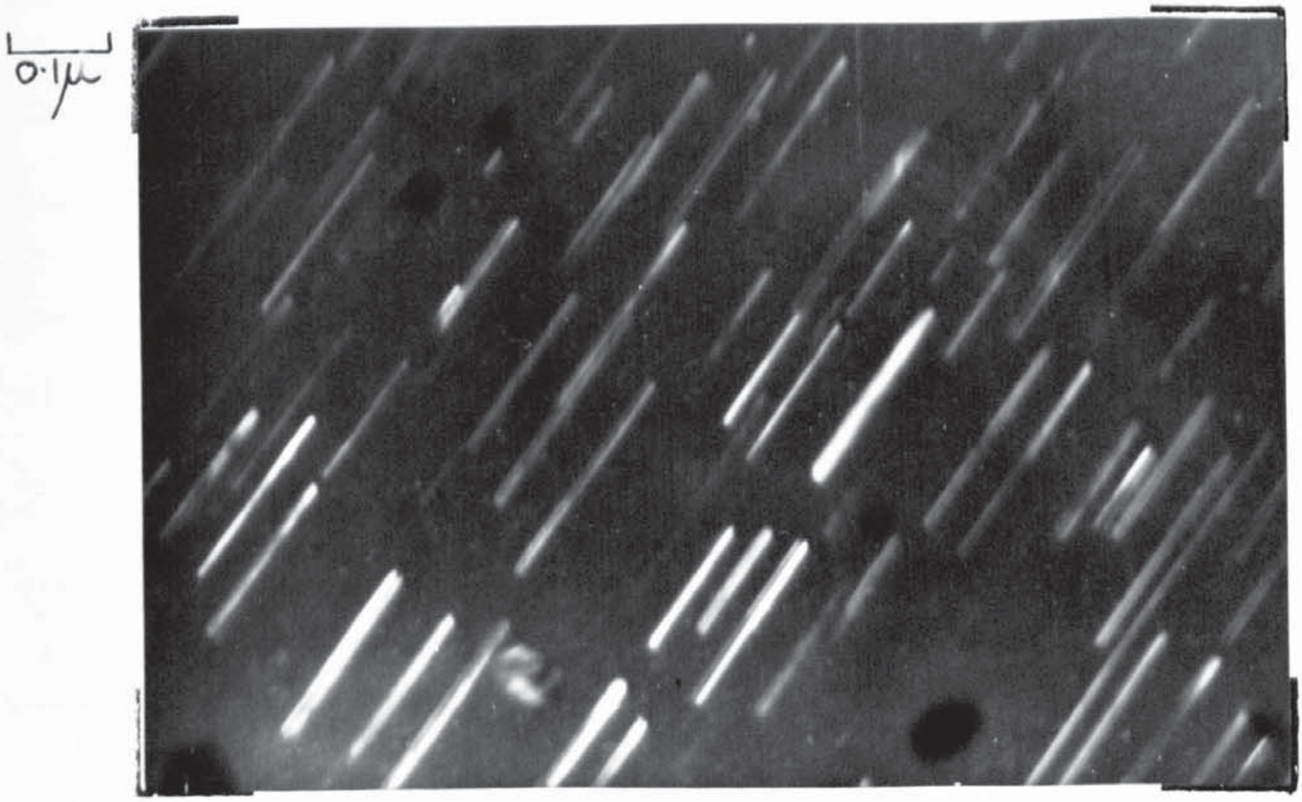

Figure 6.18. Image of area shown in 6.17, formed using a precipitate diffracted beam.

Ageing at 210°C..

Fig. 6.20 (1142) shows the structure after 48 hours ageing and needle lengths of 30,000 A° have formed. The most significant difference between the precipitation (at normal ageing temperatures) in ZW6 and Z6 is the almost complete absense of the discs of $MgZn_2^2$ from ZW6. It was observed on a few occasions and only unambiguously in an (0001)Mg foil.

Double Ageing.

The double ageing response was examined in this alloy and the results are shown below:-

Condition	0.1% P.S. t.s.i.	0.2% P.S. t.s.i.	T.S. t.s.i.	El.% $4\sqrt{A}$
Solution Treated	14.5	15.3	20.3	17
" "	14.3	15.1	20.3	18
16/170°C.	16.1	17.4	21.8	14
" "	16.5	17.3	22.0	10
96/65°C + 16/170°C.	17.1	18.3	22.3	10
" " "	17.0	18.2	22.6	12

There is a slight additional increase when a low temperature ageing treatment precedes the ageing at 170°C..

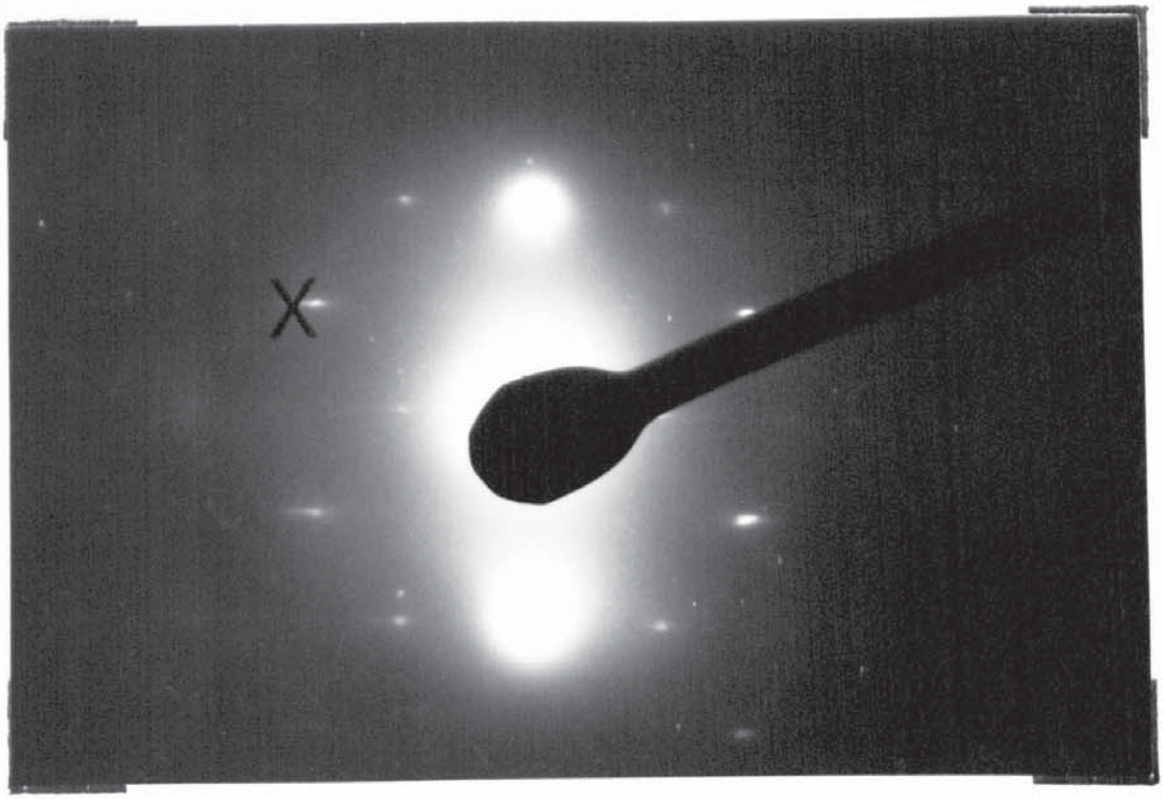

Figure 6.19. Selected area diffraction patter of 6.17 showing spot X, used for forming 6.18.

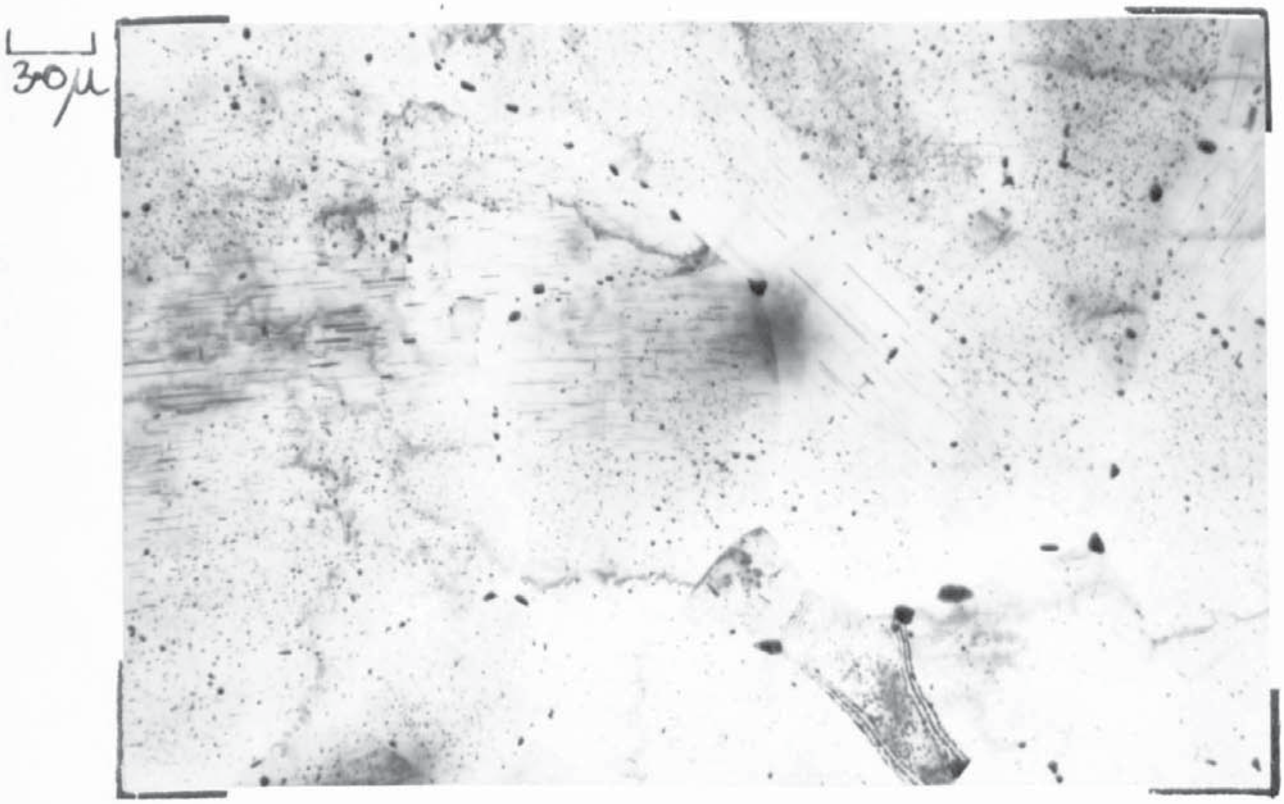

Figure 6.20. ZW6 aged for 48 hours at 210°C..

Microstructure.

Fig. 6.21 and 6.22 (298, 305) show the structure after double ageing in a $(10\bar{1}0)$Mg and (0001)Mg foil respectively and there is a general decrease in the needle length to 50-800 A° with a spacing of 50-300 A°. These illustrations are from an area almost free from the other precipitates and not representative. No useful quantitative metallographic information is available with the heterogeneous structures observed in this alloy.

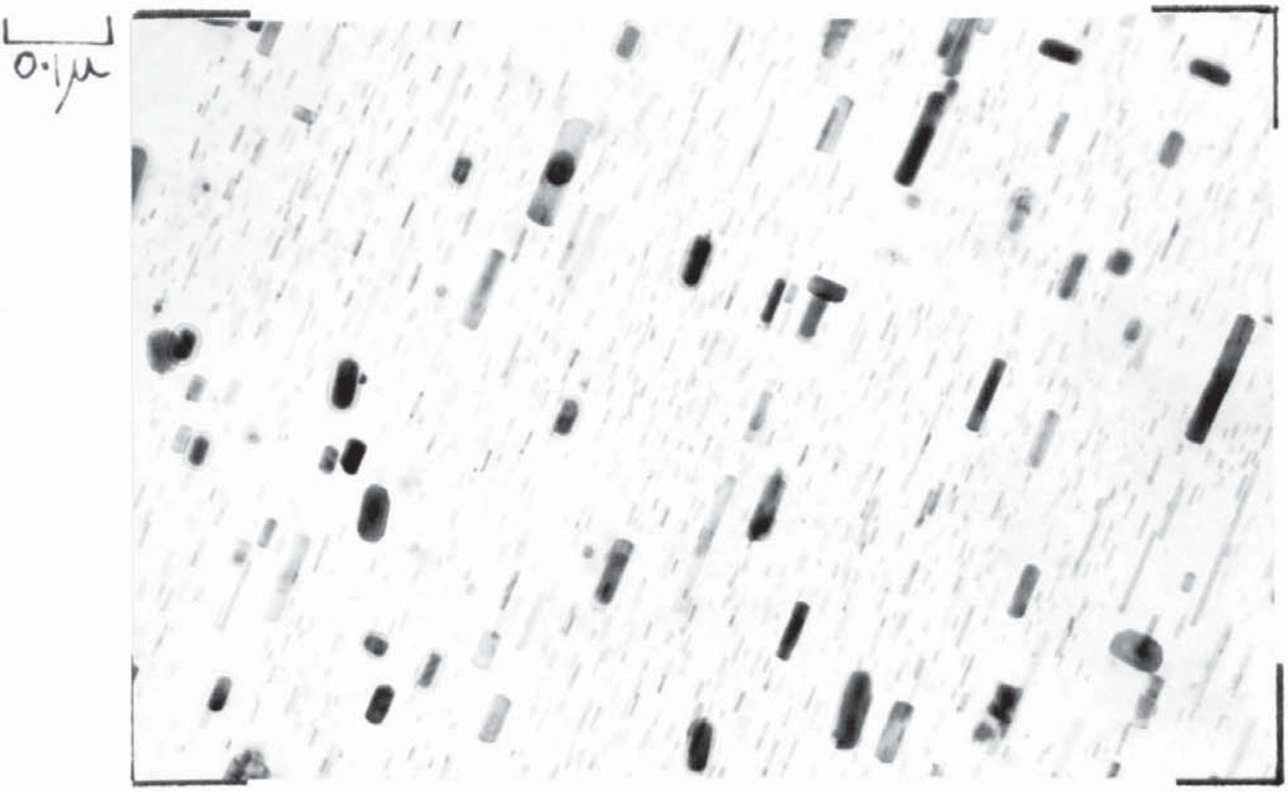

Figure 6.21. ZW6 aged for 96 hours at 65°C. followed by 16 hours at 170°C..

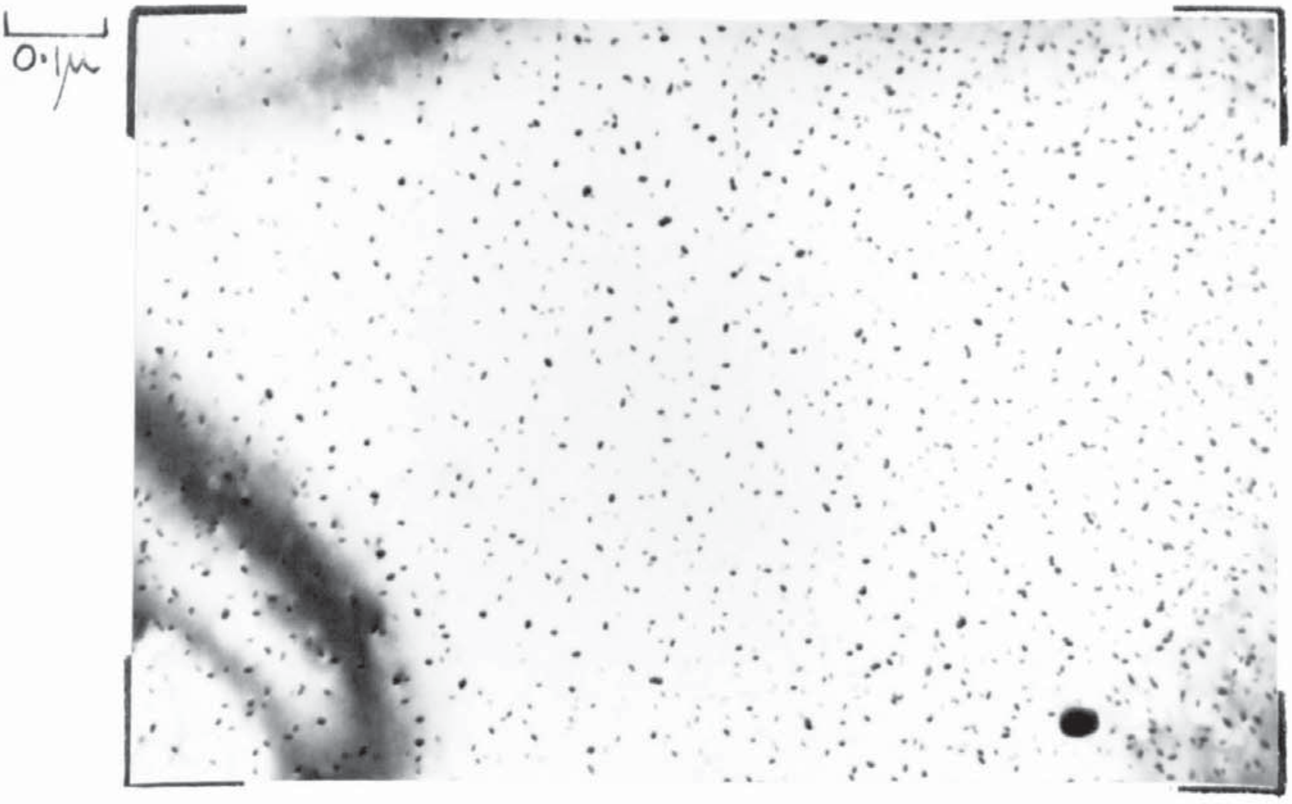

Figure 6.22. As Fig. 22 but showing the structure in an (0001)Mg foil.

Section 3 - Magnesium - 0.5% Zirconimum ZA.

This alloy has been included in the investigation in order to aid the interpretation of the high temperature precipitation in the Mg-Zn-Zr alloy. The only precipitation phenomenon usually examined in this binary alloy is the reaction between the solute and hydrogen to form zirconium hydride.

The alloy was examined after various hydriding treatments in the homogenised condition i.e. 96 hours at 600°C. In the as extruded condition a hydriding treatment of 16 hrs/460°C only was examined. As the alloy is not usually used at room temperature as a constructional alloy no room temperature properties were determined although a few high temperature tests were carried out.

Electron Microstructure.

Homogenised 96 hrs./600°C. in dry CO_2.

The moisture content of the CO_2 during this treatment was below 30 p.p.m. to avoid hydride formation from the breakdown of water vapour. The structure after this treatment was completly featureless and consisted only of grains and grain boundaries.

Homogenised and Hydrided for 16 hrs. 460°C..

Fig. 7.1 (801) illustrates the general structure of the alloy at a low magnification in a foil close to (0001)Mg. The precipitate is in the form of discs on the basal planes and in some cases as long ribbons which originate at a defect in the matrix. There is a precipitate free zone of up to 14,000 A° at

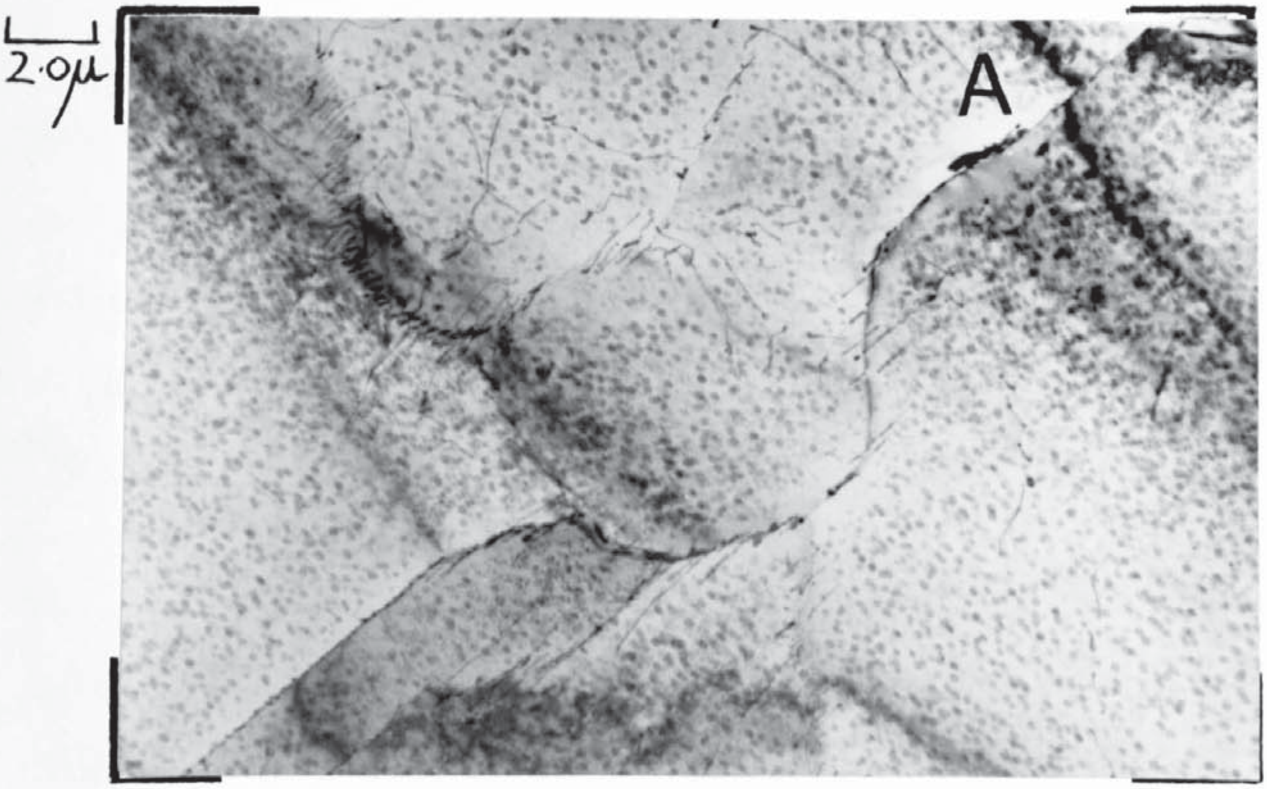

Figure 7.1. ZA homogenised and hydrided for 16 hours at 460°C..

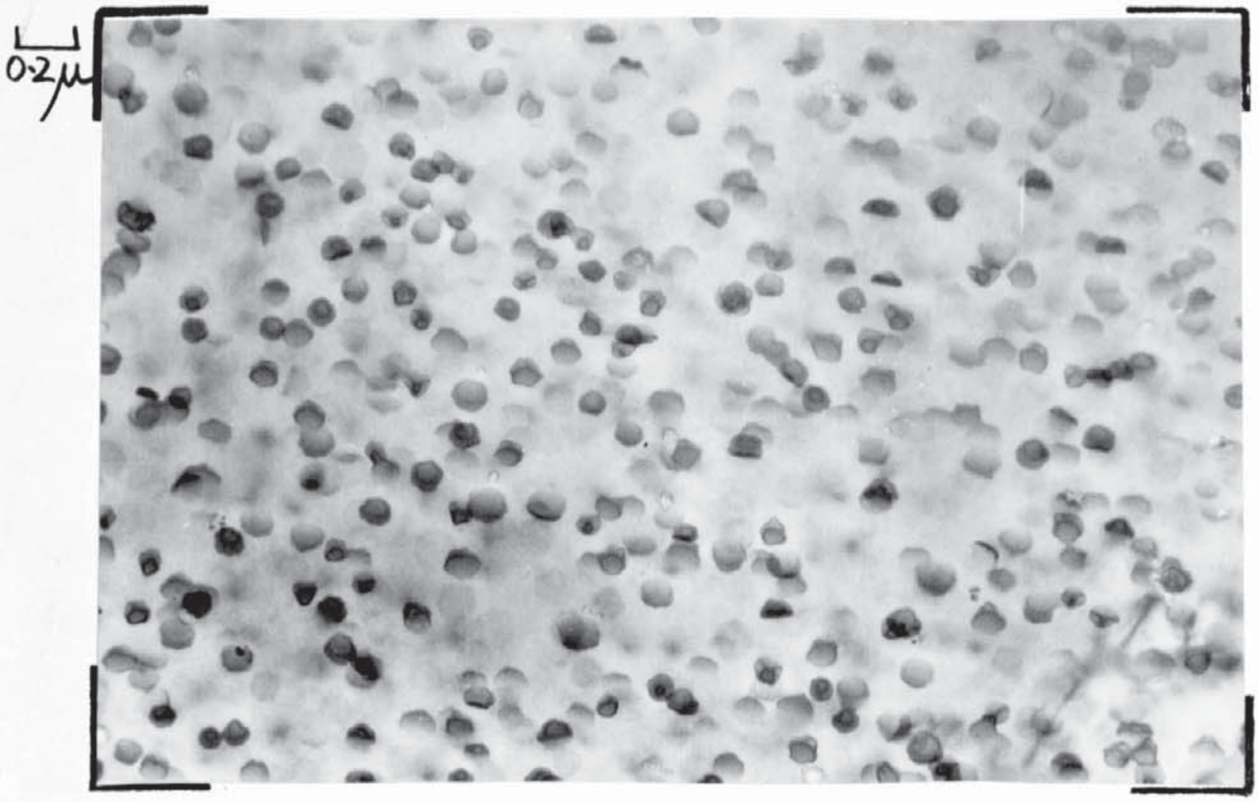

Figure 7.2. As Fig. 7.1. but showing structure in an (0001) Mg foil.

this defect in certain locations, associated with enhanced precipitation at the defect, as at A. It is also worth noting that the quantity of precipitate appears to increase within the bend contour close to A. The general structure illustrated in Fig. 7.1 does not approach that published by Harris.[24,25]

Fig. 7.2 (657) shows the structure in an (0001)Mg foil. The zirconium hydride is in the form of discs on the basal planes, and they have grown to about 1,200 A° diameter. Fig. 7.3 (655) illustrates the structure observed in a $(10\bar{1}0)$Mg foil and the discs are therefore seen on edge. They are about 60A° thick. Two features are evident in Fig. 7.3, they are a D shaped structure and a long continuous ribbon precipitate. The 'ribbon' structure originates at a fault in the matrix and it is considered to be precipitation on dislocations. A carbon 'halo' is apparent on the 'long tails'; they are therefore on the surfaces of the foil. The dislocation and subsequent ribbon precipitate are at an angle to the beam, during thinning the ribbons have been partially released and then fallen on to the surface in a random manner. The distinctly straight sections of the ribbons are not contaminated, they are therefore in the foil, and furthermore they undoubtedly go through the foil and the tails on each linear section are such that they are on the two surfaces of the foil.

The D shaped structures have originated in an identical

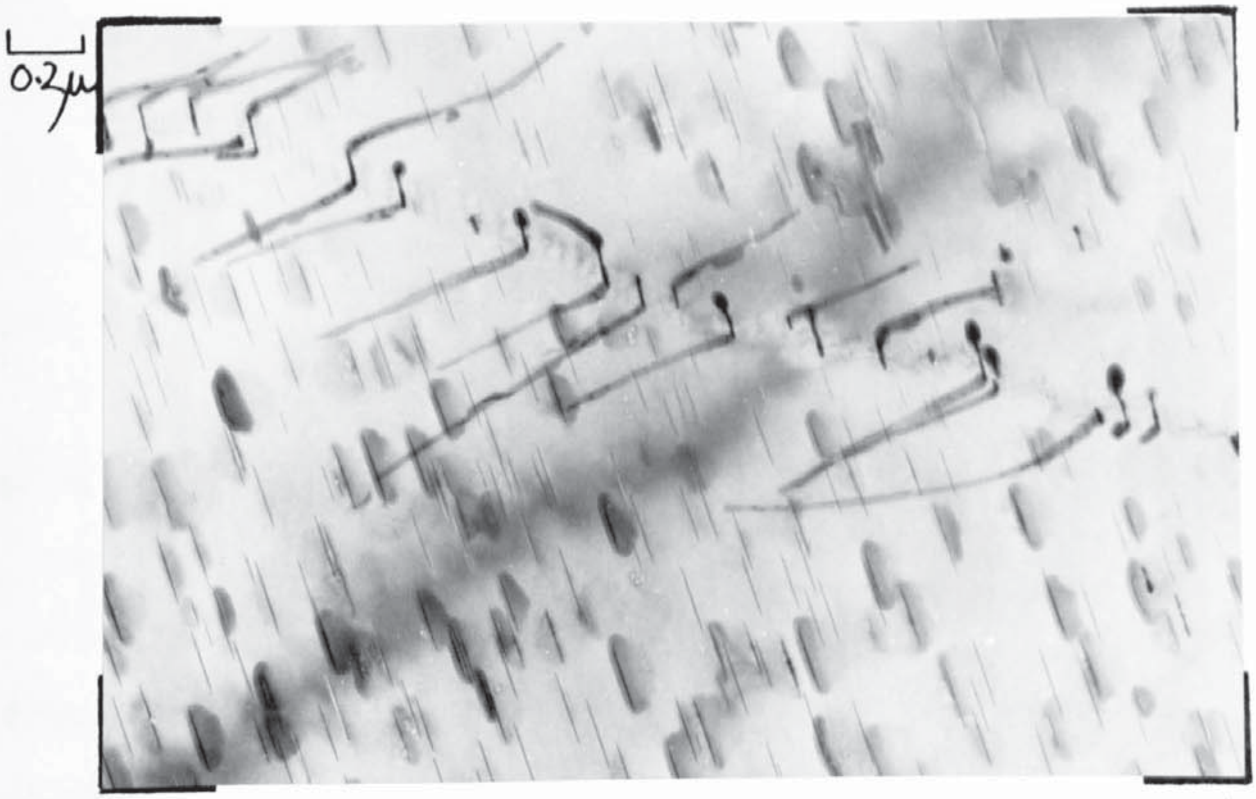

Figure 7.3. As Fig. 7.1. structure in a $(10\bar{1}0)$Mg foil.

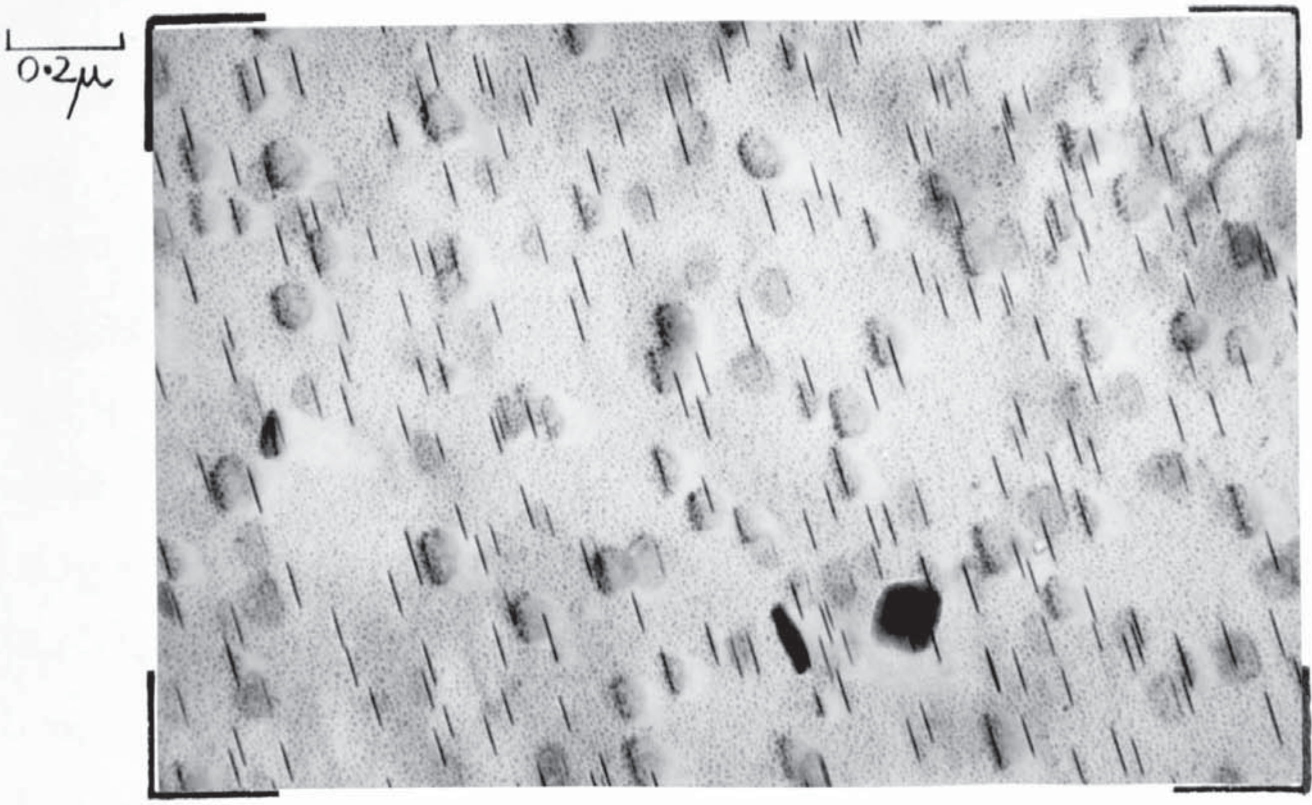

Figure 7.4. $(10\bar{1}0)$Mg foil, shadowed with Au-Pd at about 15°. Sample as in Fig. 7.1.

fashion. The discs have been exposed during thinning and when they have been just retained and gripped in the foil, they have fallen over on to the surfaces.

Conclusive proof that they are on the surface is shown in Fig. 7.4. (1074) which is of a $(10\bar{1}0)$Mg foil shadowed at about 15^{o} with gold-palladium. The light shadows from some of the rounded patches are clearly evident, those without shadows are on the other foil surface. This structure therefore does not arise from defects such as dislocation loops within the foil.

Fig. 7.5. (811) shows a grain boundary with a precipitate free zone 6,000-7,000 Å^{o} across with no concomitant precipitate at the grain boundary. This suggests a vacancy denudation hindering nucleation and not a solute depleted zone.

Fig. 7.6 (911) illustrates the precipitate imaged by normal precipitate diffraction contrast, the darker complete discs and dislocation ring contrast from the matrix. Fig. 7.7 (845) and 7.8 (844) are the images formed from the undeviated beam and a $(10\bar{1}1)$Mg diffracted beam in a foil with the (0001)Mg at approximately 60^{o} to the electron beam i.e. a $(\bar{1}2\bar{1}n)$ foil $6 > n > 4$. The dark discs have a 'halo' and a distinct light or dark spot close to their centres and are therefore considered to be on the surface. The contrast on the particles seen by dislocation ring contrast, is within the precipitate circle and suggests a disc with negative misfit through its thickness.

Figure 7.5. Showing a precipitate free zone at a grain boundary.

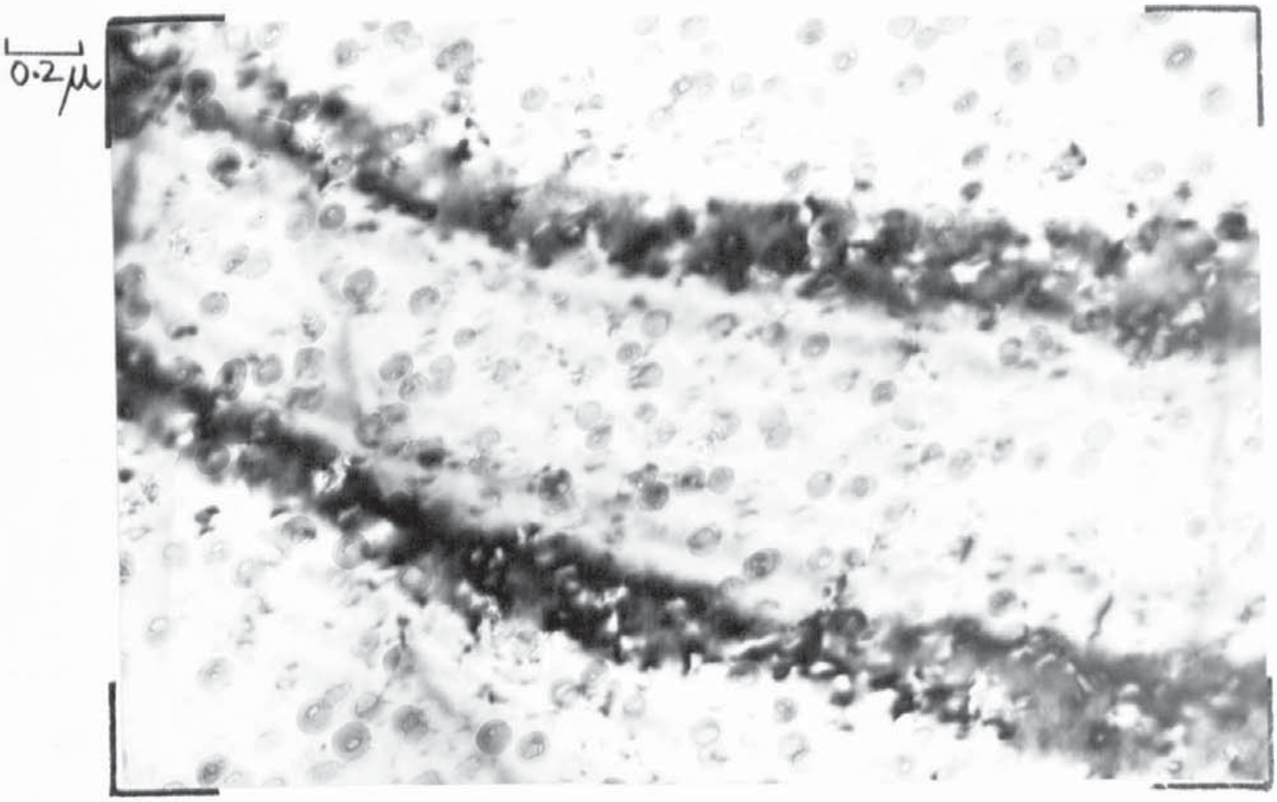

Figure 7.6. Showing thin precipitates imaged by dislocation ring contrast.

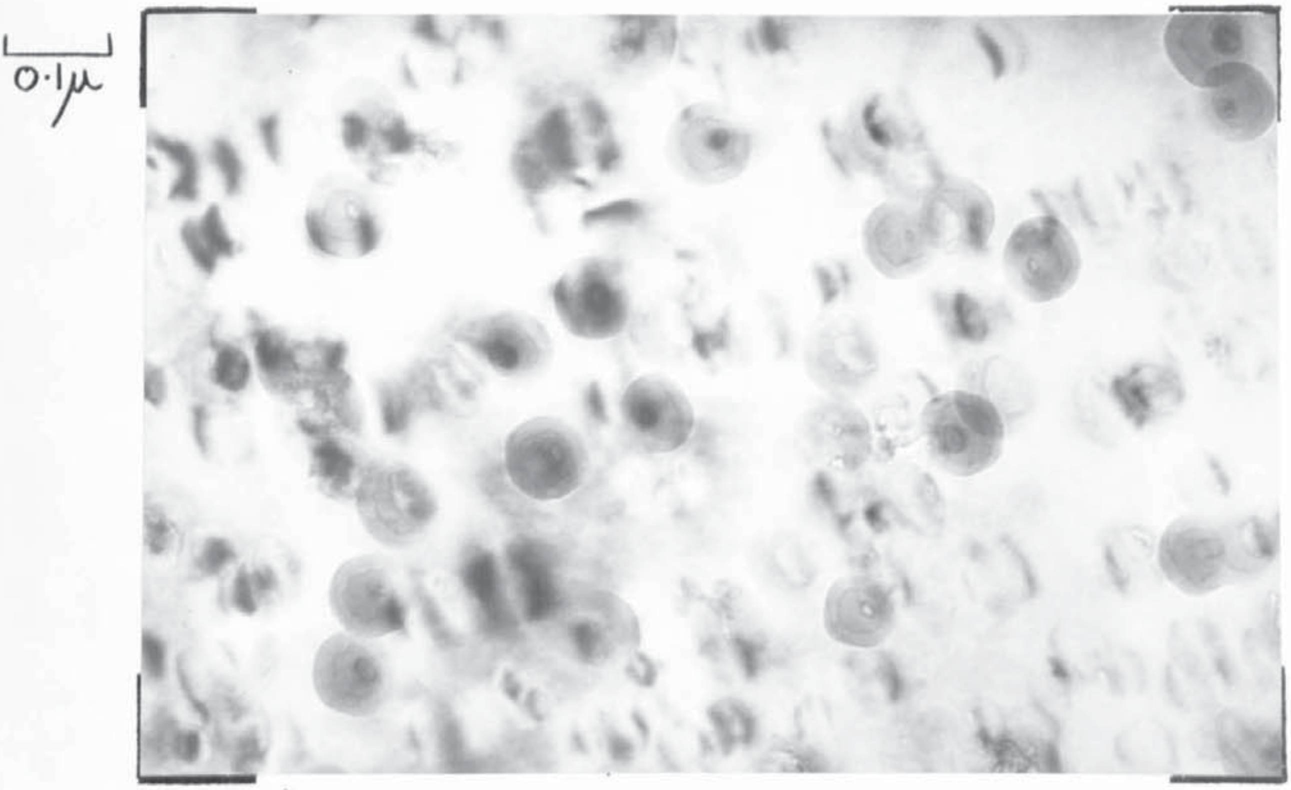

Fig. 7.7. As Fig.7.6.

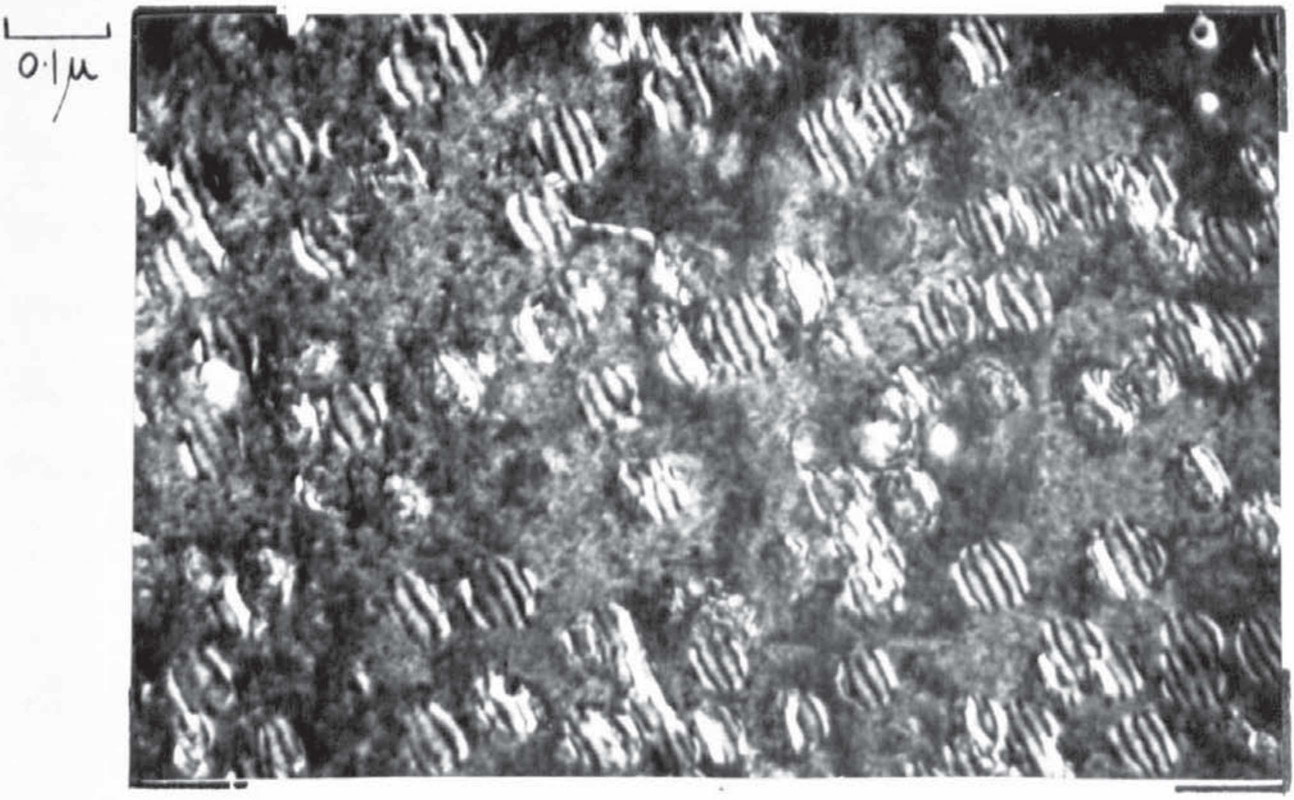

Figure 7.8. Area as shown in Fig.7.7. but imaged using a $(10\bar{1}1)$Mg diffracted beam.

The diffracted beam image shows what are considered to be interface dislocations on the faces of the discs.

As extruded and hydrided for 16 hrs./460°C..

Fig. 7.9 (893) illustrates the structure at the same magnification as Fig. 7.1. The precipitate is in homogeneously distributed and tends to be in "bands" resulting from the distribution of zirconium during the hot working process.

Fig. 7.10 (900) shows the structure in a foil with the (0001)Mg at about 80° to the electron beam. The discs are more well defined than in the homogenised and hydrided sample and they have reached about 500A$^{\circ}$ in diameter. The ribbon precipitate is fairly straight in many positions. Fig. 7.11 (923) illustrates the structure in a foil close to (0001)Mg and some of the disc precipitates have a distinct hexagonal shape. The ribbon precipitates are straight and have attained lengths of around 10,000 A$^{\circ}$. The ribbons are on the (10$\bar{1}$0)Mg planes and the two ribbons arrowed are clearly partly on the surface and partly within the foil.

Fig. 7.12 (925) illustrates the discs again in a foil close to (0001)Mg and also shows the hexagonal nature of the discs, the flat faces are parallel to the (10$\bar{1}$0)Mg planes. Additionally there are some smaller discs 100-200A$^{\circ}$ in diameter. These small and very thin discs have been imaged by dislocation ring contrast.

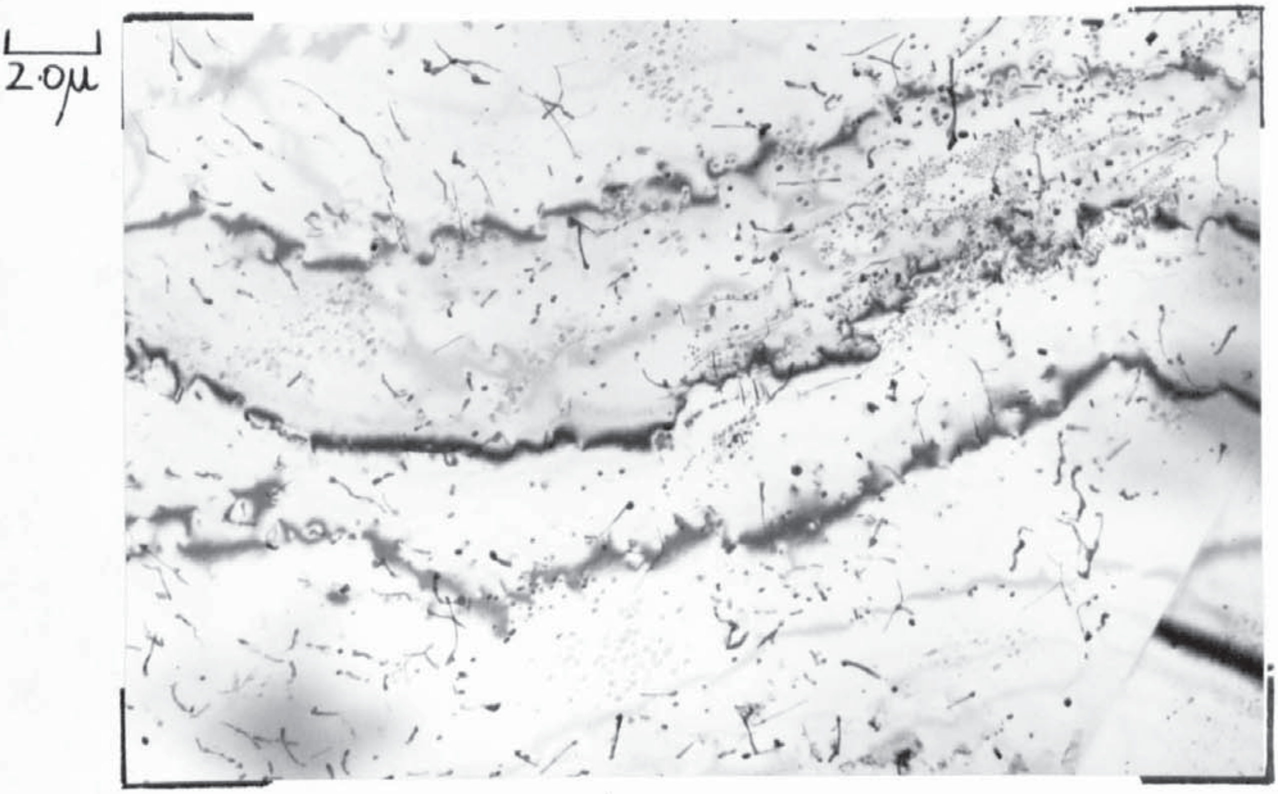

Figure 7.9. ZA as extruded and hydrided for 16 hours at 460°C..

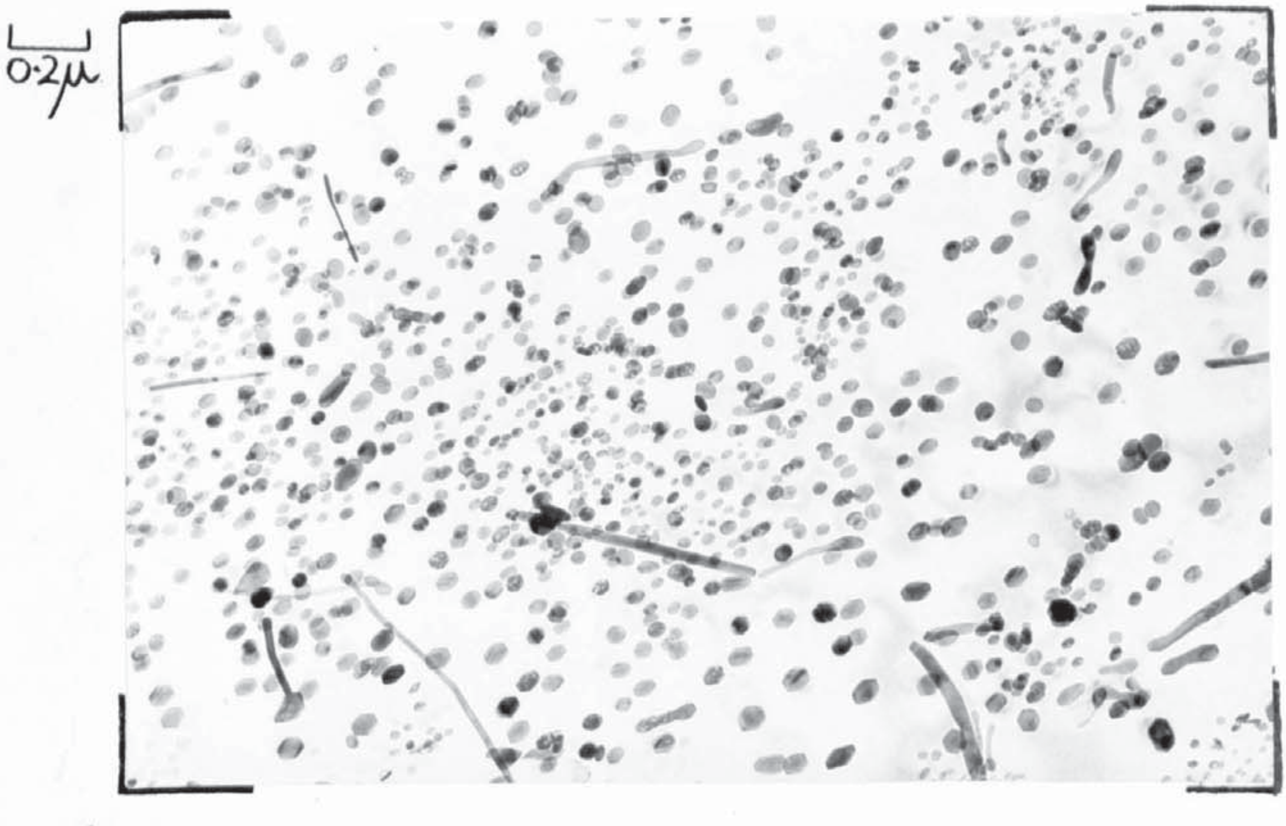

Figure 7.10. As Fig. 7.9. but showing structure in an (0001)Mg foil.

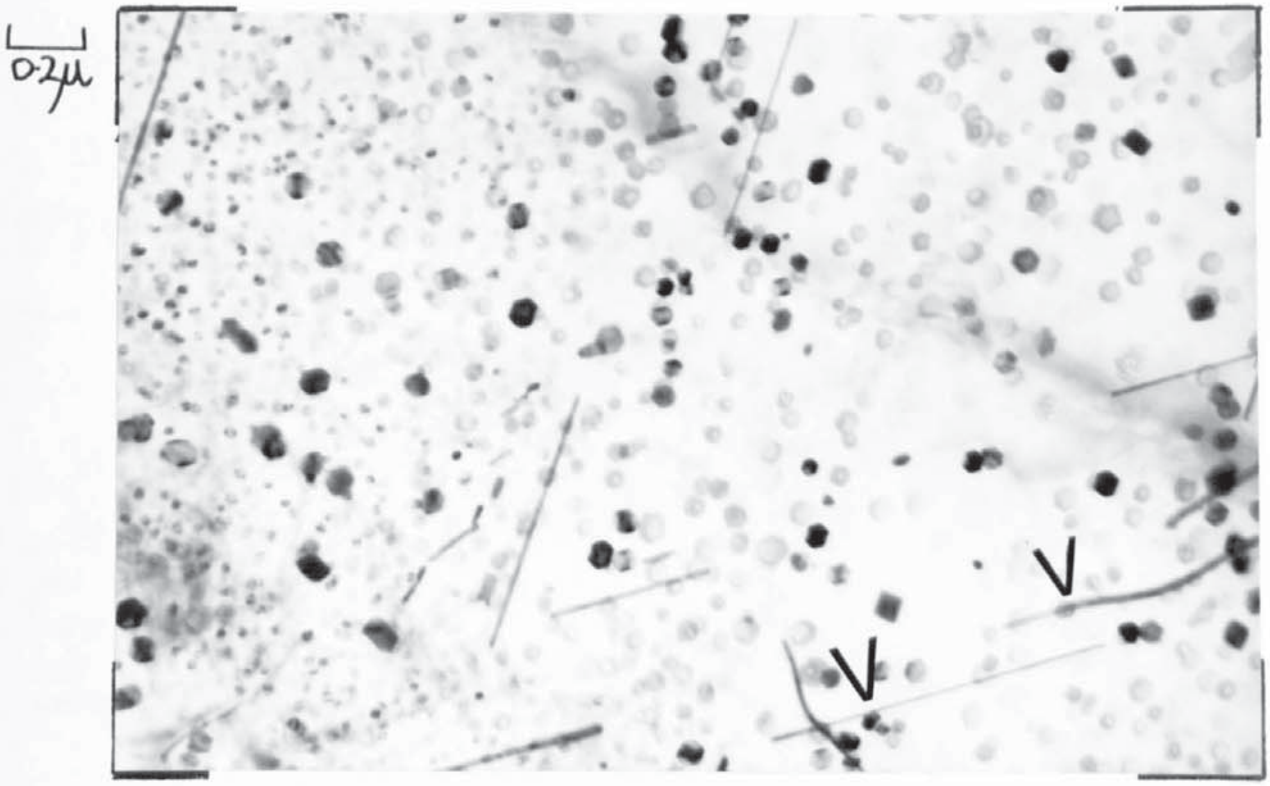

Figure 7.11. As Fig. 7.10.

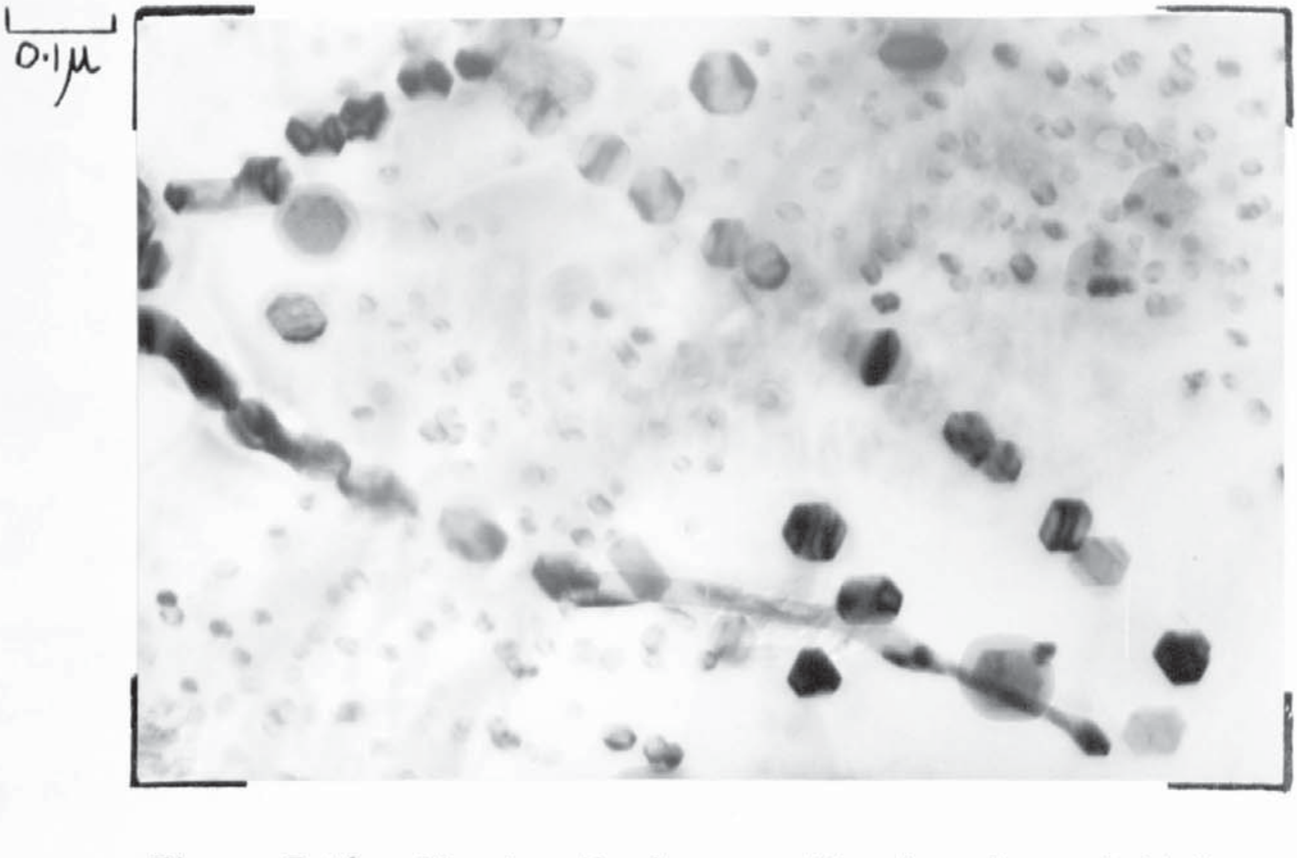

Figure 7.12. Showing the hexagonally shaped precipitates with sides parallel to $(10\bar{1}0)$ Mg.

The structure in a foil close to $(10\bar{1}0)$Mg is shown in Fig. 7.13 (897). The thicker discs seen on edge have a pronounced strain field possibly due to the difference in thermal contraction between the matrix and precipitate. There are some discs that have clearly fallen on to the surface of the foil during removal from the electrolyte. To the left of the photograph, very thin discs can be seen edge on with some that have folded over onto a surface.

The precipitate structures shown in Figs. 7.8 - 7.13 inclusive, are similar to those of Harris et al.[23,24] The particle size, in Fig. 7.11 for instance is not far from that shown in those published results. The important difference is that these results (Fig. 7.8 - 7.13) are from the alloy hydrided in the "as extruded" condition and not in the homogenised condition (96 hrs./600°C in CO_2) as used by Harris.

Homogenised and Hydrided for 10 mins./600°C..

Fig. 7.14 (947) shows the structure in a $(10\bar{1}0)$Mg foil and the discs in the foil are edge on and have folded onto a surface where they have been freed from the matrix. The discs have grown to about 3,500 -4,000 Å diameter and an additional precipitate has formed which is also flat and almost edge on in Fig. 7.14. This precipitate is well illustrated in Fig. 7.15 (948) where one has fallen on to the surface and its complex

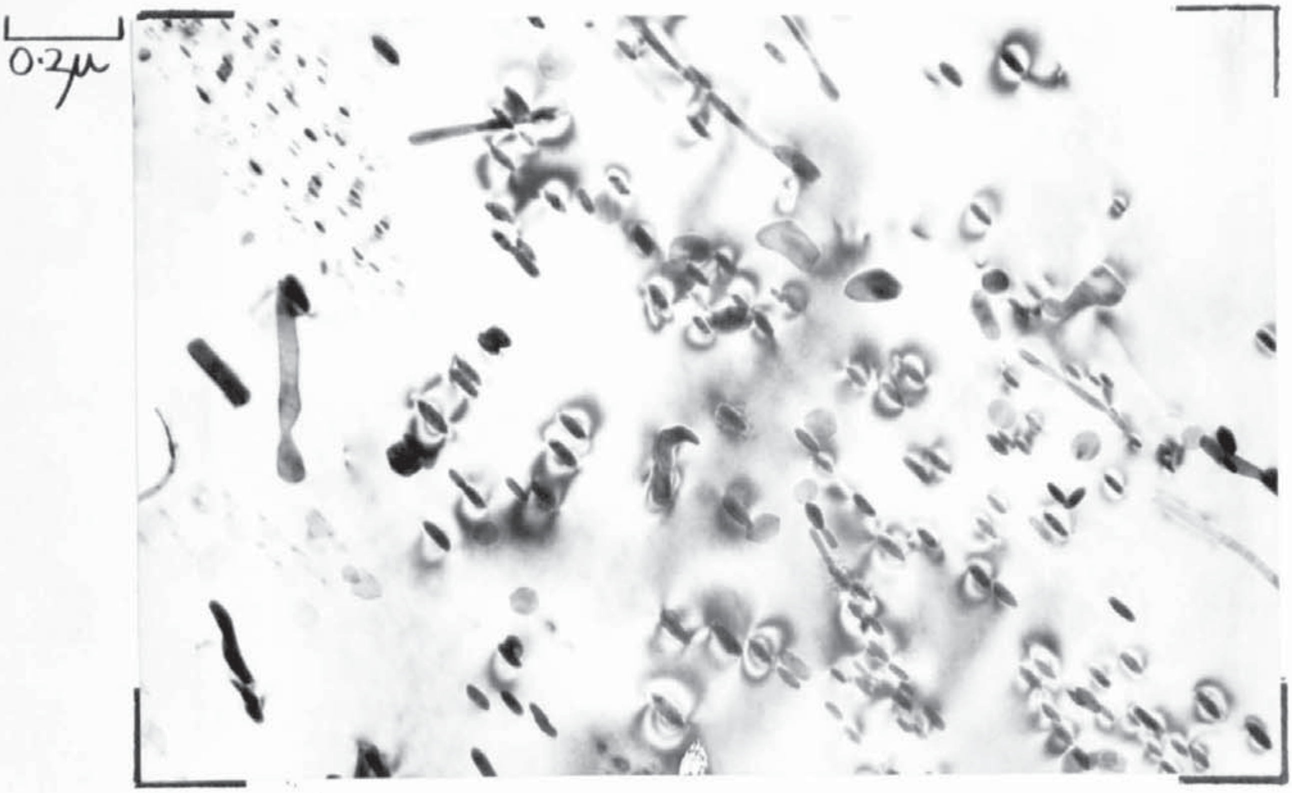

Figure 7.13. Showing the structure in a foil close to $(10\bar{1}0)$ Mg.

Figure 7.14. ZA homogenised and hydrided for 10 mins. at 600°C..

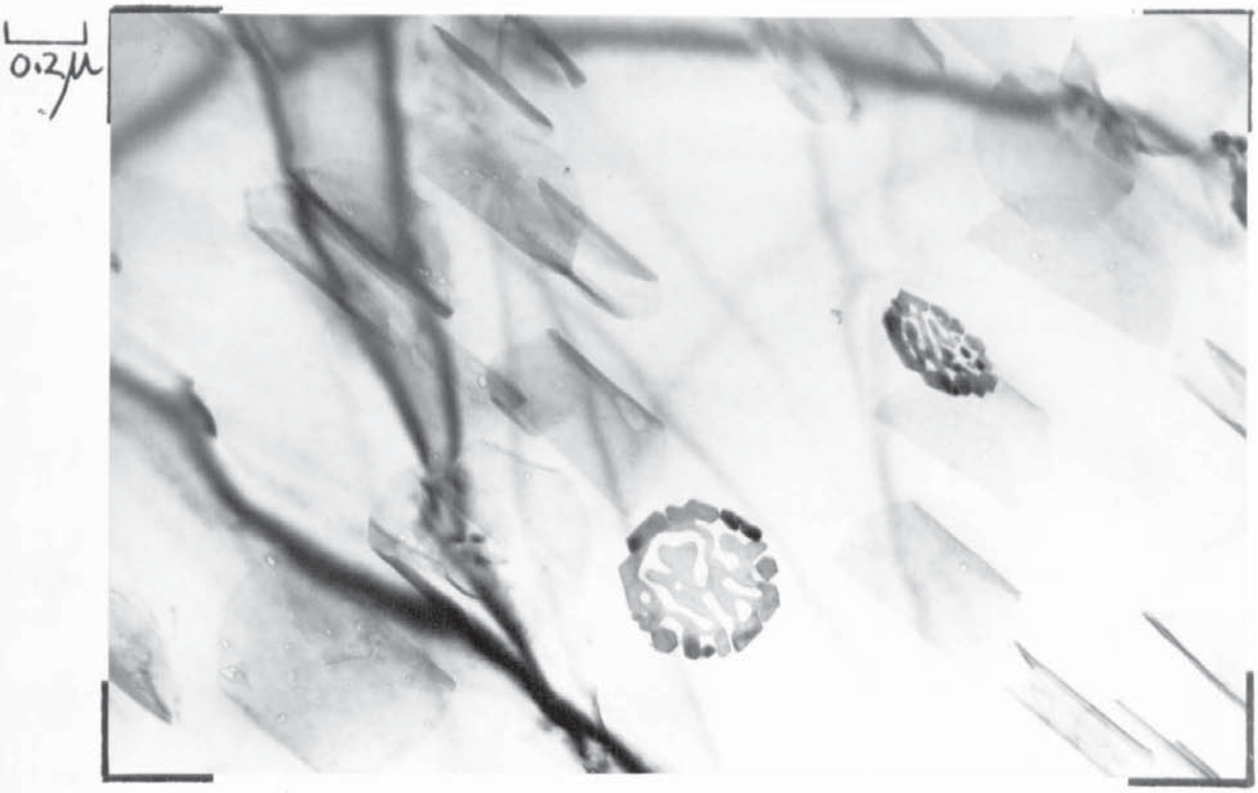

Figure 7.15. As Fig. 7.14 showing an intricatly shaped precipitate.

shape is more clearly seen.

High temperature tests.

As shown by Harris and Partridge[26] the creep ductility of this alloy is markedly dependant on its condition prior to the hydriding treatment. Three high temperature tests were carried out in the present investigation. Duplicate samples, as standard sheet specimens 0.5 inch wide and with a 3.0" parallel length, were heated to 400°C. in dry CO_2 ($<$30 p.p.m.) and the ductility measured. The results are listed below:-

Condition	Elongation on 2"
Hom. + 10 mins. in H_2 at 600°C.	8.0%
Hom. + 4 hrs. in H_2 at 570°C.	7.0%
A.E. + 4 hrs. in H_2 at 570°C.	33.0%

The low elongation of homogenised material is commensurate with a fine precipitate dispersion resulting from hydriding the alloy in this condition.

Section 4 - Magnesium - 6.0% Zn - 1.0% Mn - ZM61.

Mechanical Properties.

The change in hardness and 0.1% P.S. at various temperatures is shown in Figs. 8.1 and 8.2 respectively. There is a difference in the delay period prior to ageing and it is not feasible to directly compare the hardness with 0.1% P.S. The 0.1% P.S. results are those presented previously by the author[20] and as the tensile specimens for the Z6 and ZW6 alloys were also delayed for 8 days these results can be compared. The delay periods for the hardness specimens are also identical and the hardness curves can be compared.

The analysis of the alloy used for the hardness samples is shown by A in Table I and for the tensile properties by B. The tensile properties of alloy A were checked and the 0.1% P.S. increased by 7.7 t.s.i. on ageing at 180°C.. This is slightly lower than that of B and is in part a result of the larger grain size.

Electron Microstructure.

The alloy used for the ageing at room temperature is of composition B and that for all other ageing treatments alloy A. There was a difference between the two alloys in the solution treated condition. Undissolved intermetallic particles were present in B, which will be apparent in some of the photographs

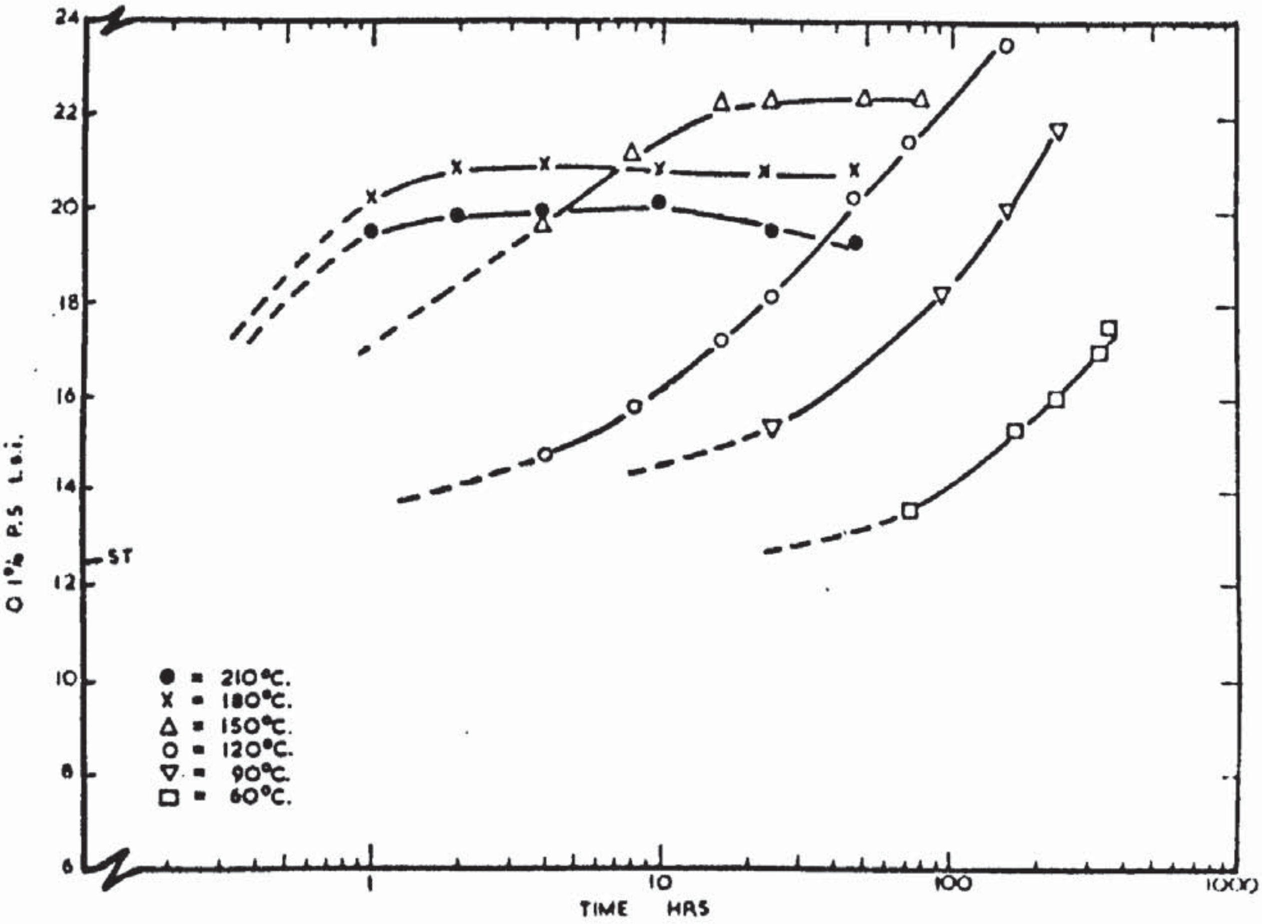

Figure 8.1.

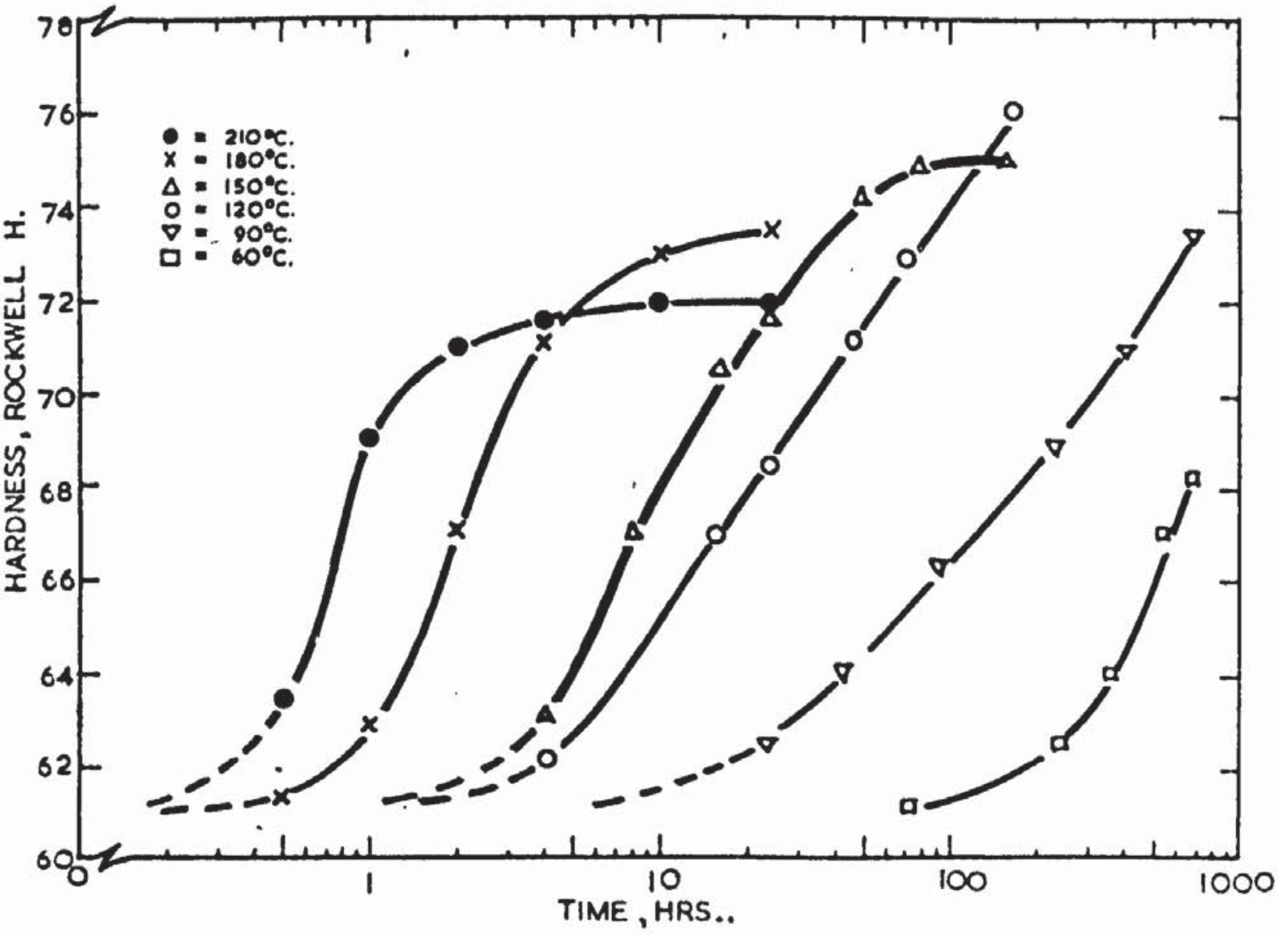

Figure 8.2.

of the alloy in the naturally aged condition. This is illustrated in Fig. 8.3 (1399) which shows the spherical particles with no orientation relationship to the matrix and randomly distributed. They are about 400 A^{o} diameter and widely spaced. These particles do not take part in the ageing process and do not change in appearance with prolonged heat treatment at 420°C.

Ageing at Room Temperature.

Fig. 8.4 (279) and Fig. 8.5 (278) show the structure after naturally ageing for 4 months. Fig 8.5 is the image formed with a $(10\bar{1}1)$Mg diffracted beam. The precipitate is visible by matrix contrast and the diffracted beam image illustrates the matrix perturbance from some of the precipitates. The foil orientation is $(\bar{1}2\bar{1}n)$, where $6 > N > 4$. The Frank sessile dislocation loops are between 2000-4000A^{o} in diameter and are in the basal planes at an angle of about 65° to the electron beam. This particular specimen was prepared from the alloy in sheet form, 0.025" thick, when foil preparation techniques were being examined and the faulted loops were not examined in detail. It is estimated from the forshortening that the foil is thicker than 1600A^{o}. Fig. 8.6 (183) illustrates the structure after 22 months at room temperature in a $(10\bar{1}0)$ Mg foil. The precipitate is visible by matrix contrast and the strain field has been resolved into its two components.

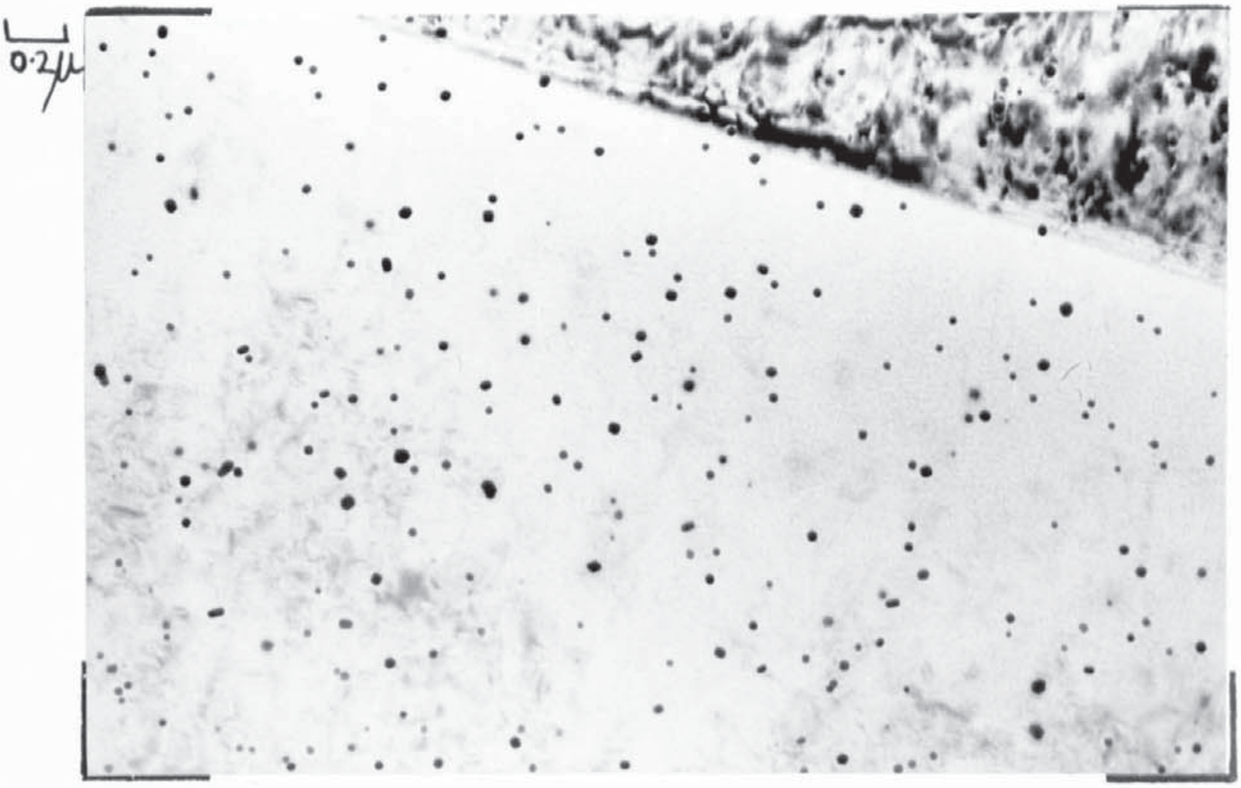

Figure 8.3. Undisolved intermetallic particles in alloy B.

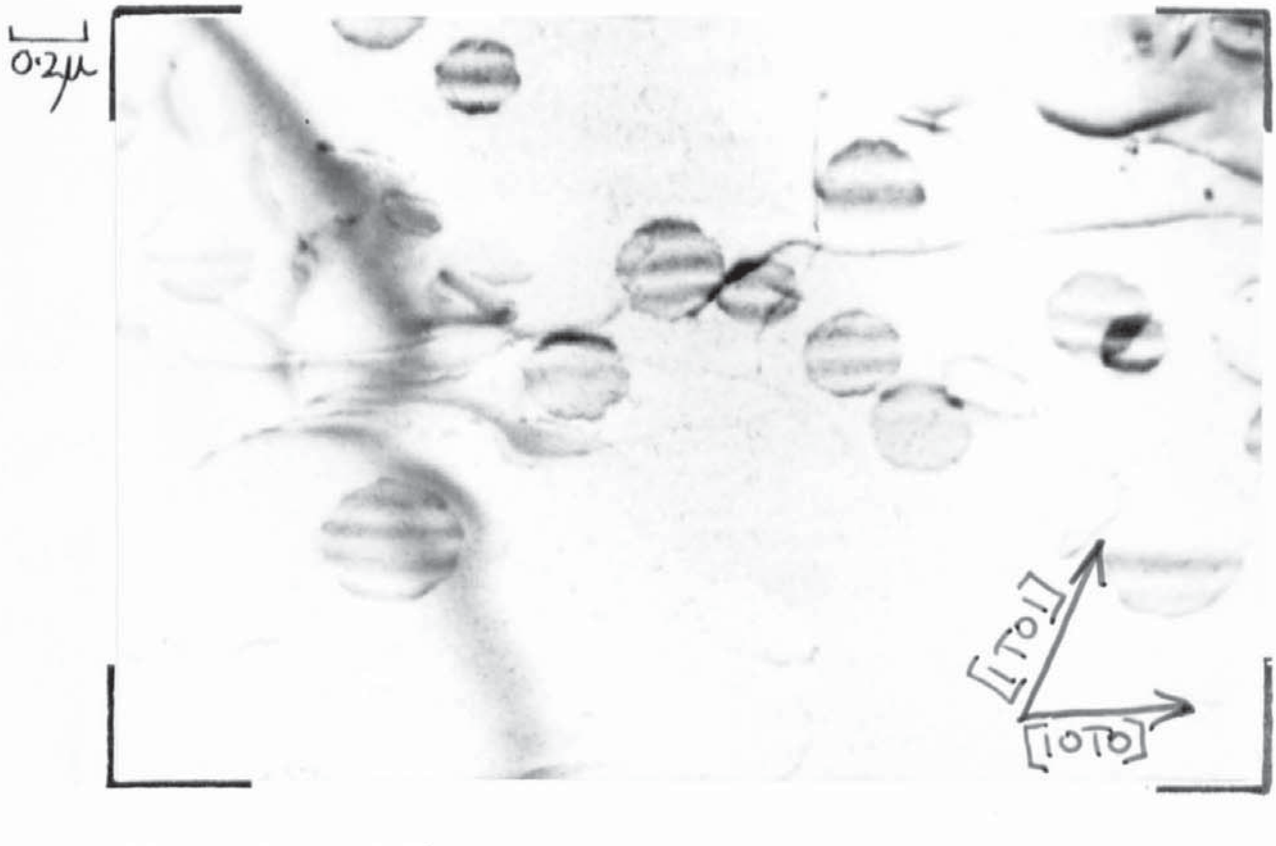

Figure 8.4. ZM61 naturally aged for 4 months.

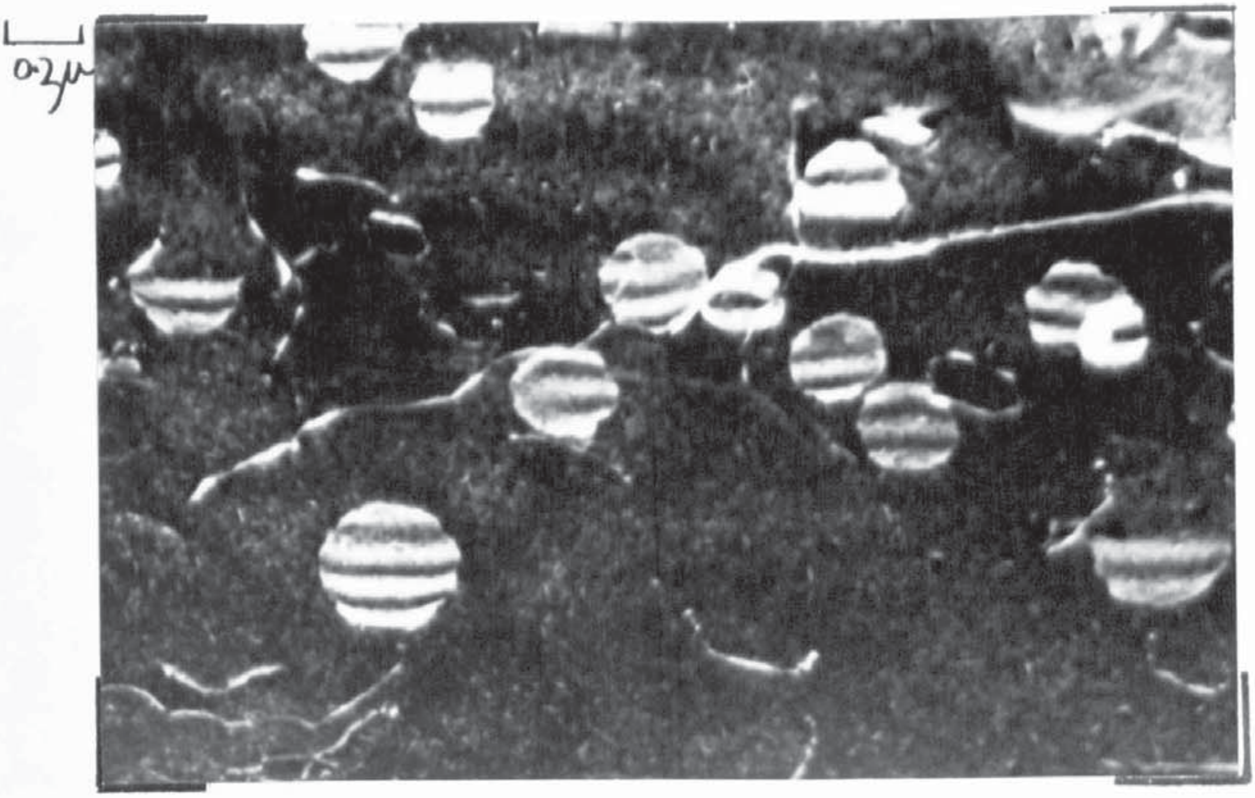

Figure 8.5. Area as in Fig. 8.4. imaged using a $(10\bar{1}1)$Mg diffracted beam.

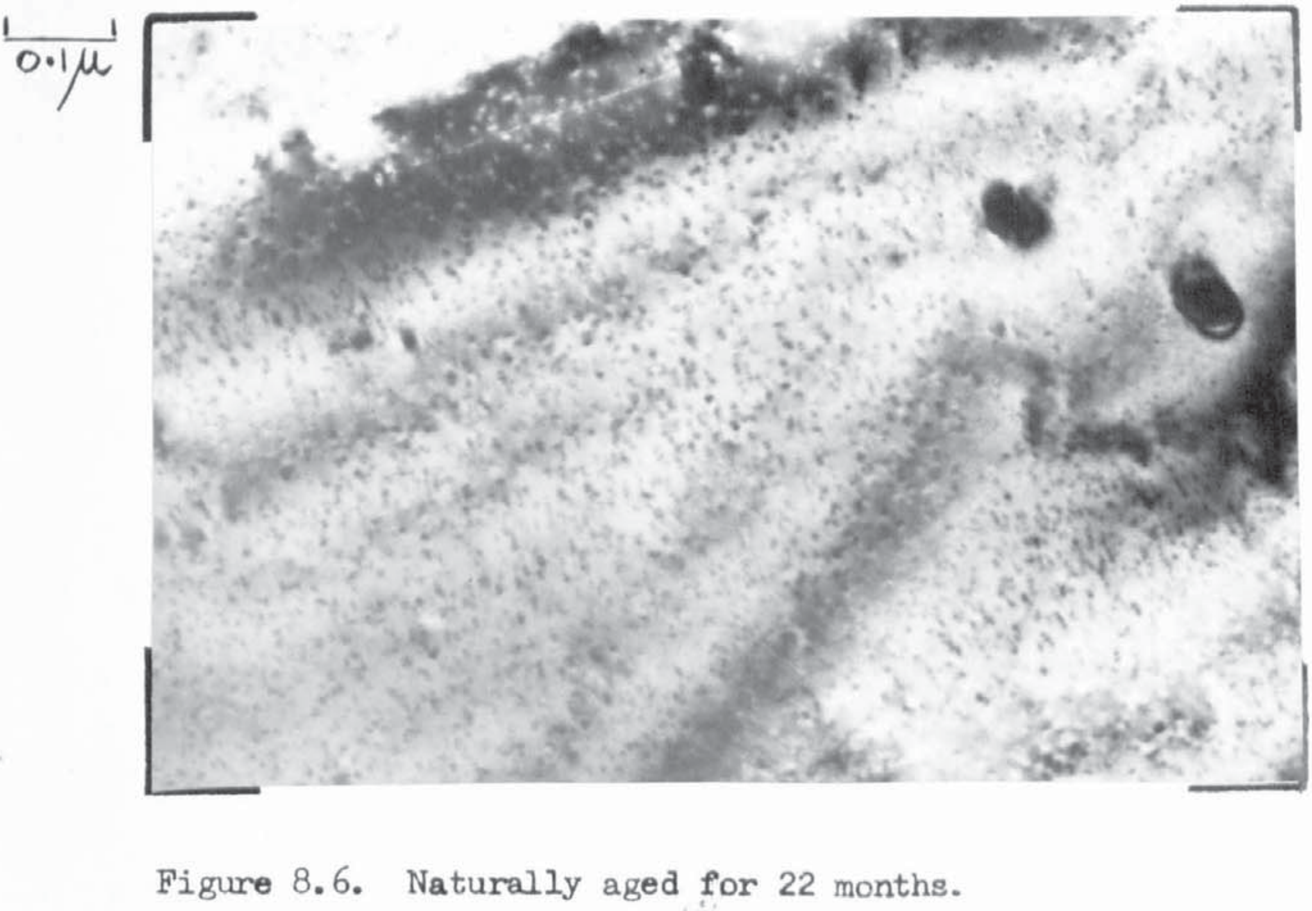

Figure 8.6. Naturally aged for 22 months.

This is the same as in Z6 and the strain field is as illustrated diagramatically in Fig. 3.4.

As with the Z6 and ZW6 alloys the line of no contrast is parallel to the (0001)Mg planes, the length is 60-80A° and its width 30-45A°.

Fig. 8.6 (a) (188A) shows the selected area diffraction pattern from the area shown in Fig. 8.6. The pattern is from a $(10\bar{1}0)$ foil orientation and the streaks perpendicular to the (0001)Mg are from the zones causing the matrix contrast in Fig. 8.6. The streaking is a result of discs on or needles perpendicular to the (0001)Mg planes. The matrix contrast in Fig. 8.6 would indicate the former. The interplanar spacings giving rise to the streaked pattern were measured and are shown below:-

Spot No.	d A°
1	2.3
2	2.14
3	4.38

The pattern is most probably a $(10\bar{1}0)$ type from a hexagonal cell. The c spacing would be 8.76 A° and the a spacing 5.4 A° and the orientation relationship.

(0001) ppte // $(11\bar{2}0)$ Mg and

$(11\bar{2}0)$ ppte // (0001) Mg.

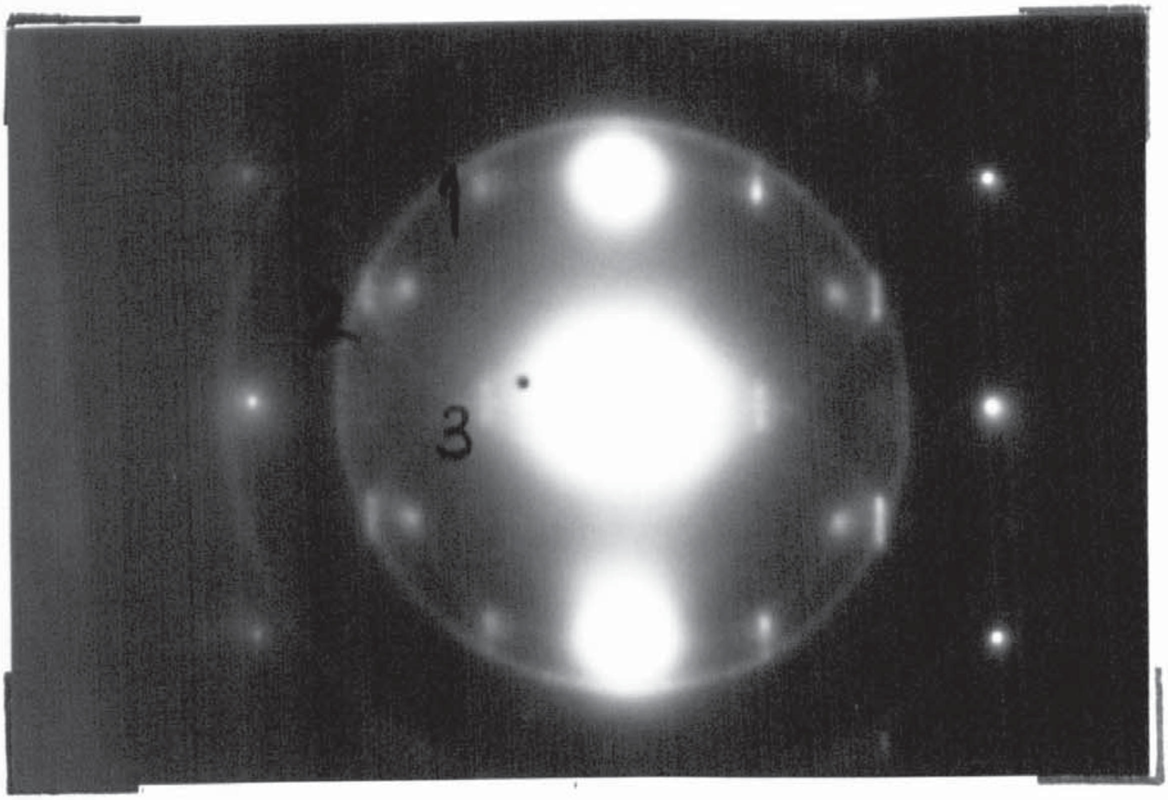

Figure 8.6(a). Selected area diffraction pattern of Fig. 8.6.

This relationship is as that for $MgZn_2$ needles reported by Gallot[3]. The change in the c and a parameters is due, it is suggested, to the presence of manganese in the precipitate, thereby forming the ternary compound previously indicated.

The geomentry of the precipitate/matrix orientation relationship is such that

$2.70\ \text{A}^\circ$ ppte // $2.59\ \text{A}^\circ$ matrix and

$1.45\ \text{A}^\circ$ ppte // $1.6\ \text{A}^\circ$ matrix

Thus the misfit in a direction perpendicular to the (0001)Mg planes is

$$\frac{2(2.70 - 2.59)}{2.70 + 2.59} = 0.04 \text{ or } 4.0\%$$

and in a direction perpendicular to the $(11\bar{2}0)$Mg planes

$$\frac{2(1.6 - 1.45)}{1.6 + 1.45} = 0.985 \text{ or } 9.8\%$$

This is shown diagramatically below and the shaded area represents the disc shaped coherent intermediate precipitate.

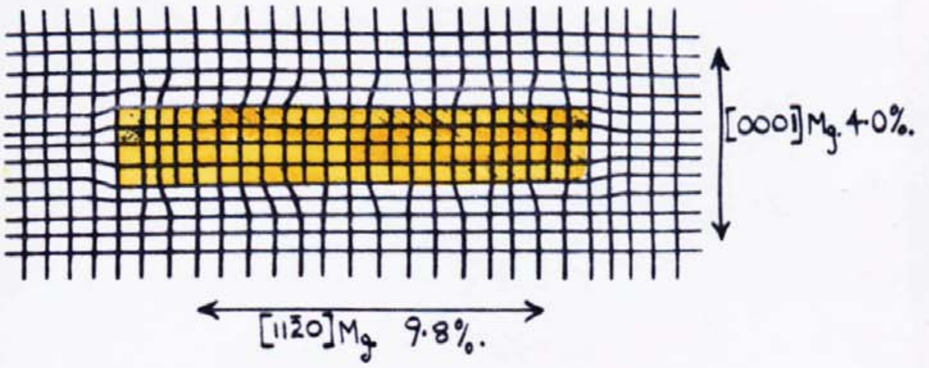

The rings in Fig. 8.6(a) are from MgO, the inner one from (200)MgO and the outer from (220)MgO.

Fig. 8.7 (698) illustrates the structure after 36 months natural ageing in a foil that is not quite a $(11\bar{2}0)$Mg foil plane. The matrix contrast is 60-80A$^{\circ}$ measured parallel to the basal planes. Fig. 8.8 (1487) shows the structure after 54 months at room temperature in a $(11\bar{2}0)$Mg foil. The two components of the matrix contrast are evident and the length of the line of no contrast is still 60-80A$^{\circ}$ and the width 30-45A$^{\circ}$. Fig. 8.9 (1402) shows a precipitate free zone about 400 A$^{\circ}$ across which arises from solute depletion. Copious precipitation is evident within the grains.

Ageing at 60°C..

The structure after 240 hours ageing is shown in Fig. 8.10 (1192) in a $(10\bar{1}0)$Mg foil. The matrix contrast from the zones is about 90-100A$^{\circ}$ across and 30-45A$^{\circ}$ wide. A transformation to a needle shaped precipiate is evident and the needles have grown to 200-300A$^{\circ}$ long and are perpendicular to the (0001)Mg. The structure after 696 hours is shown in Fig. 8.11 (1177). The length of the line of no contrast is still about 100 A$^{\circ}$ with a width of about 30A$^{\circ}$. The variation in the lengths of the lines of no contrast is illustrated in Fig. 8.12 (1175) which is an image formed with an (0002)Mg diffracted beam. The size range

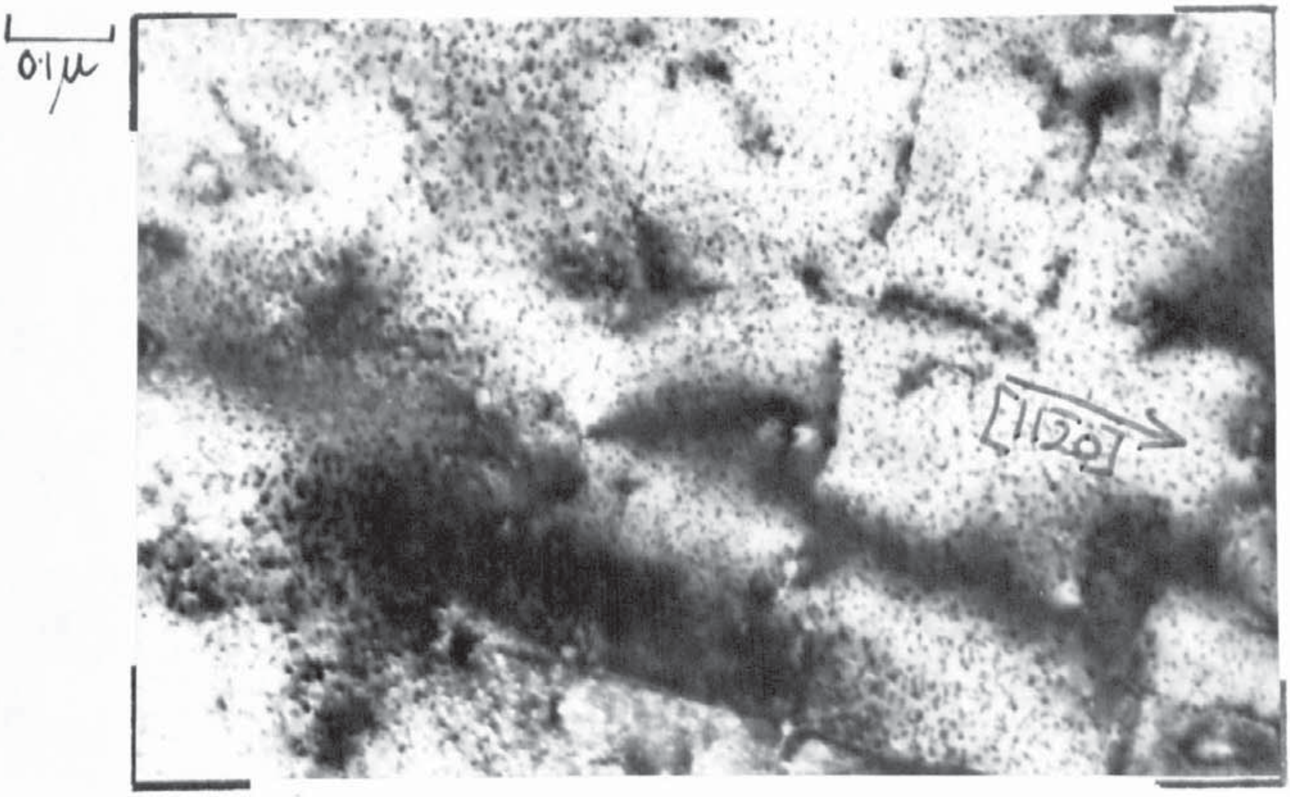

Figure 8.7. ZM61 after 36 months at room temperature.

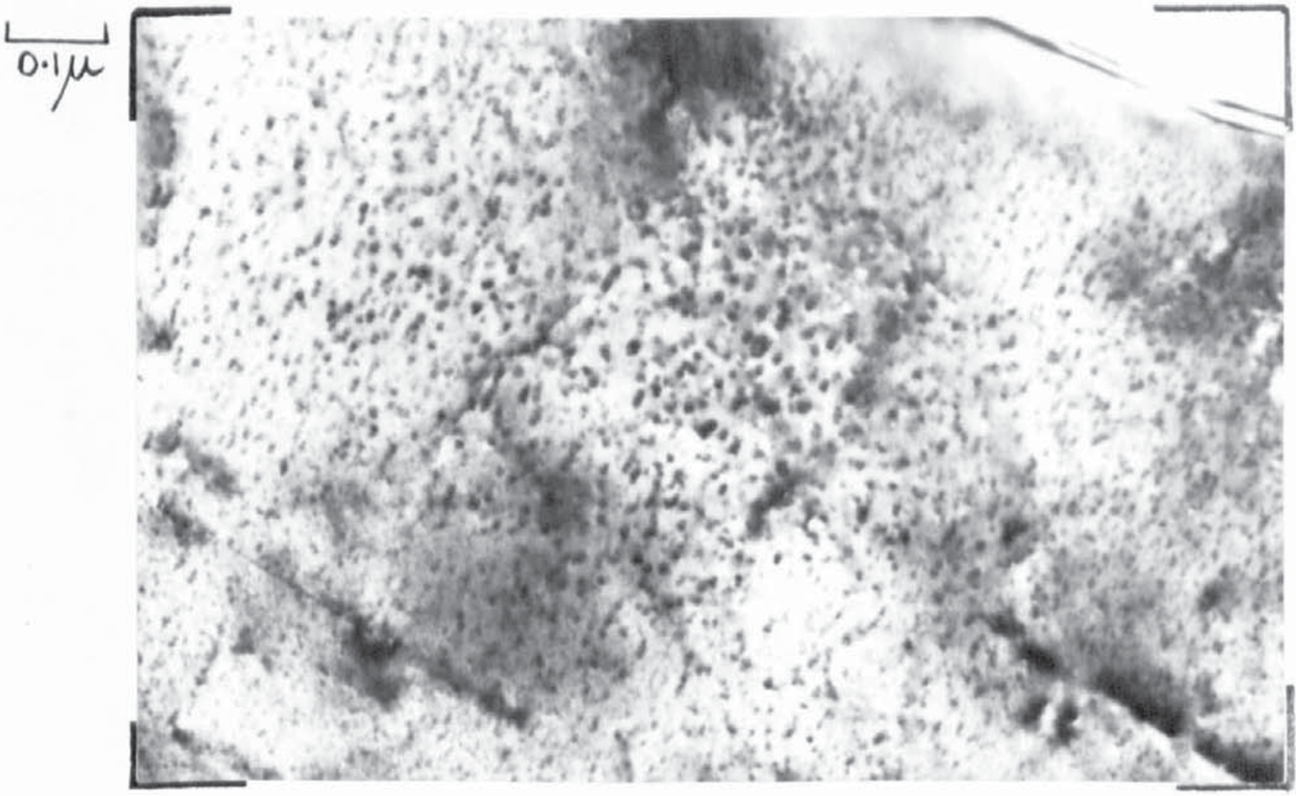

Figure 8.8. ZM61 after 54 months at room temperature.

Figure 8.9. As Fig.8.8 showing a narrow precipitate free zone.

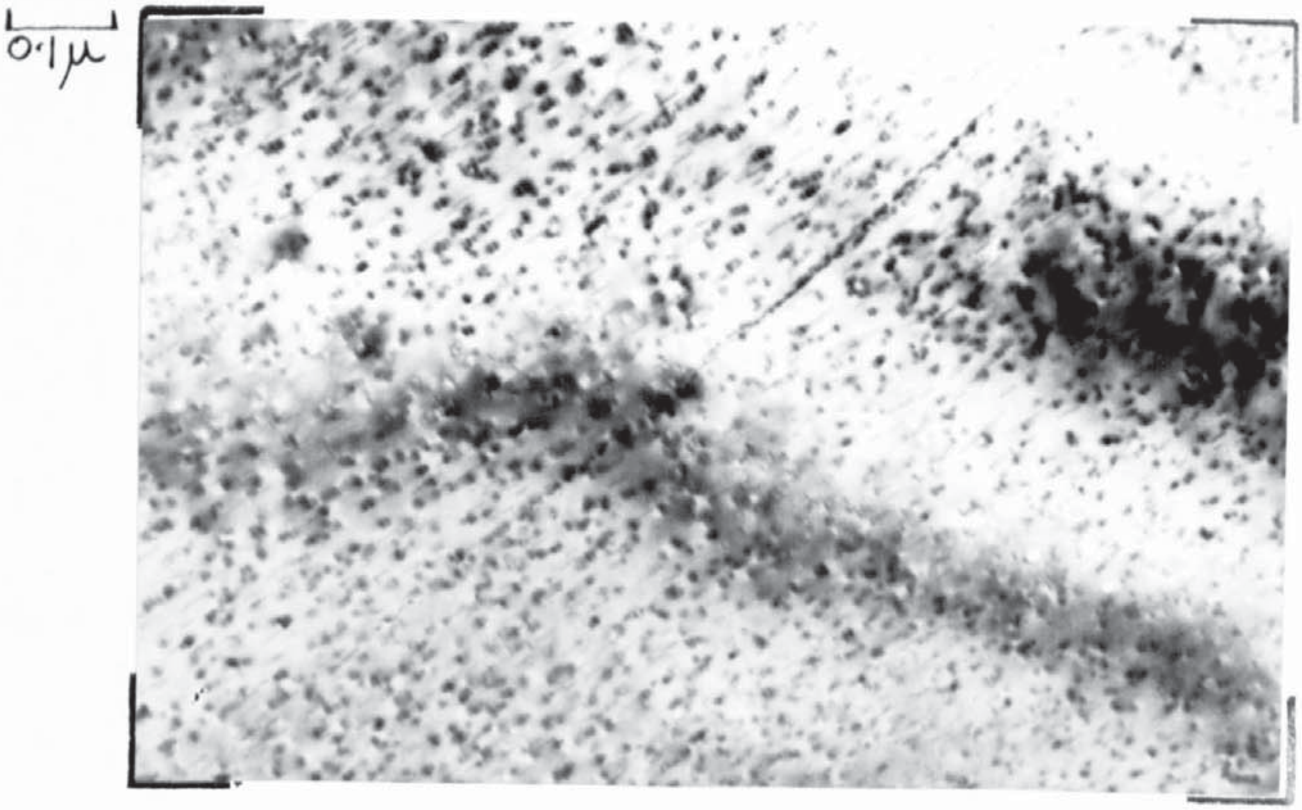

Figure 8.10. ZM61 aged for 240 hours at 60°C..

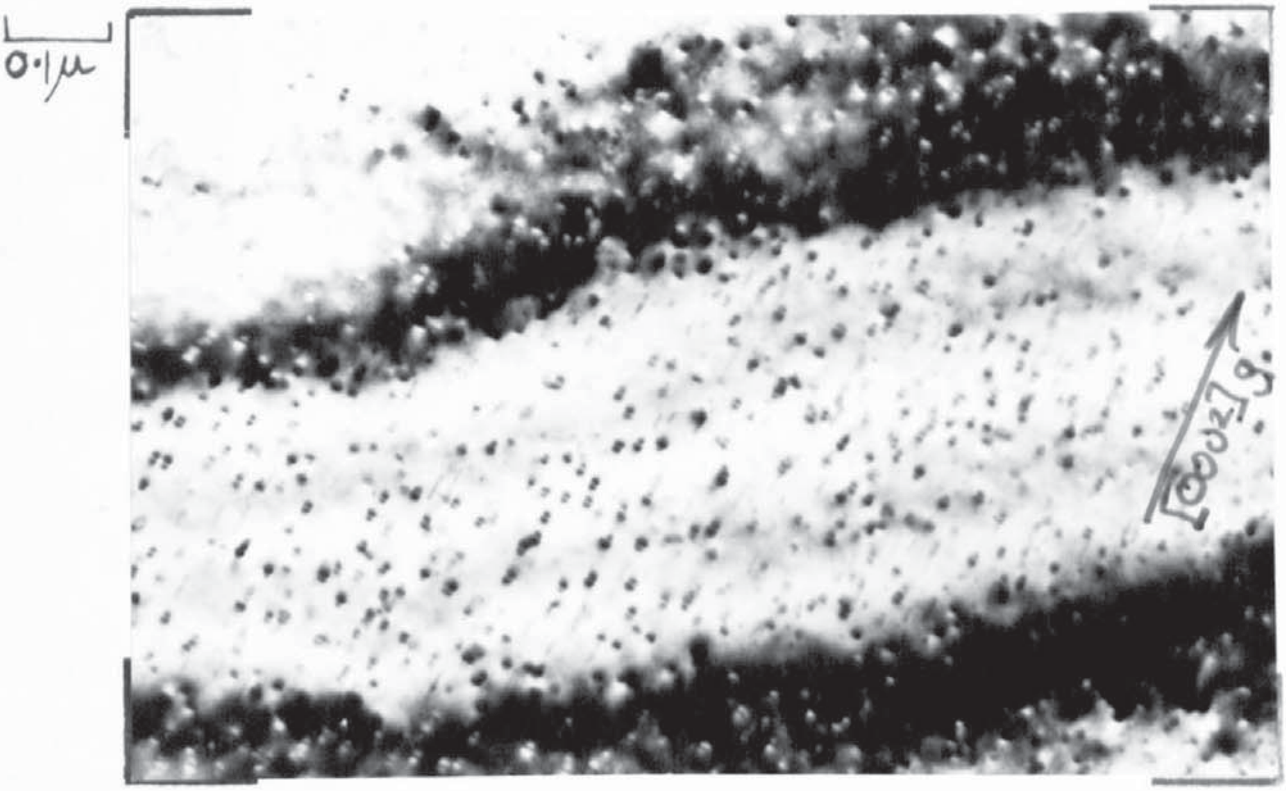

Figure 8.11. Structure after 696 hours at 60°C..

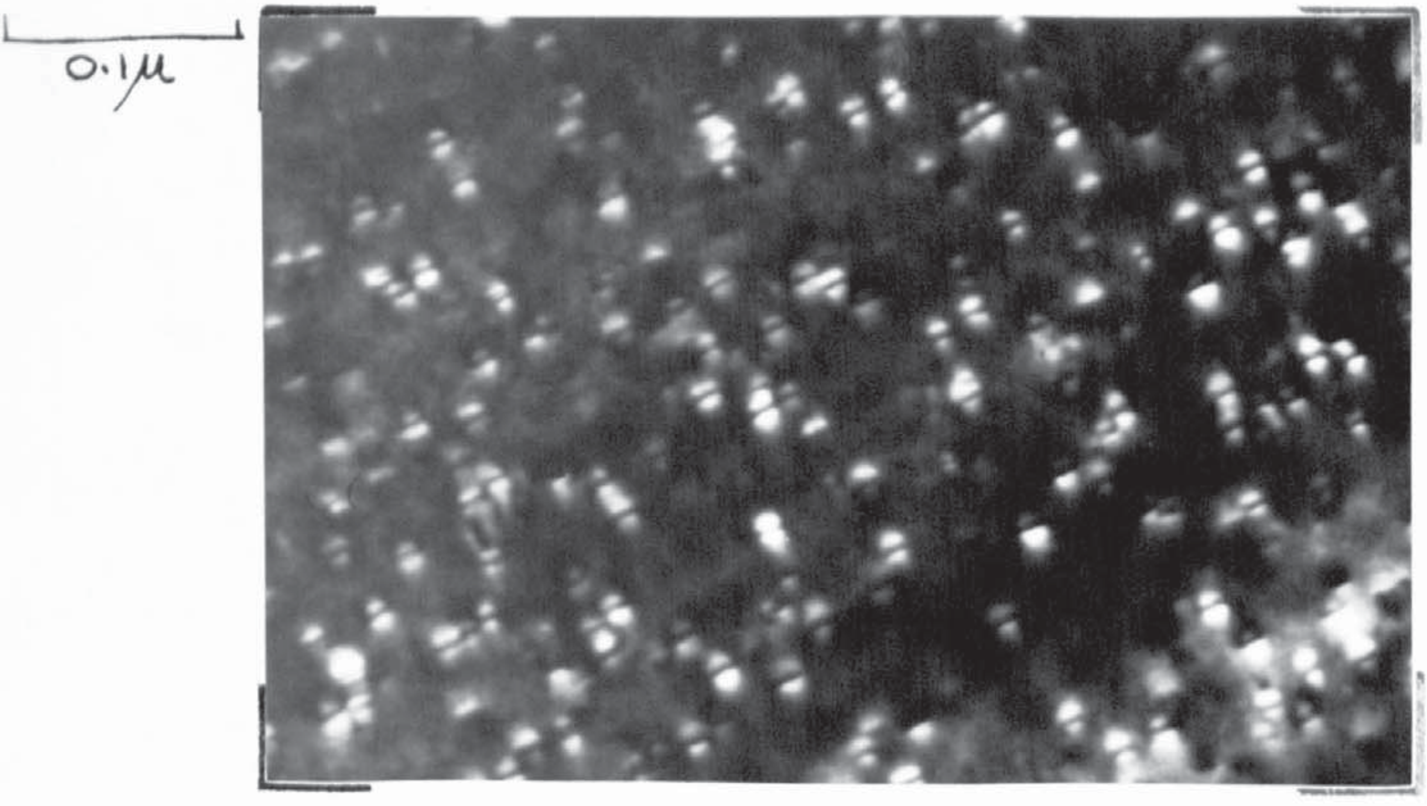

Figure 8.12. Image formed using an (0002)Mg diffracted beam.

is 40-120A° and the homogeneous distribution of these zones is shown in Fig. 8.13 (1171).

Ageing at 90°C..

The general structure after 4 and 8 hours ageing is shown in Fig. 8.14 (461) and Fig. 8.15 (442) and both of these illustrations are from foils not quite on $(10\bar{1}0)$Mg. In Fig. 8.15 some precipitates are in the form of needles perpendicular to (0001)Mg and about 100 A° long. Fig. 8.16 (445) shows the two component matrix contrast in a $(10\bar{1}0)$Mg foil. The length of the line of no contrast is 40-70A°. Needles about 120A° long have also grown after this treatment.

Fig. 8.17 (244) illustrates the structure after 48 hours ageing in a $(11\bar{2}0)$Mg foil. The needles have reached a length of 100-1000A° and a possible second structure is evident in the form ofasmall precipitate at right angles to the needles. The structure after 96 hours ageing is shown in Fig. 8.18 (1015) and Fig. 8.19 (1018) close to a $(10\bar{1}0)$Mg and an (0001)Mg foil respectively. It is not feasible to measure needle length from Fig. 8.18: there is also a light patchy preparation defect on the surfaces of this foil. There is an area towards the top of the photograph with an enhanced precipitation density due to localised heterogeneous nucleation. The spacing of the needles from Fig. 8.19 is between 50 - 600 A° and the lines of

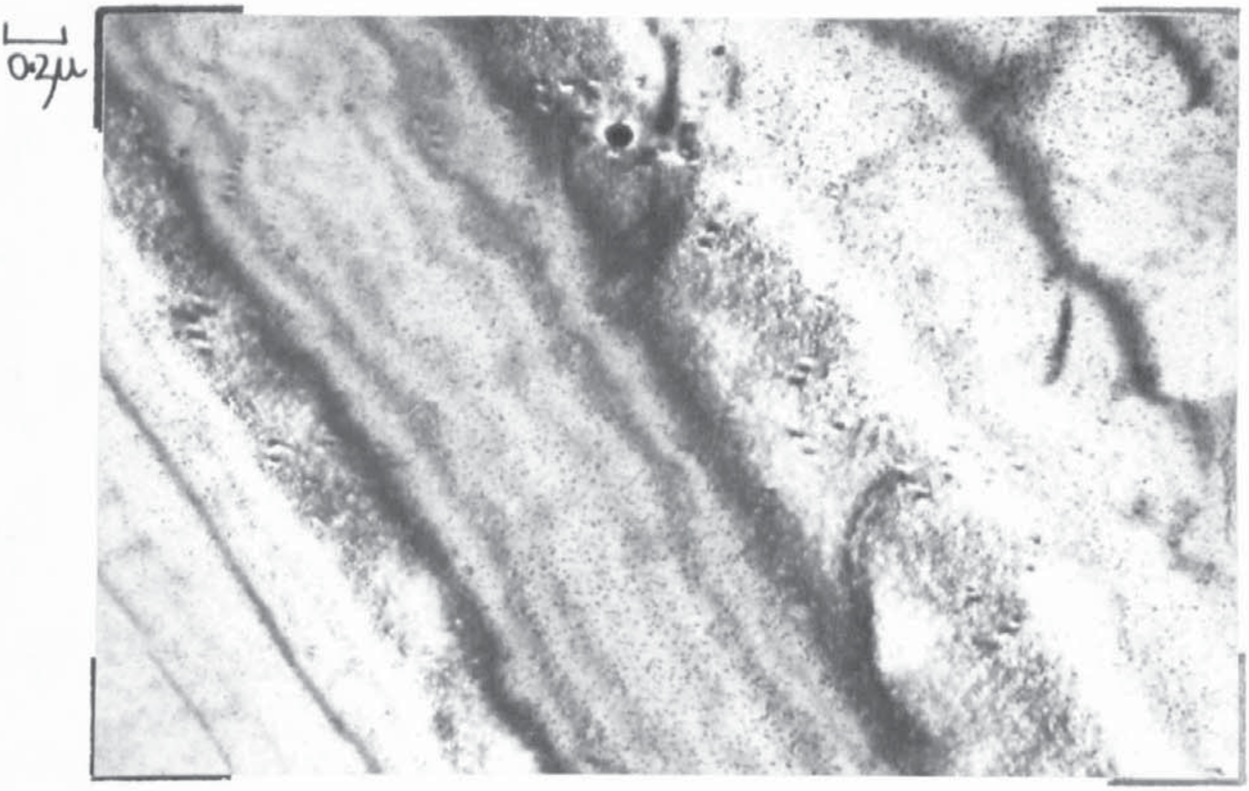

Figure 8.13. ZM61 aged for 240 hours at 60°C..

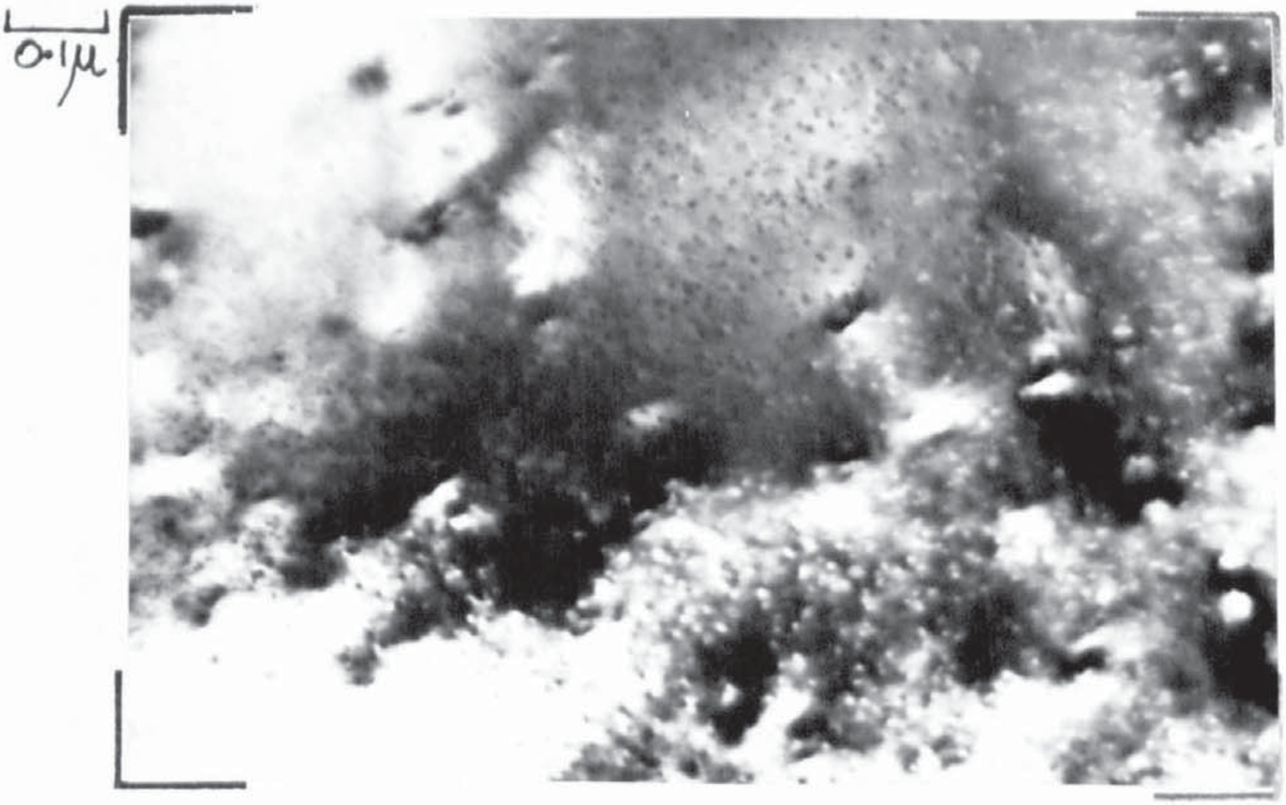

Figure 8.14. ZM61 aged for 4 hours at 90°C.

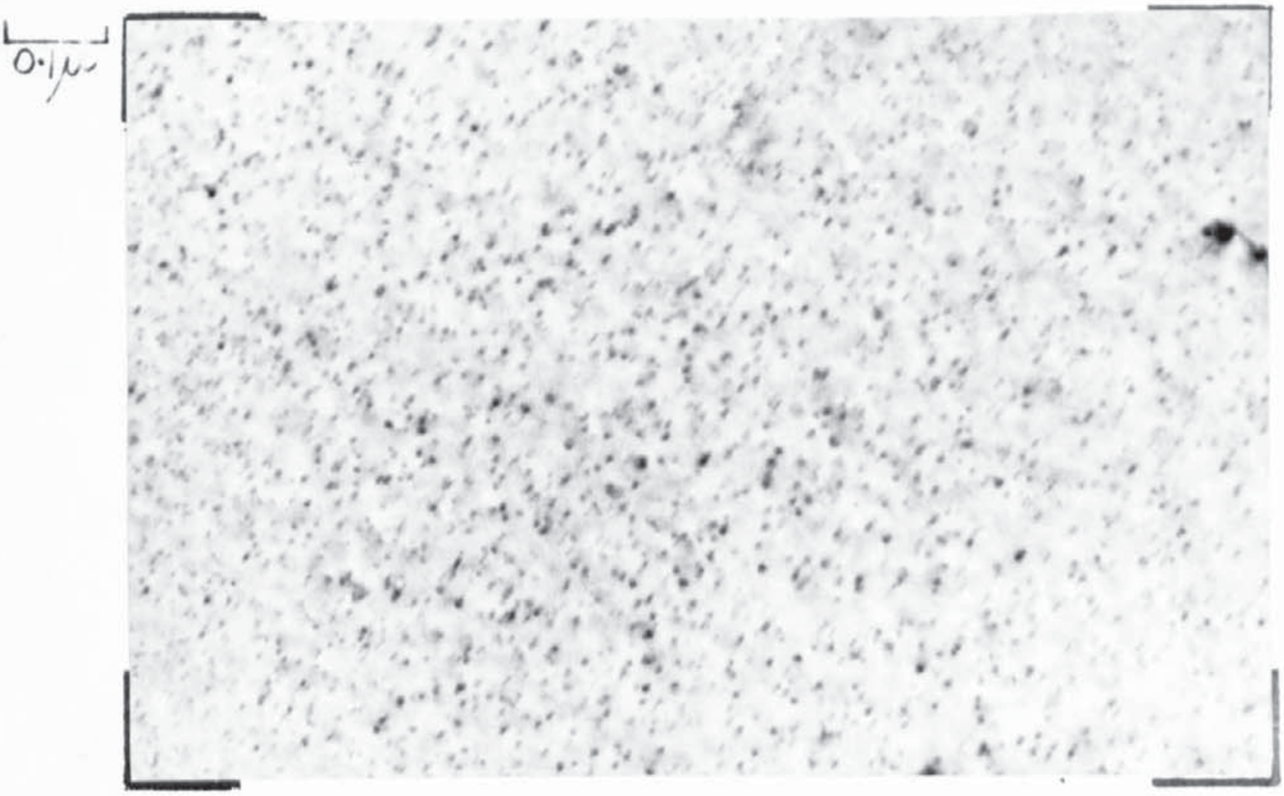

Figure 8.15. Structure after ageing for 8 hours at 90°C..

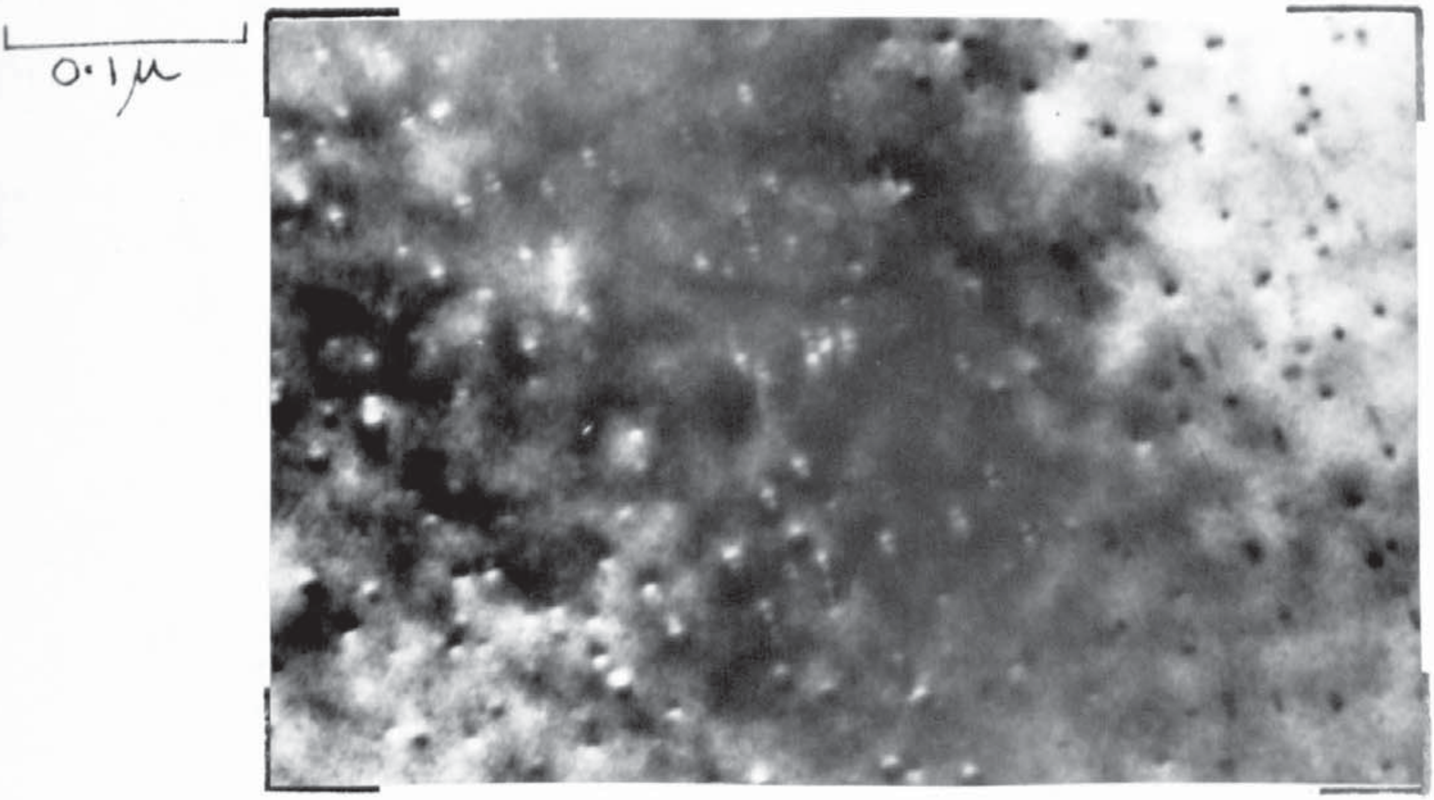

Figure 8.16. Showing G.P. zones in sample aged for 8 hours at 90°C.

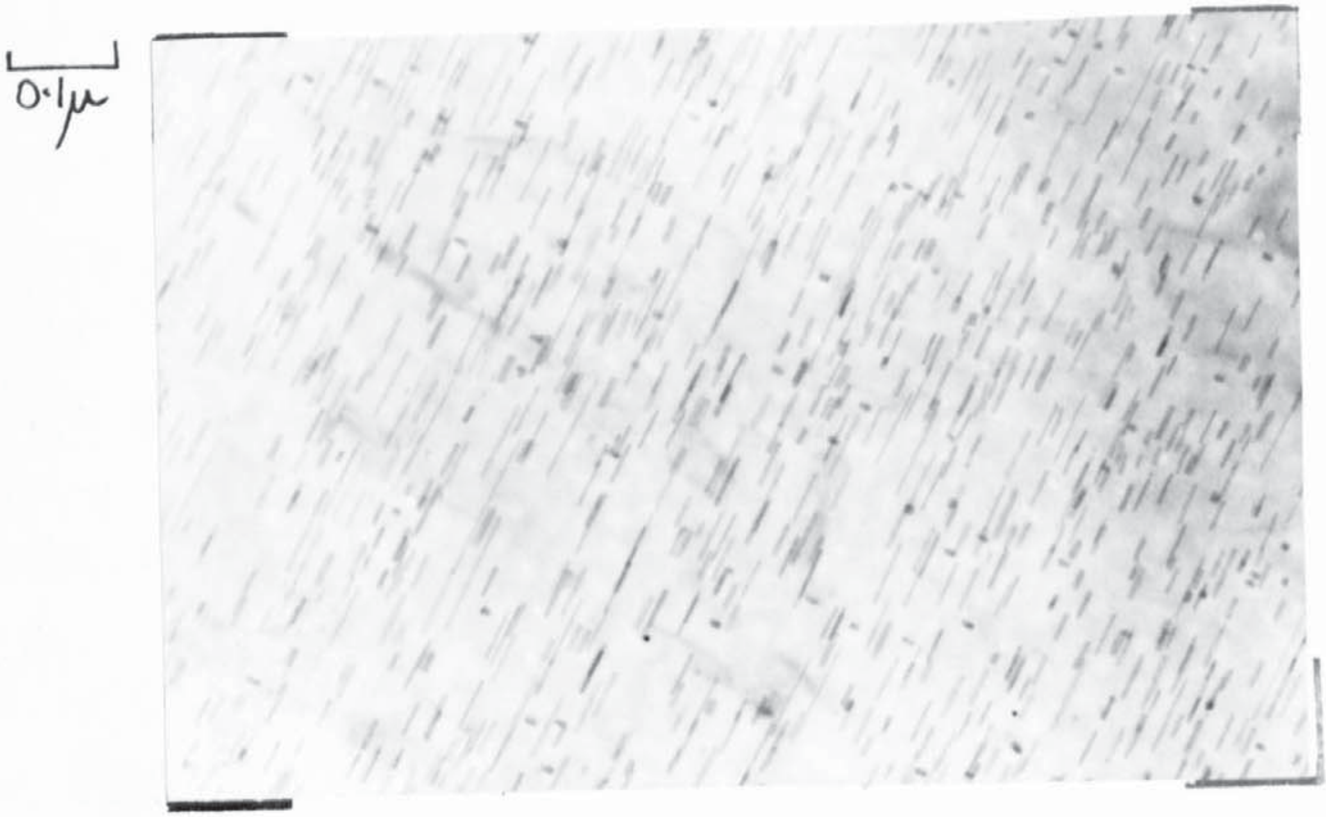

Figure 8.17. ZM61 aged for 48 hours at 90°C., Foil orientation $(11\bar{2}0)$ Mg.

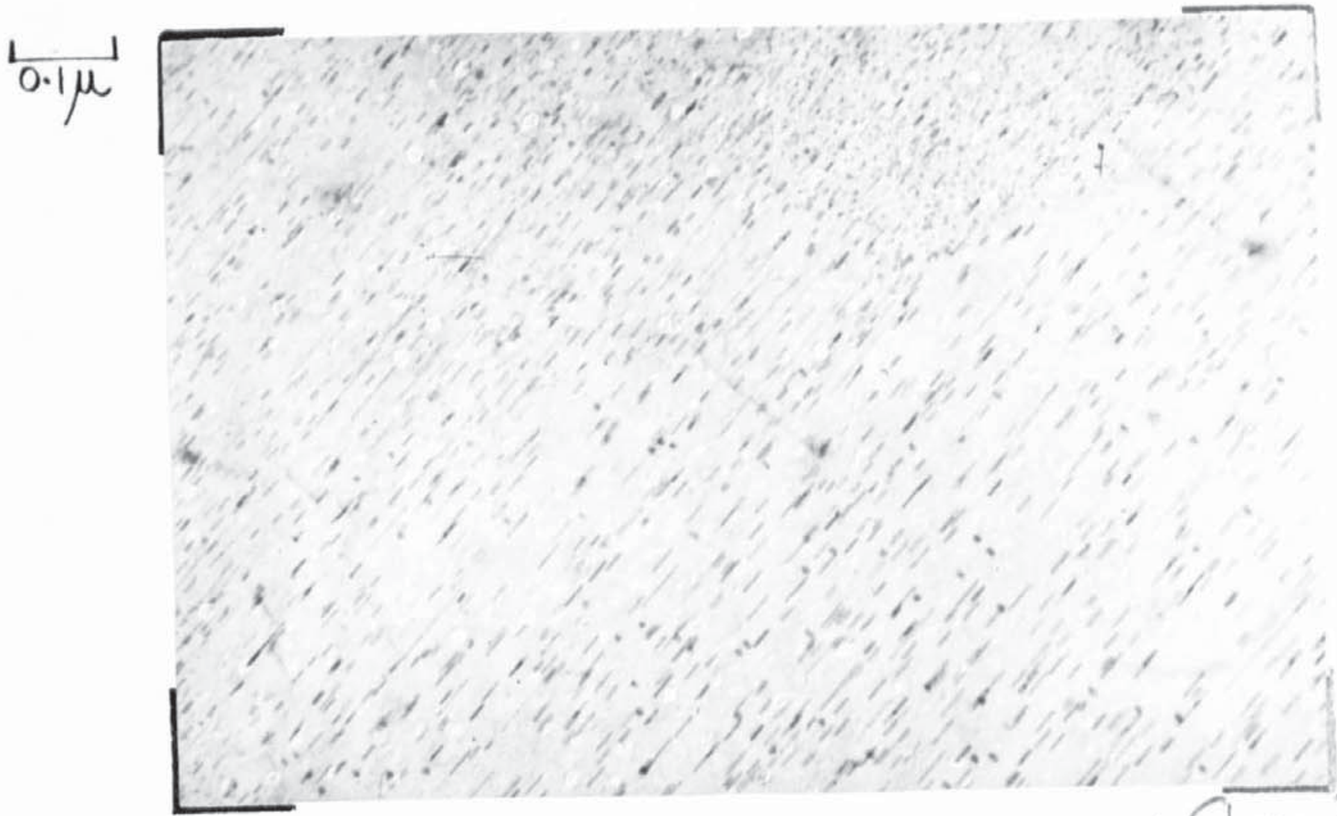

Figure 8.18. Structure after 96 hours at 90°C.. Close to $(10\bar{1}0)$Mg foil orientation.

heterogeneously nucleated precipitates are on $(11\bar{2}0)$Mg planes. A small quantity of disc shaped precipitate on the (0001)Mg planes is visible in this photograph. The diffraction pattern from an area illustrated in Fig. 8.19 is shown in Fig. 8.20 (1019). The interplanar spacing causing the spots just outside the $(10\bar{1}0)$Mg spots is 2.5A° and the angle between the planes 60°. The nearest spacing from the A.S.T.M. index for $MgZn_2$ is 2.43 and calculated, 2.49A°. The nearest spacing from the ternary compound is 2.51A°.

The calculated spacing from $MgZn_2$ is from $(11\bar{2}1)$ type planes and for the ternary from $(11\bar{2}2)$ type. The angle between $(11\bar{2}1)$ planes in $MgZn_2$ is 57° 12' and for $(11\bar{2}2)$ type at a = 5.24 and c = 17.1A° is 68° 12'. The orientation relationship of $MgZn_2^2$ discs from Gallot[3] is

$$(11\bar{2}0)\ MgZn_2^2\ //\ (10\bar{1}0)Mg$$

Clearly this relationship does not apply to the pattern shown in Fig. 8.20 as d $(11\bar{2}0)$ $MgZn_2$ is 2.60A°, also there is a preponderance of needles shown in Fig. 8.19. The orientation of $MgZn_2^1$ would produce in an (0001)Mg reciprocal lattice, diffraction spots just outside the $(10\bar{1}0)$Mg spots. These would arise from the $(10\bar{1}3)$ and $(20\bar{2}0)$ planes in $MgZn_2^1$ and d $(10\bar{1}3)MgZn_2^1$ = 2.41, d $(20\bar{2}0)MgZn_2^1$ = 2.25. The angles between $(10\bar{1}3)MgZn_2^1$ type planes is 55° 36' and $(20\bar{2}0)$ type 60°.

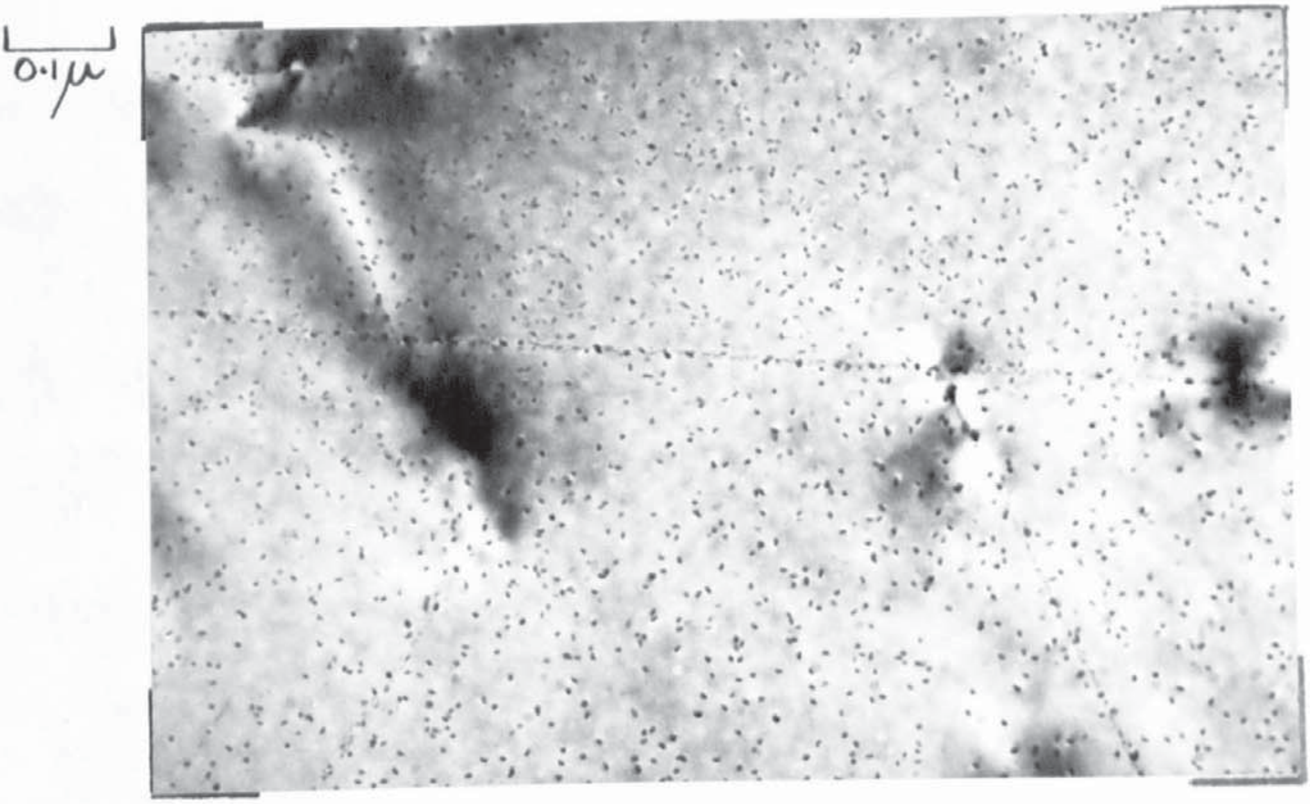

Figure 8.19. As Fig. 8.18 but showing the structure in an (0001)Mg foil.

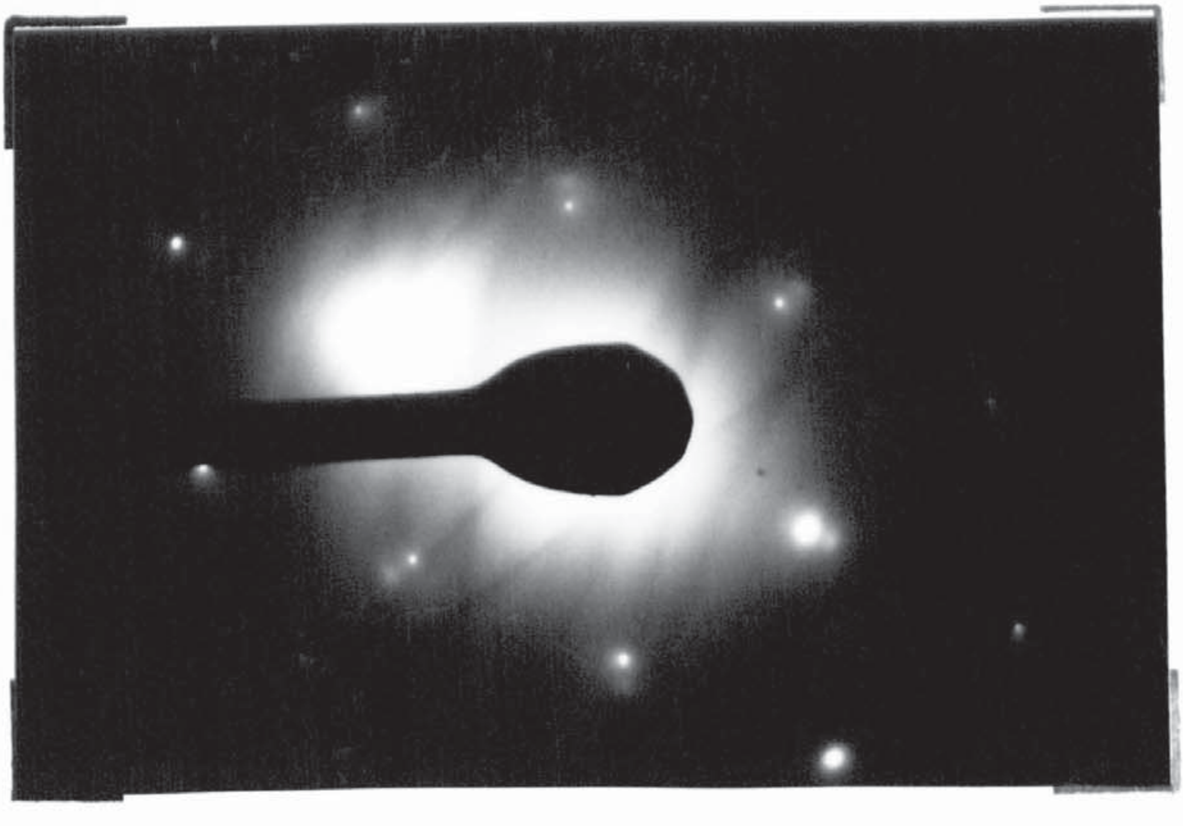

Figure 8.20. Selected area diffraction pattern of area shown in Fig. 8.19.

Ageing at 120°C..

Fig. 8.21 (1378) shows the structure after 16 hours ageing, in a foil close to $(10\bar{1}0)$Mg. The needle length is between 100A$^{\circ}$ and 3000A$^{\circ}$ with the general size between 100-1000A$^{\circ}$. There is evidence of heterogeneous nucleation, shown by the large area of fine precipiate to the centre of the photograph. Two "line" defects are also apparent at A and B. A shows two distinct lines of fine precipitate and at B a "kink" in the needle precipitate can be seen. These defects are parallel to the basal planes of the matrix.

The structure after 264 hours is shown in Fig. 8.22 (1261). Grain boundary precipitation and a very small precipitate free zone, 200A$^{\circ}$ wide is evident. The needle length is between 250-2000A$^{\circ}$, with a general range of 250-1000A$^{\circ}$.

Ageing at 180°C..

Fig. 8.23 (1372) illustrates the structure after ageing for 2 hours. Extensive precipitation has occurred with a wide variation in precipitate size: the basal planes are not quite parallel to the electron beam. It is not possible to determine the nature of the fine precipitate; it could be the early stages of needle formation or small discs on the basal planes. The needles have grown to approximately 4000A$^{\circ}$ long in some instances. In Fig. 8.24 (1373) which is of a $(10\bar{1}0)$Mg foil one or two needles

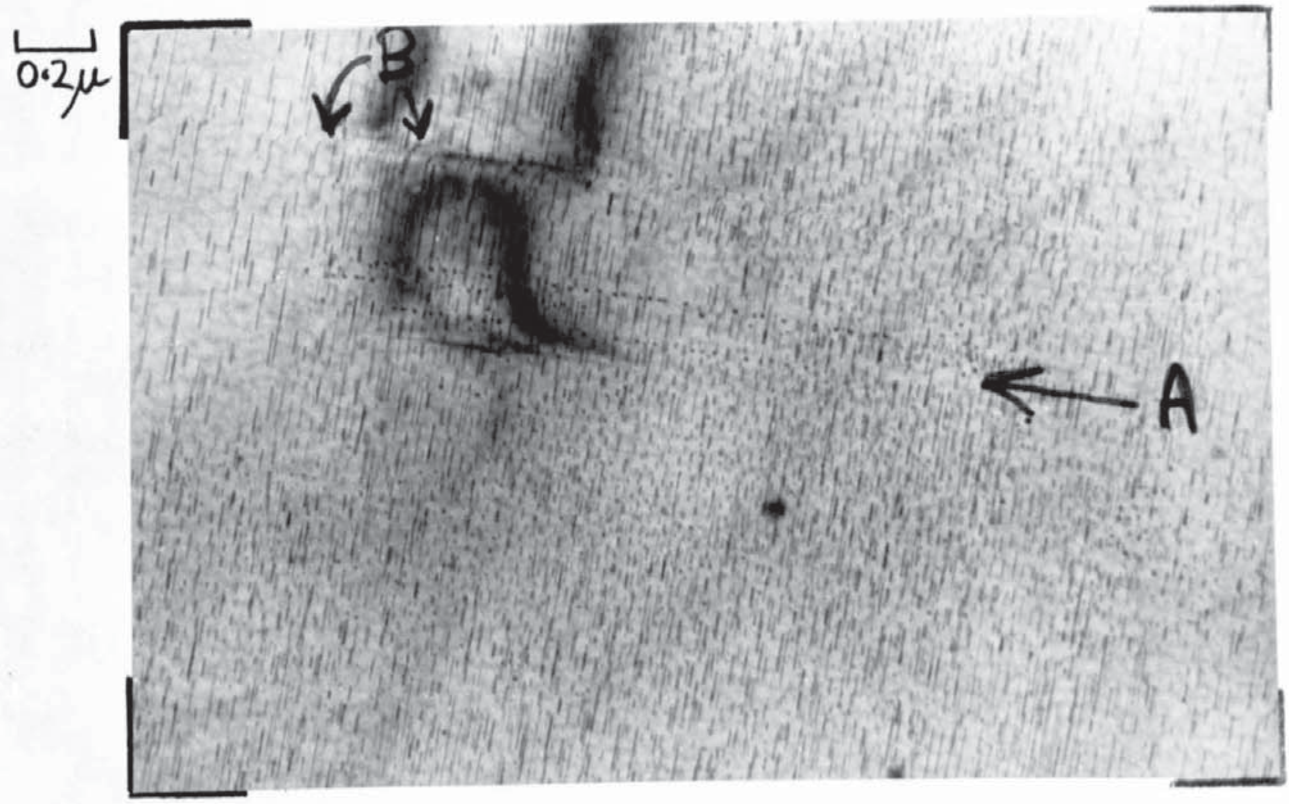

Figure 8.21. ZM61 aged for 16 hours at 120°C.

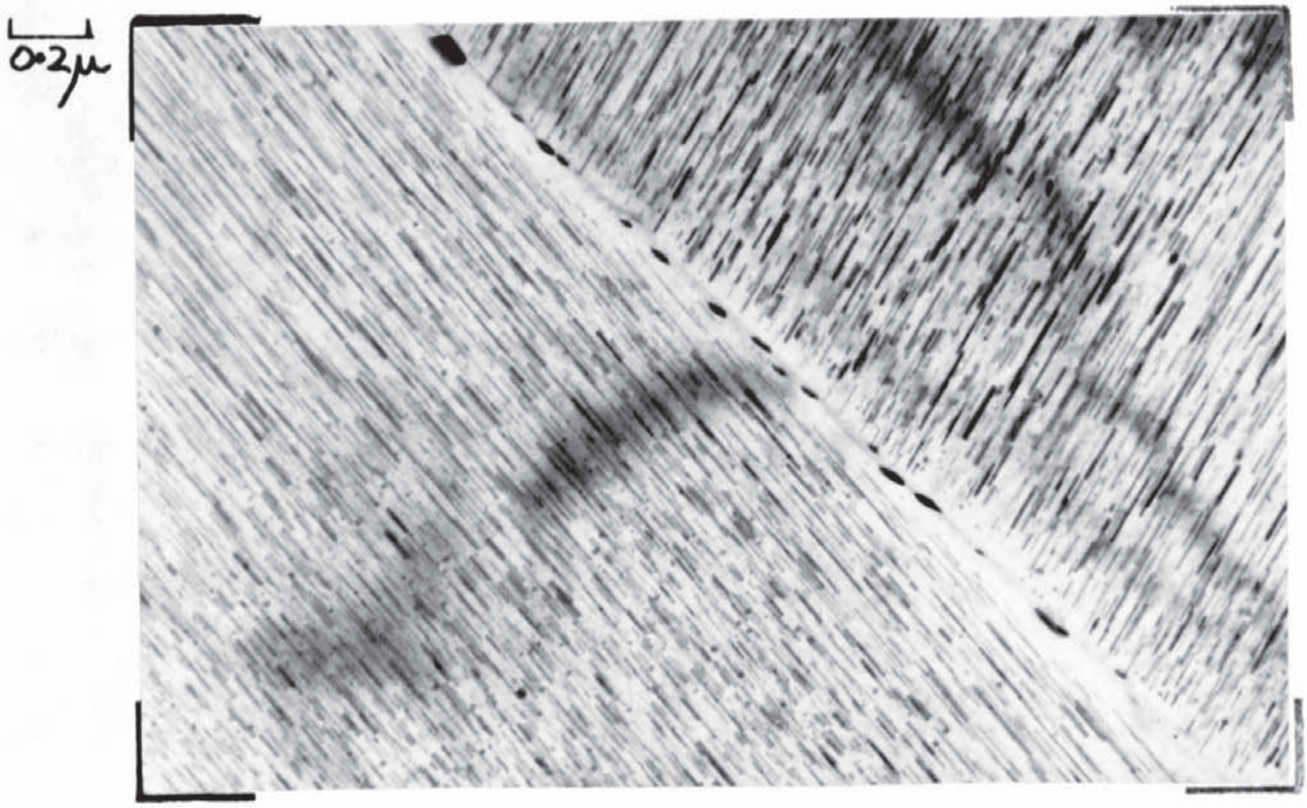

Figure 8.22. Structure after ageing for 264 hours at 120°C.

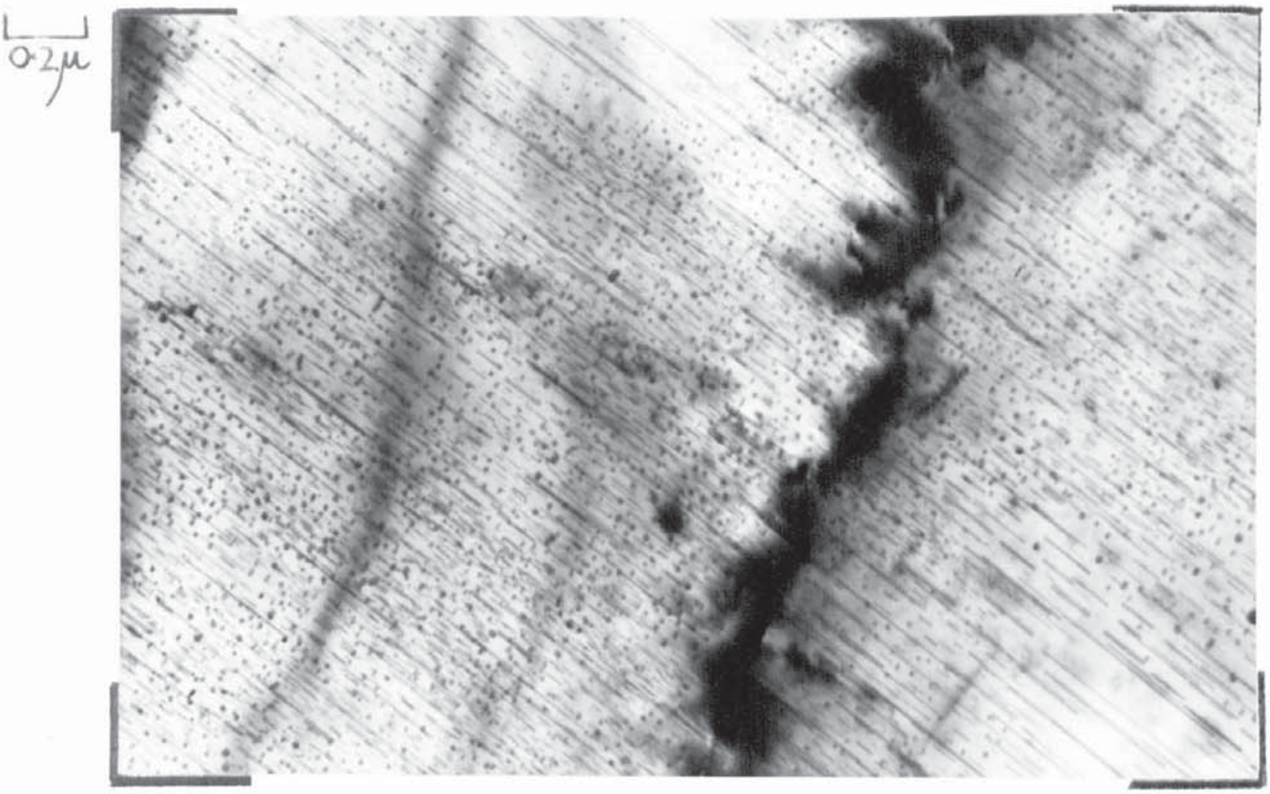

Figure 8.23. ZM61 aged for 2 hours at 180°C..

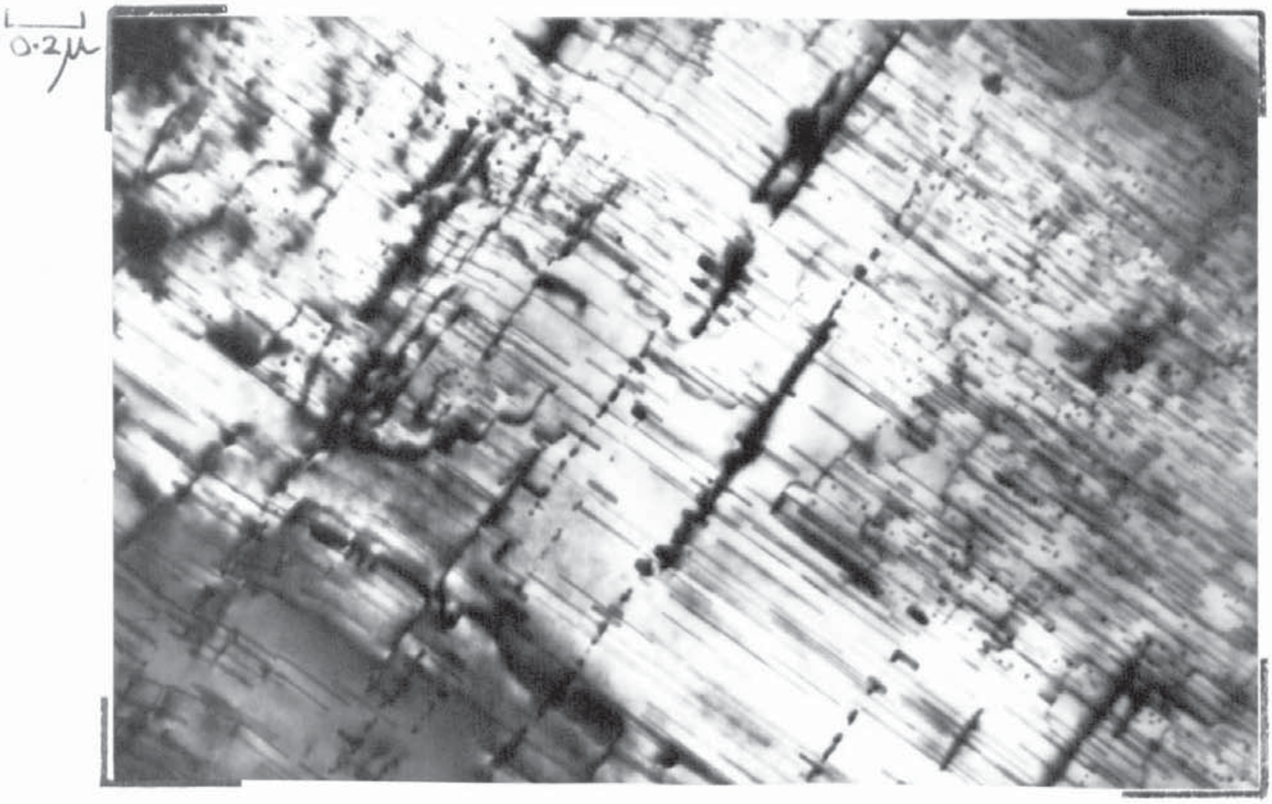

Figure 8.24. As Fig. 8.23.

have exceeded this and there is evidence of heterogeneous nucleation in the form of fine precipitates on the basal planes.

The structure in a foil with the basal planes at about 60° to the electron beam is shown in Fig. 8.25 (1362). The bands of fine precipitation are parallel to the $(11\bar{2}0)$Mg planes and the precipitate is on the $(11\bar{2}0)$ planes. The structure after 24 hours ageing is shown in Fig. 8.26 (1342) in a $(10\bar{1}0)$Mg foil. There is a wide range of needle lengths; 200-7,000A$^{\circ}$ with a more usual range limited to 200-3000A$^{\circ}$. Discs on the (0001)Mg planes are also evident. Fig. 8.27 (1341) is a diffracted beam image formed from the precipitate spot indicated in Fig. 8.28 (1348) which is a selected area diffraction pattern of the foil shown in Fig. 8.26. The d spacings from the numbered precipitate spots are shown in the table below and the diffracted beam used to form the structure shown in Fig. 8.27 is number 3.

Precipitate Spot No.	Interplanar Spacing A$^{\circ}$
1	4.22
2	2.18
3	2.21
4	1.67
5	1.43

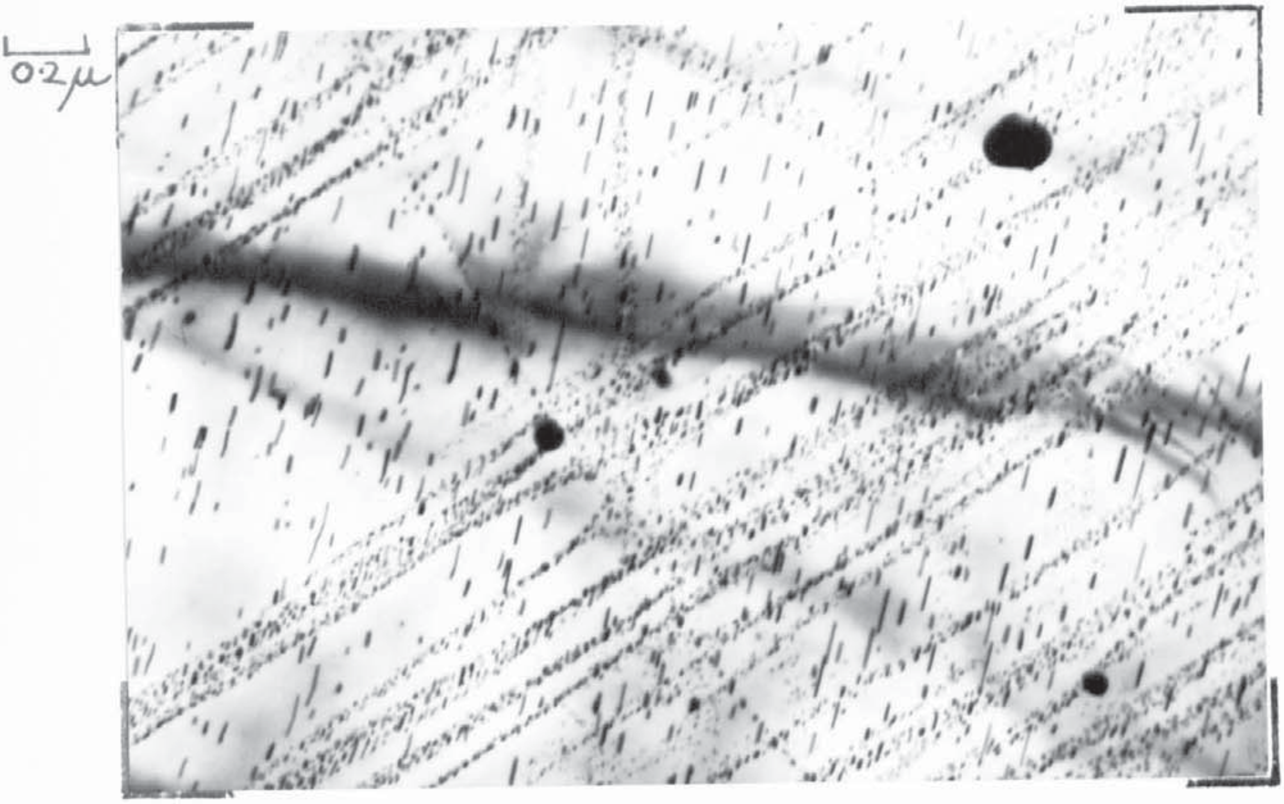

Figure 8.25. Structure after 2 hours at 180°C. (0001)Mg planes at about 60° to the electron beam.

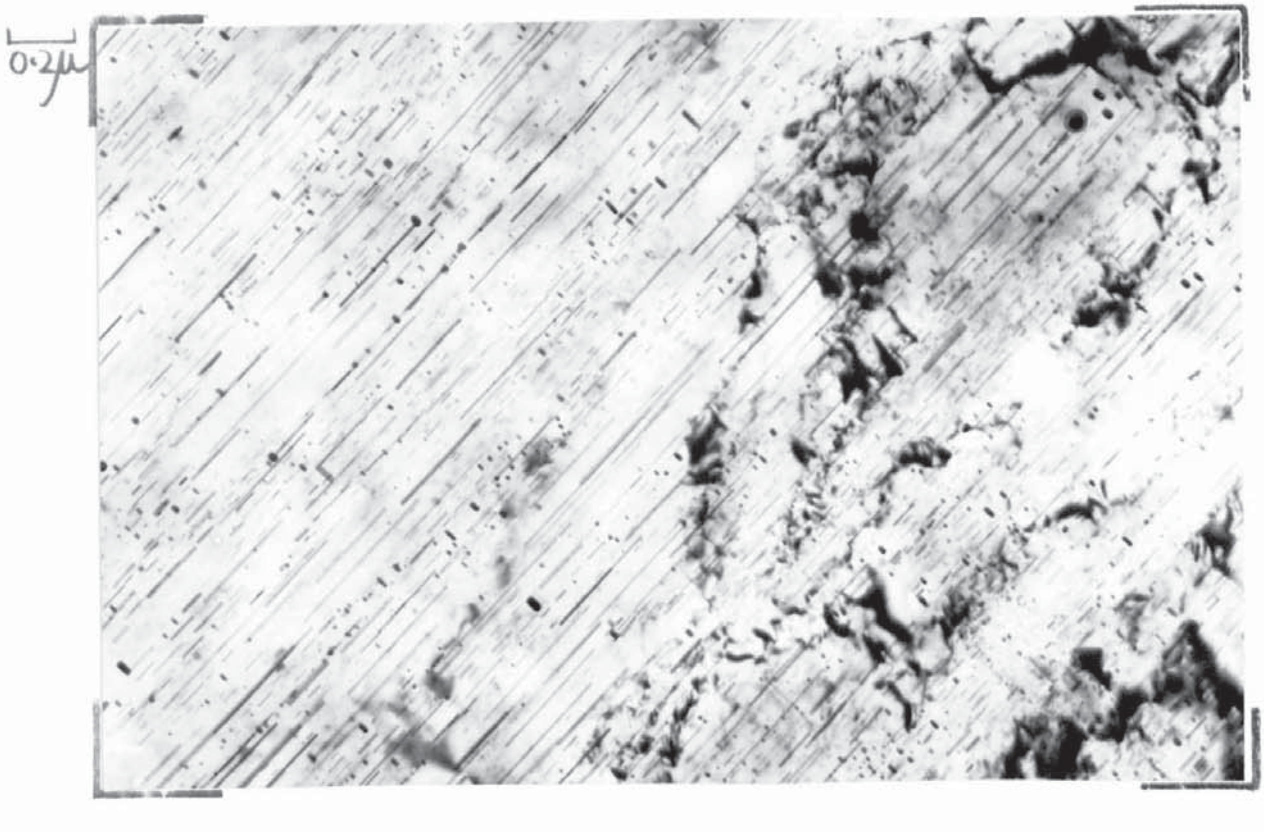

Figure 8.26. ZM61 after ageing for 24 hours at 180°C..

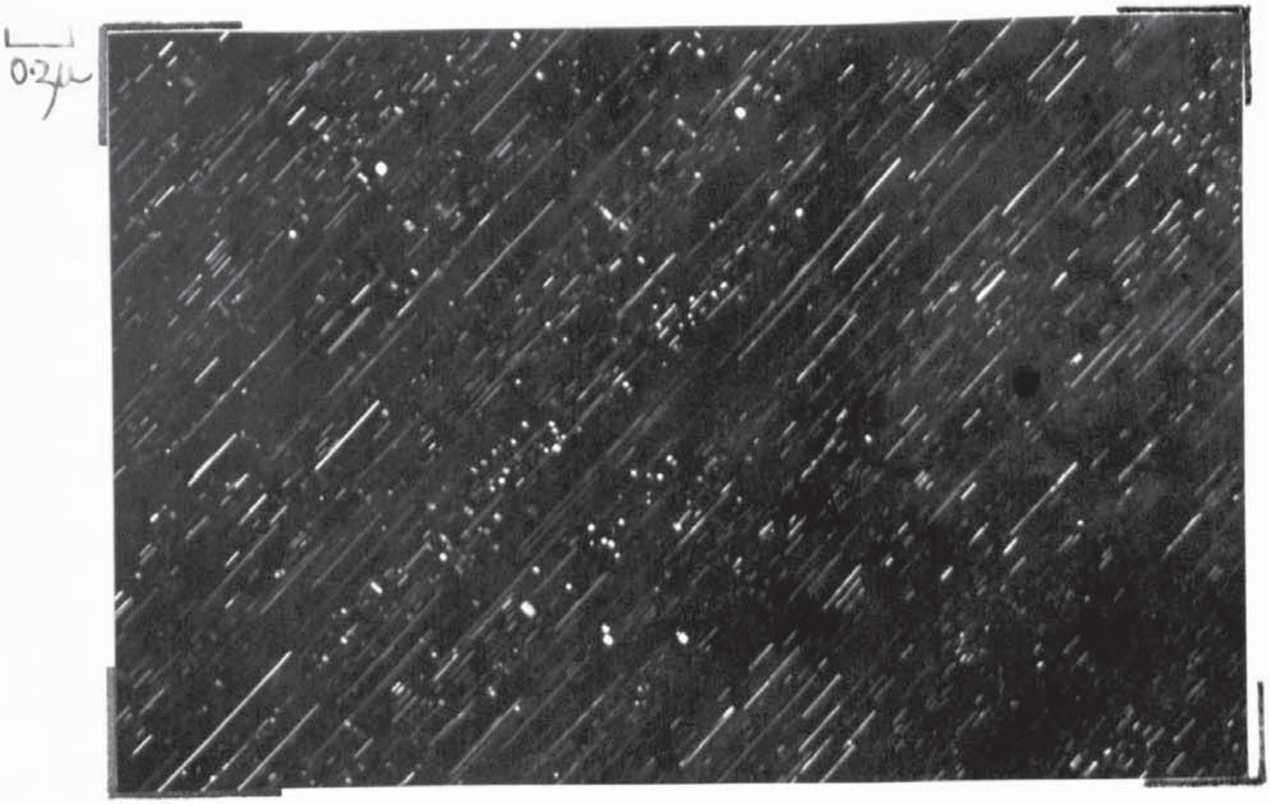

Figure 8.27. Diffracted beam image of area shown in Fig.8.26 using a precipitate beam.

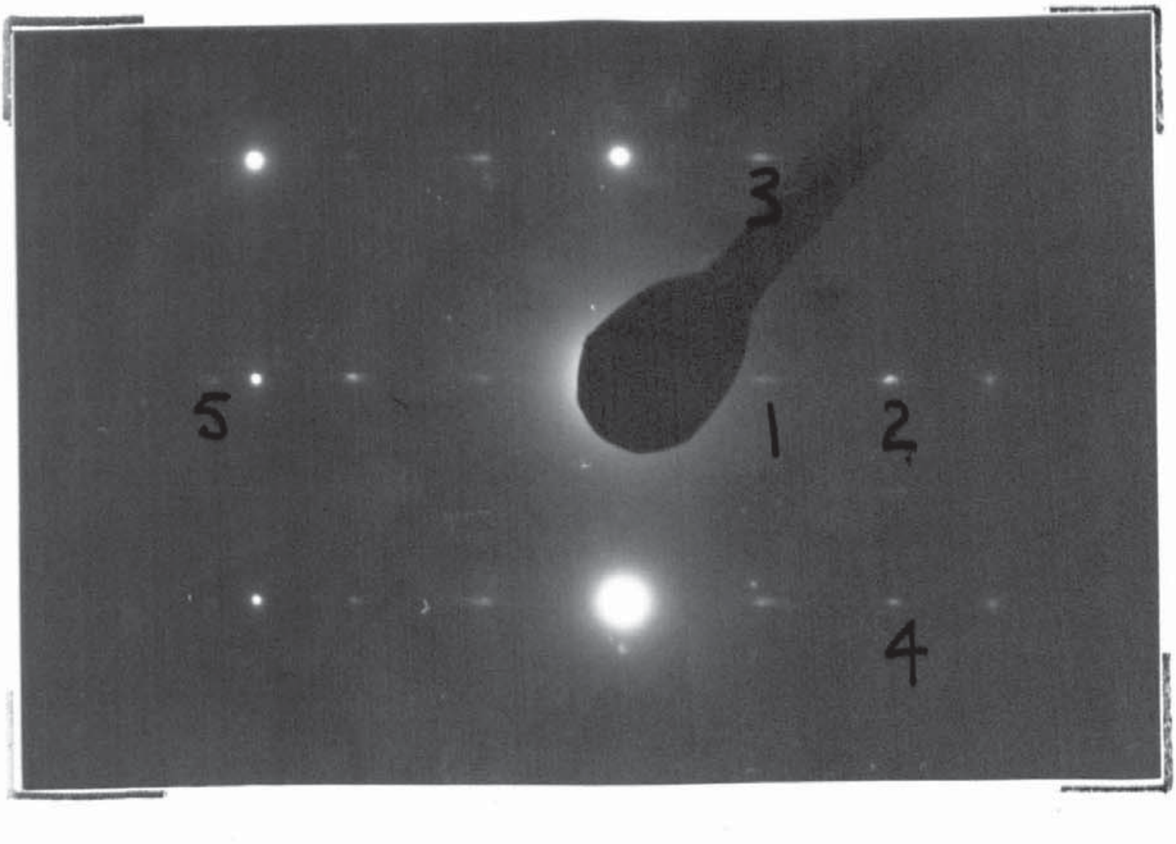

Figure 8.28. Selected area diffraction pattern of area shown in Fig. 8.26.

The most important feature of Fig. 8.27 is that both the needle and disc precipitates are simultaneously imaged from a diffraction spot arising from a spacing of 2.21A$^{\circ}$, indicating that both precipitate orientations are diffracting such that a beam is accepted by the objective aperture.

Fig. 8.29 (1346) and Fig. 8.30 (1345) are again images formed from the undeviated beam and precipitate diffracted beam respectively using conditions as illustrated in Fig. 8.28. It can be seen that needles are present as short as 90A$^{\circ}$ and that the needle labelled A is imaged only along its edges in the diffracted beam image.

Fig. 8.31 (1334) illustrates four matrix orientations resulting from a grain boundary and a defect which crosses the boundary. The orientation at the top left hand corner is almost (0001)Mg and the top right hand is this tilted through approximately 30° about the line defect. The bottom right hand section is close to $(10\bar{1}0)$Mg and the bottom left hand is rotated firstly by about 15° co-planar with the photograph surface and secondly by an unknown amount about an axis perpendicular to the first axis.

A corrosion product from the preparation process at the line defect and extensive precipitation on the grain boundary are evident. Precipitation has not occurred on the line defect and the defect does not cause a linear displacement of the grain

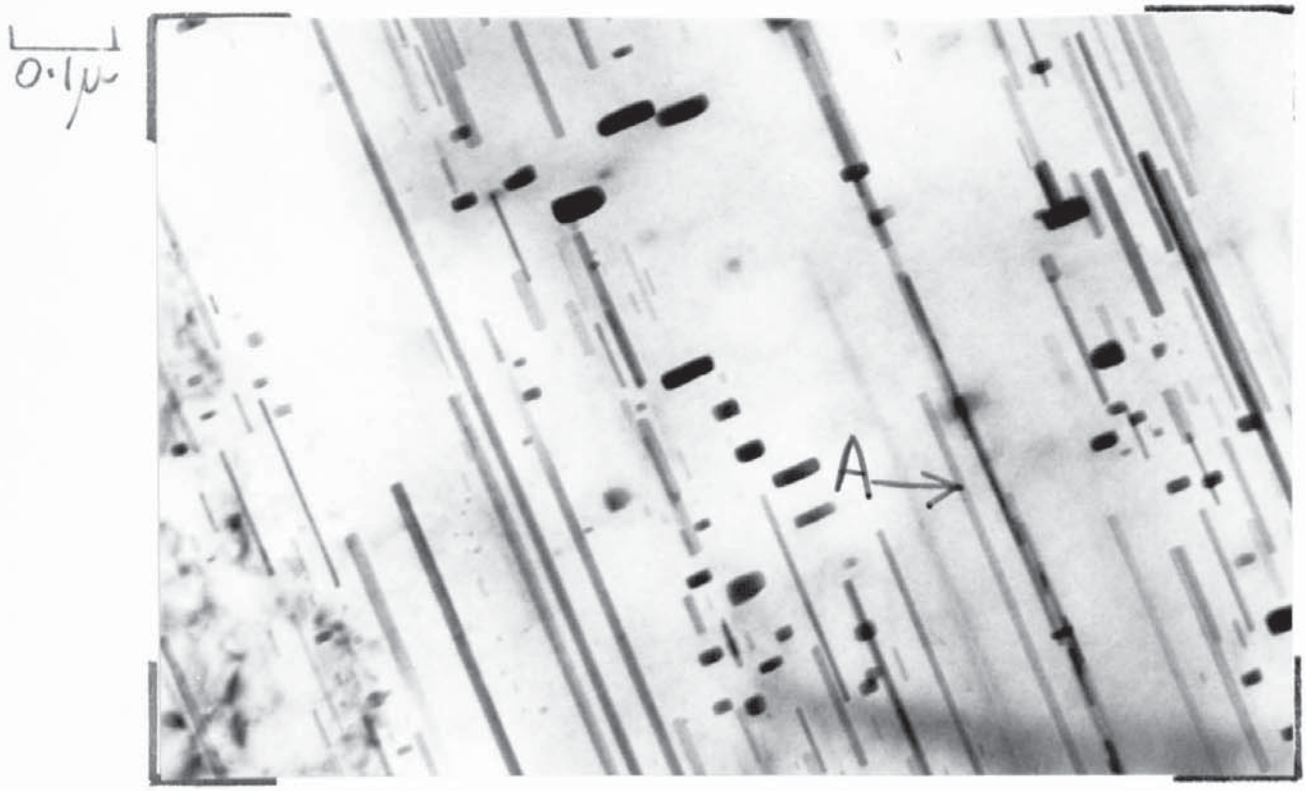

Figure 8.29. Structure after 24 hours at 180°C.

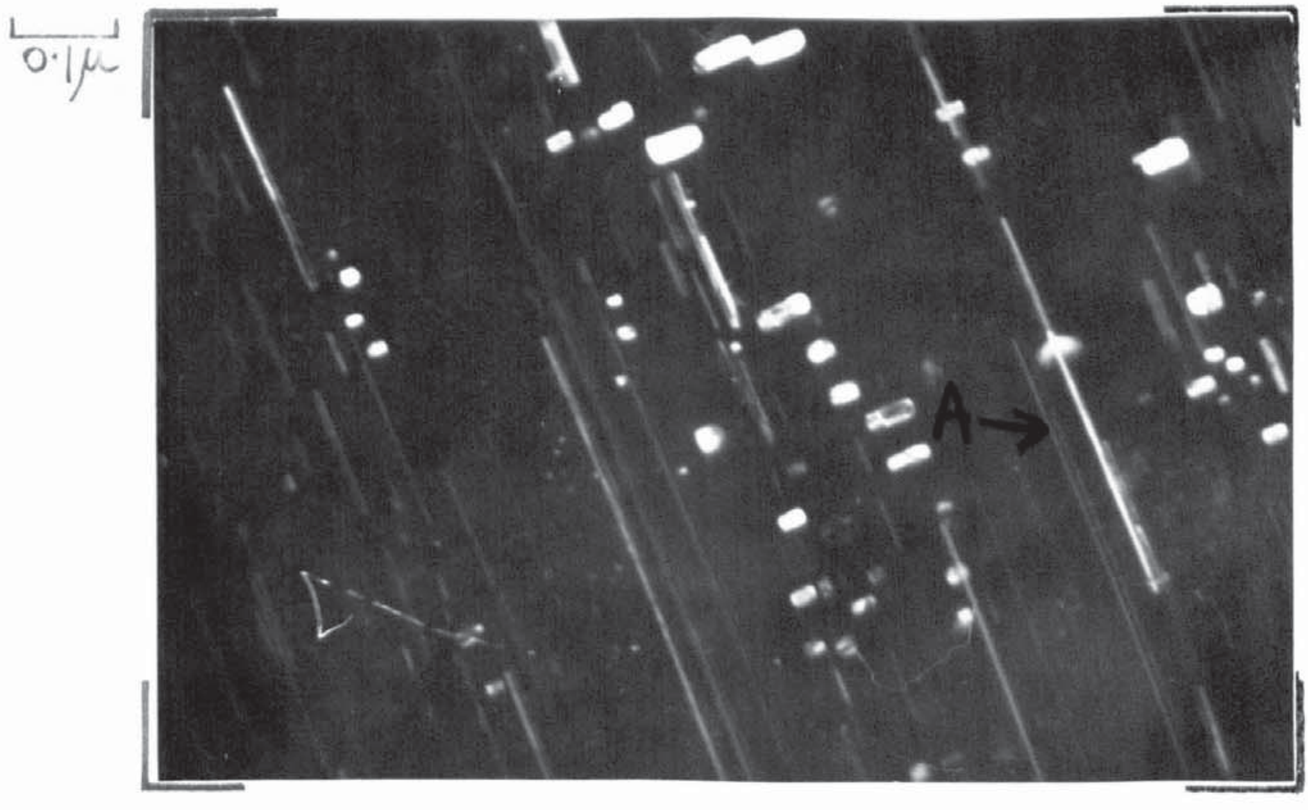

Figure 8.30. Image formed using a precipitate diffracted beam. Diffraction conditions as shown in Fig. 8.28.

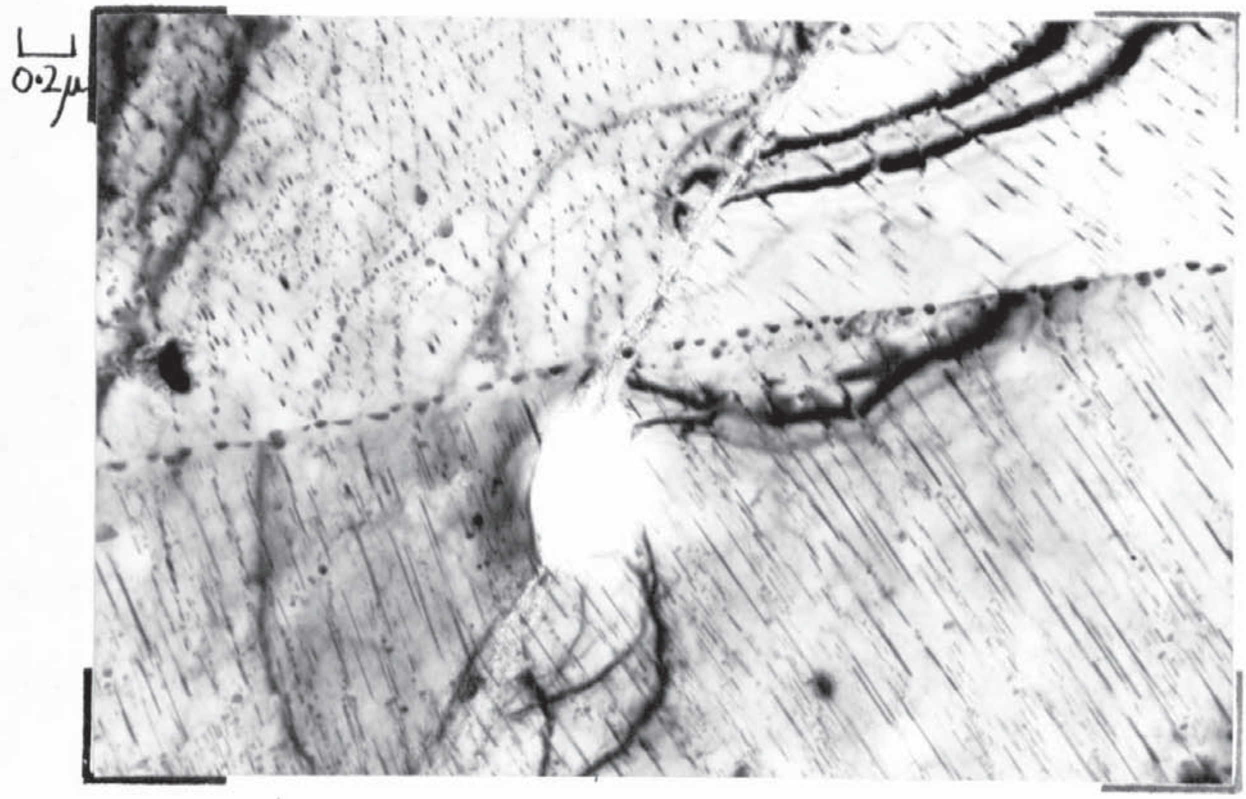

Figure 8.31. ZM61 aged for 24 hours at 180°C..

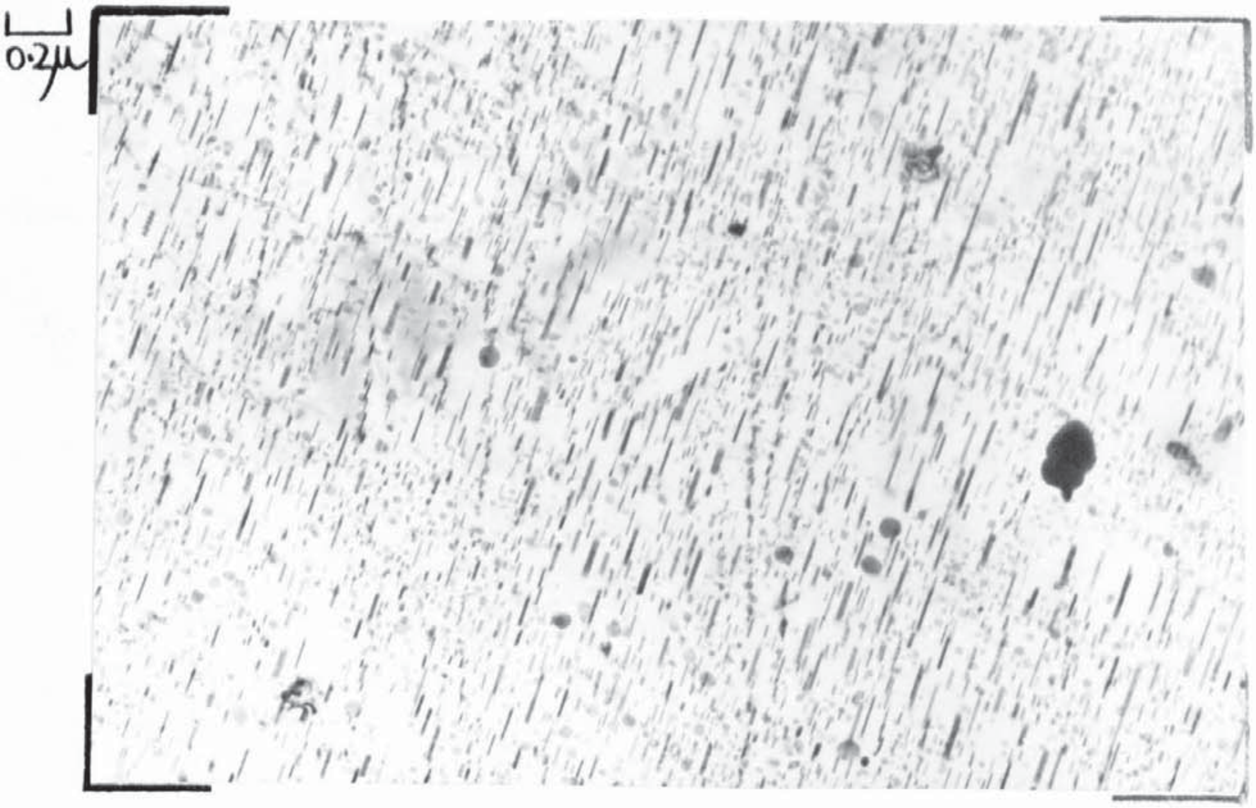

Figure 8.32. Structure after ageing for 24 hours at 210°C..

boundary line; a rotation of about 6° does occur at the defect/grain boundary intersection.

Ageing at 210°C..

The structure after 24 hours ageing at this temperature is shown in Fig. 8.32 (1322) in a foil with the (0001)Mg planes near to 60° to the electron beam. The needle precipitate is severely truncated and some of the needles toward the left of the photograph are showing a fringe contrast. There is copious precipitation of the disc shaped precipitate which has reached a diameter close to 600A°.

Needle lengths up to 14,000A° have been achieved by this thermal treatment, as illustrated in Fig. 8.33(1318) which is of a $(10\bar{1}0)$Mg foil. The precipitates are not very homogeneously distributed and there is a distinct pattern to the distribtution. Areas with long needles are relatively denuded of the disc precipitates whereas when the needle length is reduced to around 500A° there is copious disc precipitation. This structure can be seen to exist in Fig. 8.32. Furthermore the disc precipitates on the basal planes with their faces parallal to, the (0001)Mg planes, are arranged in lines either parallel or perpendicular to these matrix planes. The discs arranged in a row perpendicular to the (0001)Mg planes are generally associated with the areas of long needle precipitate or to the edge of the fine precipitate areas.

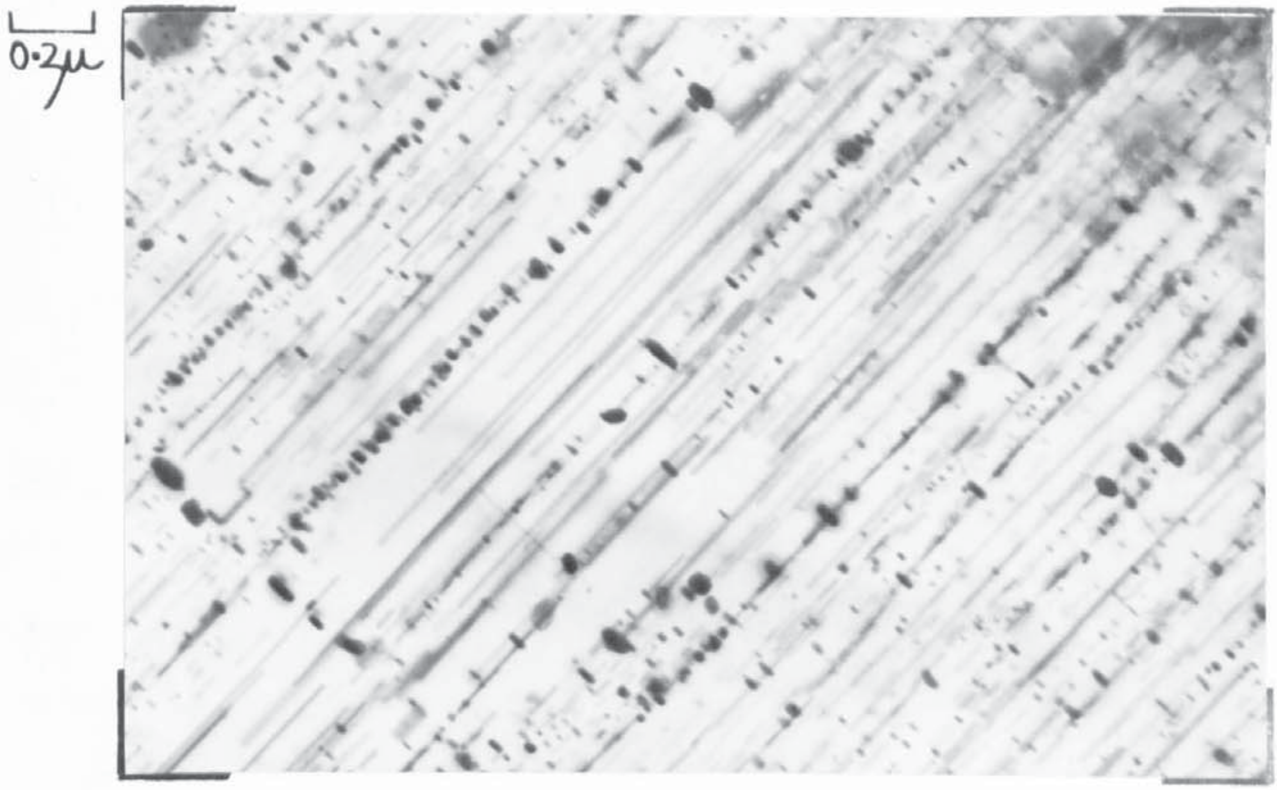

Figure 8.33. As Fig. 8.32 showing the structure in a $(10\bar{1}0)$Mg foil.

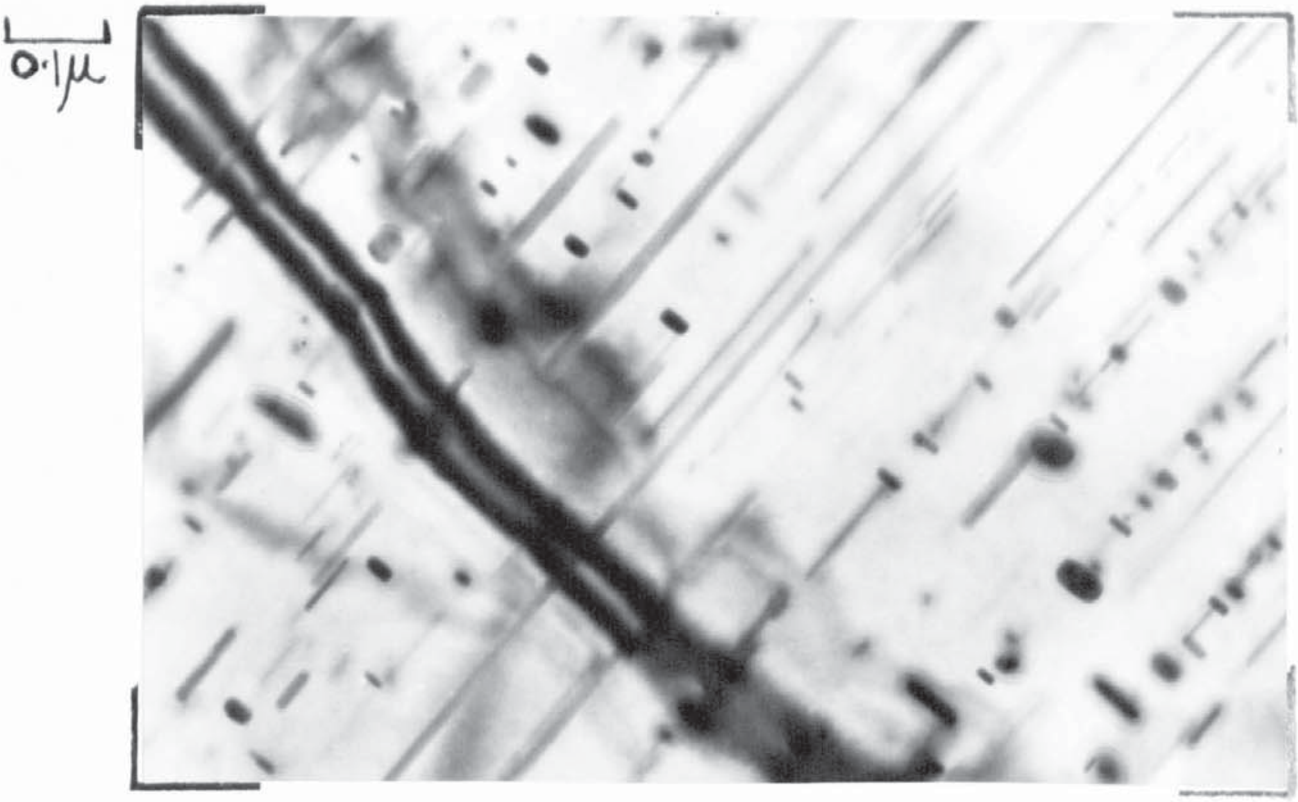

Figure 8.34. As Fig. 8.33.

Fig. 8.34 (1310) shows the structure within a 'band' of long needles. The diffraction pattern of this area is shown in Fig. 8.35 (1311) and it is of the $(10\bar{1}0)$Mg foil plane type. There are two precipitate patterns, both formed on a rectangular cross grid, one with the shorter side parallel to and one with the longer side parallel to the basal planes of the matrix. The patterns are 'streaked' in orthogonal directions, which provides a method of determining their origin. The vertically streaked pattern is derived from the disc precipitate and the horizontally streaked one from the needle precipitate.

The vertically streaked pattern could be from a $[11\bar{2}0]$ axis of a C.P.H. unit cell based on the $MgZn_2$ unit cell. It could not be a $[10\bar{1}0]$ axis because the spot labelled X would have to be $(11\bar{2}3)$. There is no diffracted beam when h + 2k is a multiple of 3 and l is odd and it is not likely to arise as a result of double diffraction[2].

Assuming a $[11\bar{2}0]$ axis then the spacings and reflections from this C.P.H. unit cell are related as shown in the following table:-

Interplanar Spacing A°	Reflection (h k i l)
8.75	0001
4.58	$10\bar{1}0$
4.12	$10\bar{1}1$
2.39	$10\bar{1}3$

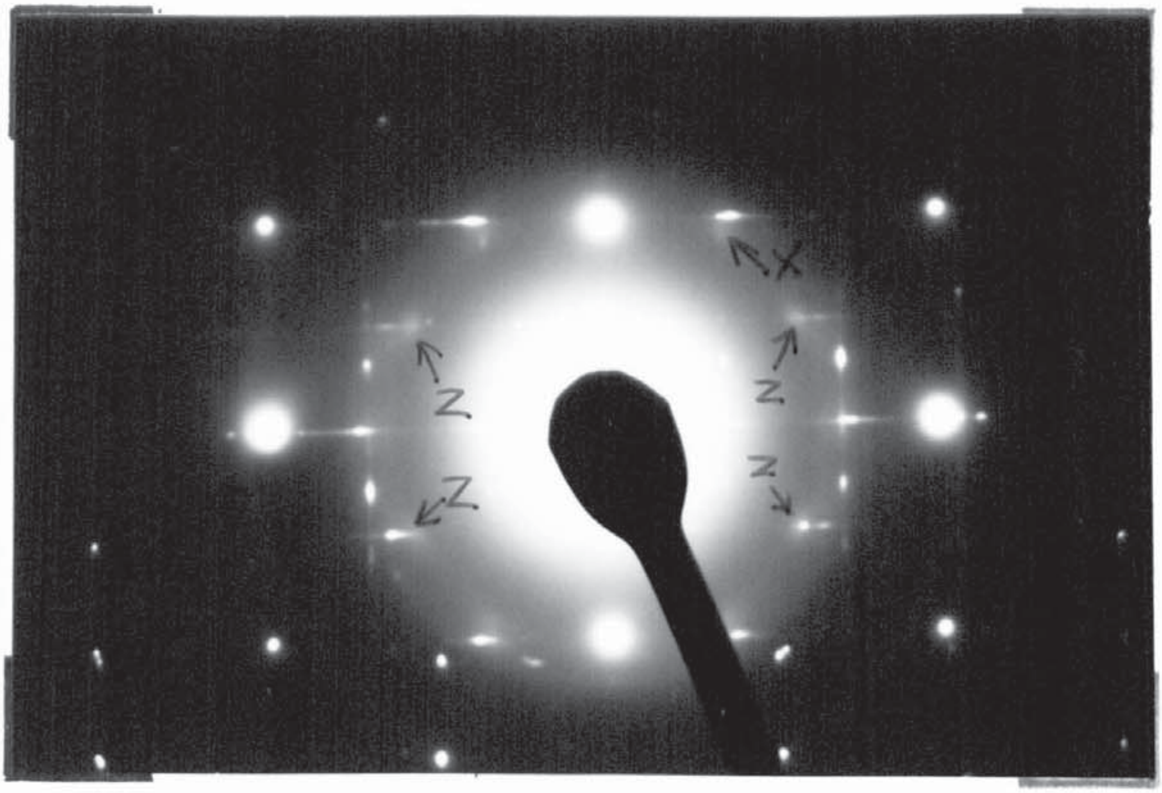

Figure 8.35. Selected area diffraction pattern of structure shown in Fig. 8.34.

Figure 8.36. ZM61 aged for 24 hours at 210°C.

Considering the precipitate pattern with horizontal streaks, the pattern from the needles. This could be a $(10\bar{1}0)$ axis of the same unit cell of the first precipitate pattern. The interplanar spacings from this second pattern and the possible reflections would then be:-

Interplanar Spacing A°	Reflection (hkil)
4.35	0002
2.6	$11\bar{2}0$
2.22	$11\bar{2}2$

The orientation relationship between these precipitates and the matrix are as follows:-

for the discs $(10\bar{1}0)$ Disc // $(11\bar{2}0)$Mg and

(0001) Disc // (0001)Mg

and for the needles

(0001) Needle // $(11\bar{2}0)$Mg and

$(11\bar{2}0)$ Needle // (0001)Mg.

These are identical to those published by Gallot[3] for $MgZn_2^2$ and $MgZn_2^1$ respectively. The essential difference is the increase in the c spacing of the precipitates in this ternary alloy. The spots labelled Z are possibly from the needle precipitate rotated by 60°, to give the same orientation relationship on the other two $(11\bar{2}0)$ type magnesium planes.

The structure within a band of short needles is shown in

Fig. 8.36 (1303) and the selected area diffraction pattern is illustrated in Fig. 8.37 (1305). The needle length is 200-4000A° and the disc precipitate has reached about 150-700A° in diameter. The diffraction pattern is of a $(10\bar{1}0)$Mg foil plane and a series of spots from an interplanar spacing of 13.0A° parallel to the (0001)Mg planes is evident.

These planes are arranged such that every fifth (0002)Mg plane at 2.6A° coincides with a precipitate plane at 13 A°. There are three precipitates present in the areas illustrated in Figs. 8.32 and 8.33. and not just two.

Direct Quenching Experiments.

The direct quenching experiments used to determine the metastable solvus for this alloy were identical to those used for the Z6 alloy.

The structure after 96 hours at 90°C. after direct quenching to this temperature is shown in Fig. 8.38 (1006), from a foil with an orientation close to (0001)Mg. There is evidence of heterogeneous nucleation, which is arrowed. Fig. 8.38 is directly comparable with Fig. 8.19, which is of the alloy quenched to room temperature prior to ageing at 90°C.. The difference between these two structures is insignificant and any difference could be related to foil thickness effects.

Direct quenching to and ageing at 120°C. for 264 hours

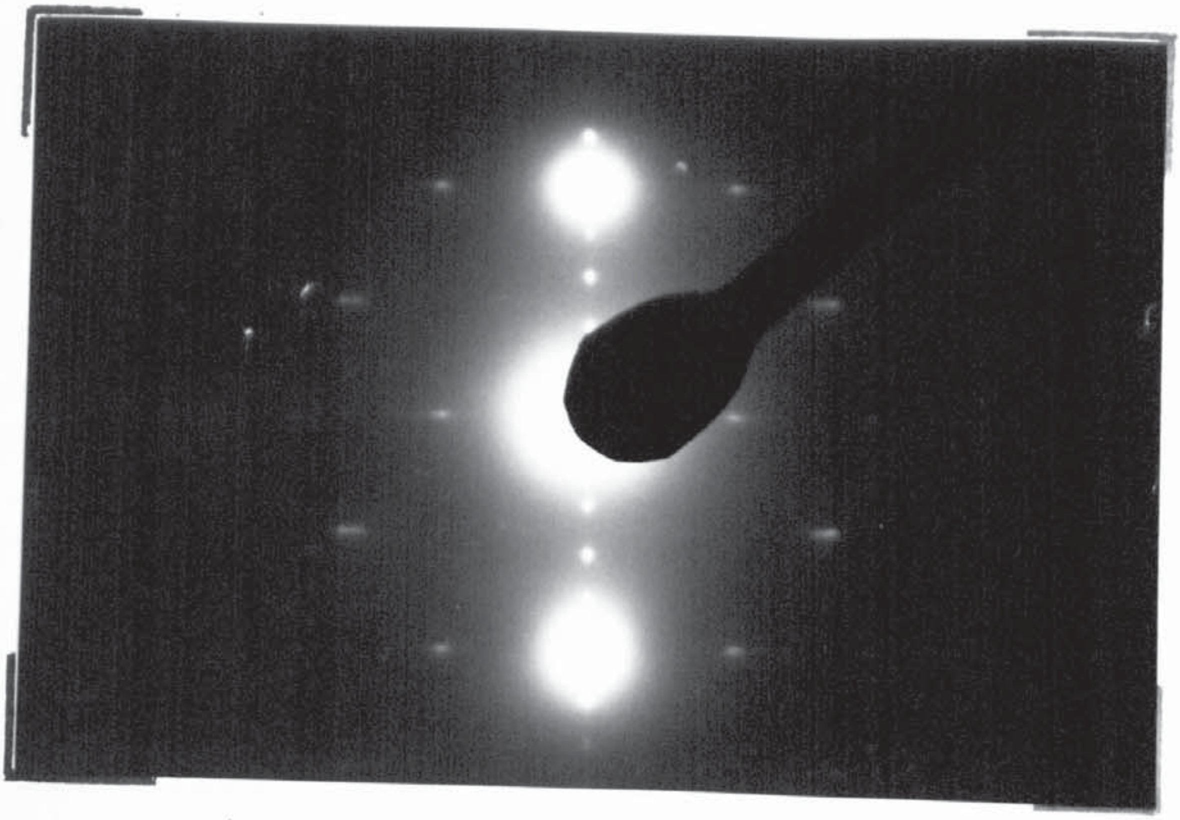

Figure 8.37. Selected area diffraction pattern of area shown in Fig. 8.36.

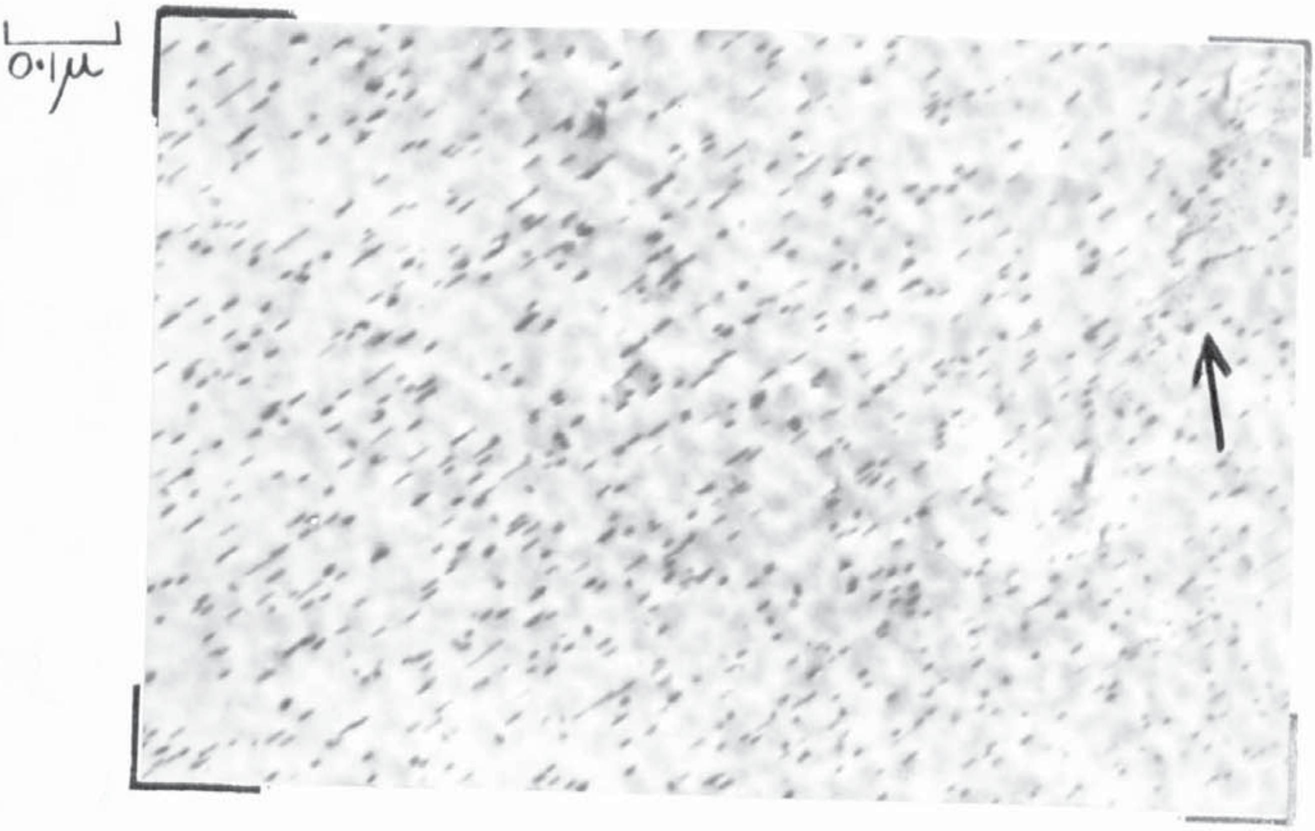

Figure 8.38. ZM61 aged for 96 hours at 90°C. after directly quenching to the ageing temperature.

produces the structure shown in Fig. 8.39 (1249) which is of a $(10\bar{1}0)$Mg foil. This is directly comparable to Fig. 8.22, which is the structure after quenching to room temperature and ageing at 120°C. for 264 hours. Again there is no significant difference between these two structures. The metastable solvus is therefore above 120°C. for this ternary alloy.

Fig. 8.40 shows the change in hardness with time at various ageing temperatures after naturally ageing for $4\frac{1}{2}$ years at room temperature. The structure prior to the artificial ageing has been illustrated in Fig. 8.8 and Fig. 8.9 and the line of no contrast from the G.P. zones was measured as 60-80 A° long by 25-40 A° wide. Assuming that this is a sphere 30 A° in diameter, it is equal to that of the zones in Z6 and about one third of that in Al-Zn alloys.[44]

From Fig. 8.40 it is evident that the metastable phase boundary (or critical temperature) is greater than 200°C or that 30 A° is above the critical zone size stable at this temperature.

Double Ageing.

The beneficial effect of the delay between solution treatment and ageing on the rate of ageing and maximum tensile properties in this alloy has been demonstrated.[20] The naturally aged sample, the structure of which has been shown in Figs. 8.8 and 8.9, was used to examine the effect of a second higher temperature

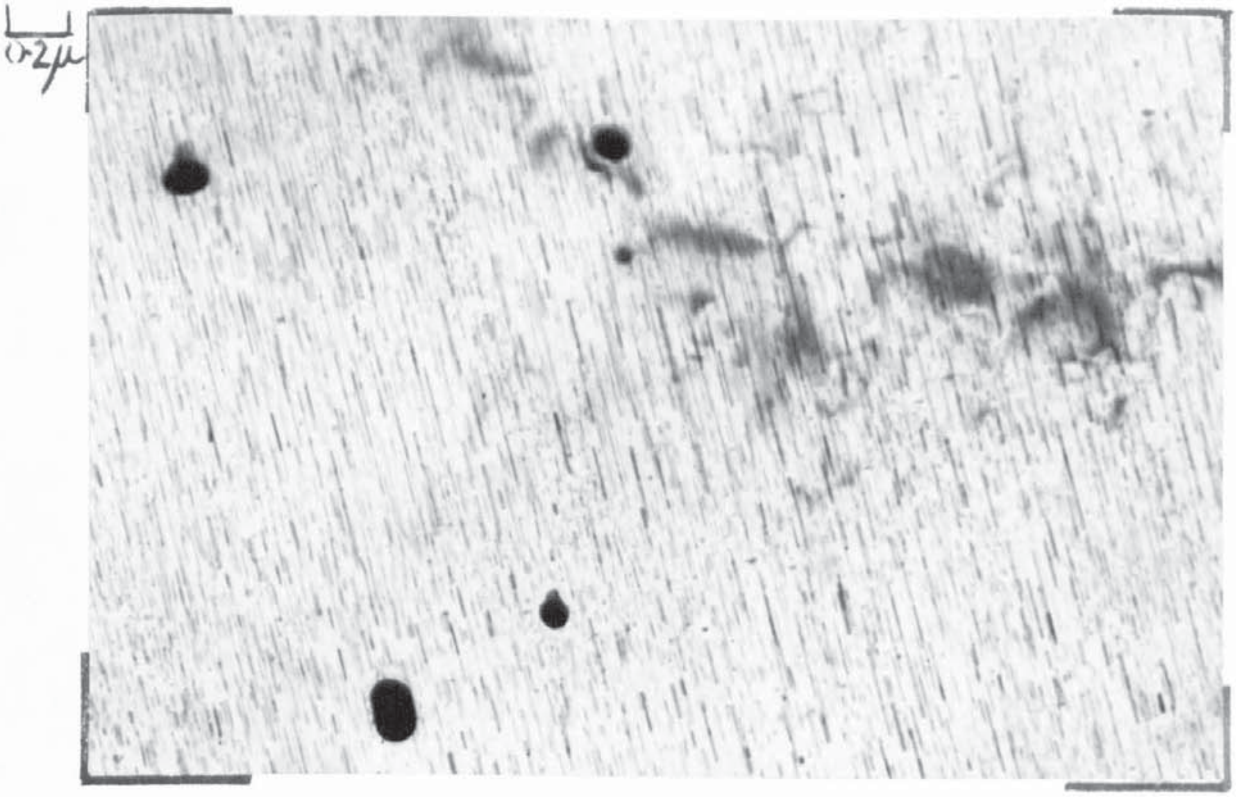

Figure 8.39. Structure after 264 hours at 120°C. after quenching directly to the ageing temperature.

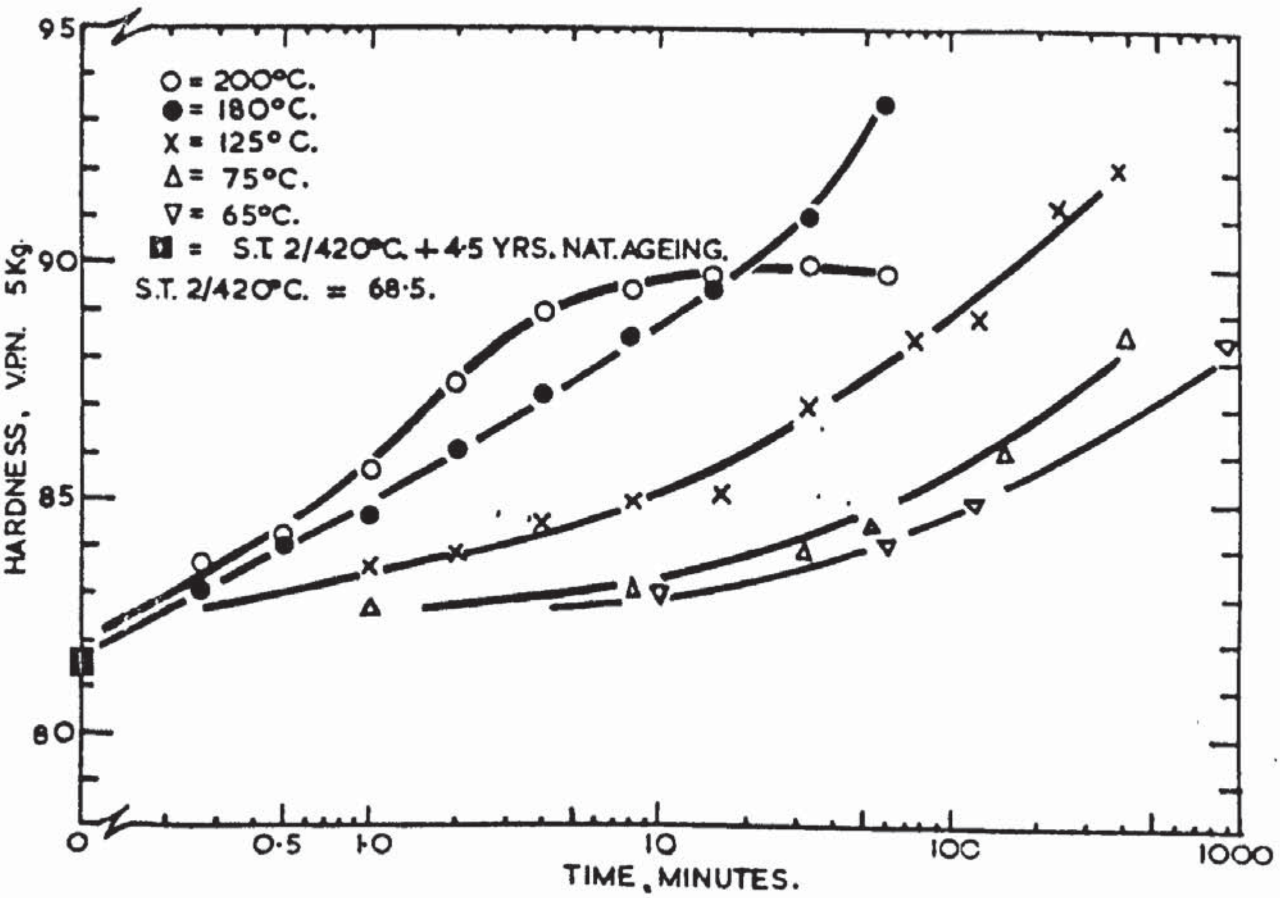

Figure 8.40. Change in hardness on artificially ageing samples naturally aged for 54 months.

treatment on the structure.

The structure after artificially ageing this sample for 1 hour at 180°C is shown in Fig. 8.41 (1508) in a (10$\bar{1}$0)Mg foil. A grain boundary with an asymmetrical precipitate free zone, can be seen to the left of the photograph. The line of no contrast is still 60-80 A° long by 25-40A° wide and the needle precipitate has reached 100-300A° in length. Fig. 8.42 (1506) shows the generally very short needles, 100-300A° long, with a few that have grown to 500-700A° in length and perhaps a little wider than the others.

The two component matrix contrast from the zones is still present as illustrated in Fig. 8.41; these have either dissolved and reformed on heating to 180°C or they have grown at room temperature to a size which is stable at 180°C..

Attempts were made to observe the growth of the zones by examining an area of a foil from the naturally aged sample and then re-examining the same area after the artificial ageing treatment (carried out in an oil bath with no contact with the oil). Beam heating was also attempted, within the microscope. Both of these experiments were unsuccessful. The results from these experiments are illustrated in Figs. 8.43 (1533) and 8.44 (1532) for the specimen aged in the oil bath, and Figs. 8.45 (1205) and 8.46 (1214) for the beam heating experiment. Figs.

0·1μ

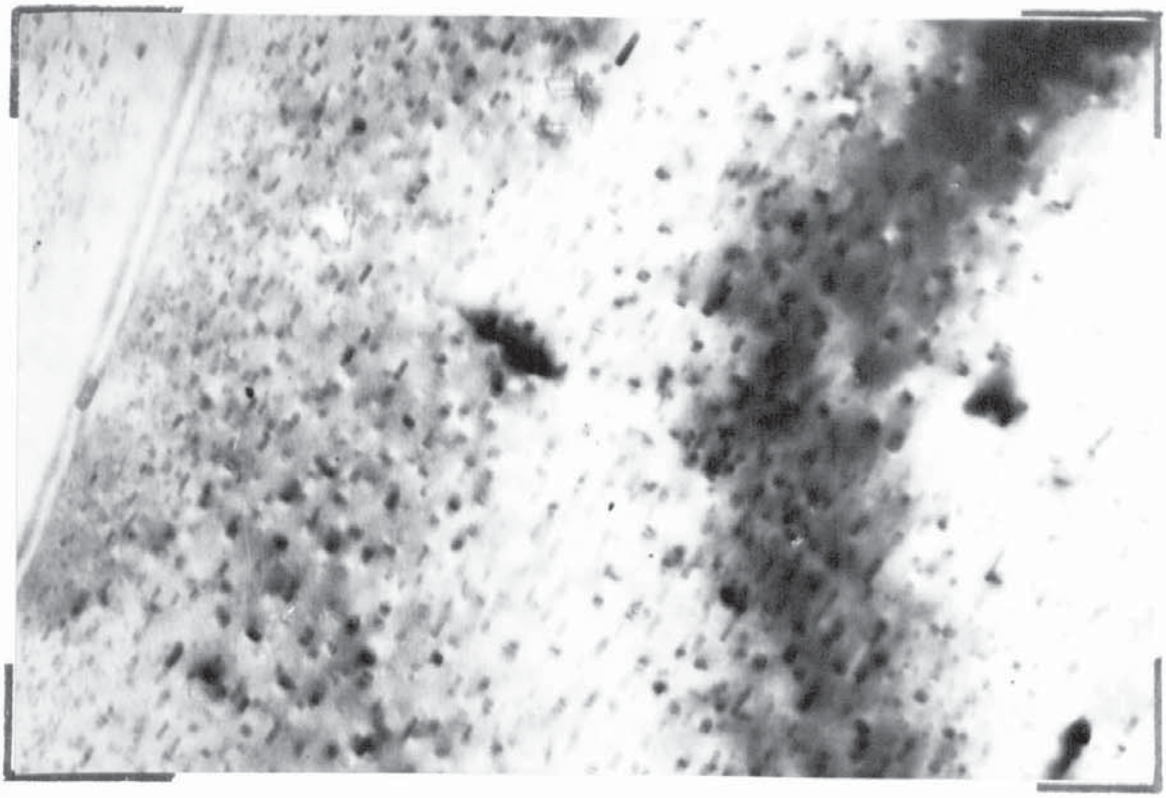

Figure 8.41. Structure after 54 months at room temperature followed by 1 hour at 180°C..

0·1μ

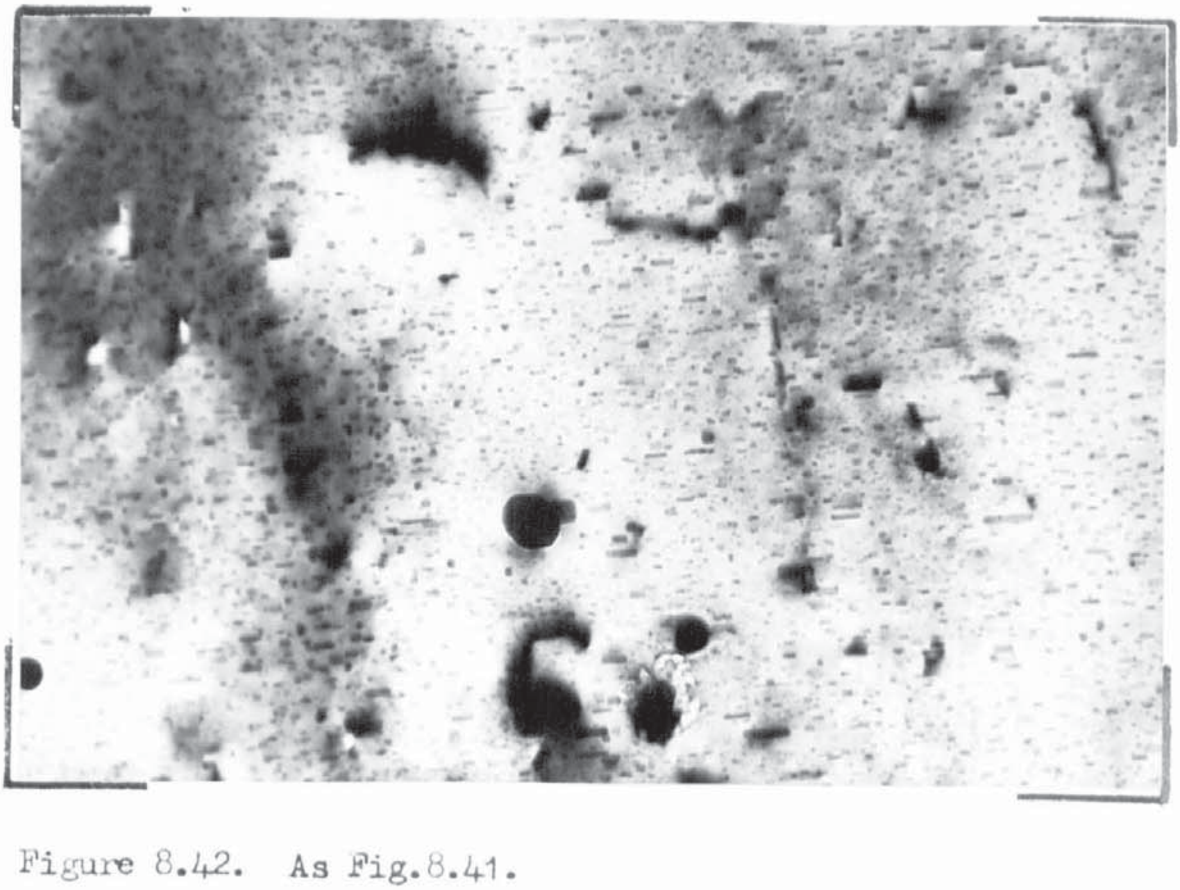

Figure 8.42. As Fig.8.41.

8.43 and 8.44, which are images from the undeviated and precipitate diffracted beams respectively, show the structure after ageing for 1 hour at 180°C.. This structure results from a nucleation and/ or growth of the precipitates at the surfaces of the foil and this structure should be compared with Figs. 8.41 and 8.42 which show the structure after ageing for the same time but in a bulk sample.

Difficulty was experienced in controlling the heating from the electron beam and invariably the sample was overheated and the structures produced bore no relation to any structures observed in samples conventionally aged. Two examples of this structure are shown in Figs. 8.45 and 46 and are undoubtedly the structure from a metal/metal oxide reaction. A structure similar to this has been reported by Douglass and Vanlanduyt[46] in titanium alloys.

The structure after ageing for 24 hours at 90°C. followed by 16 hours at 180°C is shown in Figs. 8.47 (351) and 8.48 (488). The needle length is about 300-1000A° with occasionally much longer and thicker ones, shown particularly in Fig. 8.48. The disc precipitate perpendicular to the needles is generally about 100A° in diamter and in some instances in Fig. 8.47, they could be the needle precipitate at an aspect ratio of unity. These two illustrations are directly comparable with Fig. 8.29, in terms of magnification and matrix zone axis, which was of a sample aged for 16 hours at 180°C. only. The effect of the

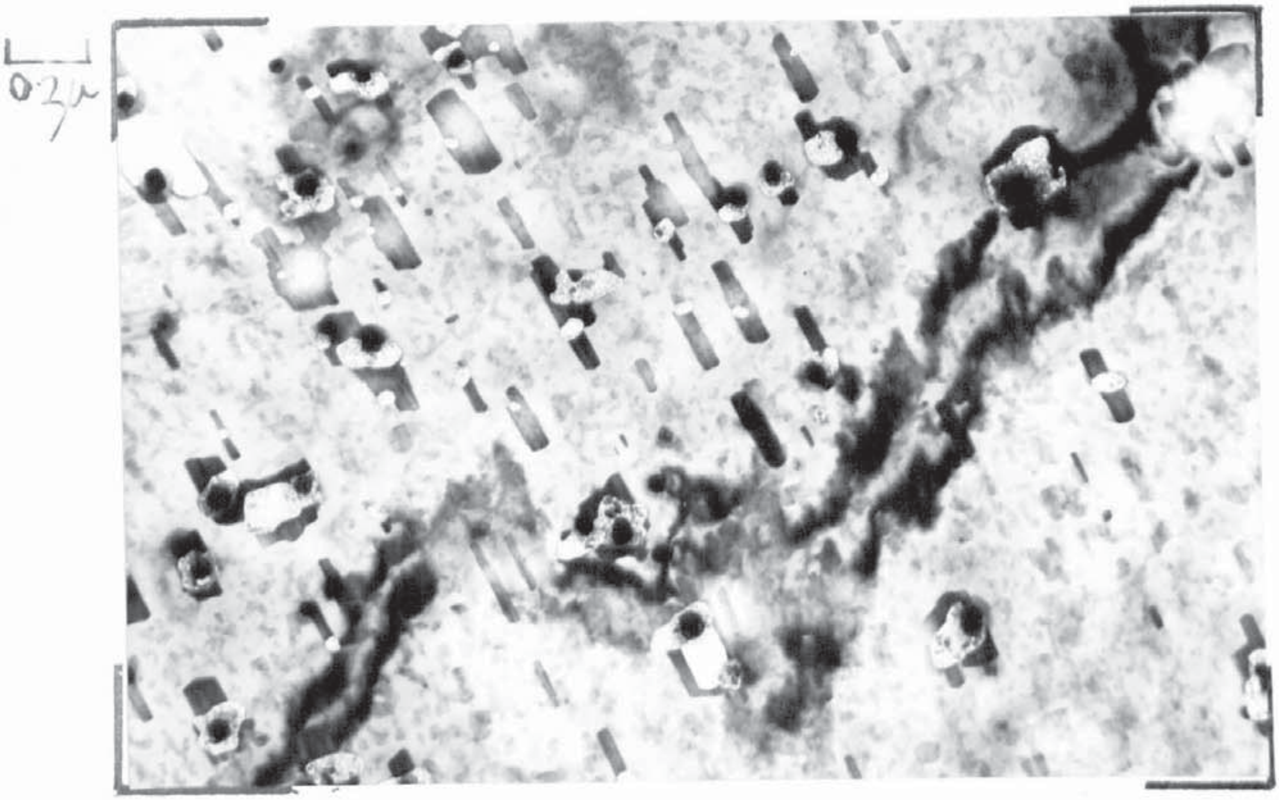

Figure 8.43. Structure after 54 months at room temperature followed by 1 hour at 180°C. Artificially aged as a foil.

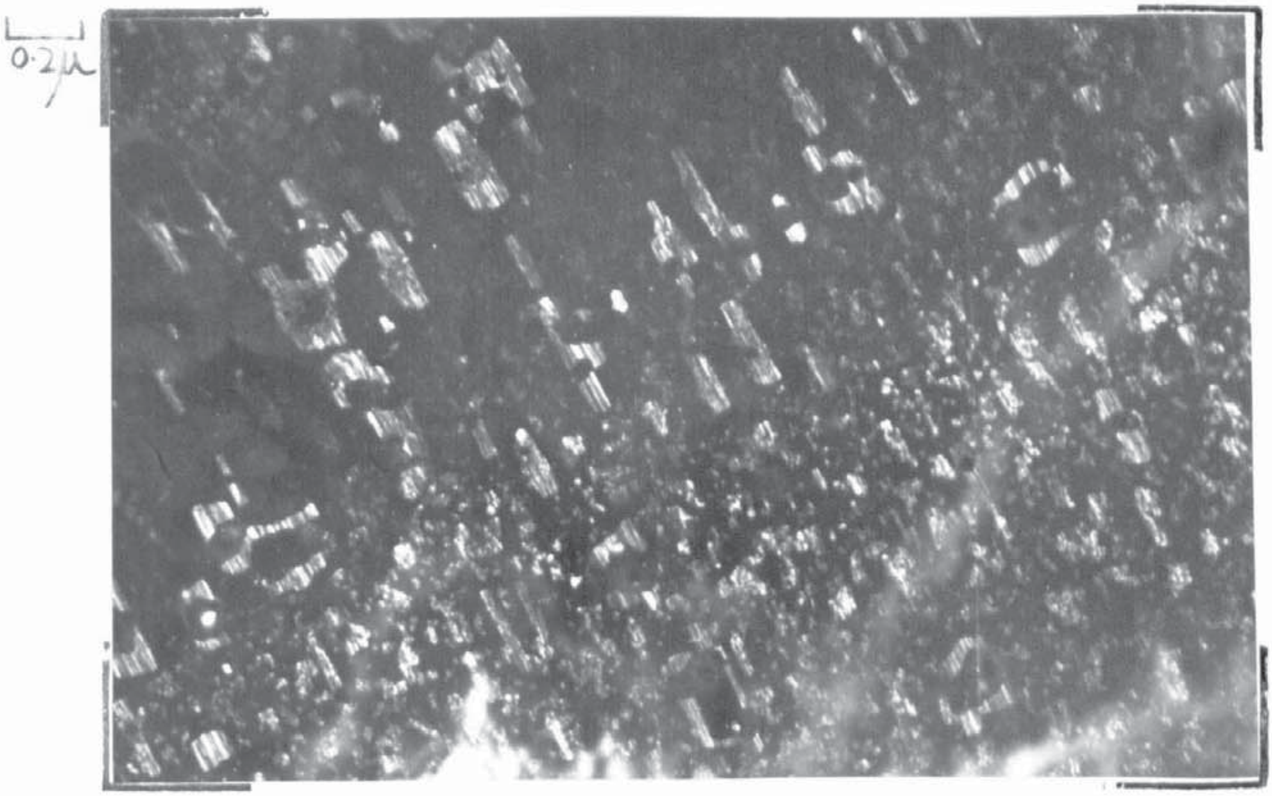

Figure 8.44. Area shown in Fig. 8.43. imaged using a precipitate diffracted beam.

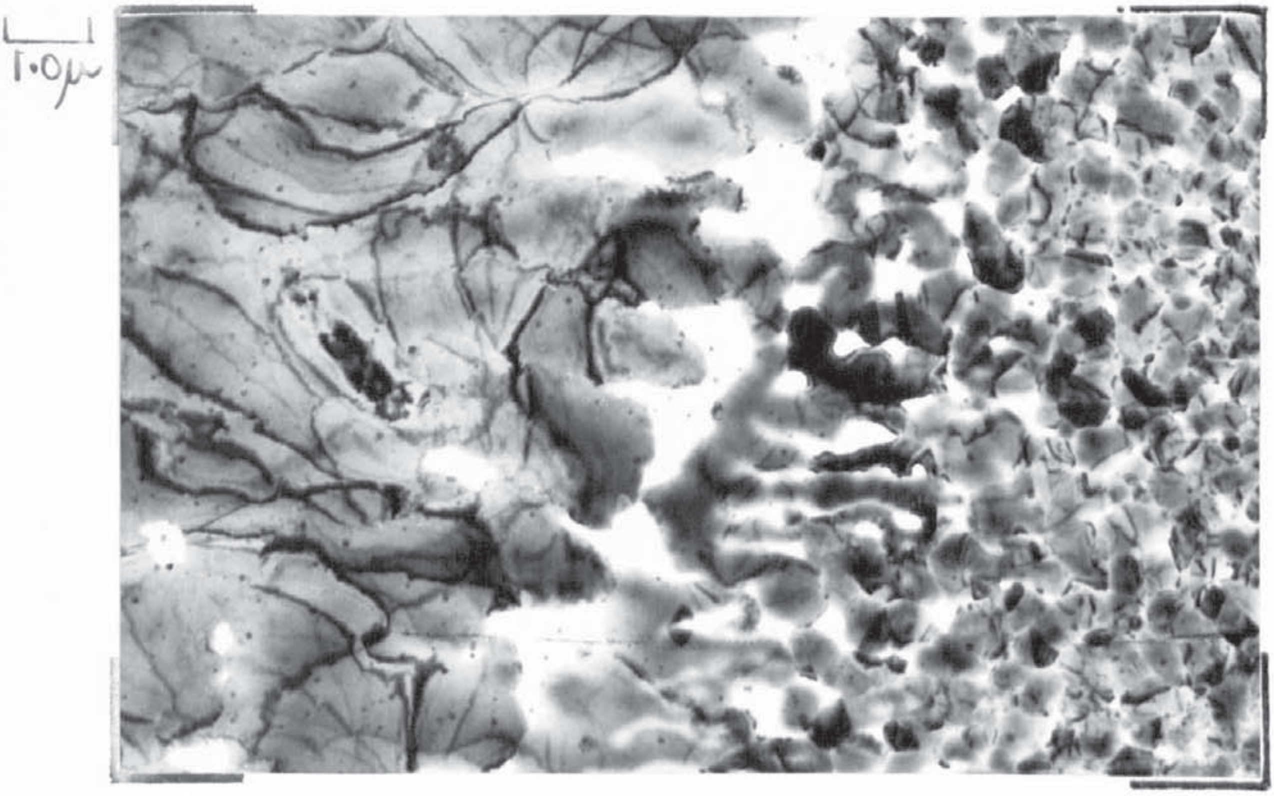

Figure 8.45. Structure after 54 months natural ageing followed by beam heating in the microscope.

Figure 8.46. As Fig. 8.45.

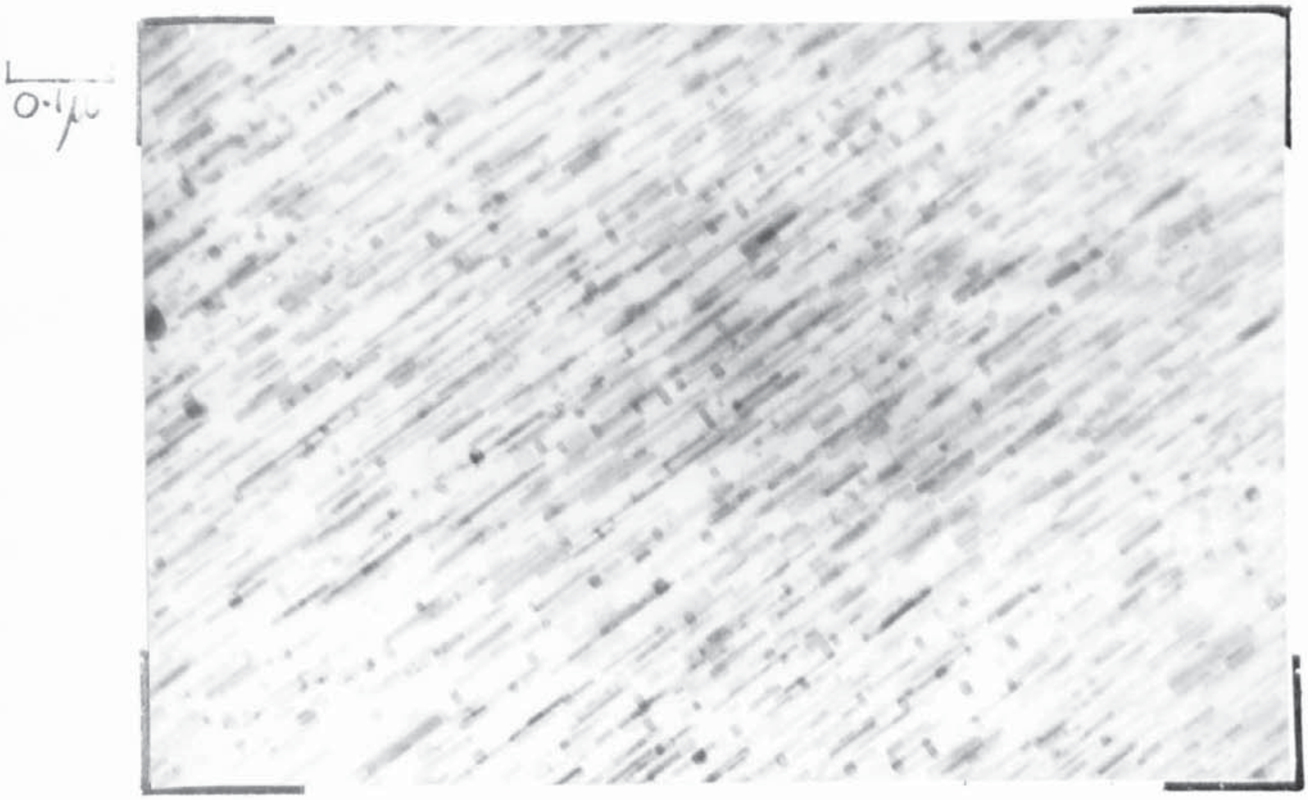

Figure 8.47. ZM61 aged for 24 hours at 90°C. followed by 16 hours at 180°C.

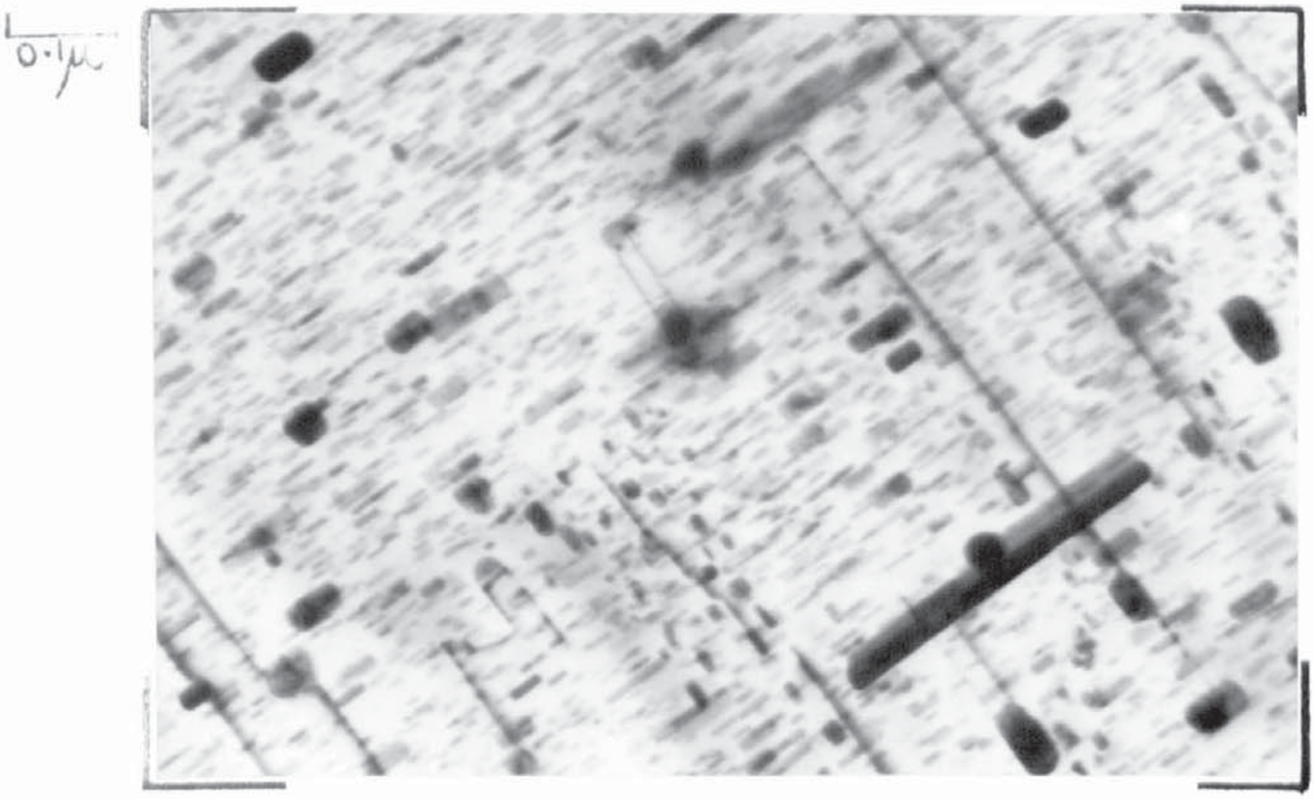

Figure 8.48. As Fig. 8.47.

double ageing treatment is immediately apparent.

Analysis of the G.P. zone Strain Fields.

Figs. 8.49 (1176) and 8.50 (1177) show the image from the undeviated and an (0002)Mg diffracted beam respectively. The direction of the operating reciprocal lattice vector is indicated. Three particles, two labelled A and one labelled B show that the in situ strain is +ve and -ve respectively. It is considered that the apparent size and asymmetry of these strain fields, which are from discs, are so dependent on the precise angle between the electron beam and the disc (which ideally should be 0°) that little reliance can be placed on this analysis.

Section 5 - Magnesium - 0.8% Manganese - Mn 80.

The precipitate in this alloy system is in the form of ribbons parallel to the $(10\bar{1}0)$Mg and perpendicular to the basal planes. The precipitating phase is α Mn.. The structures presented by Byrne[13] who examined an alloy containing 1.33% Mn are such that no confusion between α Mn and any of the precipitates observed in Z6, ZW6 and ZM61, can exist. The structures reported were obtained after ageing at fairly high temperatures, about 300°C. for times up to 16 hours. No results were presented showing the early stages of precipitation that might be expected at the lower temperatures and times used in the present investigation.

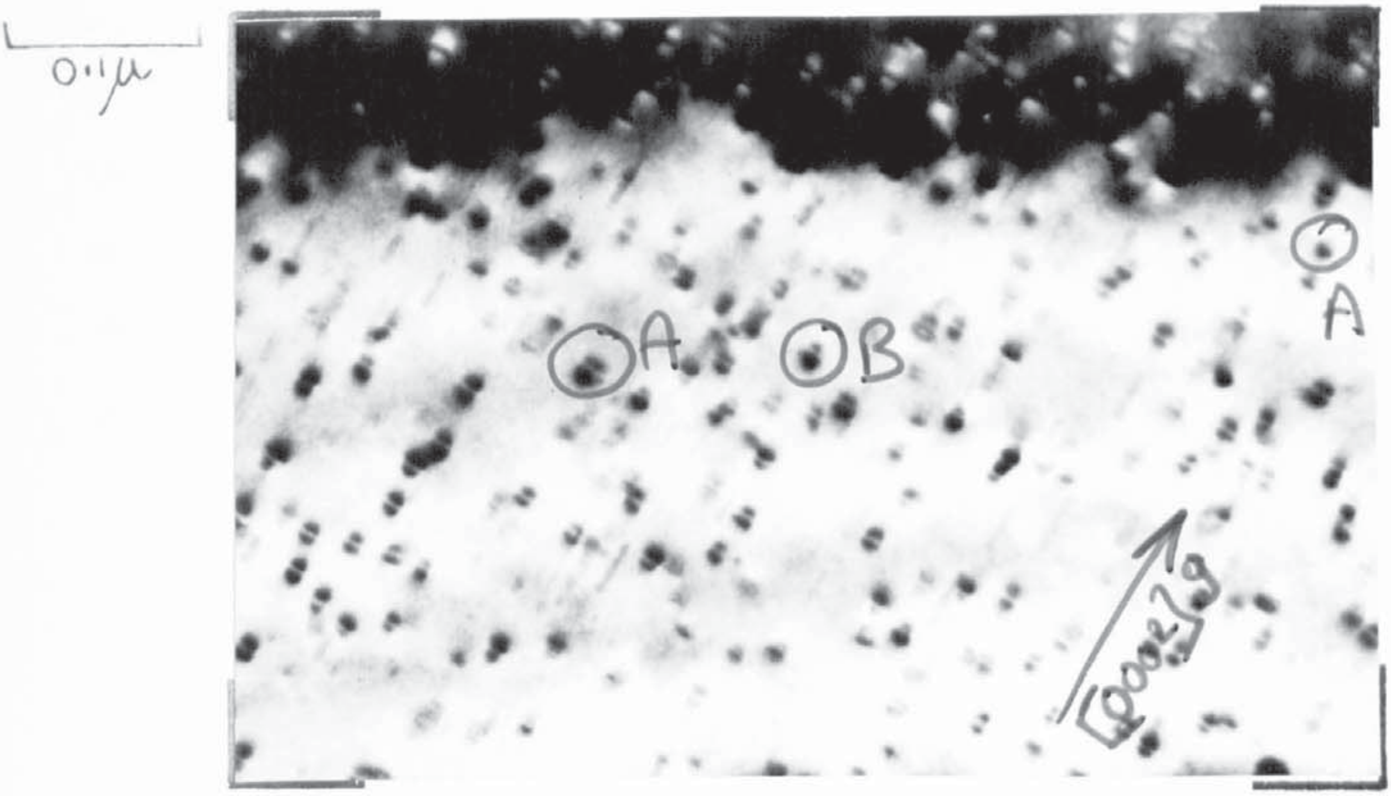

Figure 8.49. Showing part of Fig. 8.11 at a higher magnification.

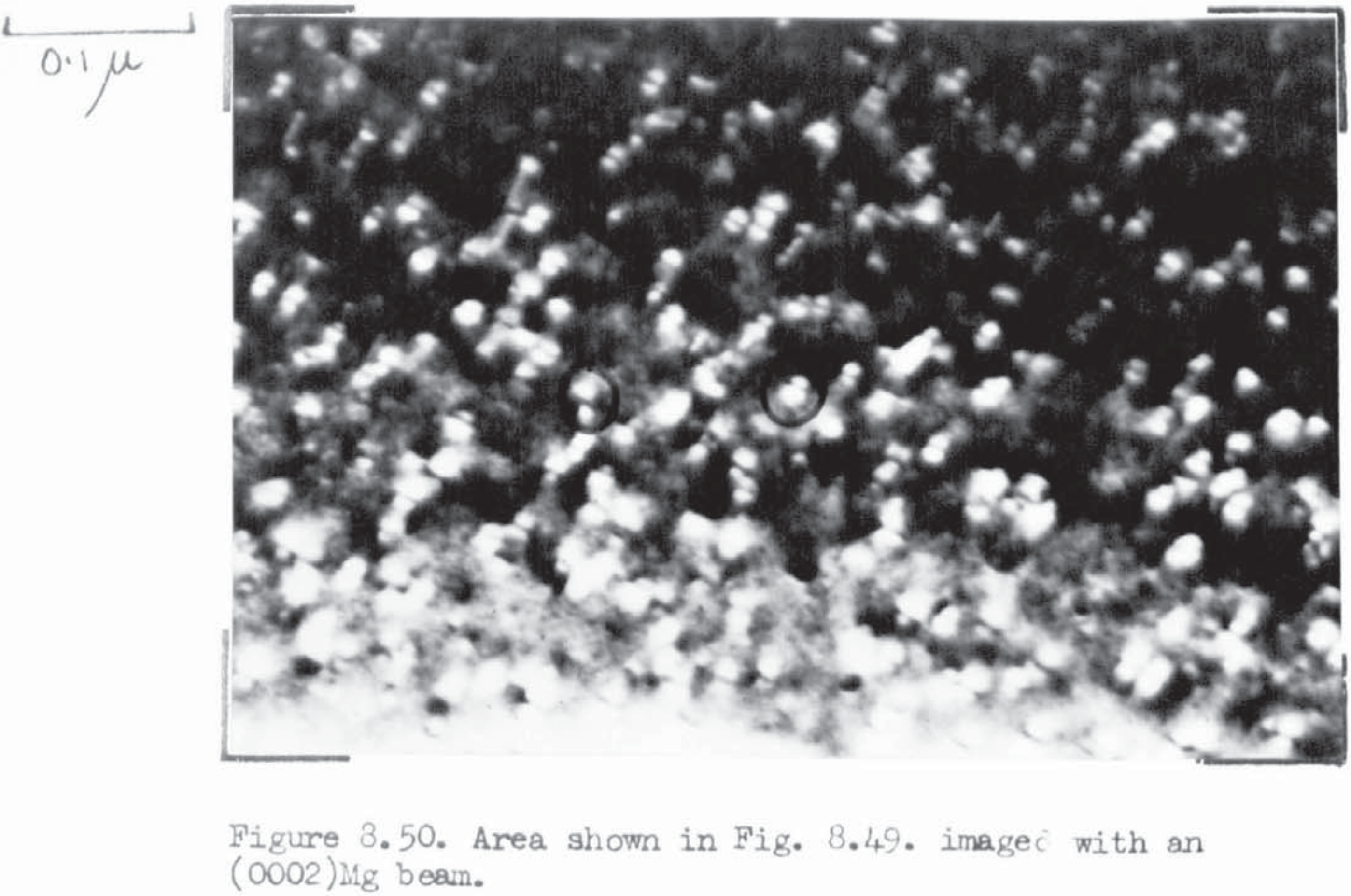

Figure 8.50. Area shown in Fig. 8.49. imaged with an (0002)Mg beam.

This alloy was therefore included in order to determine its structure after an identical heat treatment to that used for Z6, ZW6 and ZM61. The effects of heat treatment on the mechanical properties of this alloy were not determined.

Electron Microstructure.

The structures after ageing for times of up to 60 hours at 180°C., after solution treatment for 2 hours at 420°C.. W.Q. consisted of grains and grain boundaries only. No evidence of precipitation was detected. The alloy was therefore examined after ageing at 420°C. for times of up to 300 hours. Solution treatment in this instance was for 1 hour at 560°C. W.Q. The structure after 16 hours at 420°C. is shown in Fig. 9.1 (1087). Precipitation is not very extensive and the precipitate is causing matrix contrast which may result from differential thermal contraction during cooling after ageing. The foil orientation was not accurately determinable but it is near to (0001)Mg. A further structure was observed in other areas of this foil and is shown in Fig. 9.2 (1088). It is considered to be an artifact and not due to the heat treatment. Precipitation as extensive as that shown by Byrne was not observed; this could be related to the Manganese content and/or the very large grain size in this alloy and possible manganese segregation.

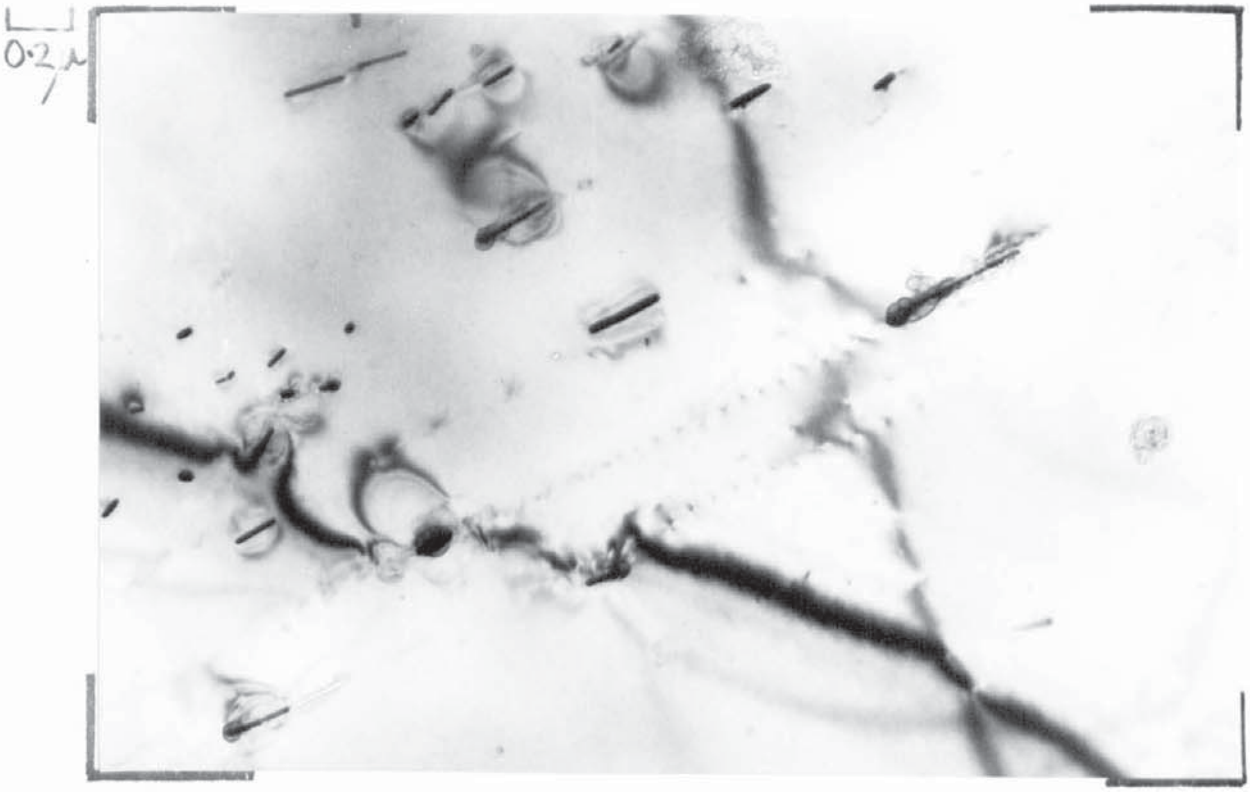

Figure 9.1. Mn80 solution treated at 560°C. and aged for 16 hours at 420°C.

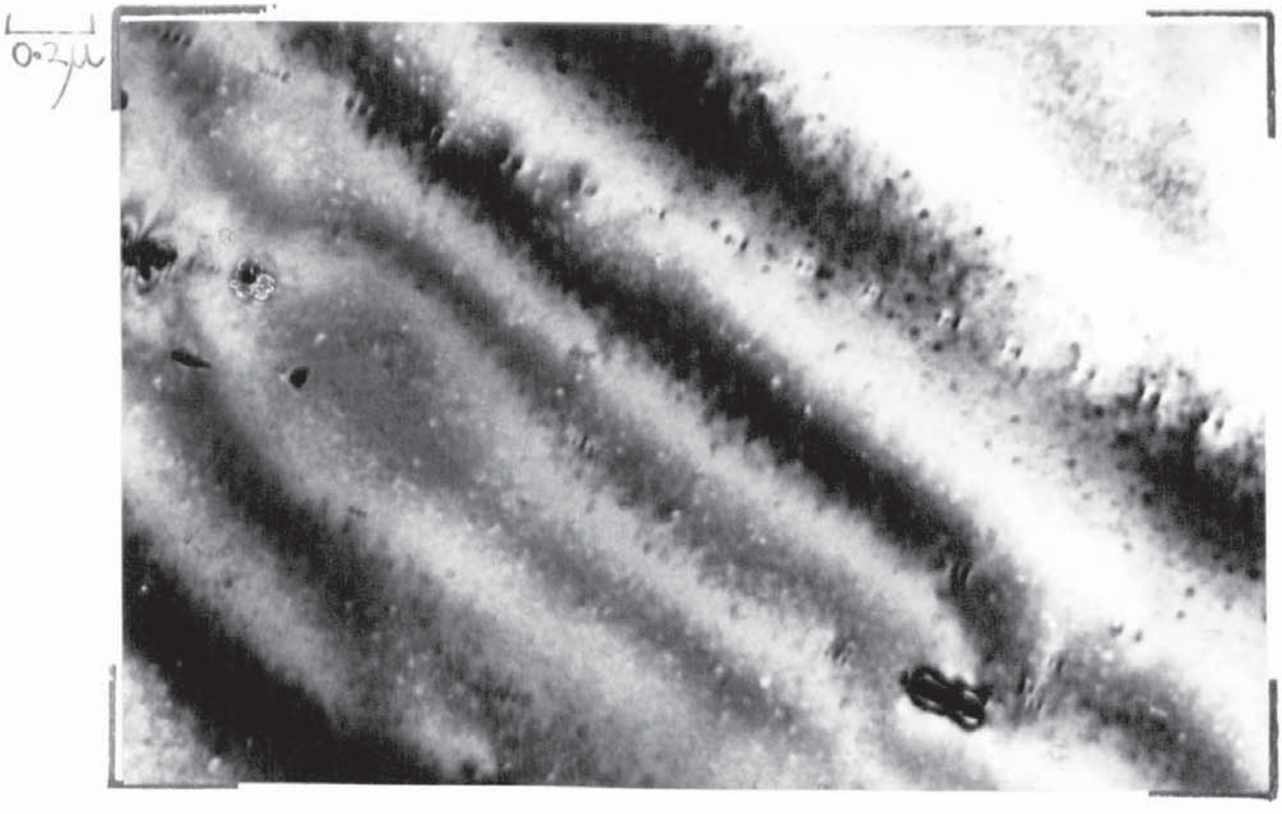

Figure 9.2. As Fig. 9.1.

Section 6 - Matrix Contrast Effects.

In most of the photo-micrographs presented in this thesis, the contrast has arisen by diffraction from the precipitate and diffracting conditions were selected that enabled the precipitate size and distribution to be easily illustrated. It is now proposed to illustrate the matrix contrast and the matrix/ precipitate contrast observed in the three alloys Z6, ZW6 and ZM61. As the matrix contrast from the disc shaped G.P. zones has been previously illustrated and analysed it will not be repeated in this section.

Magnesium - 6.0% Zinc.

Fig. 10.1 (885) shows the preferred chemical attack parallel to the (0001)Mg planes, which was referred to in the section on the experimental procedure. In Fig. 10.1 the foil orientation is such that a "kink" in the needle precipitate is evident and the preferred attack is associated with this effect. This is particularly well illustrated with the bottom kink, labelled A, where the attack is not complete. It is considered that the kink, either multi-layered slip or micro-twins due to quenching effects, was present prior to ageing. There is no evidence of needle fracture on any of the kinks. Needle fracture has been observed and will be illustrated later.

Figs. 10.2, 10.3, 10.4 (879, 880, 881) show the dramatic

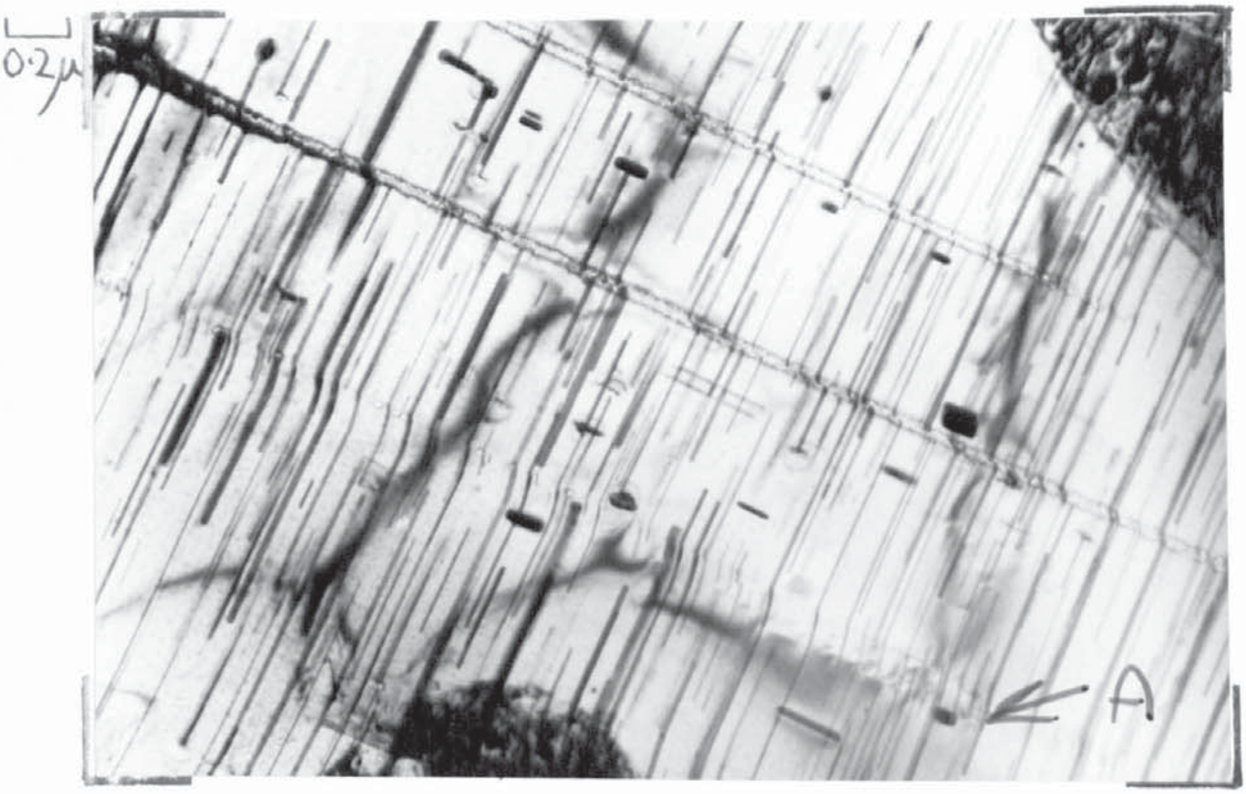

Figure 10.1. Alloy Z6, showing chemical attack associated with a 'kink' in the precipitate.

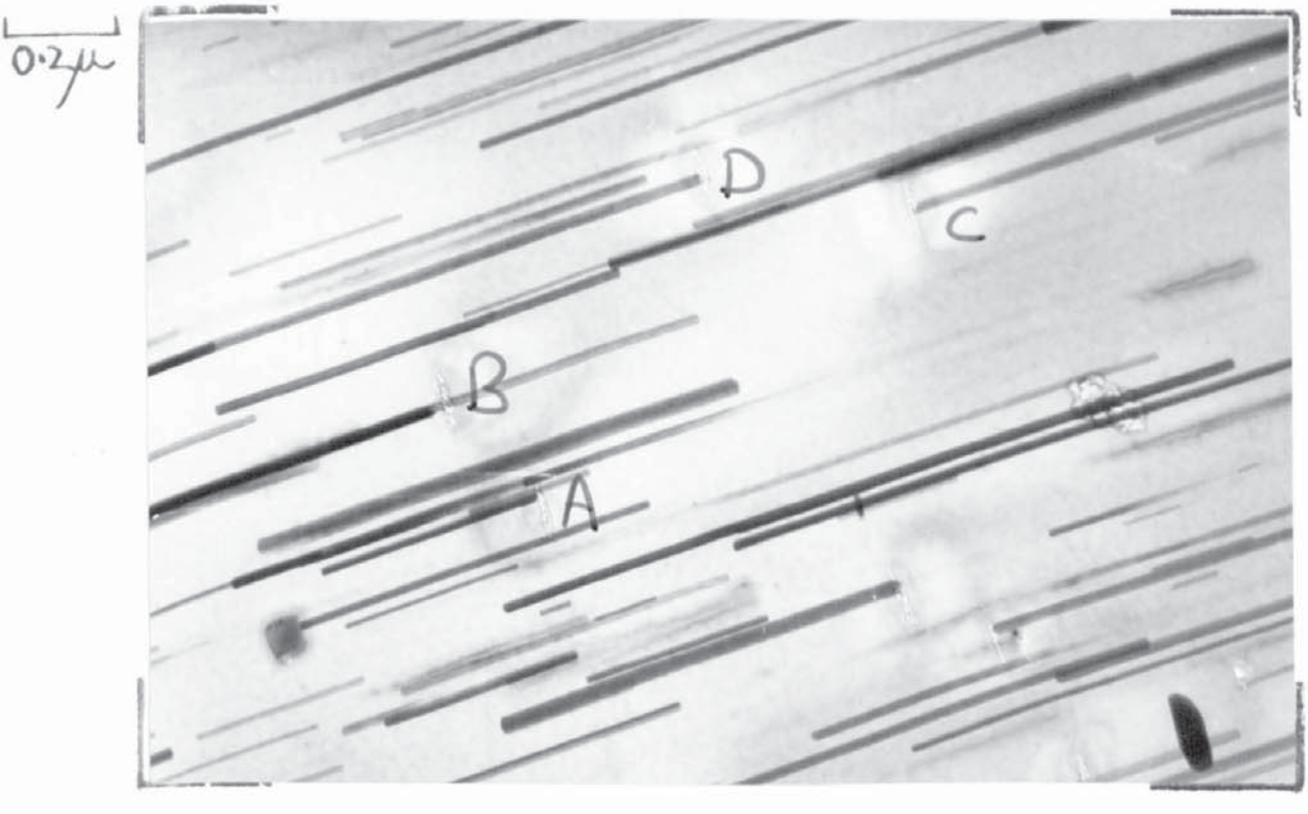

Figure 10.2. Showing a small white line defect associated with the ends of the needle precipitate.

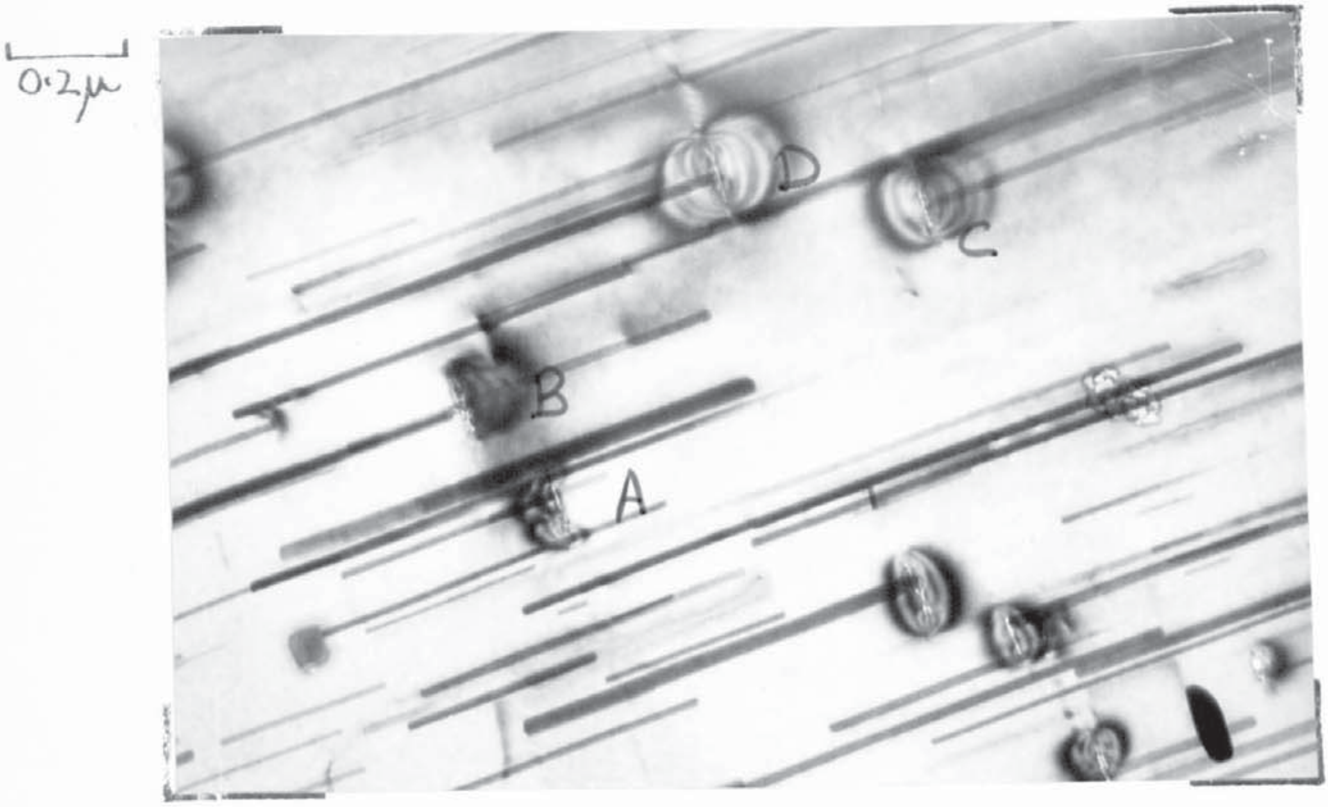

Figure 10.3. As Figure 10.2 but tilted slightly.

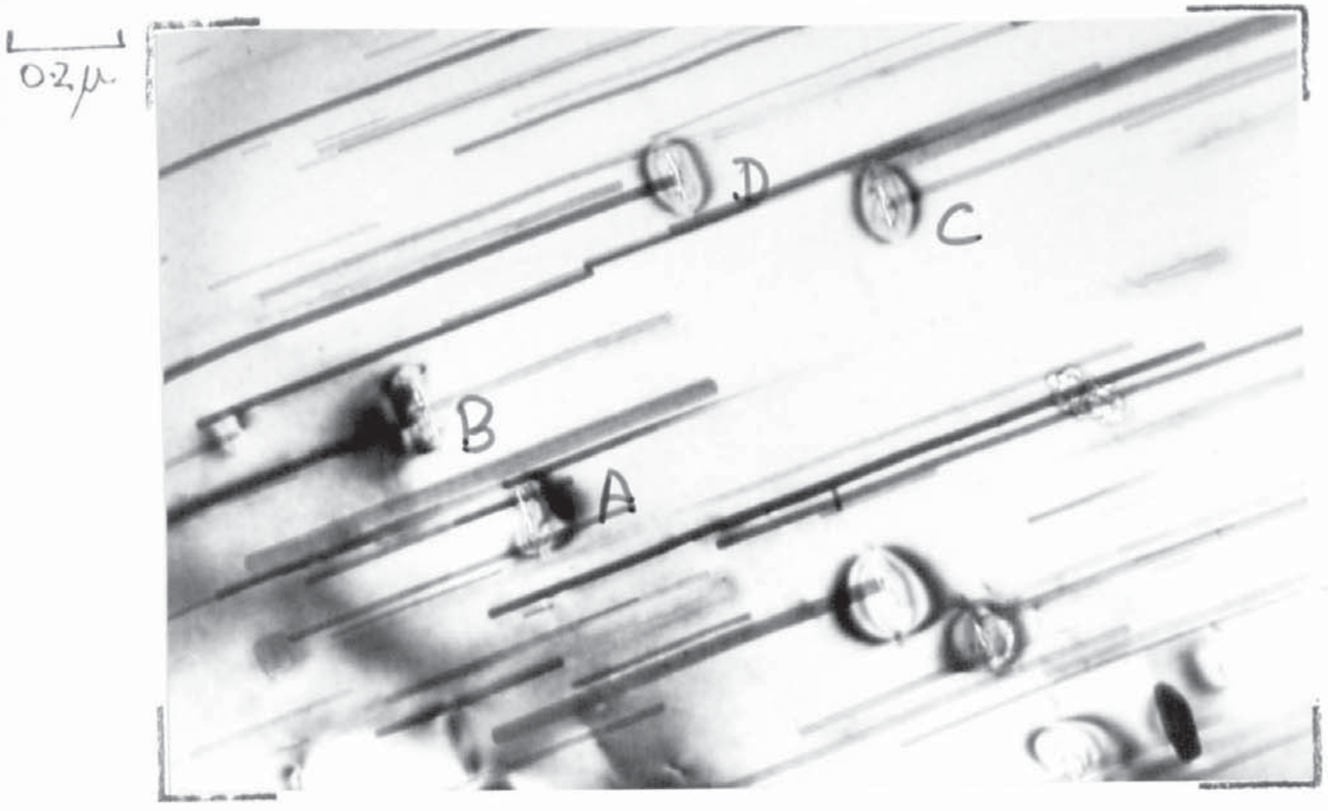

Figure 10.4. As Figure 10.3 tilted further still.

effect of changing the operating reciprocal lattice vector on the artifact illustrated in Figs. 4.5 and 4.6. The vector for Fig. 10.2 is $(10\bar{1}0)$Mg with a rotation through 90° to an (0002)Mg vector for Fig. 10.4. The light corrosion product on the (0001)Mg can be seen in Fig. 10.2 and each of these coincides with the end of a needle precipitate. A strain field resulting from this defect is detectable as a lightening of the matrix. Altering the vector to (0002)Mg causes the more familiar dark strain fields and they are not always symmetrical. At A and B between tilting from Fig. 10.2 to 10.3 and 10.4 the strain fields are very asymmetrical and the asymmetry is reversed between Fig. 10.3 and 10.4. Locations C and D clearly show the reversal of contrast accompanying the tilting.

Fig. 10.5 (574) shows severe matrix strain associated with the $MgZn_{2}^{1}$ needles. At A the strain fields are about 2,500 A° in length, along the needles. Adjacent needles are equally effected and this continues across the whole of the photograph. This also applies at the location shown at B but the strain field length is only 800°A in this case. This effect is shown on a finer scale in Fig. 10.6 (506) and the spacings are not regular. Although they are close to 300 A° long, it is possible that these are interface dislocations, with spacings between 480 and 1200 A°.

Interface dislocations at a needle in a $(11\bar{2}0)$Mg foil are shown in Fig. 10.7 (509). The needle is partially coherent, and

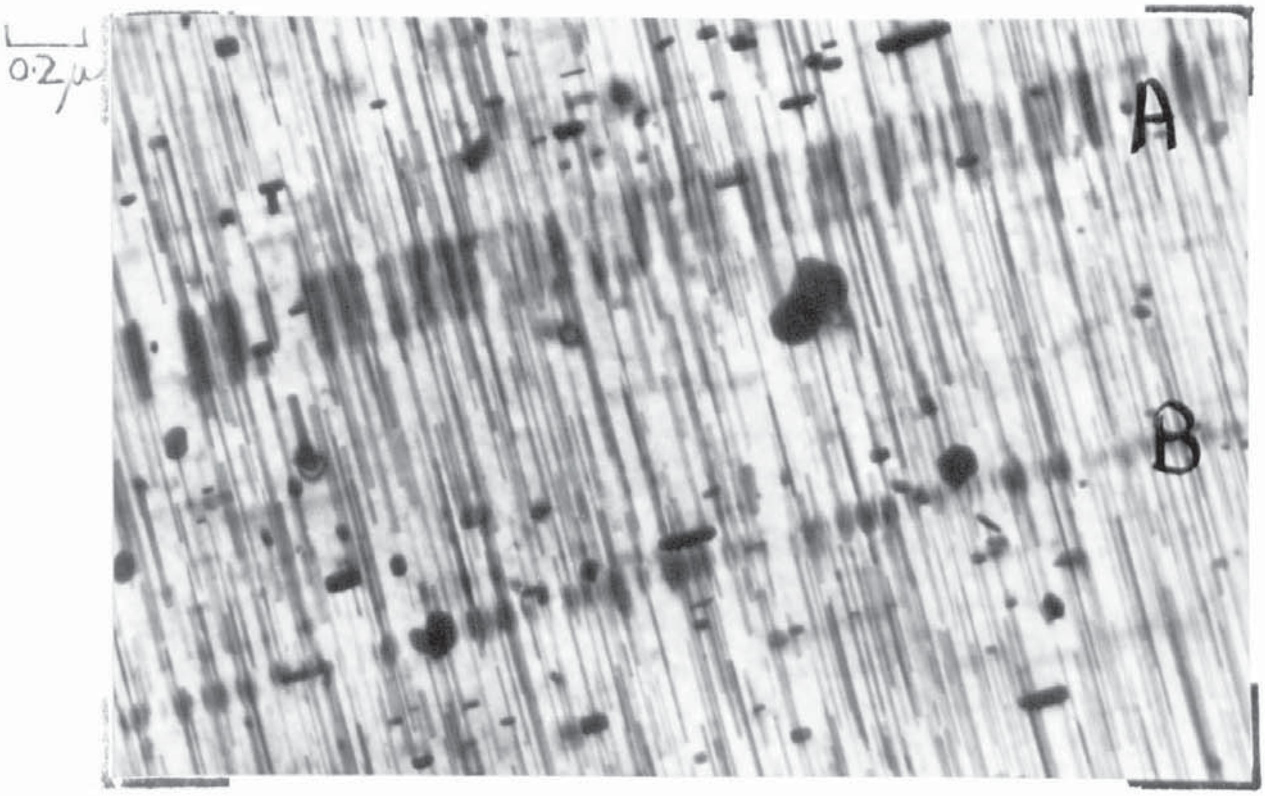

Figure 10.5. Showing matrix contrast associated with the needles.

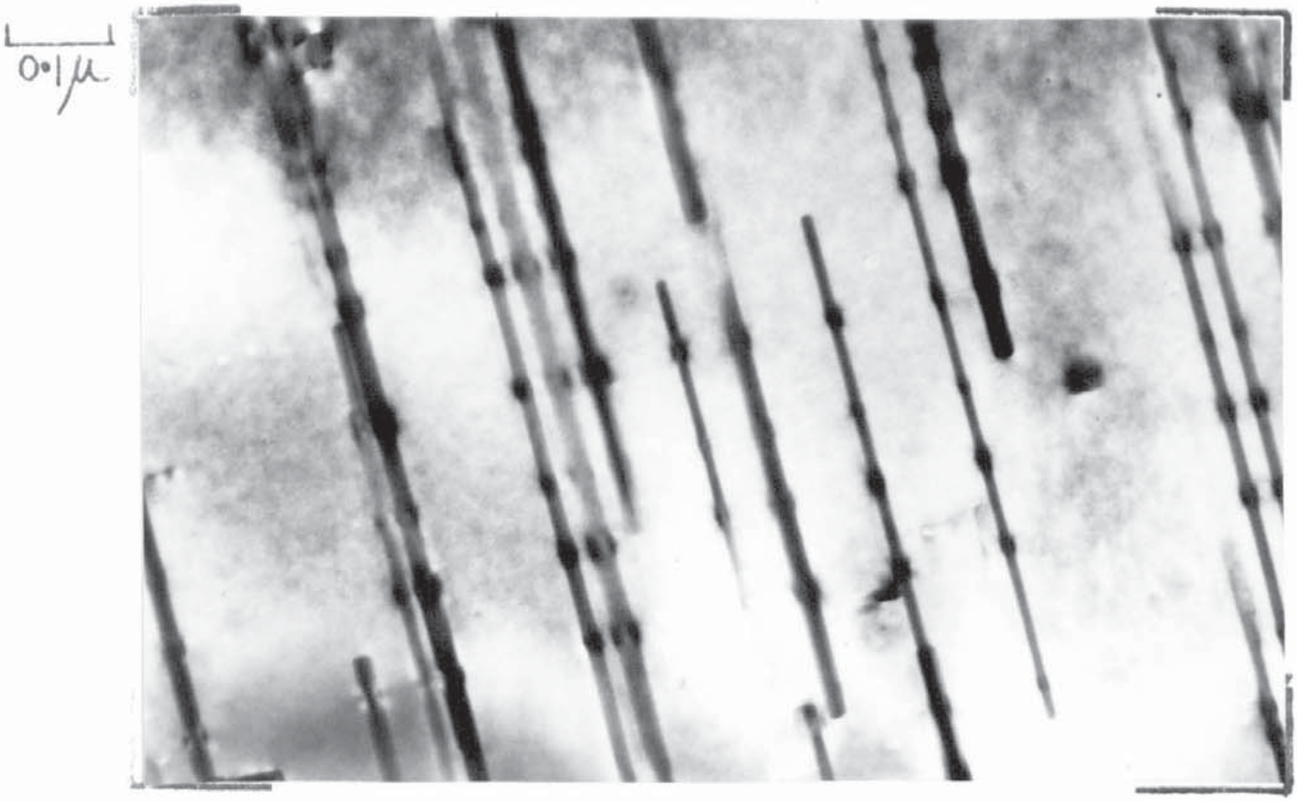

Figure 10.6. As Fig. 10.5.

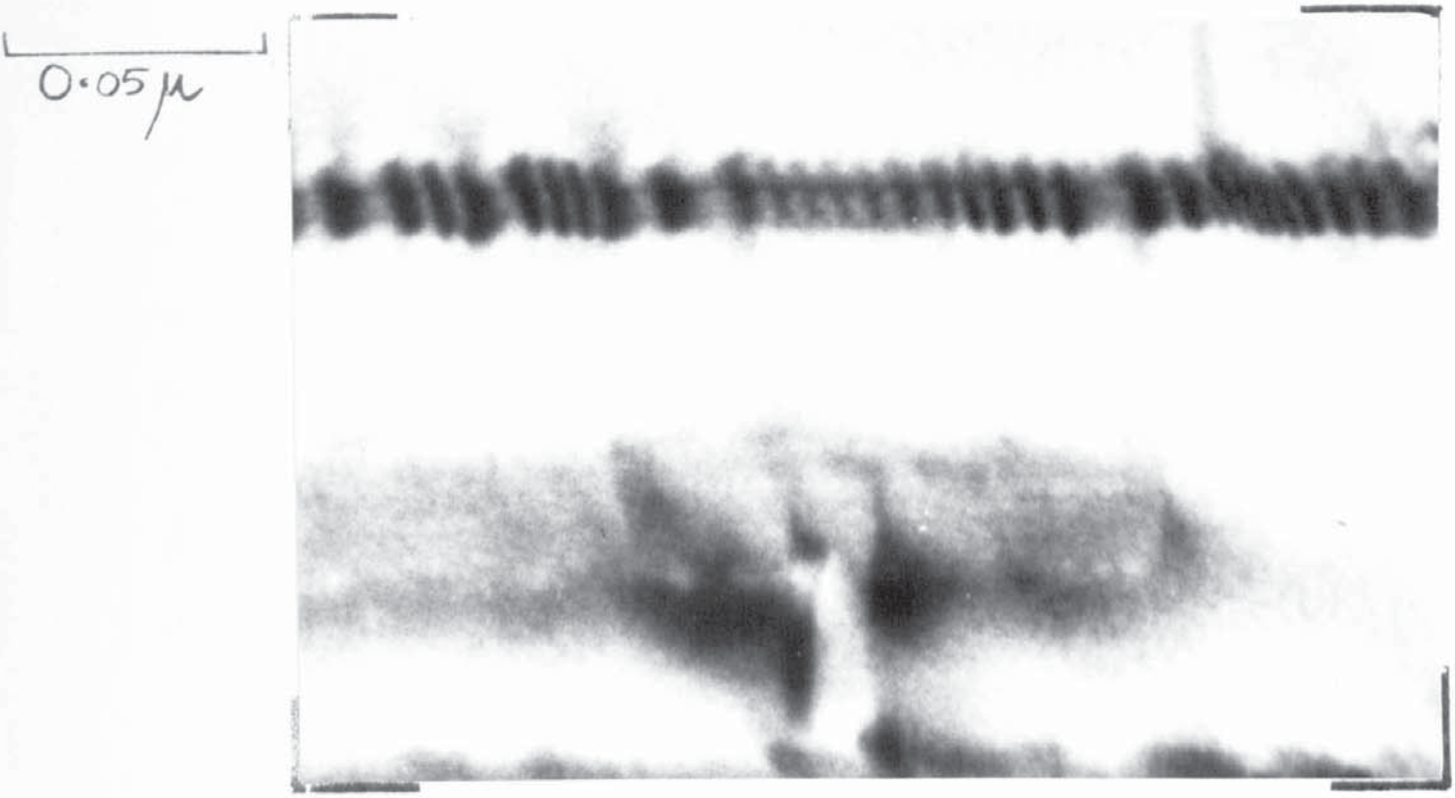

Figure 10.7. Illustrating interface dislocations on the needle precipitate.

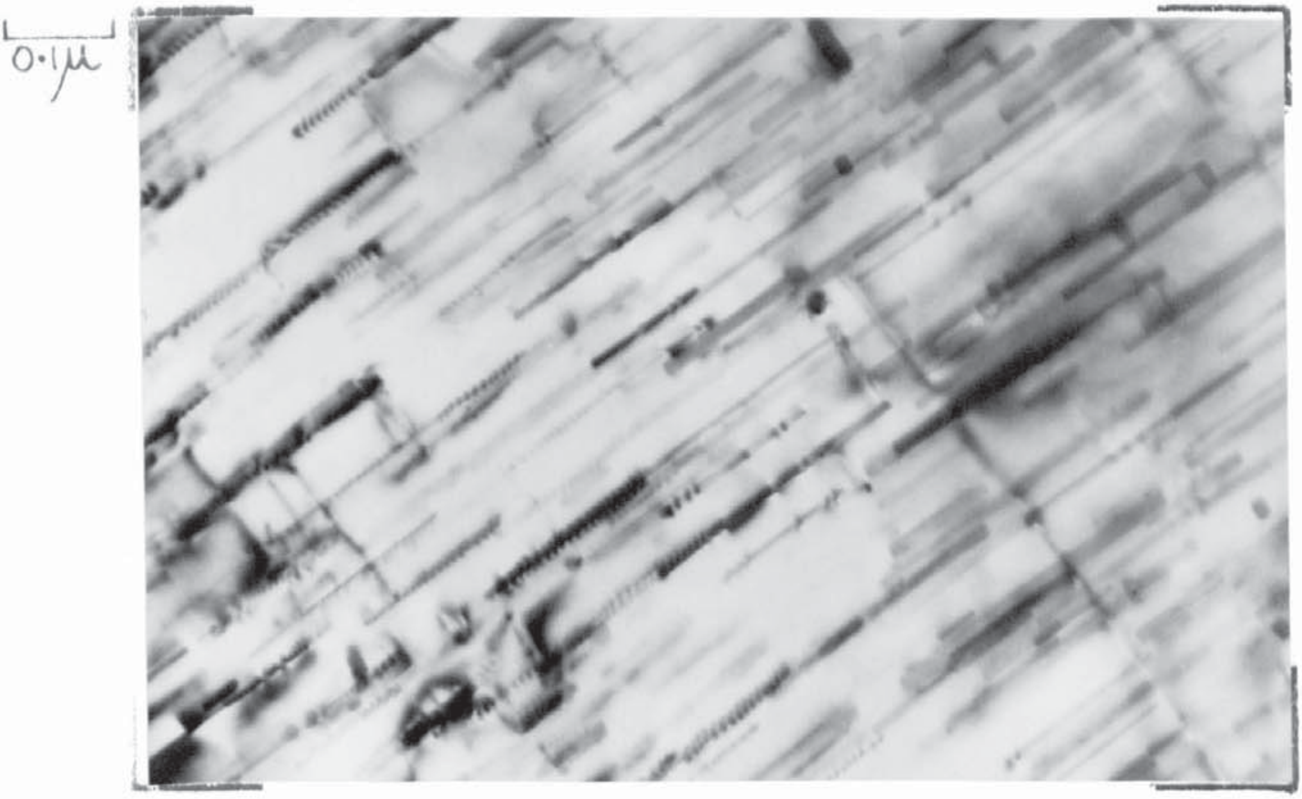

Figure 10.8. Showing interface dislocations with a distinct "arrowhead" appearance.

the interface dislocations are 55 - 60 A$^{\circ}$ apart and are inclined at about 76° to the (10$\bar{1}$0)Mg planes. The spacing is not absolutely regular and it was not possible to relate any mismatch to the dislocation repetition.

Fig. 10.8 (1550) is from a (11$\bar{2}$0)Mg foil and interface dislocations are again evident. In this instance some of the dislocations have a distinct 'arrowhead' appearance along the needle length, with a spacing of 65A$^{\circ}$.

Magnesium - 6.0% Zinc - 1.0% Manganese.

Extensive matrix strain along the needle precipitate was observed in this alloy and is shown in Fig. 10.9 (371). The matrix strain is better illustrated using a matrix diffracted beam for imaging and this is shown in Fig. 10.10 (1356), which is from a (10$\bar{1}$0)Mg diffracted beam. The foil orientation is (11$\bar{2}$0)Mg and the needle length has reached 1,200 A$^{\circ}$ in some cases.

Interface dislocations were also observed periodically, they also took an "arrowhead" appearance as in the Z6. This is shown in Fig. 10.11 (364). In this instance the spacing is 75 A$^{\circ}$, which is 10 A$^{\circ}$ larger than that of the interface dislocations on the needle precipitate in the Z6 alloy.

The presence of the matrix contrast on the interface dislocations shown in Figs. 10.9, 10.10 and 10.11 is contradictory

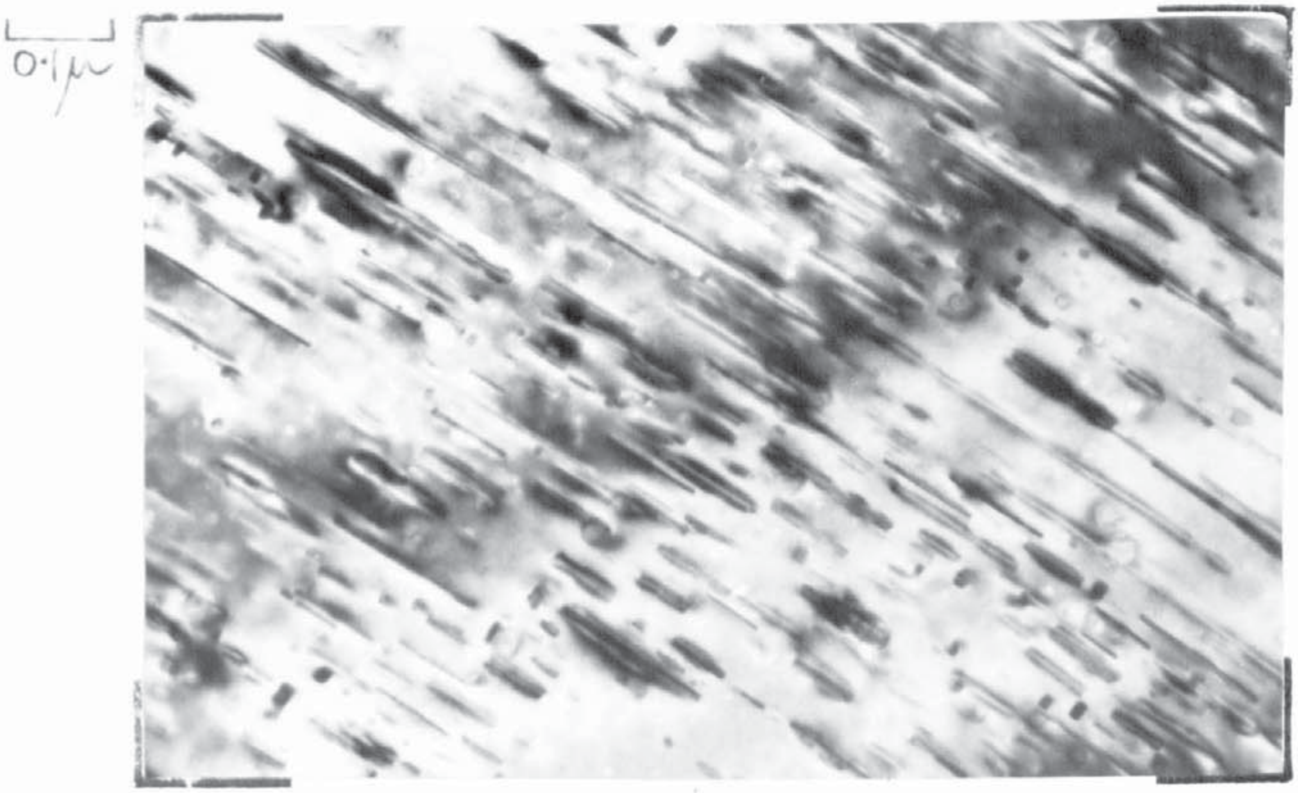

Figure 10.9. Alloy ZM61, showing extensive matrix contrast along the needle precipitate.

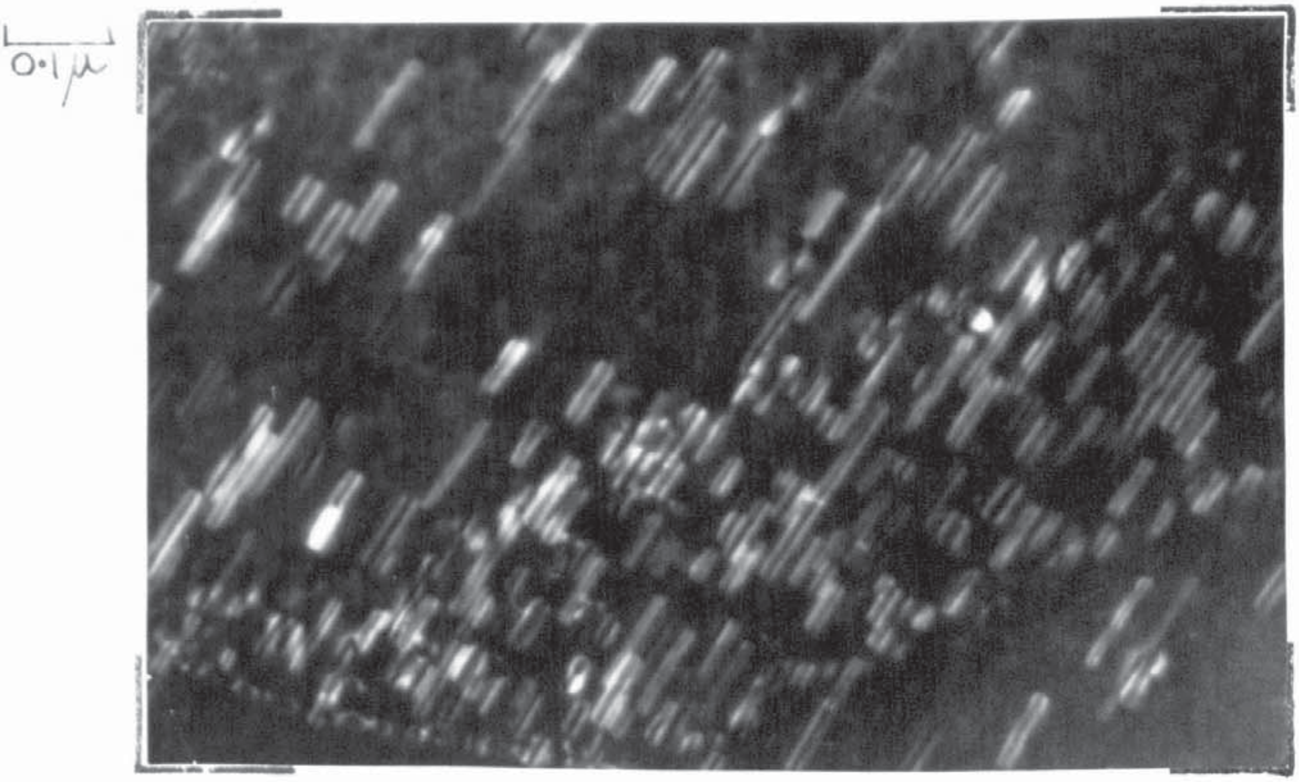

Figure 10.10. Image formed from a $(10\bar{1}0)$Mg diffracted beam showing matrix contrast as in Fig. 10.9.

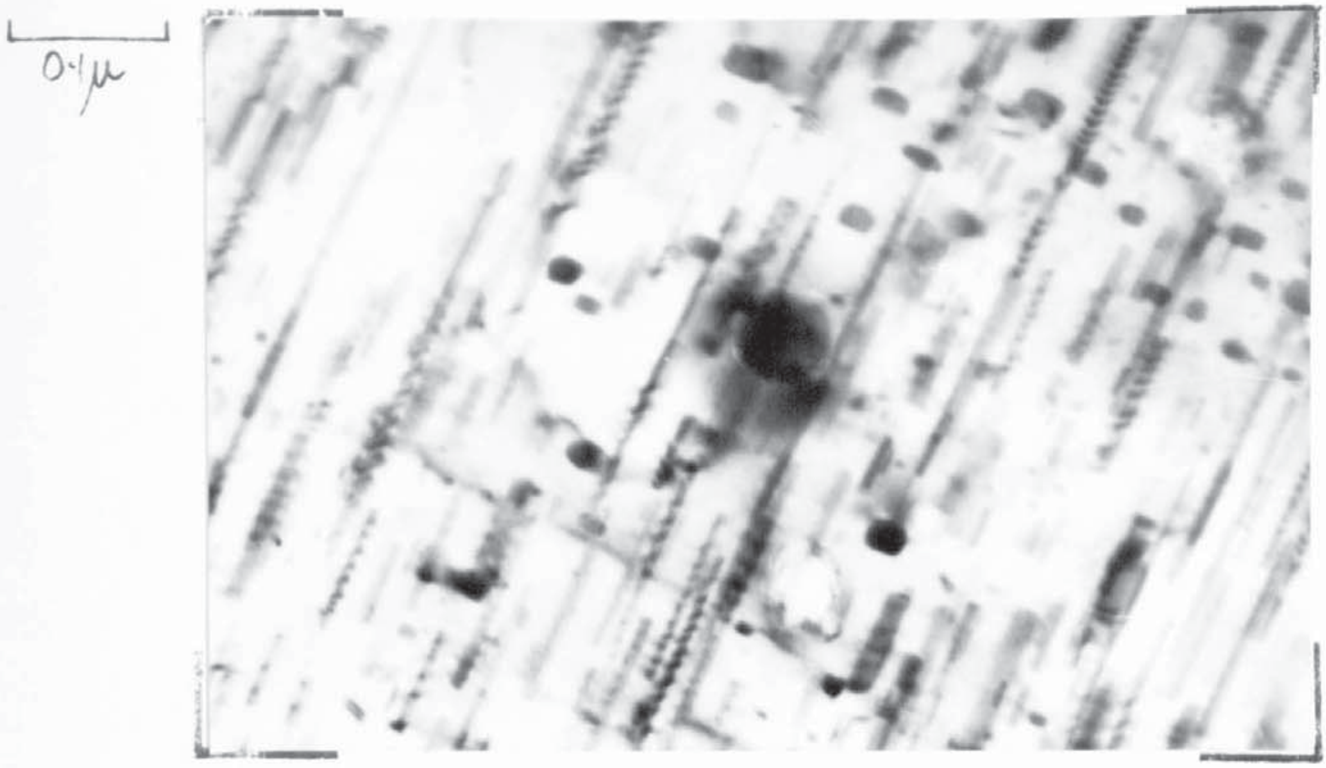

Figure 10.11. Showing interface dislocations with an 'arrowhead' appearance as shown in Z6.

Figure 10.12. Matrix contrast associated with the needles. (0001)Mg foil slightly tilted.

in that the extended matrix contrast indicates coherency strains and the interface dislocations, a partially coherent structure. The effect is possible if different faces of the needle precipitate are differently matched to the matrix.

An illustration of this is shown in Fig. 10.12 (359) which is of a foil slightly tilted off (0001)Mg. Some of the needles are showing matrix contrast from the two opposite faces and this is shown particularly well at A. Needles not showing this effect, because of an unsuitable reflecting vector, at B for instance, must be at one of the other two possible orientations. Only one of these three precipitate orientations has therefore been imaged with its matrix strain in Fig. 10.12. The other two faces of this precipitate, it is suggested, are partially coherent and not showing any strain. With a $(11\bar{2}0)$ or $(10\bar{1}0)$Mg foil orientation it is probable that some needles will show the matrix strain and others, the interface dislocations.

Dislocation Loops / Matrix Faults.

Dislocation loops showing a fault type fringe contrast within the loop have been observed and were illustrated in Figs. 8.4 and 8.5. The loops were between 2000-4000A^{o} in diameter and in the basal planes of the matrix.

Fig. 10.13 (1510) shows fringe contrast from faults in the basal planes of an aged sample. The image was formed using a

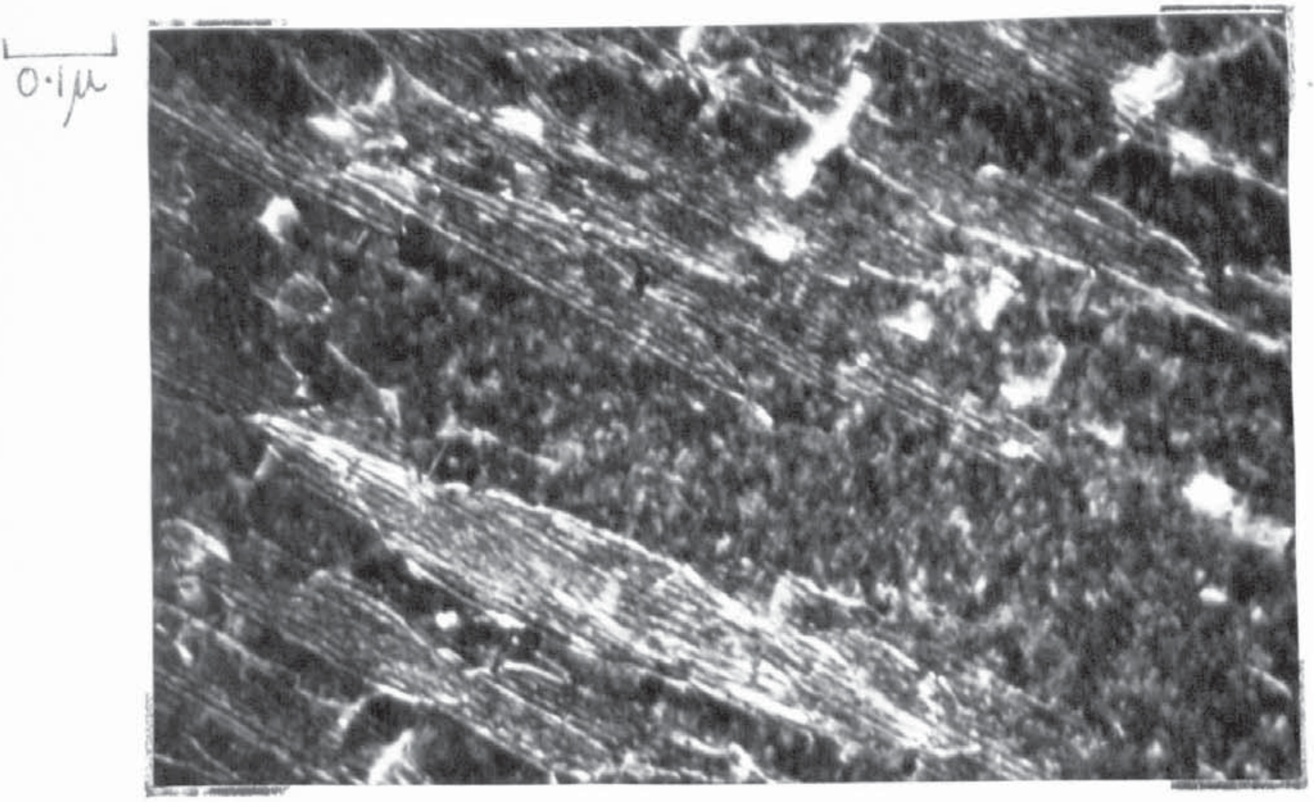

Figure 10.13. Showing faults in the basal planes imaged using a $(10\bar{1}0)$ diffracted beam.

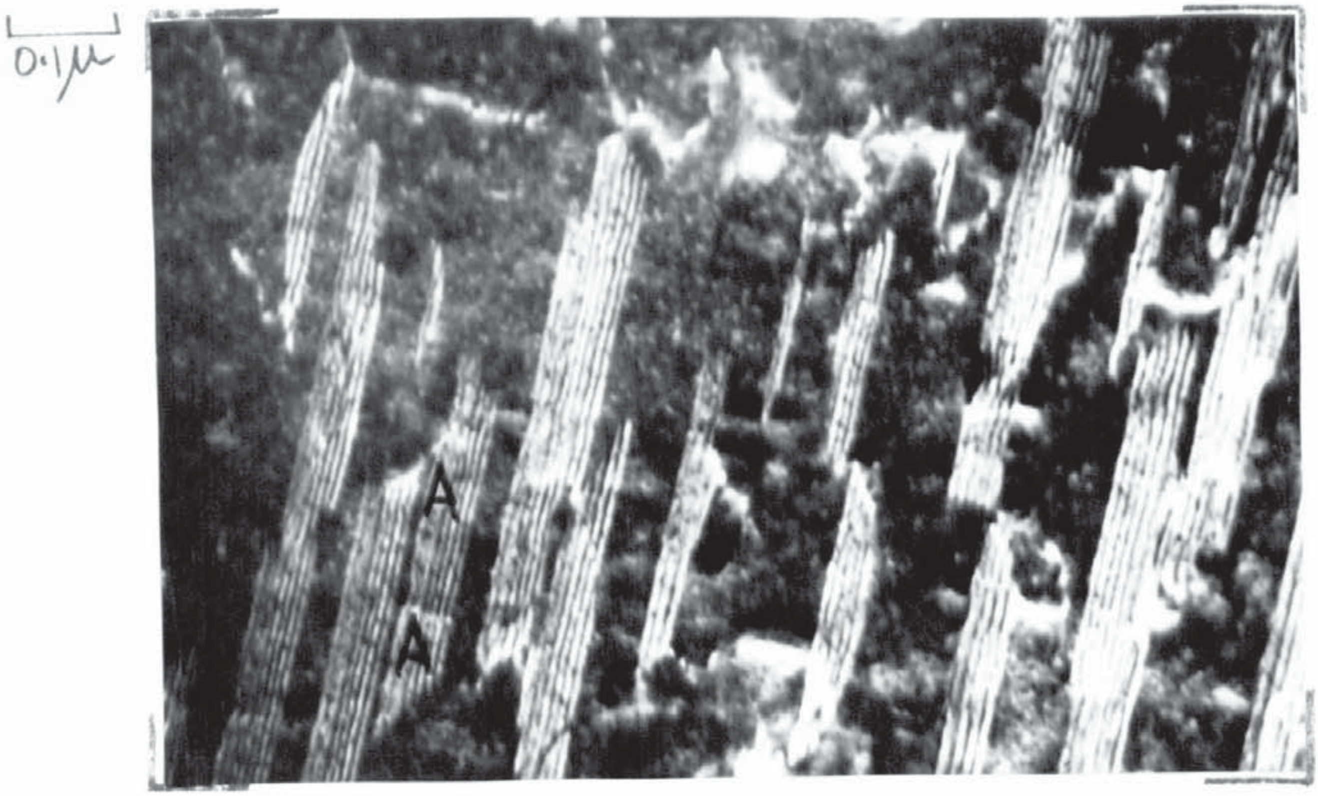

Figure 10.14. As Fig. 10.13.

(10$\bar{1}$0)Mg diffracted beam in a foil with the (0002)Mg planes at about 30° to the beam and there is no regular shape to the faults.

Fig. 10.14 (1524) shows fringe contrast from faults having a definite circular shape; the foil orientation is as for Fig. 10.13. Where the edge of the fault is curved, it is generally concave to the fringe contrast, showing that the fault is probably a loop. There are two exceptions, labelled A, where the curvature is convex to the faulted regions. This sample was heat treated as a foil. A surface nucleation and/or growth phenomenon could account for the presence of these loops, but not the faults shown in Fig. 10.13 which are in a sample aged prior to thinning.

Precipitate/Matrix Contrast:- Moiré Patterns.

When the discs of $MgZn_2^2$ in Z6 are very nearly perpendicular to the electron beam, and with a (10$\bar{1}$0)Mg vector operating a Moiré pattern is formed. Fig. 10.15 (1571) illustrates this effect and the pattern has an irregularity due to a fault in the matrix, precipitate or at the interface. This pattern is formed by the mechanism shown diagramatically in Fig. 3.8(a). Fig. 10.16 (1389) is another pattern showing a dislocation imaged by the mechanism shown in Fig. 3.9.

These patterns result from the interaction of the (10$\bar{1}$0)Mg planes with the (11$\bar{2}$0) $MgZn_2^2$ planes. Using the data published by

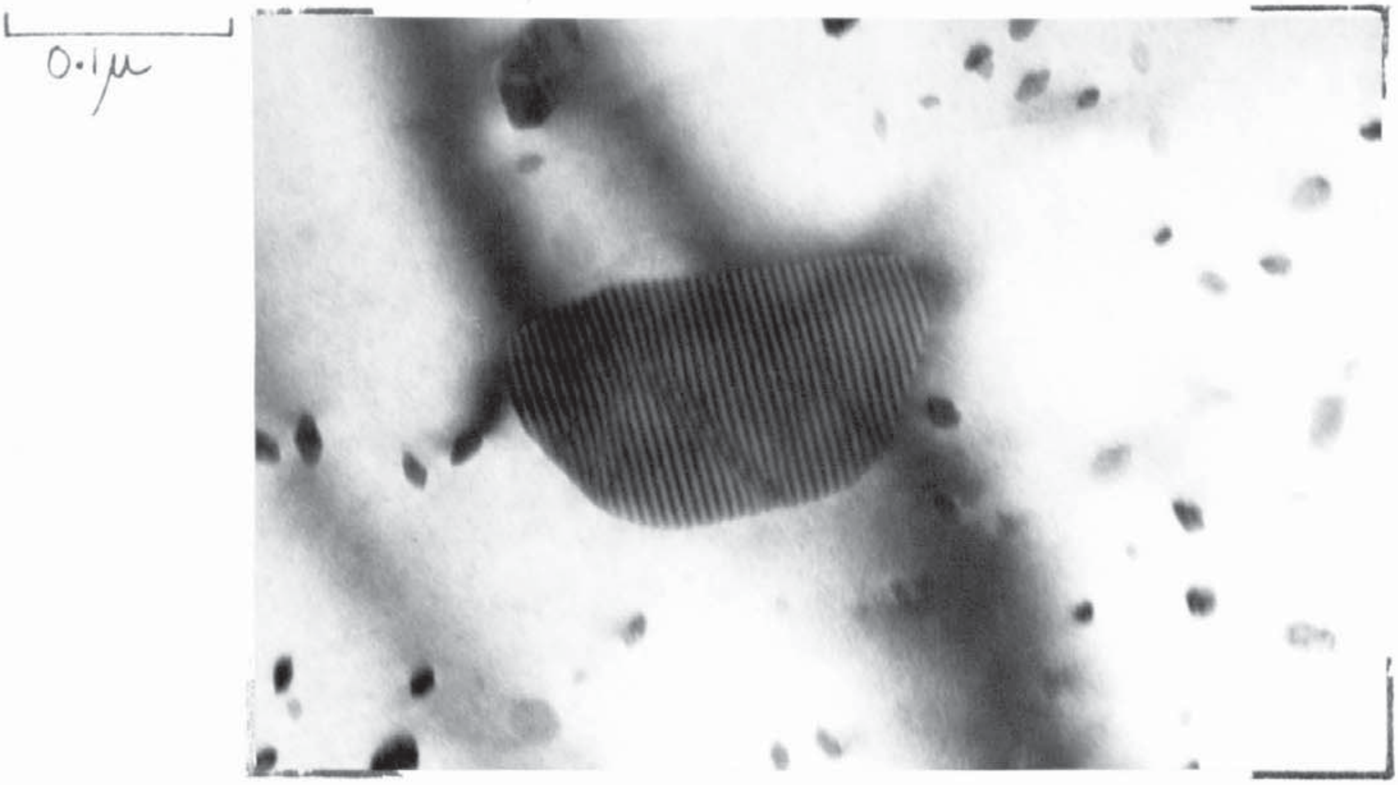

Figure 10.15. Moiré pattern observed in Z6

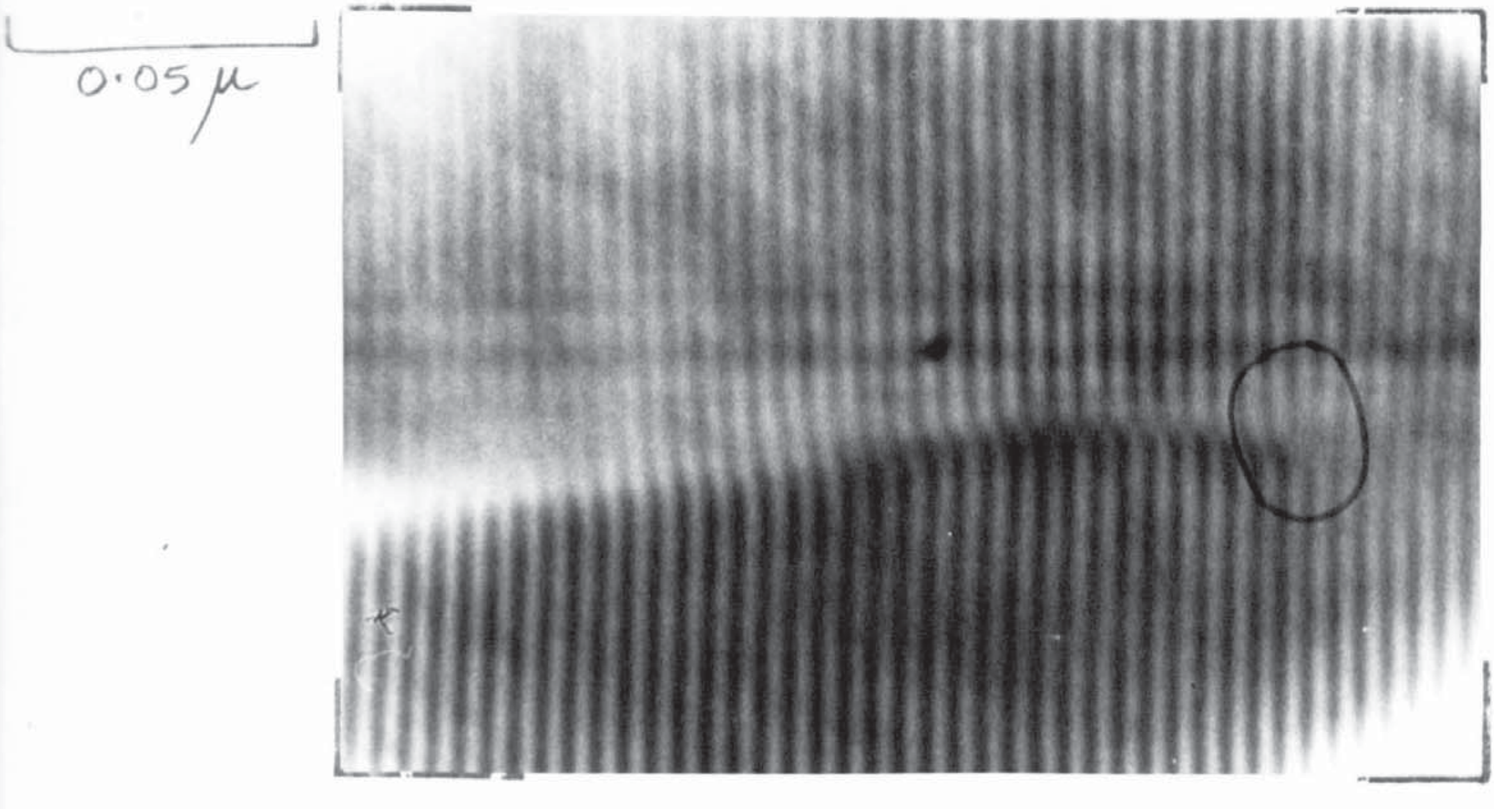

Figure 10.16. As Fig. 10.15.

Busk[43] and assuming the equilibrium concentration of zinc at the ageing temperature i.e. 2.0 wt.% or 0.75 at.%, the spacing of $(10\bar{1}0)$Mg is 2.77A°. The spacing of the $(11\bar{2}0)MgZn_2^2$ is more difficult to determine. The value assuming a unit cell of $\underline{a}$ = 5.2 A° c = 8.48 A° is $^a/2$ i.e. 2.6 A° but the nearest spacing to this in the A.S.T.M. index is 2.63 A°. With the calculated value the Moire spacing is 42.3 A° but with the measured value the spacing is 52.0 A°.

There is an added complication in that the results published by Gallot[3] for a sample aged at 250°C give a $(11\bar{2}0)MgZn_2^2$ spacing of 2.549 A° i.e. $\underline{a}$ = 5.098 A° assuming the $(10\bar{1}0)$Mg spacing from Busks[43] data, is 2.769 A°. This would give a Moire spacing of 32.1 A°.

The measured spacing in Fig. 10.16 is 49.2A°; this of course assumes that the magnification of the microscope is as indicated, which is unlikely. Using the three calculated values of the Moire spacing and comparing them with the measured value, the nominal 120,000 X setting on the microscope is 139,000, 114,000 or 185,000 times.

Alloy ZW6.

Moiré patterns were observed on the precipitate formed during solution treatment. Fig. 10.17 (1148) illustrates this and there are two patterns, one of about 120 A° and the other at about 70 A°.

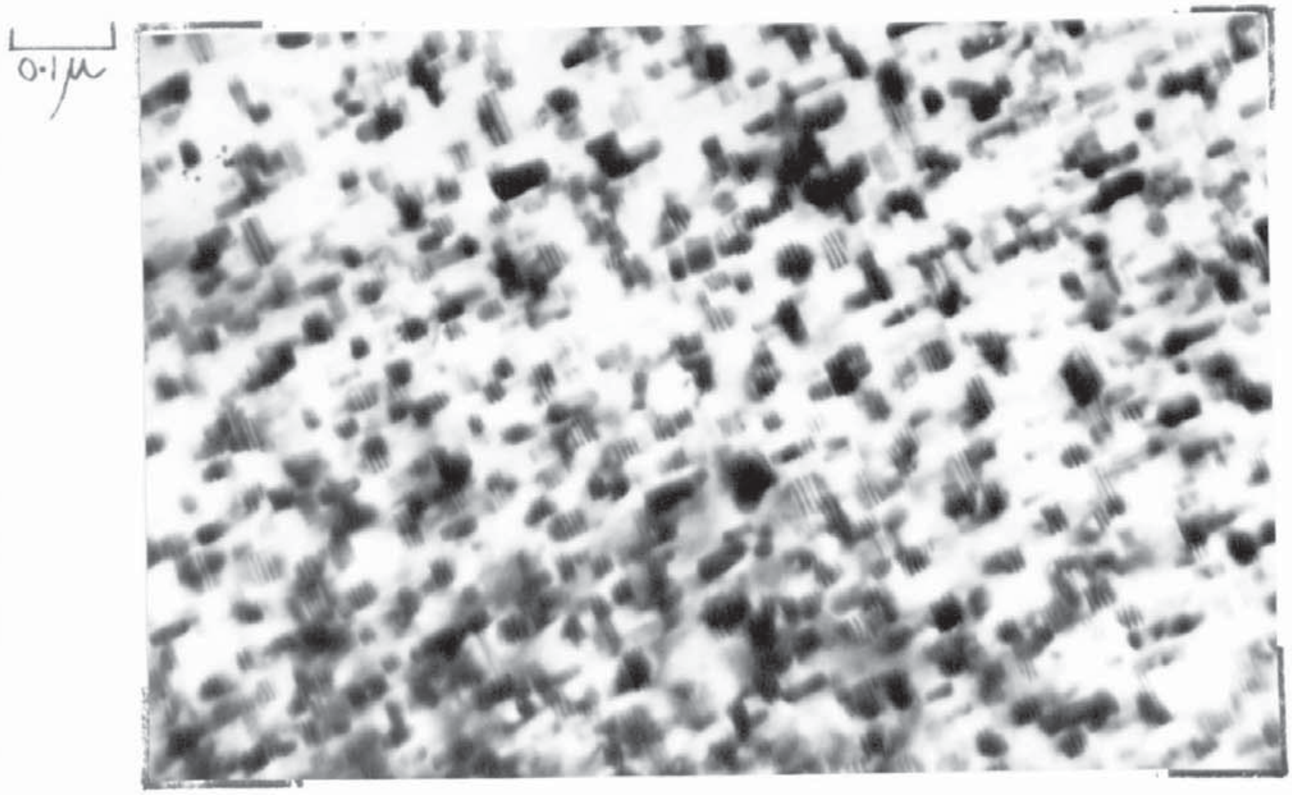

Figure 10.17. Moiré pattern on the high temperature precipitating phase in alloy ZW6.

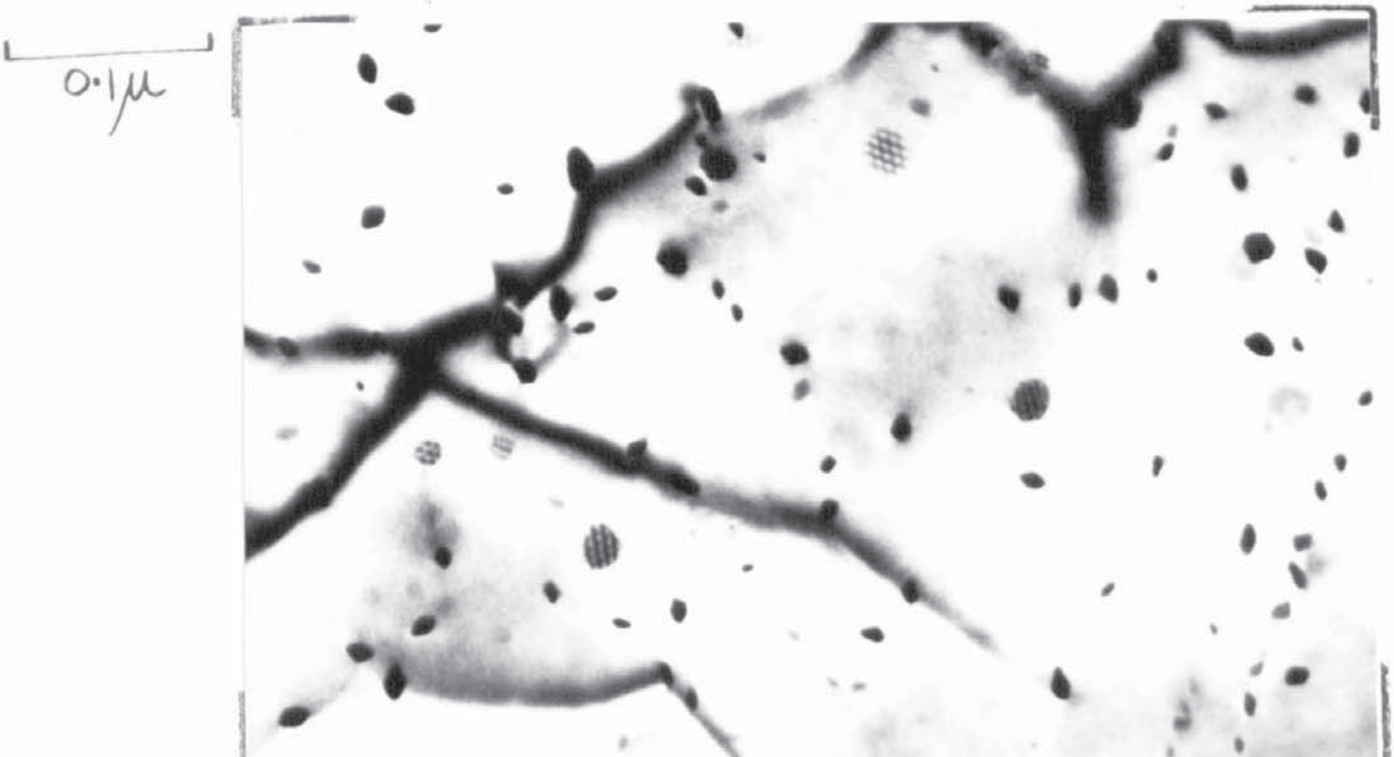

Figure 10.18. Triple Moiré pattern on the disc precipitate in ZM61.

The patterns are parallel to the magnesium basal planes and are therefore a combination of the (0002)Mg and planes in the precipitate. Assuming the (0002)Mg spacing is 2.591, close to the solution treated value for the binary Mg-Zn alloy, the precipitate spacings are

(i) 120 A^{o} spacing :- 2.53 or 2.65 A^{o}

(ii) 70 A^{o} spacing :- 2.48 or 2.69 A^{o}

There are many possibilities as to the nature of this compound although it is likely to be a ZnZr compound. The possibilities with the relevant d spacings are shown in the following table.

Zn_2Zr (F.C.C.)		Zn_2Zr_3 tetr.		ZrH. F.C.T.		ZrH_2 F.C.T.	
d	hkl	d	hkl	d	hkl	d	hkl
3.70	200	2.92		2.75	111	2.76	111
2.63	220	2.69		2.48	002	2.45	200
2.23	311	2.57		2.38	200	2.29	002
		2.52					
		2.44					
		2.41					
		2.28					

Alloy ZM61.

The patterns obtained on the $MgZn_2^2$ discs in Z6 were also obtained on the discs in this alloy. In this case the triple pattern was obtained and is shown in Fig. 10.18 (316) and the diffraction pattern in Fig. 10.19 (317) which is an (0001)Mg type. The cross section of the needle precipitate, a parallelogram, is clearly seen to the bottom left of Fig. 10.18.

Assuming the precipitate pattern is also an (0001) type in a C.P.H. structure, then the pattern is formed by an interaction of the $(10\bar{1}0)$ Matrix planes with the $(11\bar{2}0)$ Precipitate planes. Using the matrix spacing to calibrate the camera constant the $(11\bar{2}0)$ Precipitate spacing is 2.63A° giving an a spacing of 5.26 A°. The calculated $(11\bar{2}0)$ spacing of $MgZn_2$ is 2.60 A°, to give an a spacing of 5.2 A°.

A further possibility on the evidence presented in Fig.10.19 is that the precipitate pattern is from a F.C.C. (111) reciprocal lattice section. The precipitate spot close to the $(10\bar{1}0)$ matrix spot would be a $(2\bar{4}2)$ type. This would give an a spacing of 12.9 A° in the F.C.C. symmetry.

With the precipitate as a hexagonal unit cell the c spacing cannot be determined but the orientation relationship is:-

$(10\bar{1}0)$ Precip. // $(11\bar{2}0)$ Matrix and

(0001) Precip. // (0001) Matrix.

which is the same as the $MgZn_2^2$ discs in Z6.

or for the F.C.C. symmetry:-

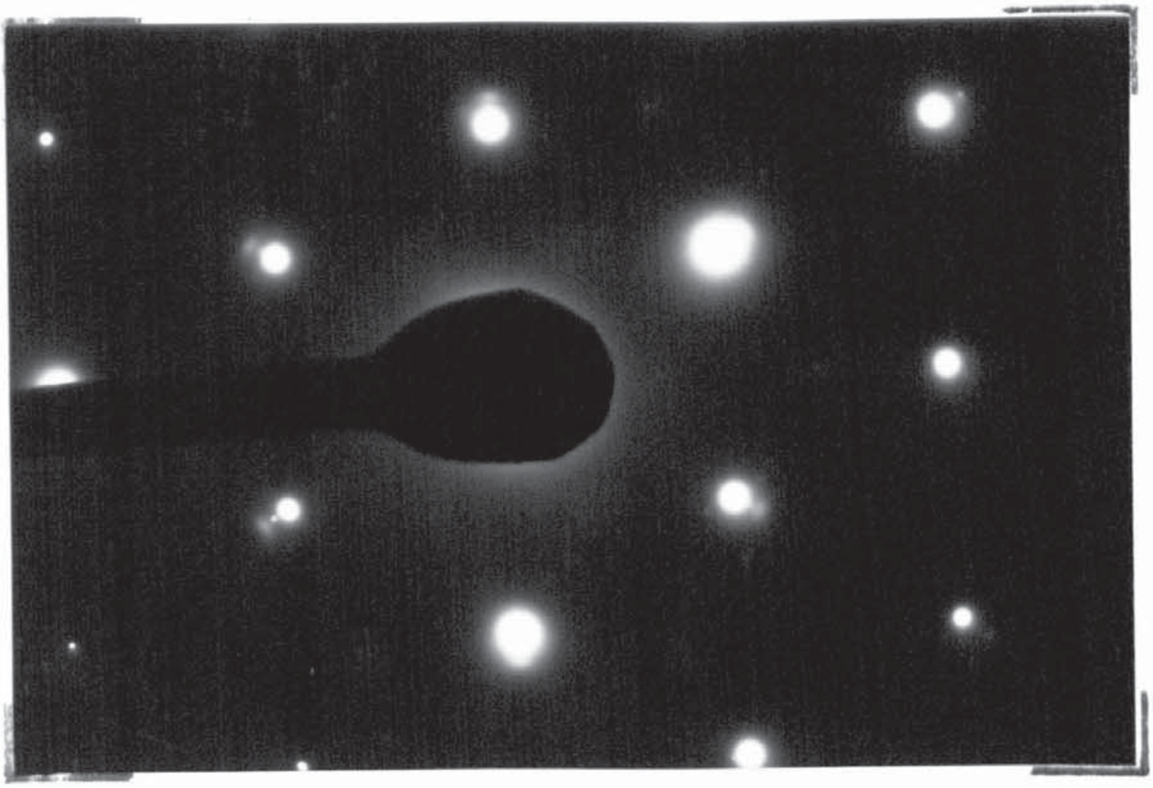

Figure 10.19. Selected area diffraction pattern of Fig. 10.18.

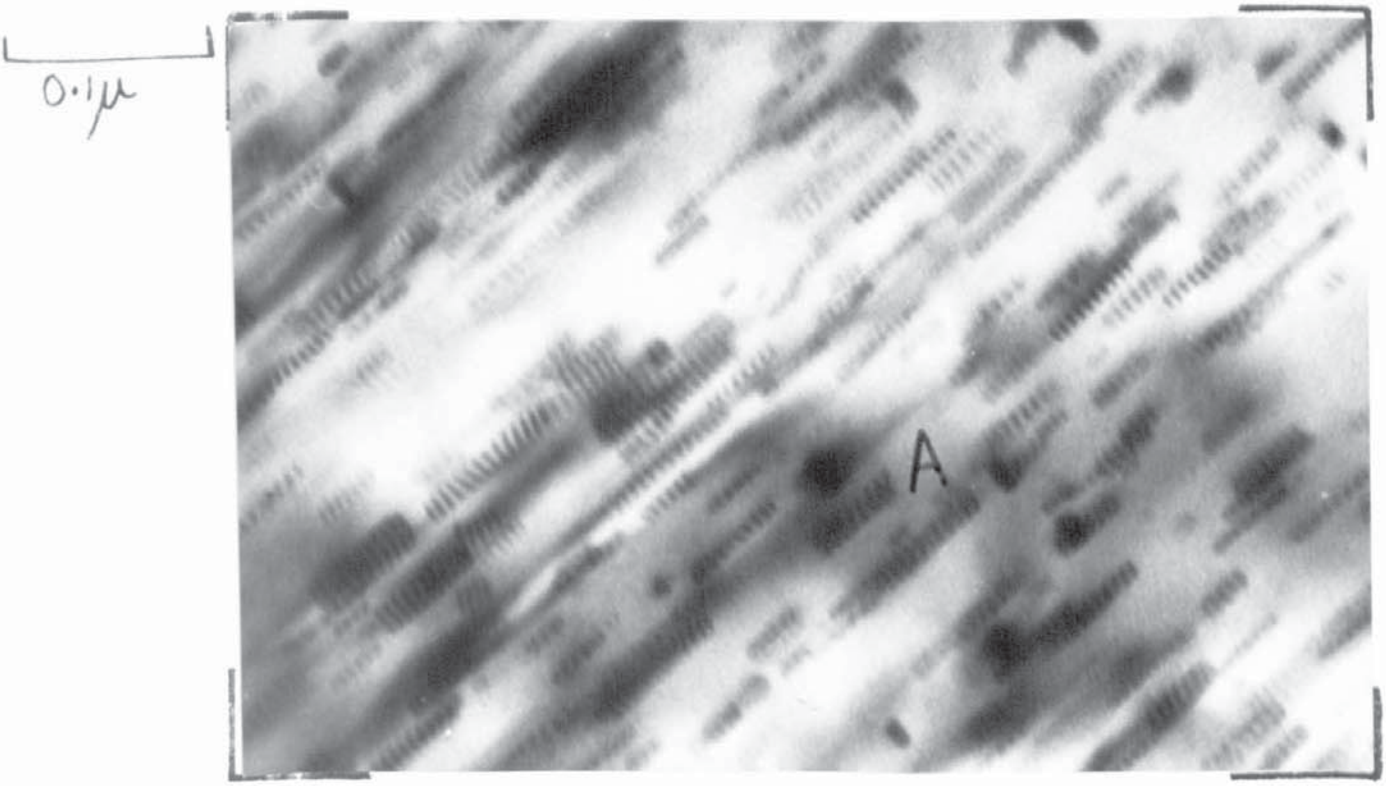

Figure 10.20. Moire pattern on the needle precipitate in ZM61.

(220) Precip. // $(11\bar{2}0)$ Matrix and

(111) Precip. // (0001) Matrix

This is the usual close packed plane/direction relationship between F.C.C. and C.P.H. symmetries. This solution is considered unlikely as it would require the 7.45 A$^{\circ}$ to be parallel to the (0001) Matrix planes. It has already been shown that the spacing in the disc precipitates parallel to the (0001) Matrix planes is 8.75 A$^{\circ}$. The measured spacing of the Moiré pattern is 51A$^{\circ}$ and the calculated value from the diffraction pattern is 52 A$^{\circ}$.

A Moiré pattern on the needle precipitates was also observed and this is shown in Fig. 10.20 (483). The spacing is 55 A$^{\circ}$ and is formed from the interaction of the (0002) Matrix planes with a spacing of 2.48 or 2.73 A$^{\circ}$. The pattern is distorted in some cases and a 'spiral' type contrast can be seen on the precipitate labelled A. There are differences in the pattern spacing on the needles and this is possibly due to the rotation of some of the needles about the $[0001]$ Mg to comply with the three $[11\bar{2}0]$ type directions. The foil is either a $(10\bar{1}0)$ or $(11\bar{2}0)$ type. The 2.48 A$^{\circ}$ spacing is close to the $(11\bar{2}2)$ spacing at 2.506 A$^{\circ}$ in the ternary phase and to the $(11\bar{2}1)$ spacing of MgZn$_2$. The closest measured spacing in MgZn$_2$ is 2.43 A$^{\circ}$.

Precipitate Fracture.

As pointed out by Byrne[10] the spacing of the needle precipitate in the Mg-Zn alloy examined by Clark[18] could be related solely to the specimen size. Byrne indicated that the needle spacing of 330-660 A° in his bulk samples would require a particle cutting mechanism and that the 1000-2000 A° spacing in Clarks specimens is borderline for this mechanism.

Fig. 10.21 (834) illustrates the result of the severe deformation occurring in the 'necked' region of a fractured tensile bar. The alloy is ZW6 and it is in the solution treated and aged for 16 hours at 180°C. condition. Complex dislocation/precipitate interaction and needle fracture are clearly evident. The foil orientation was not determinable and as the foil is obviously not of the (0001)Mg type, accurate precipitate spacing cannot be determined.

Fig. 10.22 (829) shows extensive plastic deformation and flow along a grain boundary which has widened and become indefinate; the needles within the flowed region are severely deformed and those within the grains are distorted.

Fig. 10.23 (832) is from an indeterminable foil orientation but the needles are inclined between 30-50° to the electron beam. The needles have not only fractured, they have also been separated by the continued plastic deformation of the matrix.

Fig. 10.24(172) is from a position slightly removed from the

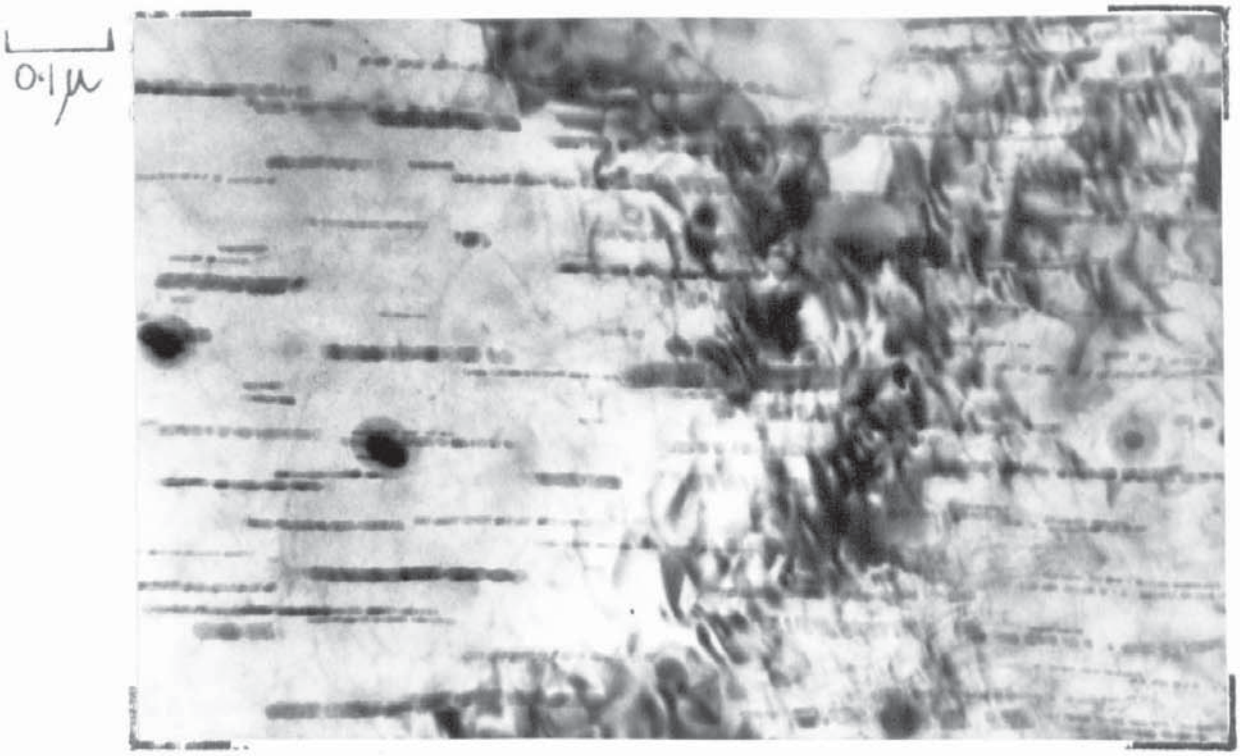

Figure 10.21 Precipitate fracture in the necked region of a tensile bar.

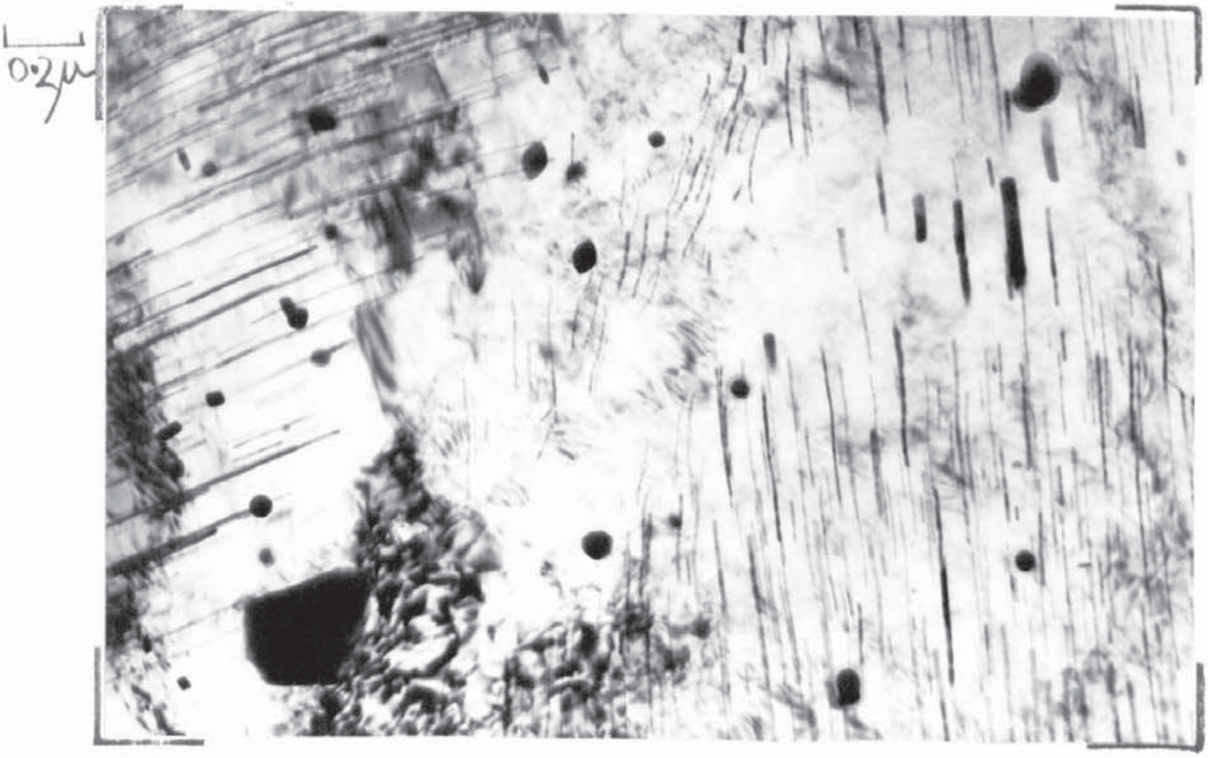

Figure 10.22. Showing extensive plastic deformation and needle displacement.

Figure 10.23. Showing fracture and separation of the fracture surfaces.

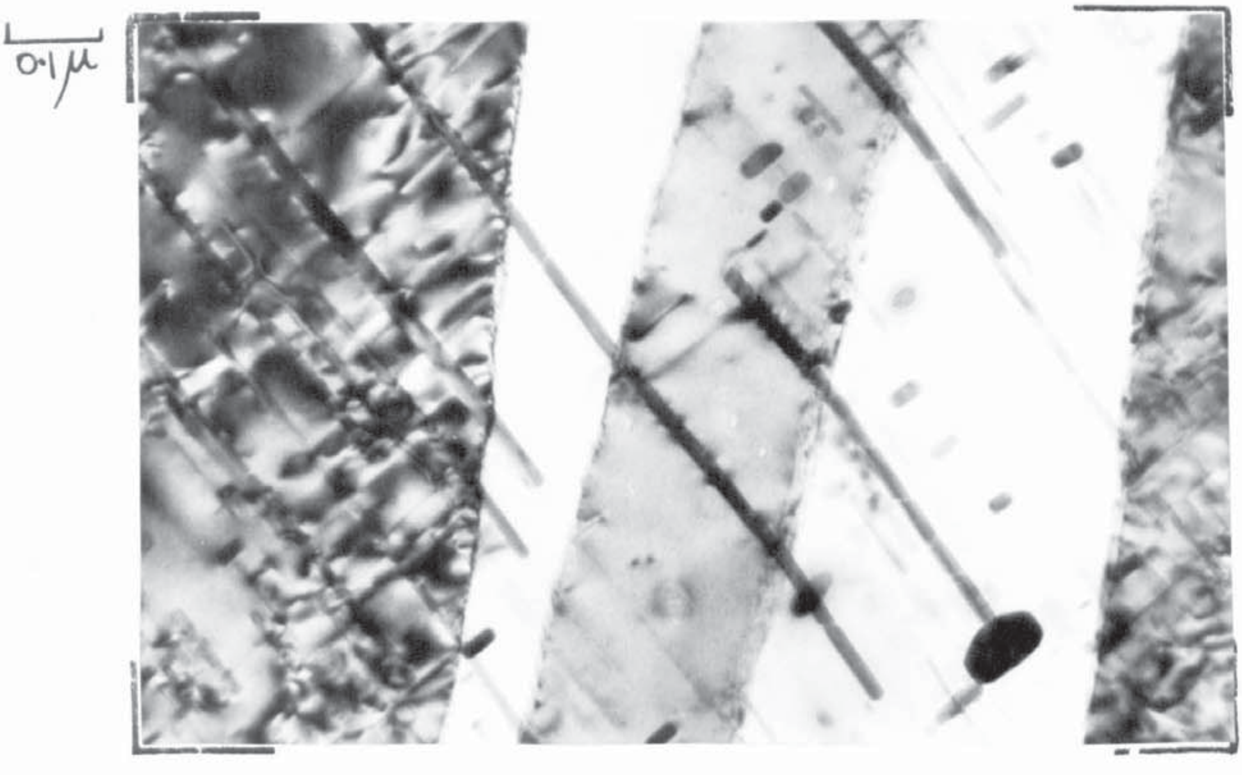

Figure 10.24. Structure in an area slightly removed from the 'necked' region.

necked region of the tensile bar. The needles are distorted and have in some cases fractured. The angles of the fractures are 63 and 75° to the axis of the needles. The needle spacing cannot be satisfactorily determined.

Discussion of Results.

Mechanical Properties.

To facilitate comparison of the ageing response in the three alloys, Z6, ZW6 and ZM61, Figs. 5.4 and 5.5, which are the hardness and 0.1% P.S. curves of Z6 are repeated with the corresponding curves for ZW6 and ZM61 superimposed such that the solution treated values coincide. Fig. 11.1 shows this composite for the hardness changes and Fig. 11.2 for the 0.1% P.S. values. Considering the hardness changes, the essential difference between Z6 and ZM61 is the higher ageing rate at temperatures of 180°C and below, of ZM61. The only similarity between the ZW6 and Z6 (and ZM61) results is the time to reach maximum hardness. The ageing response of ZW6 at 210, 180, 150 and 120°C is less than that of Z6 and ZM61. At 90°C. it is somewhat superior to Z6 but still inferior to ZM61 and at 60°C. practically identical to Z6, ZM61 is still superior.

The tensile properties of Z6 after ageing at 180°C are in reasonable agreement with the results reported by Hall,[19] although the additional response from the double ageing in this investigation was not as great and the properties are generally 1-2.0 t.s.i. **lower.** This is likely to be due to an extrusion size effect. Furthermore, the ageing response at 180°C is close to that indicated by the author[20] by interpolating the results presented for the Mg-Zn-Mn alloy, to zero % manganese.

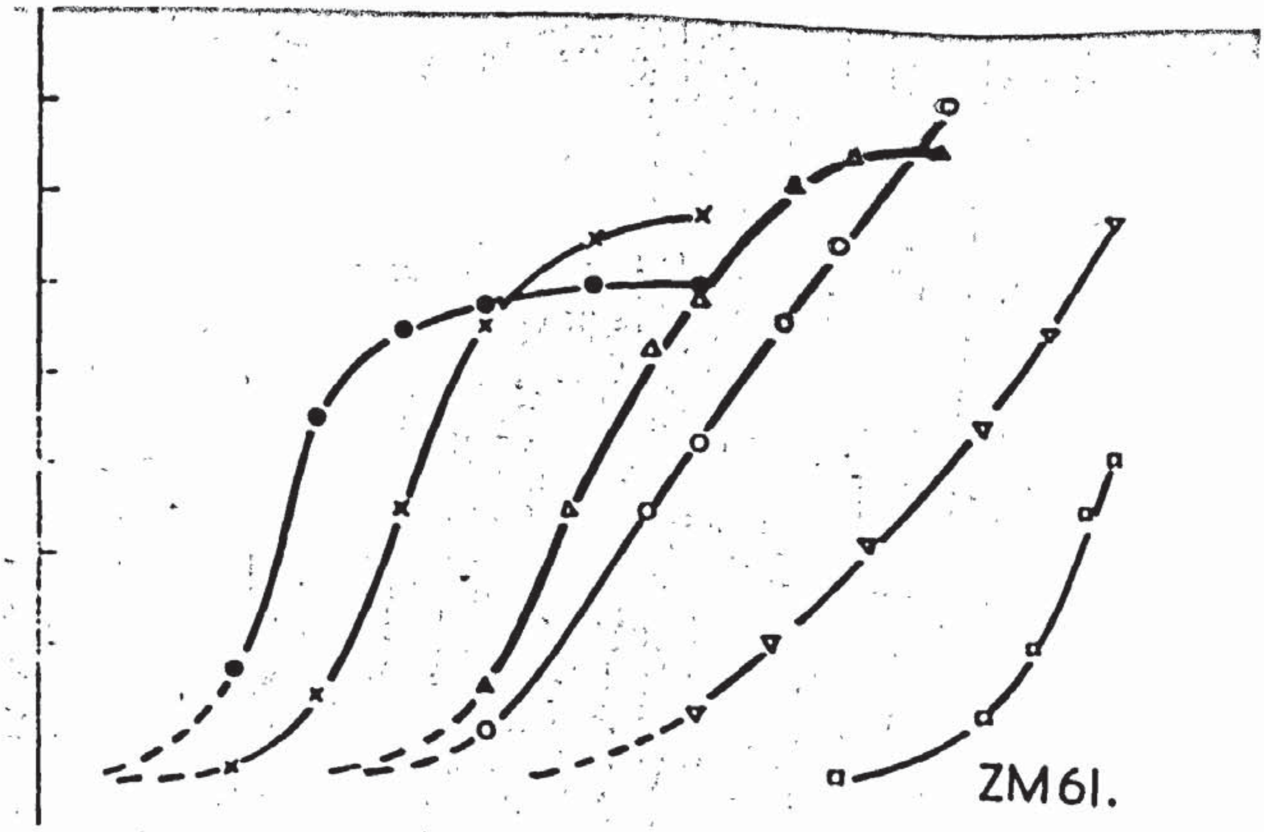
ZM61.

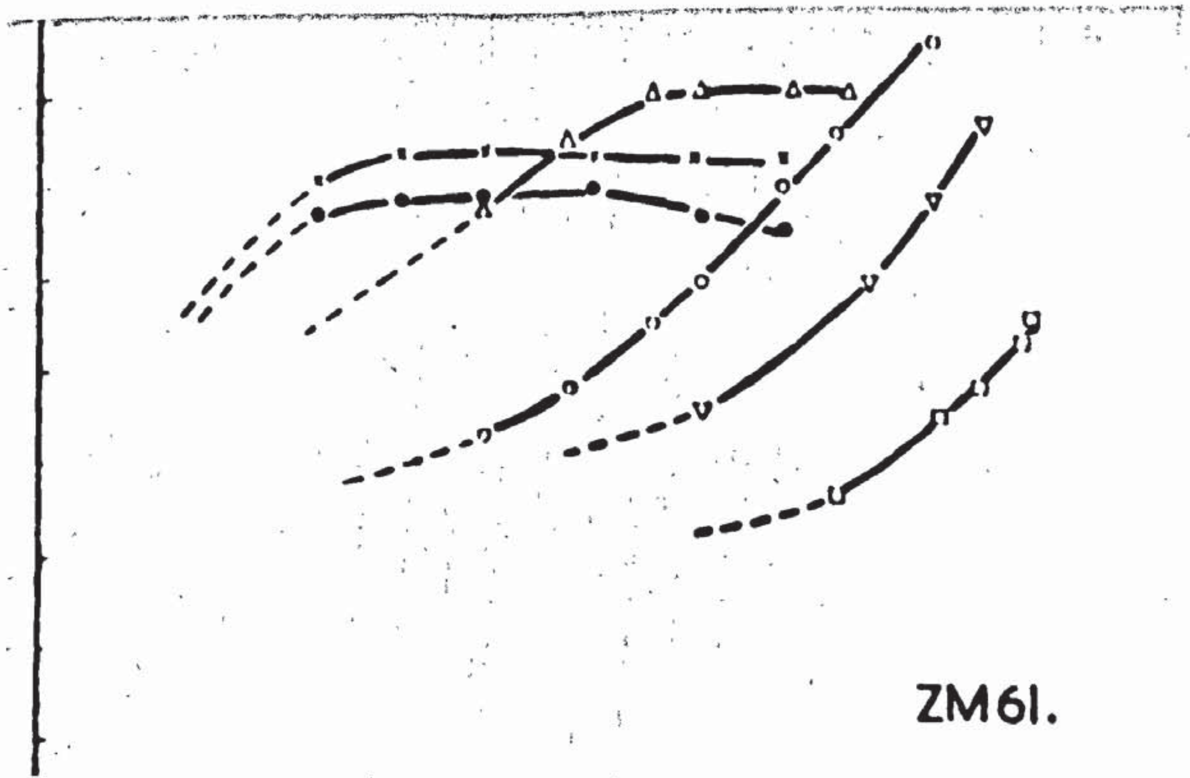
ZM61.

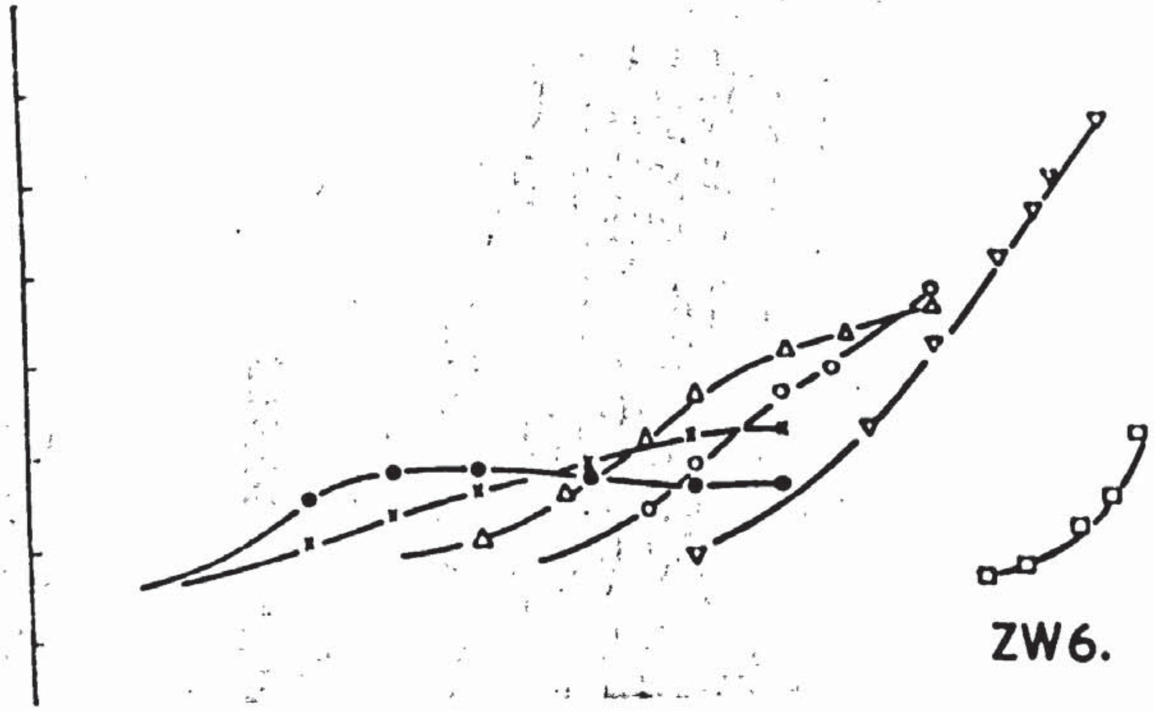

ZW6.

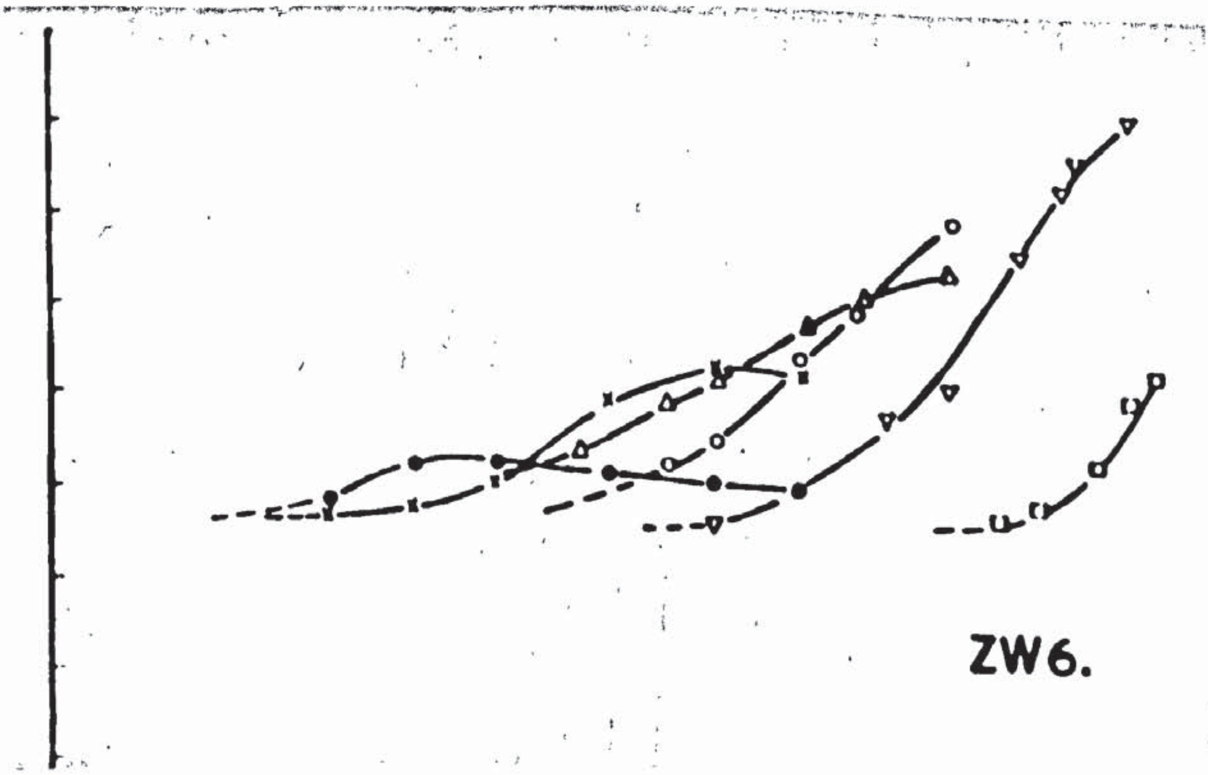

ZW6.

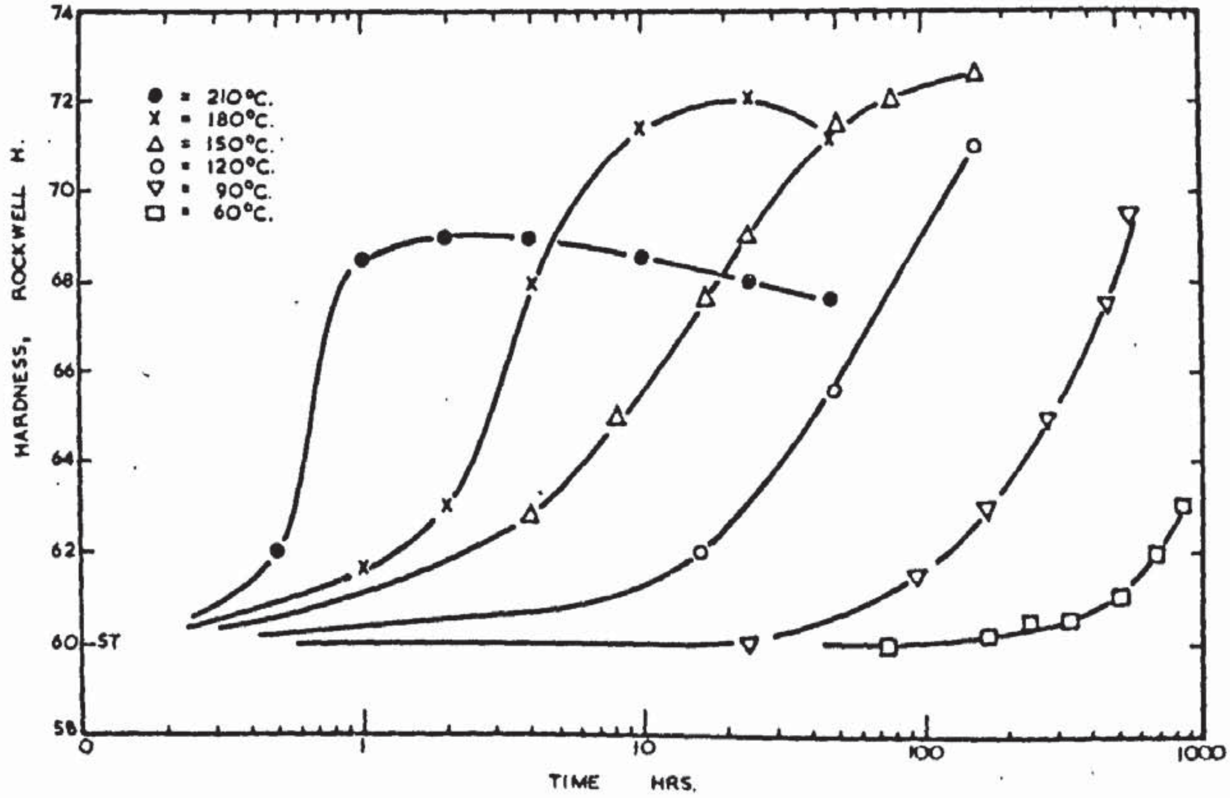

Figure 11.1.

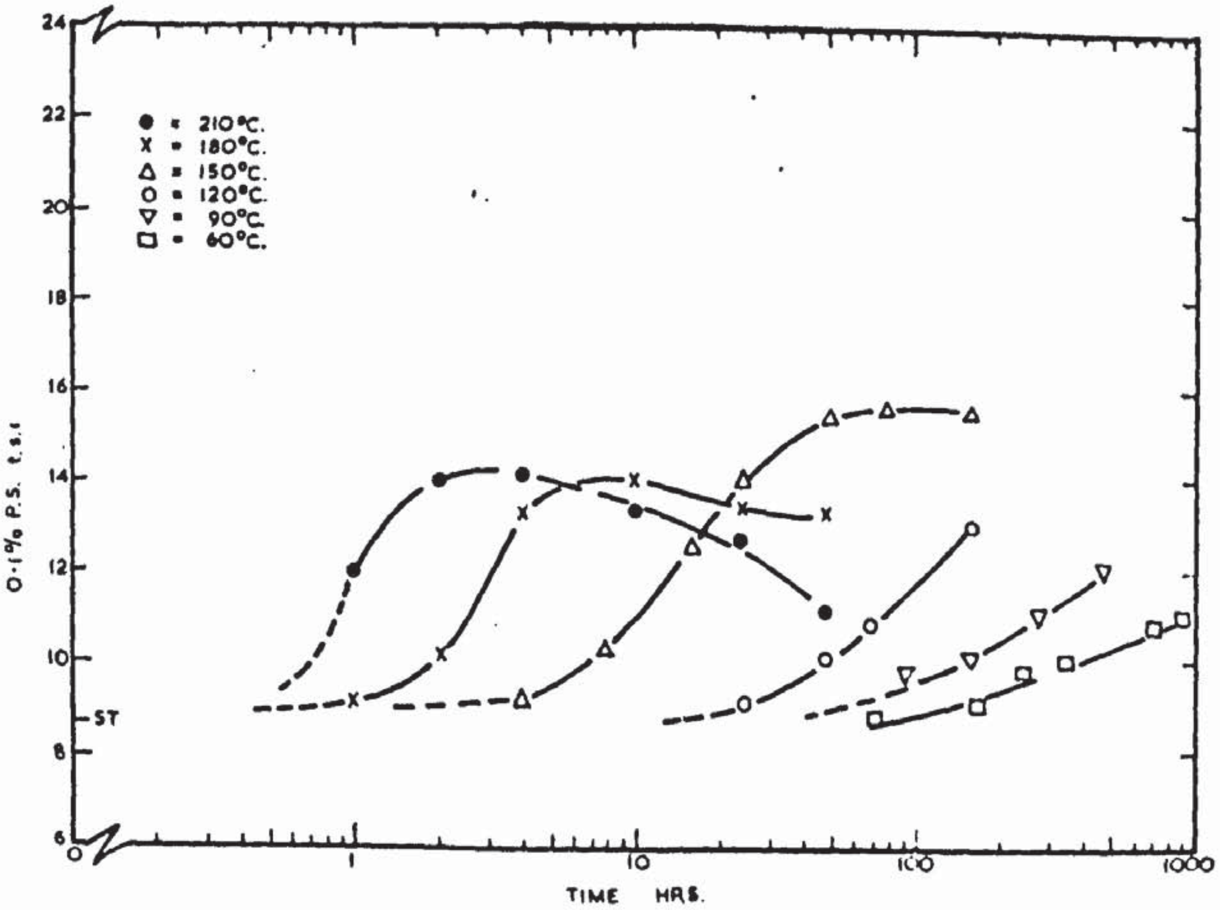

Figure 11.2.

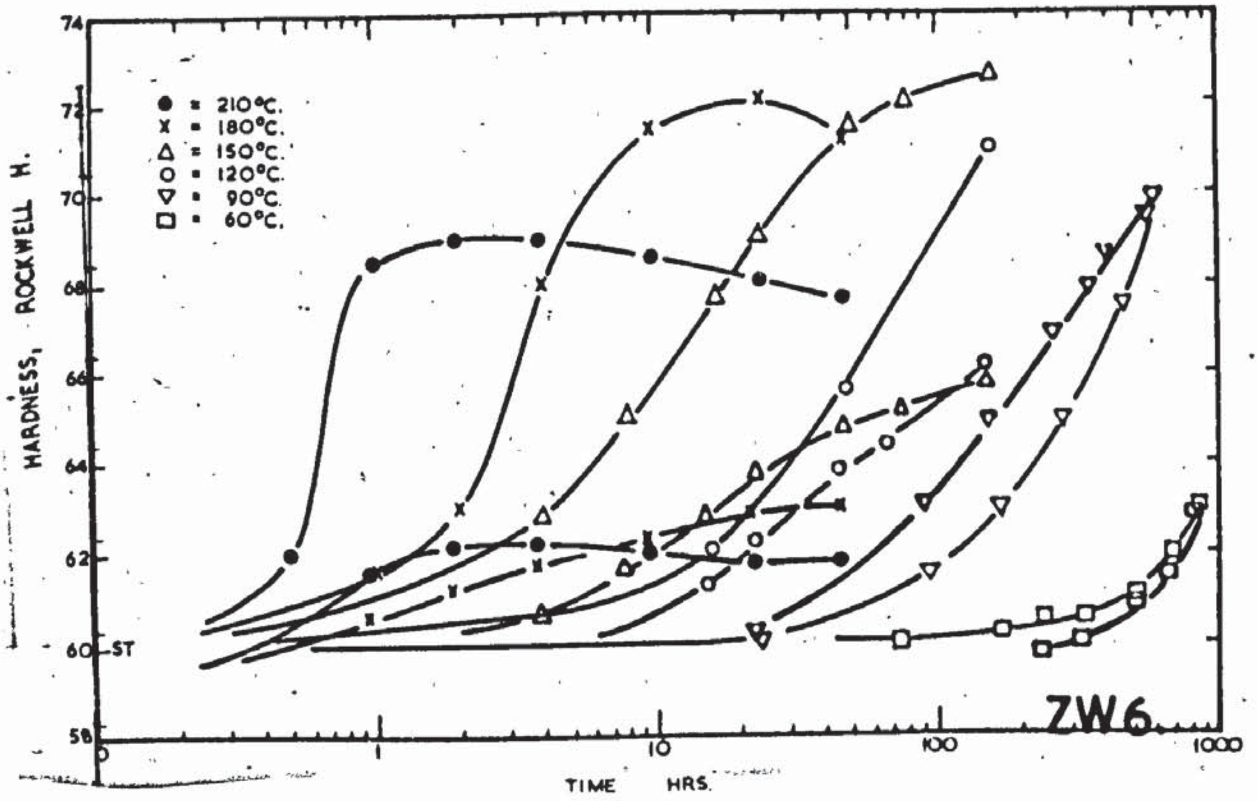

Figure 11.1.

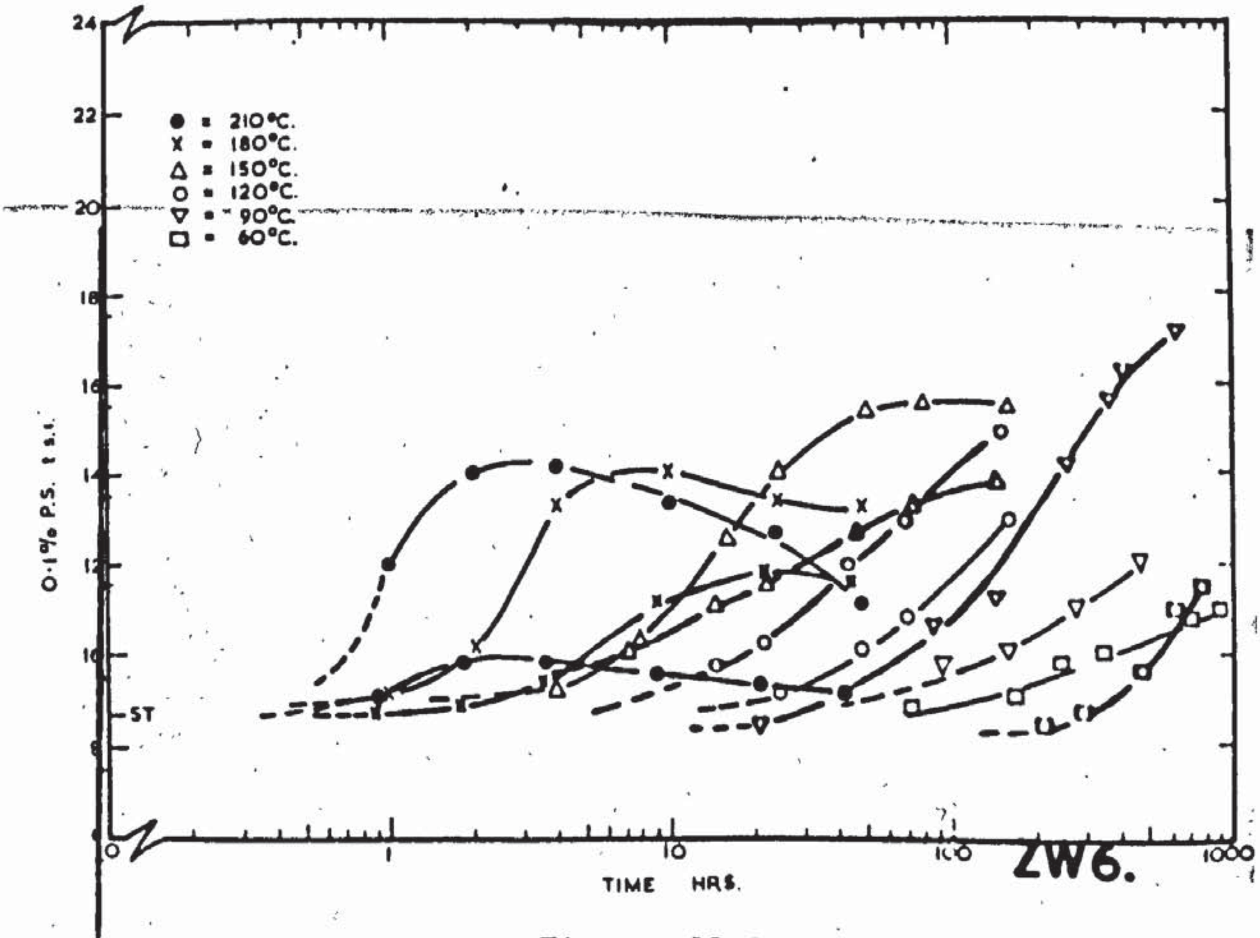

Figure 11.2.

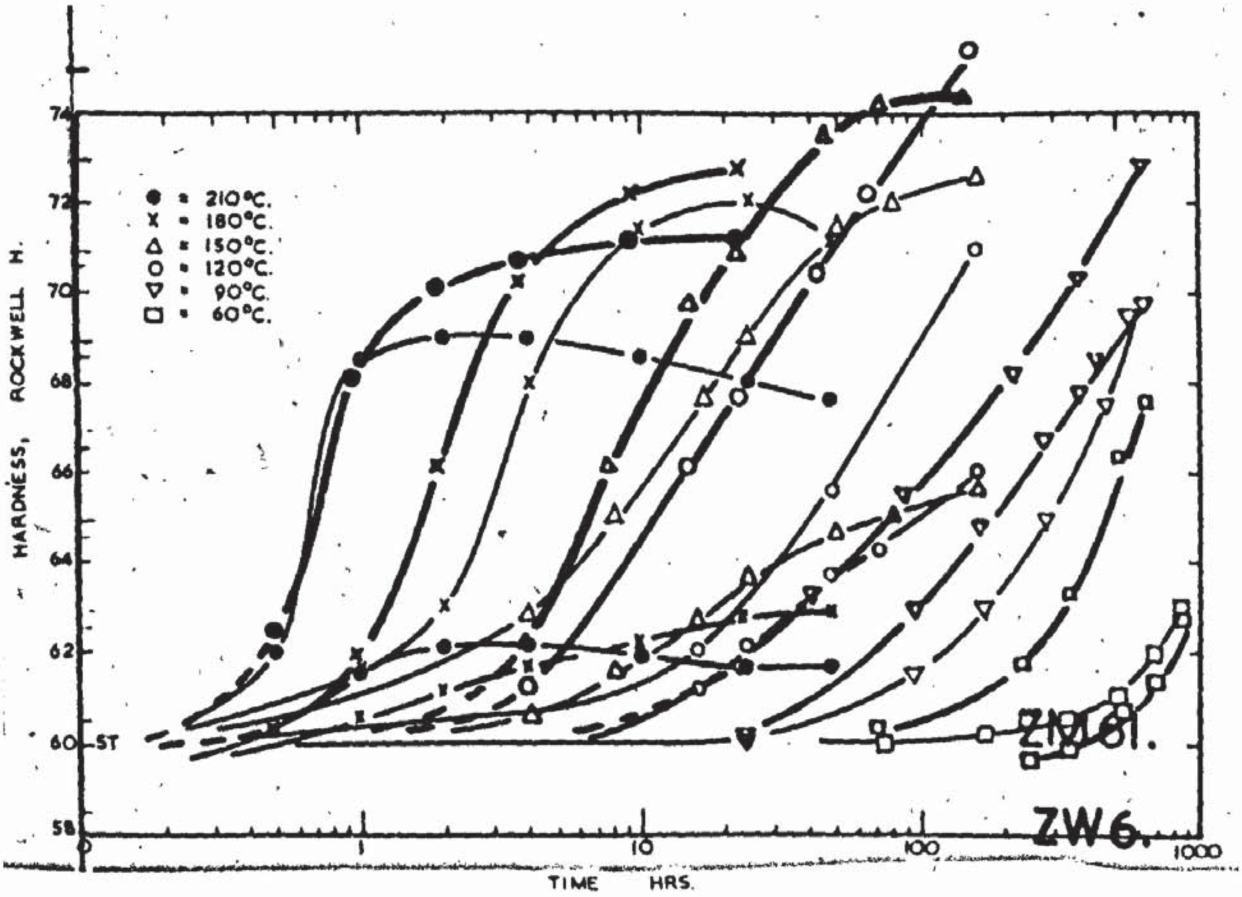

Figure 11.1.

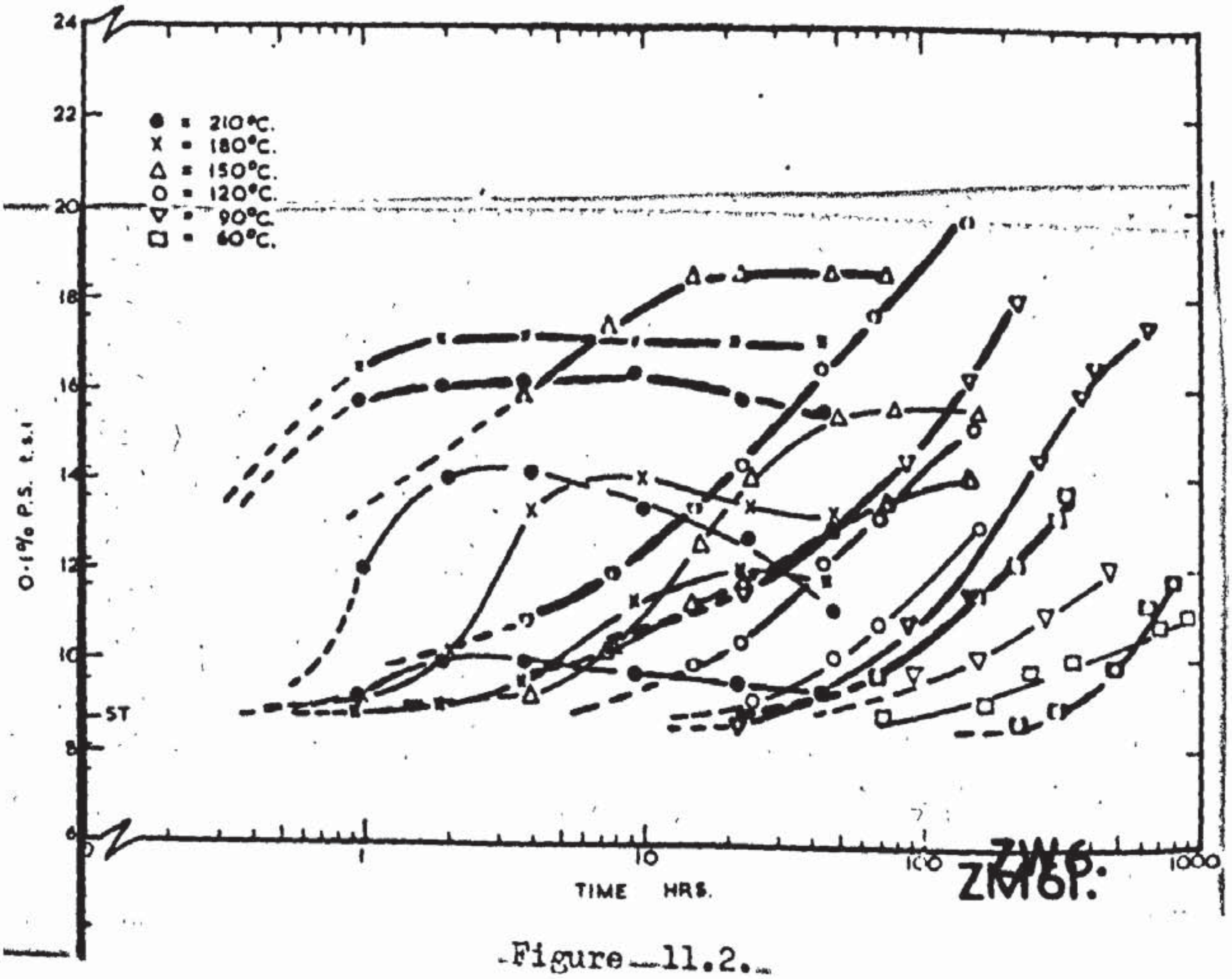

Figure 11.2.

A dramatic difference in the ageing rates between the three alloys is illustrated in Fig. 11.2. These curves were determined after an 8 day natural ageing period which is favourable to ZM61.

The electron microstructure of ZW6 has indicated the reason for the poor response of this alloy in terms of hardness and 0.1% P.S.. Zinc must be lost from the matrix due to the formation of a zinc-zirconium compound during solution treatment or pre-heating prior to hot working. The importance of this transformation is that on ageing at the lower temperatures the alloy will tend to behave as a more dilute Mg-Zn alloy. The ageing response will be consequently reduced. An interesting feature is that ZW6 aged at 90°C has a response superior to that of Z6. This has enabled ZW6 to attain quite high values for the 0.1% P.S., up to 22.0 t.s.i. after times of about 700 hours.

This is caused by the low temperature ageing treatment strengthening the relatively weak precipitate free areas left after the high temperature precipitation. When the precipitate size from the low temperature ageing approaches that formed during solution treatment the total result is a very marked strengthening. This has occurred with the 90°C treatment and has been illustrated in Fig. 6.13.. It is worth noting the poor response when the precipitate size is much larger than that previously present, after ageing at 180 or 210°C. for instance. This low temperature ageing contribution is not sufficient and the alloy remains relatively weak. It is considered that ZW6 can be regarded as a dilute Z6 alloy from the age hardening aspect, and it will not be discussed further.

The rapid ageing rate and high maximum 0.1% P.S. of ZM61 is clearly seen and the electron metallography has reflected this rapid change. The higher maximum properties have been shown to be related to a finer precipitate structure.

It has not been possible to explain the discrepancy between the ageing response of Z6, determined in this investigation and that of Clark, by differences in microstructure. It is considered to be due to a texture difference between the two materials. Twinning is a common deformation process in close packed hexagonal alloys at room temperature and the associated lattice movement can alter the ability of the matrix to accommodate the applied stress. For instance if a compressive stress is applied perpendicular to the basal planes then twinning will be possible. Thus if the basal planes in a sample are nearly parallel to the surface on which a hardness impression is made, twinning will not occur. The depth of penetration will therefore be less than if twinning could occur, which would happen if the basal planes are perpendicular to the surface. An apparent difference in hardness would result and the former situation will give the higher hardness. This is also true for applied stresses in directions making angles of approximately 50° with the hexagonal axis.

These effects could explain the discrepancy between the present results and those of Clark in that the two fabrication techniques have led to a texture difference. No indication of the fabrication process is given by Clark but if his $\frac{1}{8}$" x 1" bar stock was manufactured by rolling, a highly textured product would result. The basal planes would be inclined to within 15° of the rolled surface resulting in a 'no twin' situation on hardness testing that surface, with a resulting high hardness value. The similarity between the hardness values on longitudinal and transverse faces of samples in this investigation indicates a relatively isotropic structure. It is worth noting from Fig. 5.2 that of the three alloys examined, Z6 is the least isotropic.

The response to double ageing in the two alloys Z6 and ZW6 was determined and the additional response on the 0.1% P.S. in the binary Mg-Zn alloy at 170°C. after pre-ageing for 96 hours at 65°C. shown to be between 1.0 and 1.5 t.s.i.. With the Mg-Zn-Zr alloy this difference is only about 0.8 t.s.i.. This compares with an estimated 2.2 - 2.5 t.s.i. for the above temperatures for the Mg-Zn-Mn alloy. The effect of the low temperature ageing treatment on the rate of ageing at 170°C. was not determined, but it would be expected that the rate of ageing would be increased.

Advantages from double ageing treatments have been well known for well over twenty years and Wassermann[47] has demonstrated an increase of 16 X in the resistance to stress corrosion by varying the ageing treatment in two Al-Zn-Mg alloys. This is shown below with alloy composition, heat treatment and life in days of a loop test from a direction transverse to the rolling direction, with alternate dipping in 3.0% NaCl for 10 minutes followed by 50 minutes drying.

Composition:- 4.3% Zn, 2.5% Mg, 0.6% Mn Solution Treated for 1 hour at 500°C. W.Q..

Condition	0.2% P.S. t.s.i.	Life, days
5 days at 80° C.	22.2	136
5 days at 80° C. + 1 hr/150°C.	19.6	$\gg$ 2,160
2 days at 80° C.	17.7	383
2 days at 80° C. + 1 hr/170°C.	22.8	$\gg$ 2,160

With a copper containing alloy:-

Composition:- 4.2% Zn, 2.2% Mg, 0.6% Mn and 1.8% Cu.

Solution treated for 1 hour at 450°C. W.Q..

Condition	0.2% P.S. t.s.i.	Life days
5 days at 100°C.	26.0	990
5 days at 100°C. + 5 hrs/150°C.	26.6	$\gg$ 2,160

It is important to note that the improved resistance to stress corrosion is not associated with low tensile properties and in the copper free alloy a stronger sample in fact has about 5 times the resistance of a sample of the alloy with lower tensile properties.

Wassermann also clearly demonstrated the beneficial effect of double ageing on the tensile properties. This is shown below for the previously mentioned copper free alloy.

Condition	0.2% P.S. t.s.i.	U.T.S.t.s.i.
S.T. + 12 hrs. at 150°C. No delay	18.4	24.1
S.T. + 48 hrs/70°C. + 10 hrs. 150°C.	24.8	28.5

Hardy[45] in 1949 offered a satisfactory explanation for this phenomenon by invoking a critical size of nucleus formed at the lower temperature which is also stable at the higher temperature. This will cause a refinement of the precipitate usually formed when ageing at the second temperature only, thereby improving the properties. It is not important what this critical size (d_{crit} in Fig. 2.5 in this thesis) refers to, whether it be G.P. zones or a distinct precipitate, it is the stability of the size that is important. The results of the present investigation have shown that in the Mg-Zn-Mn alloy, discs approximately 60 A° in diameter and about 30 A° thick are stable over a wide range of temperature, 20-180°C.. The response to double ageing will depend on the number of zones/precipitates that exceed this size when the second ageing temperature is 180°C. .

Furthermore if the number is small then ageing at the higher temperature could result in an abnormally coarse precipitate and lower mechanical properties. With an increase in the number above this critical size, such that it exceeds the number of nucleation sites normally available during the high temperature ageing treatment, a refinement of the precipitate will result. The first situation will result in a detrimental effect and the second will produce a beneficial effect of the first low temperature ageing cycle, as indicated previously.

Clearly the rate of zone/precipitate formation during the first stage of the ageing treatment is an important factor and any difference in double ageing effects in different alloys can readily be explained by invoking any difference in d_{crit} and/or the factors controlling the rate of G.P. zone/precipitate formation or re-solution on raising to the second higher temperature.

In the Mg-Zn-Mn alloy after 22 months natural ageing the matrix contrast from the disc shaped G.P. zones indicated a zone diameter of 60-80A°. After 54 months naturally ageing although the number of zones had increased the maximum diameter was still 60-80 A°. The G.P. zone diameter after ageing at 60°C. for 240 and 696 hours was shown to be 90-100 A° These two results indicate strongly that the G.P. zone size is essentially temperature and not time dependent.

A second factor therefore now has to be considered, not only is the rate of zone formation important but the size to which they can grow at a constant temperature, will also have a controlling effect on the seeding at the higher temperature. If the limiting size is below the critical size then no precipitate refinement will occur. The optimum results will occur when the maximum G.P. zone size is just greater than the critical size and solute is therefore not consumed in unnecessary growth of the zones.

Electron Microstructure.

An important feature of the electron microscopy is that the structures presented are from samples on which actual mechanical properties were determined. The foil preparation technique developed enabled the structure of bulk material to be determined. The structures obtained can be related therefore directly to the mechanical properties. Furthermore, the comments of Byrne[10] on sample size are not applicable, as all heat treatments for the tensile and hardness specimens were done in the form of ¾" diameter bar 9" long. The samples for the direct quenching experiment were only .025" thick, and these were compared only with the same sized samples quenched to room temperature and not with samples treated in bulk form.

The formation of a number of different artifacts on the foil surfaces has been encountered and a method developed for their removal. These can lead to difficulties, particularly when the heat treatment is such that G.P. zones are expected. The investigation has shown that the G.P. zones in Z6 and ZM61 are in the form of discs on the (0001)Mg planes. It is considered that the reported observation of G.P. zones in Mg - 5.6% Zn after only 6 hours at 70°C. and at a magnification of 13,500 times, by Murakami et al[17] is in fact due to the presence of one of these artifacts.

The dramatic effect of foil orientation on the appearance of the precipitate has been clearly shown. This is due to the symmetry of the hexagonal unit cell in that the plane multiplicity is less than that found in the two cubic symmetries. This applies to the (0001) planes in particular, and has led to difficulty in resolving the two components of the matrix contrast from the disc shaped zones on the basal planes. Furthermore, measurement of the true precipitate size and distribution is hindered. The morphology of the precipitate in Z6, ZW6 and ZM61, needles perpendicular to the basal planes, means that needle length can only be measured in a foil with a $(10\bar{1}0)$ or $(11\bar{2}0)$ foil plane and the foil surfaces perpendicular to the basal planes. A situation where the first condition occurs and not the second is well illustrated in Fig. 5.36. When needles of up to 27,000A° can form as shown in Z6, the above conditions are essential but difficult to achieve.

Foil orientation effects have undoubtedly contributed to the significant difference in the numbers of needles/square micron reported by Hall and those in this investigation. Ageing for 10 hours at 180°C produced a needle density of 100-130 per square micron (determined from an (0001) foil), compared to the 40 per square micron of Hall. It has also been observed that double ageing increases this 100-130 to 300-360 per square micron with only a small improvement in properties. All of these results do not take account of foil thickness and are therefore speculative in that the differences outlined could be explained simply by invoking a thickness difference. It is proposed not to use a difference in number of precipitates to illustrate any difference between samples and/or alloys, but to use needle length as a nucleation criterion. This is possible in Z6, ZW6 and ZM61 as the needles grow perpendicular to the basal planes and true needle length measurements are possible if the conditions previously outlined are operative. If it is assumed that the chances of needles coalescing is small then the needle length will provide an indication of the number of active nuclei in that increasing the number of nuclei will cause a decrease in the final length of the needles at a constant initial solute concentration.

The orientation relationships between $MgZn_2^1$ and $MgZn_2^2$ and the matrix reported by Gallot[3] were confirmed but $MgZn_2^2$ was observed after ageing for 96 hours at 90°C.. The minimum time and temperature required for its appearance from Gallots results is 72 hours at 150°C.. The equilibrium triclinic Mg_2Zn_3 was not examined in detail in this investigation.

The ageing sequence in the Z6 alloy ~~at temperatures of 60°C and less~~ has been shown to be

$$\begin{tikzcd} & \text{Needles of } MgZn_2 \text{ such that (0001) ppte } \perp \text{ to (0001)Mg.} \\ \text{Disc shaped zones on (0001) planes} \arrow[ur] \arrow[dr] & \\ & \text{Discs of } MgZn_2 \text{ such that (0001) ppt // (0001)Mg.} \end{tikzcd}$$

At ~~At higher temperatures~~, 90°C. or above, the $MgZn_2^2$ precipitate as discs on the (0001)Mg planes can co-exist with the $MgZn_2^1$ needles.

There is a marked similarity between the microstructures of Z6 and ZM61 in terms of precipitate morphology but a marked difference in terms of precipitate size and distribution. The spacing between the precipitates, length of the needle precipitate and diameter of the disc precipitate are always less in ZM61 than in Z6. The maximum size of these two precipitates in ZM61 was generally one quarter of that in Z6 after comparable heat treatments. This indicates that the nucleation step in the ternary alloy is considerably easier than in the binary alloy.

Considering alloys Z6 and ZM61, ageing at 180°C after 8 days delay gives an increase in 0.1% P.S. of 5.4 t.s.i. and 8.5 t.s.i. respectively. Double ageing the Z6 adds about another 1.0 - 1.5 t.s.i. but gives a significant decrease in the needle length (compare Fig. 5.44 with 5.45). If the difference in ageing response were due to a difference in the G.P. zone solvus temperature, it becomes difficult to explain the reason for the response in Z6 being always less than that of ZM61. Ageing both alloys below their solvus and then above to achieve a double ageing response from precipitate refinement alone should produce an equal ageing response. Hall[19] has reported a double ageing response on the 0.1% P.S. of 8.0 t.s.i. for an alloy close to Z6 but an increase of only 2.0 t.s.i. on the T.S.. This investigation gave 6.5 t.s.i. and 3.5 t.s.i. on the 0.1% P.S. and T.S. respectively. The Mg-Zn-Au alloy also examined by Hall gave an ageing response of 8.9 t.s.i. on the 0.1% P.S. and 6.6 t.s.i. on the T.S.. It is suggested that a texture difference between samples is having an indeterminable effect on these properties. For example, the 0.1% P.S. of the Mg-Zn-Au alloy is reported to be higer than that of the Z6 (9.1 t.s.i. and 7.3 t.s.i. respectively) whilst the T.S. is lower (14.3 t.s.i. and 17.3 t.s.i.).

The direct quenching experiments have shown that the G.P. zone solvus for both the Z6 and ZM61 is greater than 120°C..

The reversion experiments have also shown a similarity between these two alloys. These results indicate either a G.P. zone solvus greater than 200°C. or that a disc shaped zone 60-80A° in diameter and 25-40A° thick is stable at 200°C, which could be above the solvus.

It is of little practical consequence which of these is operative, the results will be very similar. Direct quenching experiments are essentially used to determine a critical temperature, as previously defined, and not to control this temperature. Although it has provided a method for explaining delay effects at room temperature prior to artificial ageing, direct quenching, because of the practical difficulties is of little importance in the non-ferrous industry. Additionally with the wide variation in cooling rates after solution treatment of large section sizes on an industrial scale, it is possible that the structures reported, in many aluminium alloys generally from small, rapidly quenched speciments , are only representative of a small proportion of industrially heat treated alloys. This along with a significant variation in the rate of heating to the ageing temperature probably serves to make the reported structures even less representative of the structure of aluminium alloys in the condition in which they are actually used.

Nucleation of the Precipitates.

As indicated previously an important factor controlling the nucleation of a second phase is the accommodation of this new phase in the solid solution. It has been shown by Nabarro[48] that the energy associated with any dilatational effects and the coherency strain energy are lower for a plate or disc shaped particle than for a sphere. The initial stage in the precipitation in Z6 and ZM61 has been shown to take the form of disc shaped zones on the basal planes.

Kelly and Nicholson[1] considering the morphology and crystallography of precipitation in many alloy systems indicated that when the matrix elastic constants are anisotropic the precipitate forms as discs. The maximum strain energy of the precipitate is accommodated in the direction of minimum elastic modulus i.e. discs on $\{100\}$ planes in most F.C.C. alloys

In magnesium the elastic modulus is a maximum in the 0001 direction[49] at 7.3×10^6 lbs/in^2. In the $[11\bar{2}0]$ direction it is 6.54 lbs/in^2 and the minimum occurs at an angle of 53°45' to the $[0001]$ direction and the value is 6.2×10^6 lbs/in^2. These values are at room temperature. Alloy additions do not change them significantly but there is a decrease in modulus to 5.5×10^6 lbs/in^2 at 300°C. (assuming an initial average of 6.5 $\times 10^6$ lbs/in^2).

The disc shaped zones in Z6 are not growing in the direction of minimum modulus, but they are growing at right angles to the direction of maximum modulus. The growth of $MgZn_2$ as needles ($MgZn_2^1$) or discs ($MgZn_2^2$) such that a given crystallographic direction is at right angles in these two forms, indicates a delicately balanced nucleation process. Increasing the temperature of ageing increases the amount of 'disc' oriented $MgZn_2$. This is probably related to a change in the anisotropy of the elastic constants with temperature such that this orientation is favoured.

An important consequence of this is that if the nucleation step is carried out and continued at a low temperature, 70°C or lower for instance and the transition from disc shaped G.P. zones to needles has progressed significantly then on increasing the ageing temperature thesewill act as nuclei for continued needle growth at this second ageing temperature. Needles perpendicular to the basal planes are the most efficient shape and orientation to inhibit dislocation movement since the Burgers vector of dislocations contributing to plastic deformation of magnesium are in the basal planes. With an increase in the needle orientation at the expense of the disc, a 'double' ageing phenomenon is possible, which is not necessarily related to the G.P. zone solvus temperature.

In the ternary Mg-Zn-Mn alloy the zones are also in the form of discs on the $(0001)_{Mg}$. Electron diffraction from samples naturally aged have shown the zones to be of a hexagonal crystal structure with an orientation relationship of

$(11\bar{2}0)$ ppte. // (0001) Mg and
(0001) ppte. // $(11\bar{2}0)$ Mg.

The corresponding lattice spacings are

(a) 2.70 A° ppte // 2.59 Mg and
(b) 1.45 A° ppte // 1.60 Mg.

As the precipitate is in the form of a disc both its face and its edge can be treated as a planar interface. The strain from the disc will be relieved when an interface dislocation is nucleated. This is dependent on the Burgers vector of the dislocation. In (a) above, which is the situation with regard to the thickness of the disc, a dislocation can nucleate when the disc has attained a thickness given by

$$\frac{2.59 \times 10^{-8}}{4.0 \times 10^{-2}} = 65A^{\circ}$$

In case (b) the diameter of the disc for the nucleation of a dislocation is

$$\frac{1.6 \times 10^{-8}}{9.8 \times 10^{-2}} = 16A^{\circ}$$

These values can be regarded as the lower limit, as nucleation of the interface dislocation may be difficult. The "arrowhead" dislocations observed in the Mg-Zn and Mg-Zn-Mn alloys were spaced at 55-60 and 70-75 A° respectively. According to the measured and calculated (11$\bar{2}$0) spacings of $MgZn_2^1$ the misfit in the $[0001]$ Mg direction is 0.386% and 1.53% respectively. This should result in the nucleation of an interface dislocation at 670 and 169 A°, respectively. Figure 10.6 illustrated a possible instance where the interface dislocations are widely spaced at 500 - 1200 A°, indicating extended coherency.

Considering the diameter of the disc, the misfit, using the calculated interplanar spacing is

$$\delta = \frac{2(1.60 - 1.42)}{1.6 + 1.42} = .012 \text{ or } 12\%$$

This will cause nucleation of a dislocation every 13 A°, which is slightly less than that in the Mg-Zn-Mn alloy.

An additional complication arises as a result of the cross-section shape of the needles, in the form of a parallelogram with its faces parallel to $[11\bar{2}0]$ Mg. This was shown in Fig. 10.18 and is represented schematically below:-

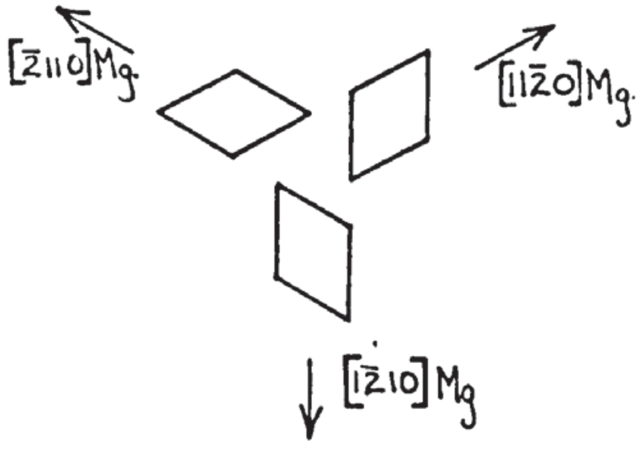

It is evident that in either a $(10\bar{1}0)$ or $(11\bar{2}0)$Mg foil three aspects of the needles will be observed and at any one instant only one of these orientations will be favourably oriented to show contrast from interface dislocations.

The role of vacancies in the nucleation of the zones in Z6 and ZM61 is not precise. Clearly defined precipitate free zones comparable to those published by Lorimer and Nicholson[34], were not observed during this investigation.

Jacobs and Pashley[35] have indicated that a wide P.F.Z. is usually expected over a range of 50°C. below the critical temperature. As no P.F.Z. was observed after ageing at 120°C., either after direct guenching or after quenching to room temperature, it is reasonable to assume that the critical temperature for Z6 is nearer to 200°C than reported[19] 75-80°C.. This must also be true of ZM61. Nucleation occurring very close to the grain boundaries has been shown in Figs. 5.17, Z6 aged at 90°C. and Figs. 8.8, 8.9 ZM61, room temperature. The structures shown in Figs. 8.23, 24, 25, ZM61 aged at 180°C and Fig. 8.33, at 210°C. could be the result of a combination of hetrogeneous and homogeneous nucleation. The precipitate on the $(11\bar{2}0)$ planes illustrated in Fig. 8.25 could arise from slip during the quenching operation. In Fig. 8.33, which is from a foil orientation almost perpendicular to that shown in Fig. 8.25, it could be argued that the precipitation to the upper left is due to homogeneous nucleation and that the sparse, coarser precipitate, due to heterogeneous nucleation. Fig. 8.25 could possibly be invoked to provide an opposite explanation.

The effect of increasing time on the G.P. zone size in ZM61 has been demonstrated and the line of no contrast at 60-80A° is quite constant for times up to 54 months. At 60°C. times of 240 and 696 hours have produced maximum lengths of 90-100A° in both instances. Transformation to the needle precipitate was evident after 260 hours at 60°C, thus the length of the line of no contrast at 90-100A° must represent its maximum size at this temperature. No attempt has been made to count the numbers of G.P. zones because of the dramatic effect of foil thickness, but the above result indicates that the maximum size is temperature dependent and not time dependent. The zone growth rate and associated matrix contrast is ZM61 or Z6 is such that further research should enable a separation between 'thermodynamic' and 'kinetic' theories to be achieved by direct observation of the zones thereby not having to rely on a coarsening heat treatment which introduces a size/stability effect.

It is suggested that the more rapid nucleation in ZM61 when compared to Z6 is due to the effect of the manganese directly and not due to vacancies. It is possible that the manganese atoms modify the precipitate/matrix interface thereby decreasing the activation energy for nucleation. A similar overall effect is possible if the precipitating phase were different. Manganese dissolved in the $MgZn_2$ to form the ternary compound is therefore a possibility. The electron diffraction results have shown that the c spacing of the precipitate in the ternary alloy is 8.7A°, which is greater than that of $MgZn_2$. The ternary compound in which the interplanar spacings have been measured and compared with those from a unit cell of a - 5.24 and c = 17.1, was extracted from a more concentrated alloy as reported previously by the author.

This unit cell has certain features similar to that of $MgZn_2$ and the electron diffraction results have not permitted differentiation between them. For instance the interplanar spacings of planes of the type (hkio) will be practically identical. Other planes in the larger unit cell of the ternary compound can be indexed in the smaller cell. For instance the (0002) spacing in the larger will be close to the (0001) spacing of the smaller and $(11\bar{2}2)$ planes in the larger, close to $(11\bar{2}1)$ in the smaller. The electron diffraction results have shown an increase in the c spacing of the precipitate and the 8.7 A° spacing previously referred to is considered to be the (0002) ternary compound spacing, giving a c spacing of 17.4 A°. This is slightly larger than the 17.1 A° measured value.

This similarity between these two compounds and the unreliable interplanar spacings of $MgZn_2$ have hindered the achievement of precise results.

The results from the Mg-Zn-Mn alloy demonstrate that nucleation of the precipitates is easier than in the binary Mg-Zn alloy. The misfit in the $[0001]$ Mg direction in the ternary alloy is about 4.0% and about 10% in the $[11\bar{2}0]$ Mg direction. This compares with something between about 0.5 and 1.5% for the MgZn alloy in the $[0001]$ Mg direction and about 12% in the $[11\bar{2}0]$ Mg direction.

The zones in both alloys are in the form of discs, the difference between the two alloys in terms of rapidity of zone formation must occur at this stage. The misfit in the radial direction of the disc is 10% and 12% for the ternary and binary alloy and the discs have grown in a direction perpendicular to the direction of maximum elastic modulus. The difference between the misfits is such that the zones in the ternary alloy would be expected to form more readily than in the binary alloy. The misfit in the $[0001]$ Mg direction about 4% and 1% for the ternary and binary respectively, clearly indicates the reason for the precipitates to grow as needles in this direction. The difference between the two precipitate misfits is such that growth of the needles in the binary alloy will be easier than in the ternary alloy.

Magnesium - Zirconium.

The results of the hydriding treatment on this alloy were not as previously reported, when the alloy was hydrided in the homogenised condition. It is clear that the results of Harris et al are the result of hydriding material always in the as extruded condition. The moisture content of the CO_2 used as a protective atmosphere must have caused extensive hydriding thereby preventing the diffusion of the zirconium. The distribution of zirconium in the structures presented therefore is essentially as that of the alloy in the as extruded condition.

The homogeneous distribution of zirconium hydride obtained in this investigation as shown by Fig. 7.2 for instance, is the result of homogeneously distributing the zirconium prior to any hydriding having taken place. This structure is therefore representative of a homogenised and hydrided magnesium - zirconium alloy.

The discs of zirconium hydride are on the (0001)Mg planes and the very thin, presumably coherent discs, have been imaged by dislocation ring contrast. This contrast was mistaken by Mushovic[27] for matrix strain contrast with the assumption that the precipitate was spherical.

The results of this examination of the Mg-Zn alloy proved that the high temperature precipitating phase in ZW6 was not zirconium hydride.

CONCLUSIONS.

1. The G.P. zones in Z6, ZW6 and ZM61 are in the form of discs on the matrix basal planes.

2. The G.P. zone solvus or critical temperature of Z6 and ZM61 is above 120°C..

3. Disc shaped zones 70 A° in diameter and 30 A° thick in ZM61, formed at room temperature are stable to a rise in temperature to 180°C. This zone size is the maximum observed in ZM61 after prolonged natural ageing. This size must also be equal to or greater than d_{crit}.

4. The small ageing response in ZW6 is due to the precipitation of a Zn-Zr phase during solution treatment, thereby decreasing the effective zinc content of the alloy.

5. The response to double ageing in Z6 and ZM61 can be explained by a change in the ratio between the two precipitate forms. An extensive low temperature nucleation treatment provides nuclei for the needle precipitate such that during the coarsening treatment, needles grow preferentially. This response is not related to the critical position of the G.P. zone solvus with respect to the nucleation and coarsening temperatures, it would occur if all ageing heat treatments were carried out below this solvus. The double ageing also results in a marked decrease in the length of the needle

precipitate, and the overall increase in the ageing response is due to a combination of these two processes.

6. The additional ageing response in ZM61 when compared to Z6, is due to the precipitation of a ternary compound which has a hexagonal crystal structure. The unit cell is such that there is a similarity between certain interplanar spacings in this compound and $MgZn_2$. The nucleation barrier for the ternary phase is less than that for $MgZn_2$ and zone formation at low temperatures occurs more rapidly in ZM61 than Z6.
7. The size of both the needle and disc precipitates in ZM61 is consistently less than that in Z6 or ZW6 after similar thermal treatments.
8. A uniform distribution of thin disc shaped precipitates of zirconium hydride is formed on hydriding ZA, which has been homogenised such that the zirconium is evenly distributed throughout the matrix.

REFERENCES

1. Kelly A. and Nicholson R.B., "Precipitation Hardening", Progress in Materials Science, 10 (1963).
2. Partridge P.G. Metallurgical Review 118, Metals and materials (Nov. 1967).
3. Gallot J. Ph.D. thesis, Faculty of Science, University of Rouen. (1966).
4. Fisher A. J. Inst. Met. (1941), 67, 289.
5. Fox F.A. and Lardener E. J. Inst. Met. (1943) 69, 373.
6. Talbot A.M. and Norton J.T. Trans. Am.Inst.Min.Engrs. (1936) 122, 301.
7. Leontis T.E. and Nelson C.E. Trans.Am.Inst.Min.Engrs. (1951), 191, 120.
8. Murakami Y., Kawano O. and Tamura H., Mem. Fac. Engng., Kyoto University, 24, Part 4, 411 (1962).
9. Clark J.B., Acta Met., (1968), 16, 141.
10. Byrne J.G. Scripta Met., (1968) 2, 477.
11. Grogan J.P. and Haughton J.L., J. Inst. Met. (1943) 69, 241.
12. Jones W.R.D. Inst. Met. Ann. Eq. Diag. No.28.
13. Byrne J.G., Acta Met. (1963), 11, 1023.
14. DeLuca R. and Byrne J.G., Acta Met. (1965), 13, 1191.
15. Clark J.B. and Rhines F.N., Trans. Amer. Inst. Min. Met. Eng. (1957), 209, 425.
16. Sturkey L. and Clark J.B., J. Inst. Met. (1959-60) 88, 177.
17. Murakami Y., Kawano O. and Tamura H., Kyoto University, Memoirs of Faculty of Eng. (1962), 24, 102.
18. Clark J.B., Acta Met., (1965), 13, 1281.

19. Hall E.O. J. Inst. Met. (1968), 96, 21.

20. Stratford. D.J., M.Sc. Thesis, University of Aston in Birmingham, 1966.

21. Lorimer G.W. Ph.D. Thesis, University of Cambridge, 1967.

22. Schaum J.H. and Burnett H.C., J. Res. Natl. Bur.Stand. 1952, 49, 155.

23. Greenfield P., Smith C. and Taylor A., Trans. A.I.M.E. (1961), 221, 1066.

24. Harris J.E., Partridge P.G., Eeles W.T. and Rickards G.K., J. Nuclear Mats. (1963) No. 3, 9, 339.

25. Harris J.E. and Partridge P.G., J. Inst. Met. (1964-65) 93, 15.

26. Harris J.E. and Partridge P.G., Third European Regional Conference on Electron Microscopy, p.143.

27. Mushovic J.N., Ph.D. Thesis 1967, Rensselaer Polytechnic Institute, Troy, New York.

28. Yamamoto A. and Rostoker W., Trans. A.S.M. 1958, 50 1095.

29. Sturkey L., Trans A.I.M.E. (1960) 218, 468.

30. Murakami et al op.cit (8),417.

31. Hales R. Dobson P.S. and Smallman R.E. Met.Science Journal, (1968), 2, 224.

32. Mushovic J.N. and Stoloff N.S., International Conf. on Structure of Metals and Alloys, Tokyo, 1967.

33. Nicholson R.B., J. of the Sheffield Univerity Met. Soc. (1966), 5, 19.

34. Lorimer G.W. and Nicholson R.B., Acta Met., (1966) 14, 1009.

35. Jacobs M.H. and Pashley D.W., Proceedings of Int. Conf. on Phase Transformations. Manchester, 1968.

36. Beton R.H. and Rollason E.C., J. Inst. Met. (1957-58) 86, 77.

37. Jogodzinski H. and Lavos F., Z. Metallkunde (1949), 40, 296.

38. Hardy H.K., J. Inst. Met., (1951), 79, 321.

39. Turnbull D., "Defects in Crystalline Solids" 1955, London Phys. Soc..

40. Hirsch P.B., Howie A., Nicholson R.B., Pashley D.W., and Whelan M. J., "Electron Microscopy of Thin Crystals" Butterworths, 1965.

41. Ashby M.F. and Brown M., Phil. Mag. (1963), 8, 1083.

42. McKeehan L.W., Z. Kristallogr. (1935), 91, 501.

43. Busk R.S., J. of Metals, (1950), 188, 1460.

44. Carpenter G.J.C. and Garwood R.D., J. Inst. Metals. (1966), 94, 301.

45. Hardy H.K., J. Inst. Metals, (1949), 75, 707.

46. Douglass D.L. nd VanLanduyt, J., Acta Met. (1966), 14, 491.

47. Wassermann G. Brit. Intell. Object. Sub. Cśte. Gp.2., Publ. No. HEC03757, 1946.

48. Nabarro F.R.N., Proc. Roy. Soc., A175, (1940), 519.

49. "The Technology of Magnesium and its Alloys", F.A. Hughes and Co. Ltd., London.

Acknowledgements

The author is indebted to the Science Research Council for the award of a maintainance grant and to Birmetals Ltd., for additional financial support and supply of materials. The author is also indebted to Mr. Fisher of Magnesium Elektron Ltd. for carrying out the hydriding treatments on the Mg-Zr alloy.

The author records his gratitude to Dr. Arrowsmith, his supervisor and to Professor Alexander for provision of facilities in the Dept. of Metallurgy in The University of Aston in Birmingham.

APPENDIX

The complete ageing curves for Z6 and ZW6 are shown in Figs. A1 to A12. The Z6 was solution treated at 380°C. and the ZW6 at 420°C. both for 2 hours followed by water quenching.

Figures A1 to A6 are for Z6 and A7 to A12 for ZW6.

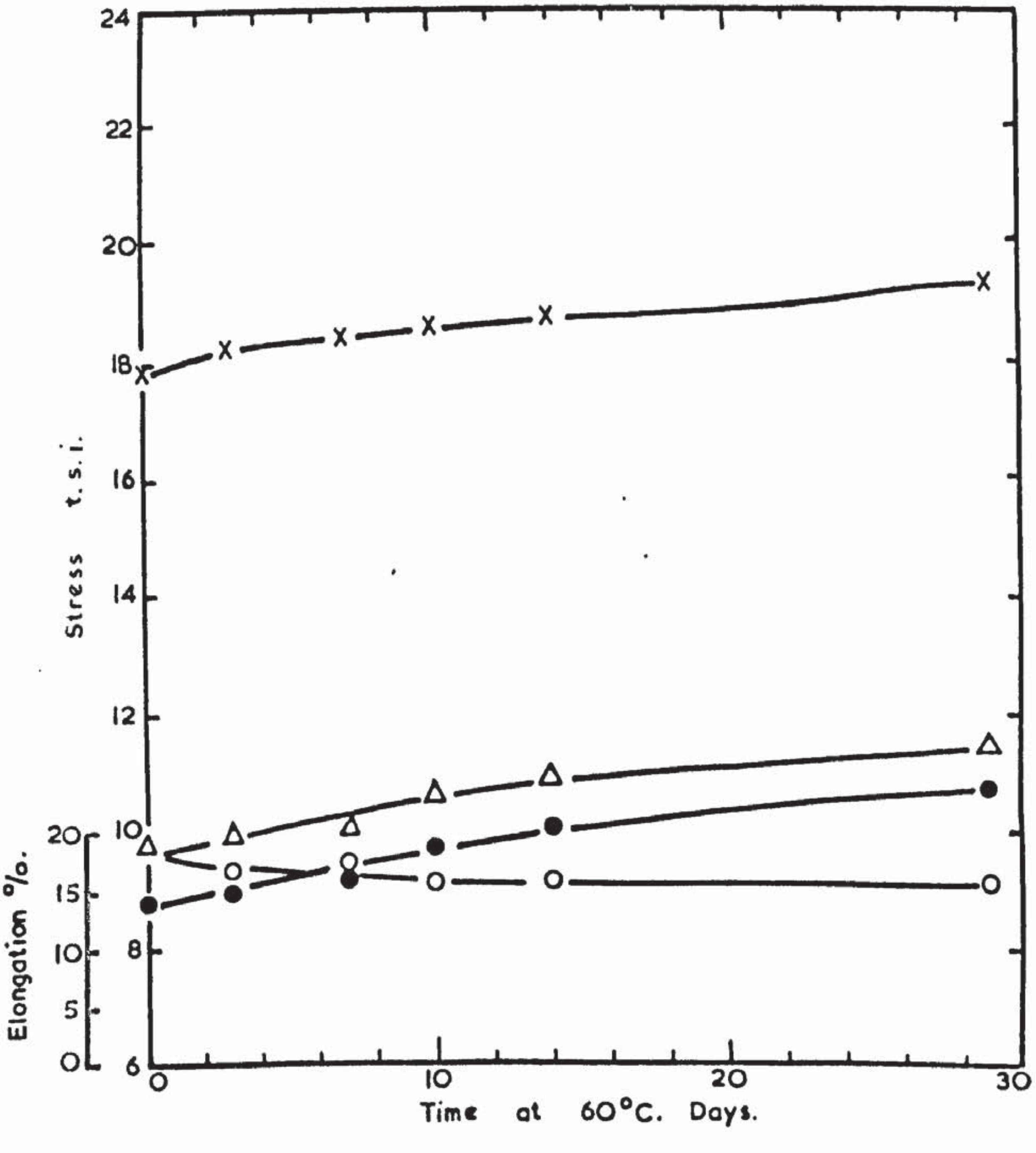

Stress t.s.i.
24
22
20
18
16
14
12
10
8
6
Elongation %.
20
15
10
5
0
0
10
20
30
Time at 60°C. Days.

Figure A1

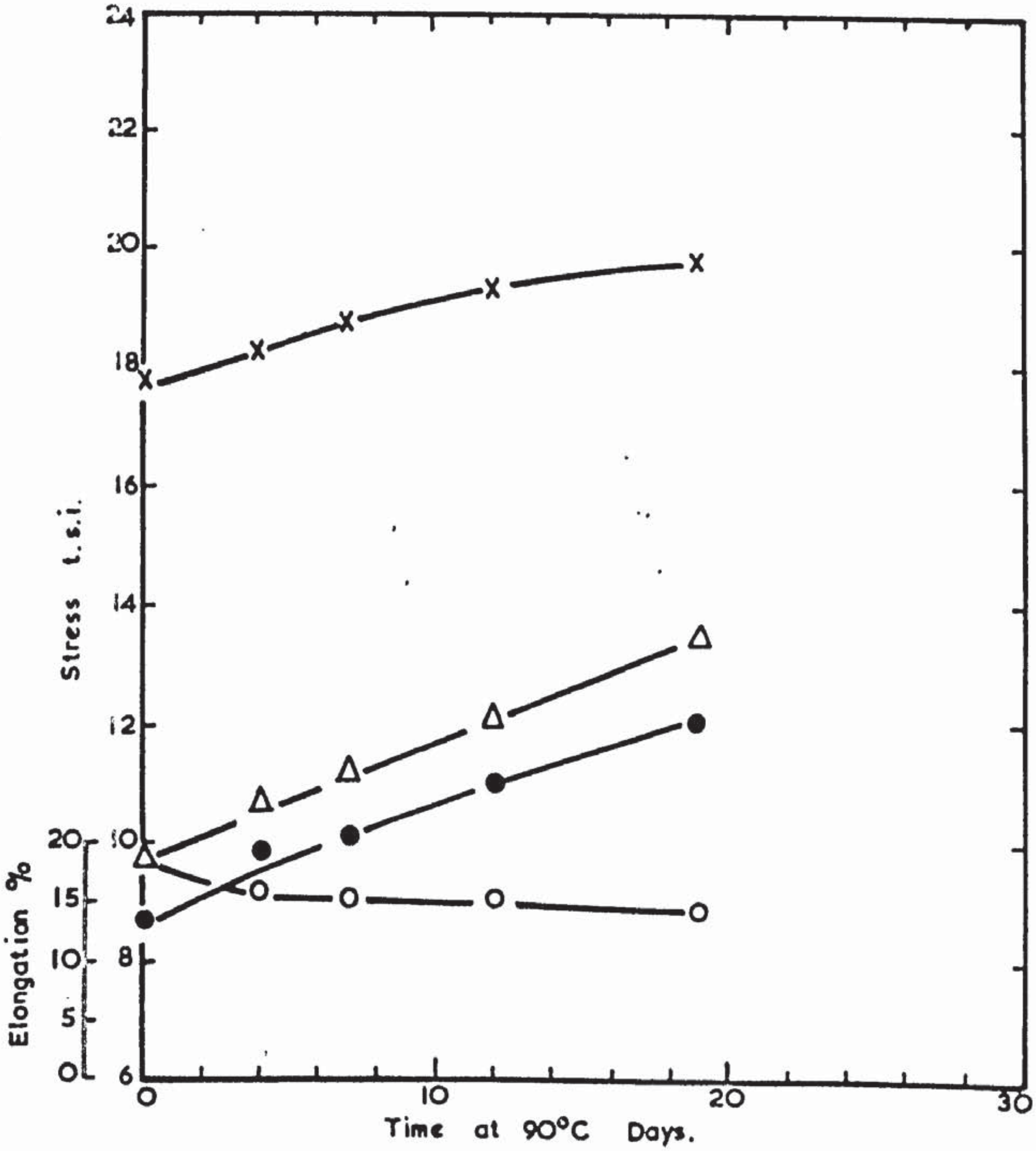
24
22
20
18
16
14
12
10
8
6
20
15
10
5
0
Stress t.s.i.
Elongation %
0
10
20
30
Time at 90°C Days.

Figure A2

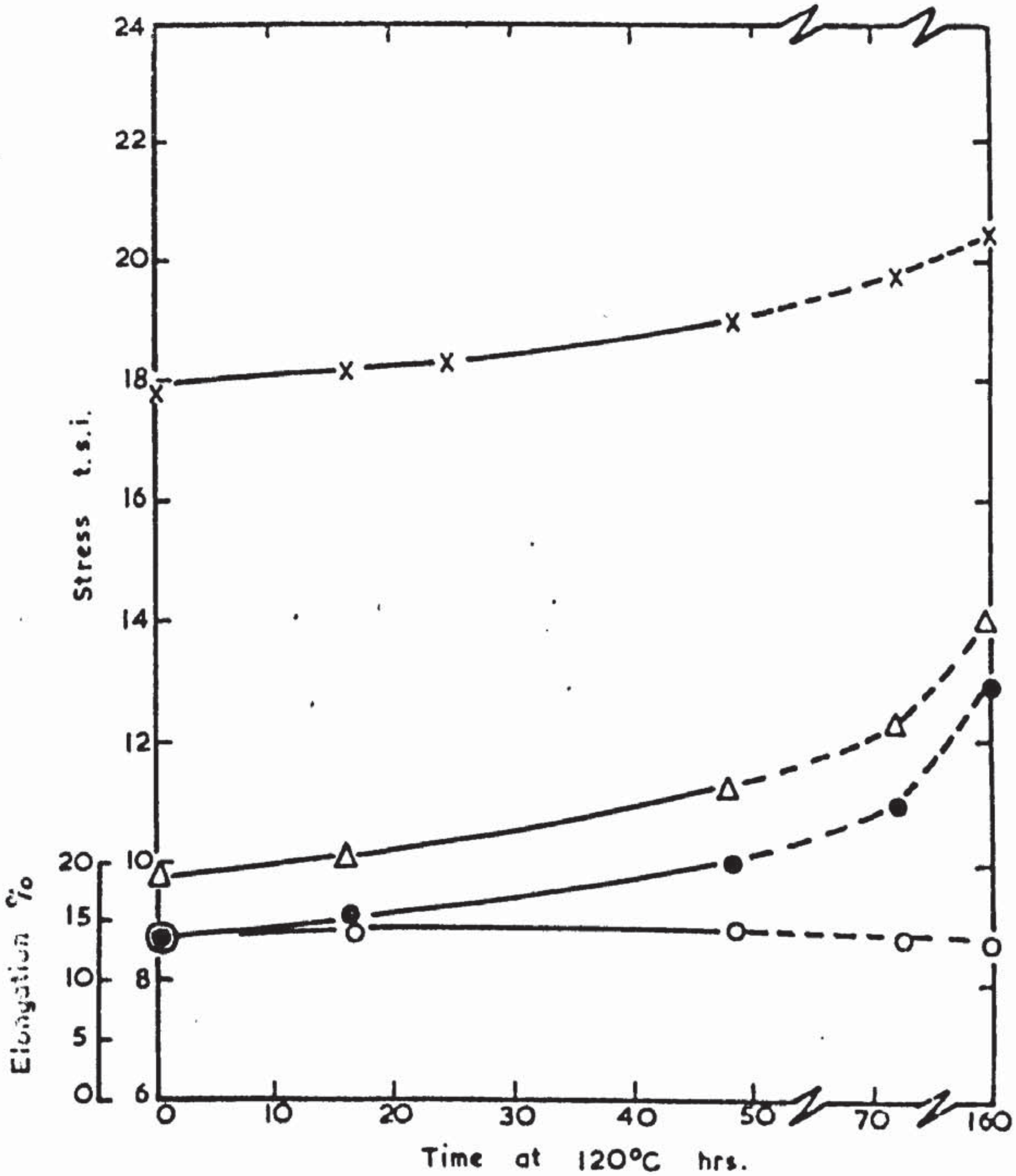

24
22
20
18
16
14
12
10
8
6
Stress t.s.i.
20
15
10
5
0
Elongation %
0
10
20
30
40
50
70
160
Time at 120°C hrs.

Figure A3

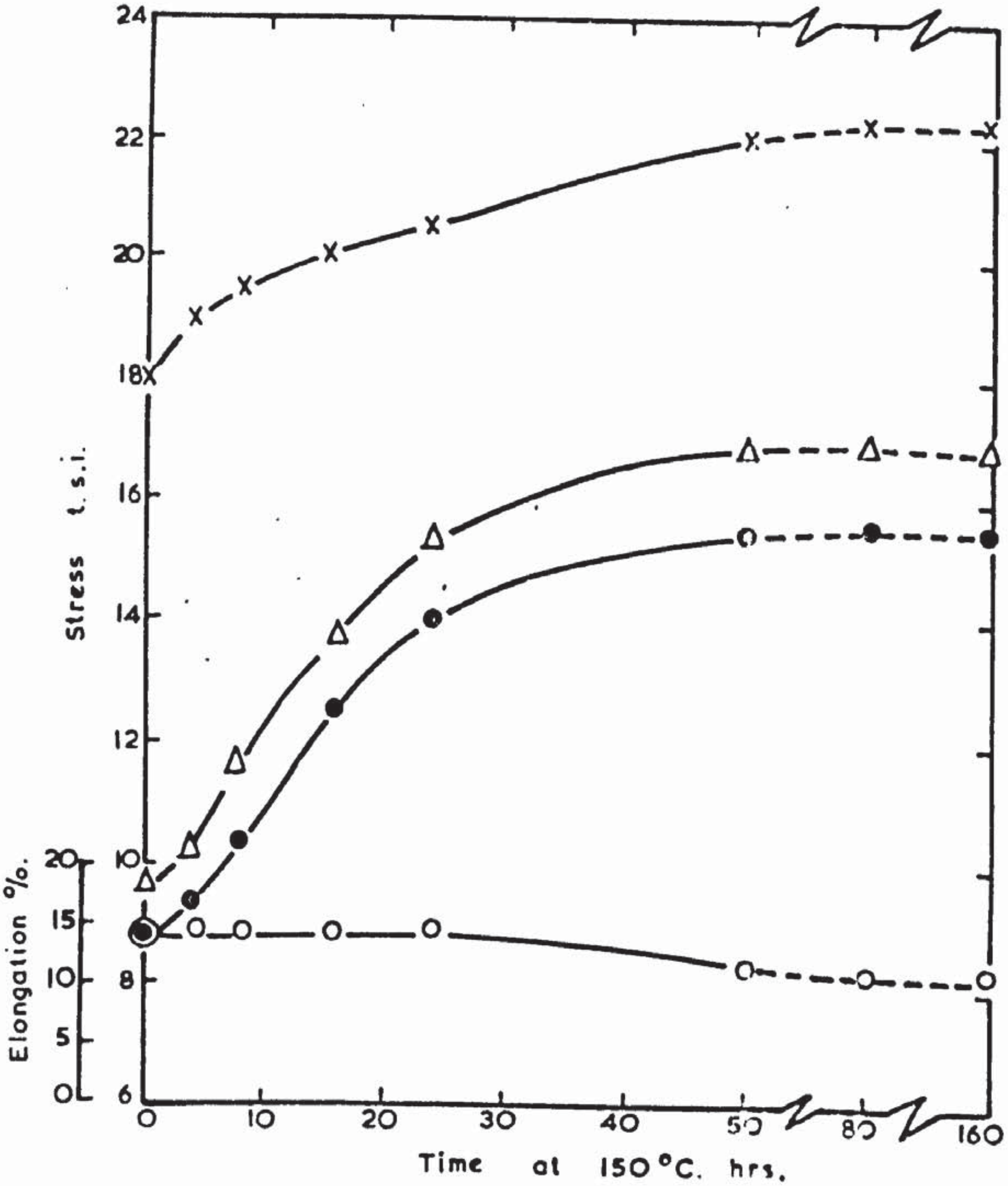
24
22
20
18
16
14
12
10
8
6
Stress t.s.i.
Elongation %.
20
15
10
5
0
0
10
20
30
40
50
80
160
Time at 150 °C. hrs.

Figure A4

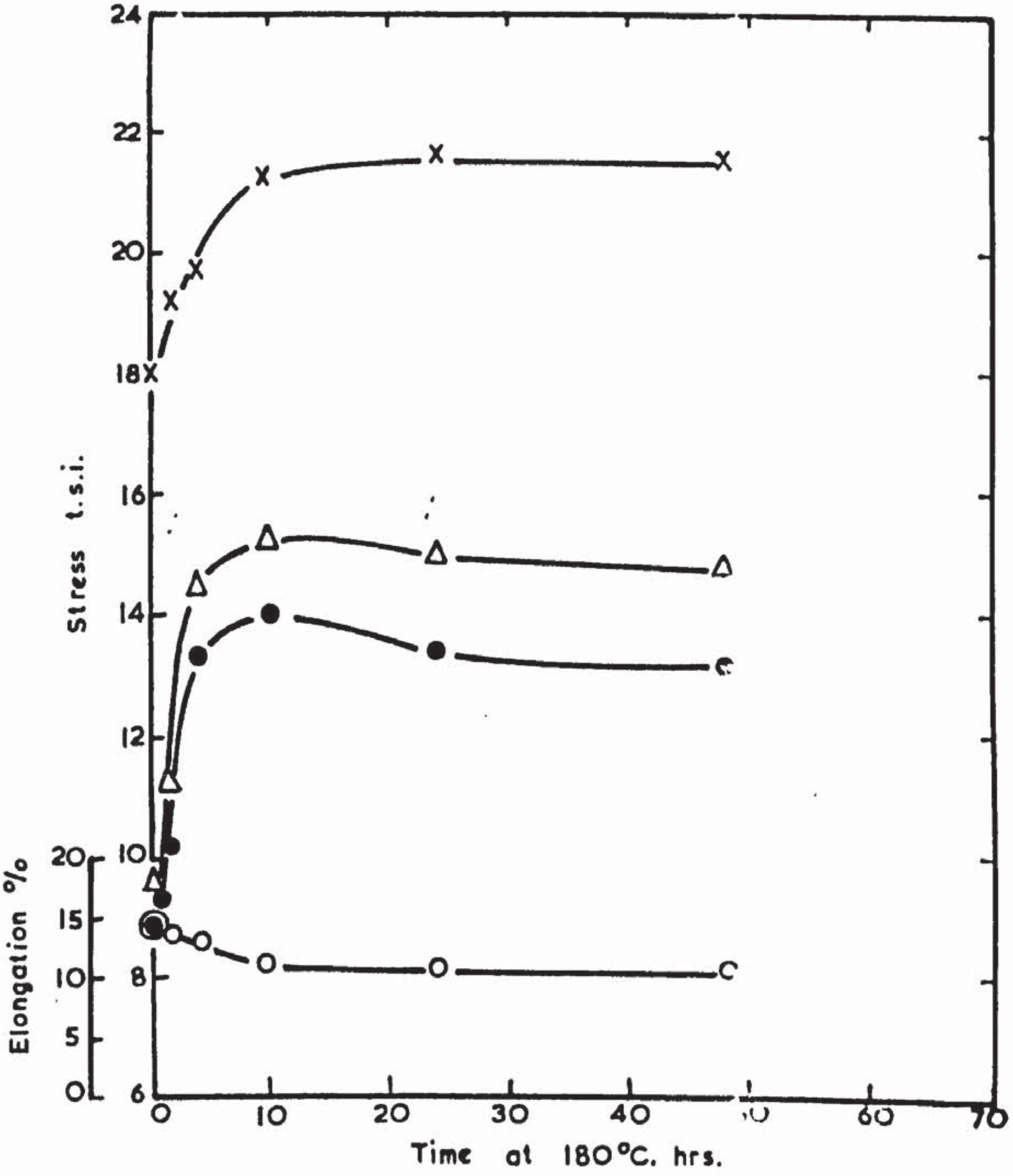
24
22
20
18
16
14
12
10
8
6
Stress t.s.i.
20
15
10
5
0
Elongation %
0
10
20
30
40
60
70
Time at 180°C. hrs.

Figure A5

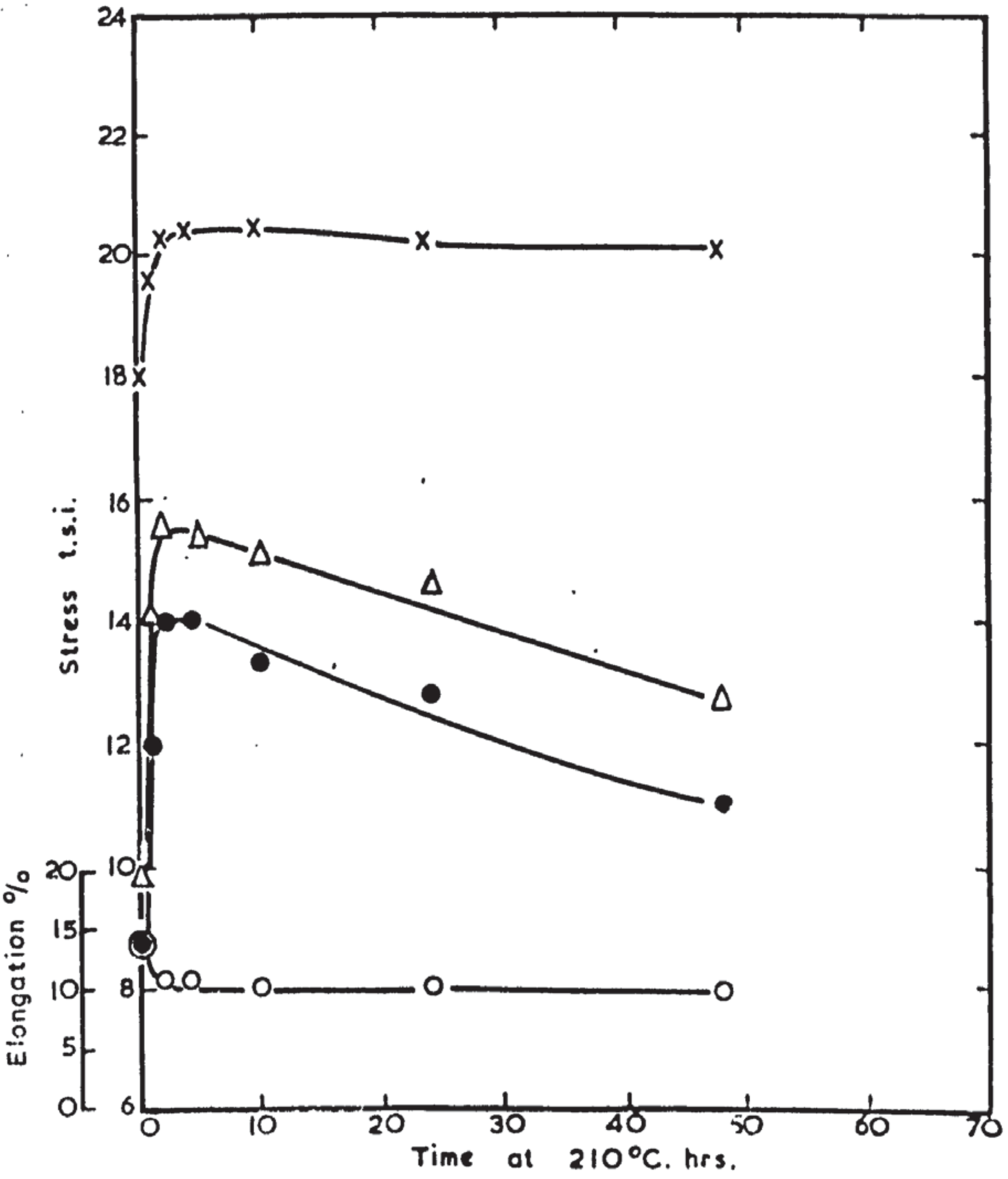
24
22
20
18
16
14
12
10
8
6
Stress t.s.i.
Elongation %
20
15
10
5
0
0
10
20
30
40
50
60
70
Time at 210°C. hrs.

Figure A6

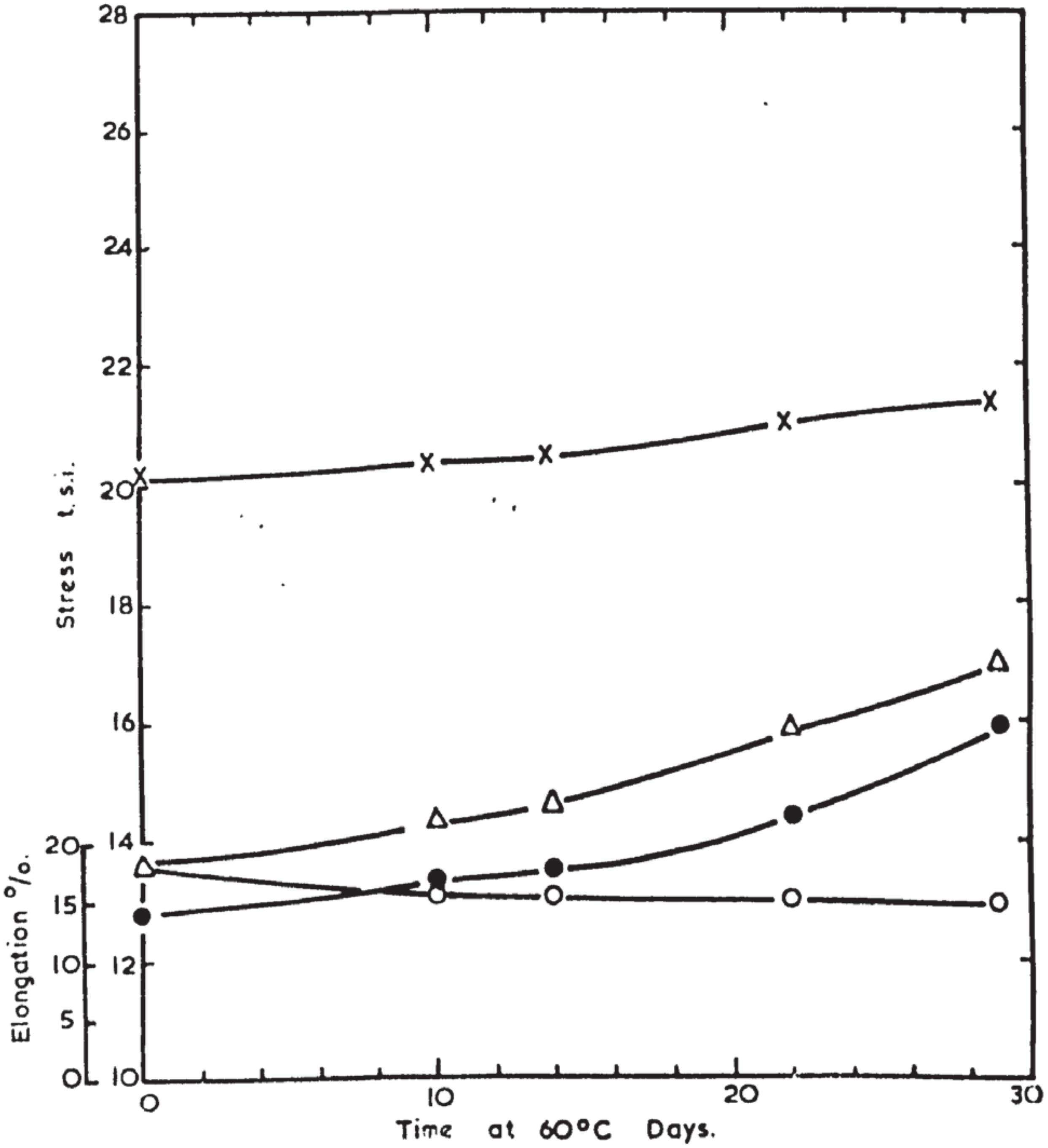

28
26
24
22
20
18
16
14
12
10
Stress t.s.i.
20
15
10
5
0
Elongation %
0
10
20
30
Time at 60°C Days.

Figure A7

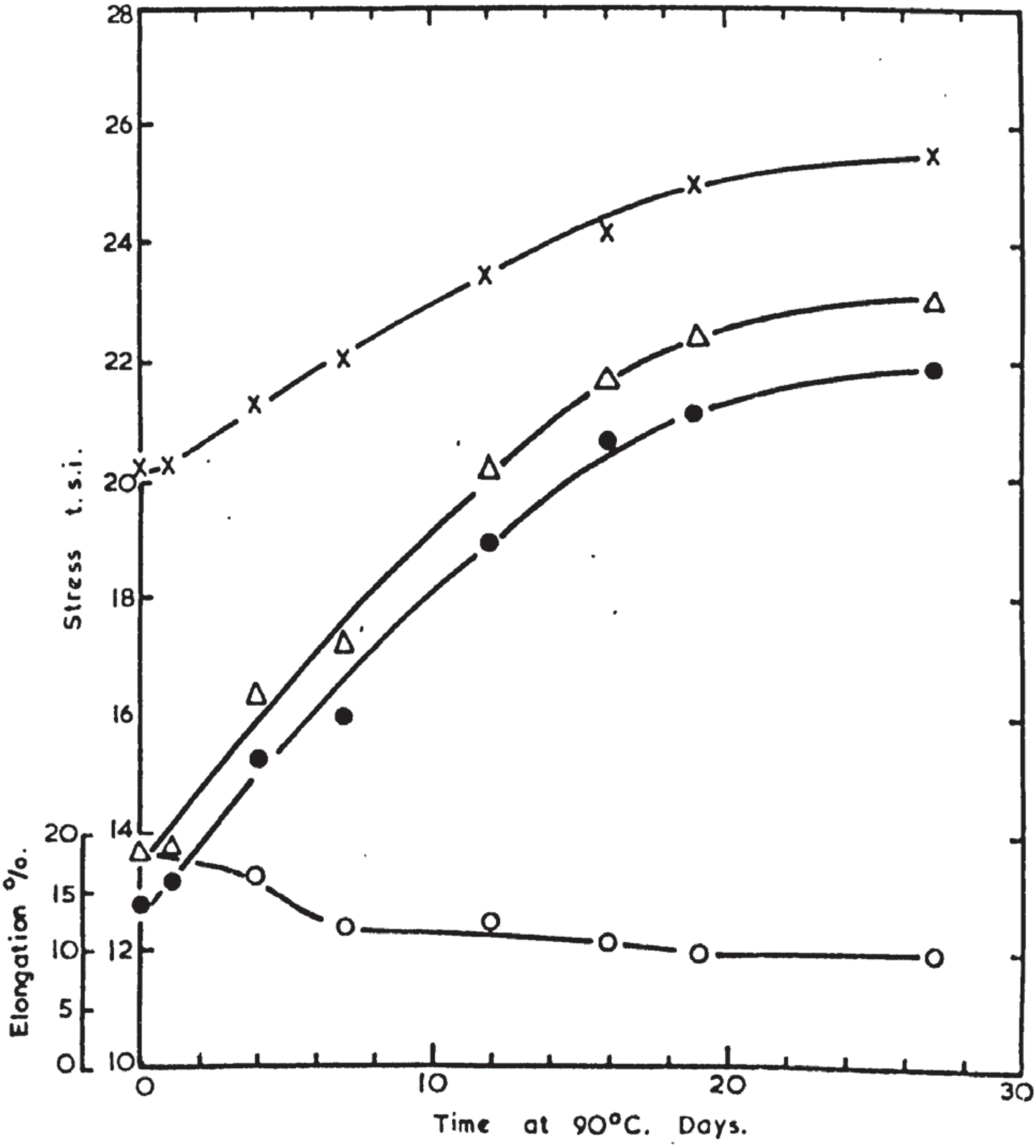

Stress t.s.i.
28
26
24
22
20
18
16
14
12
10
Elongation %.
20
15
10
5
0
Time at 90°C. Days.
0
10
20
30

Figure A8

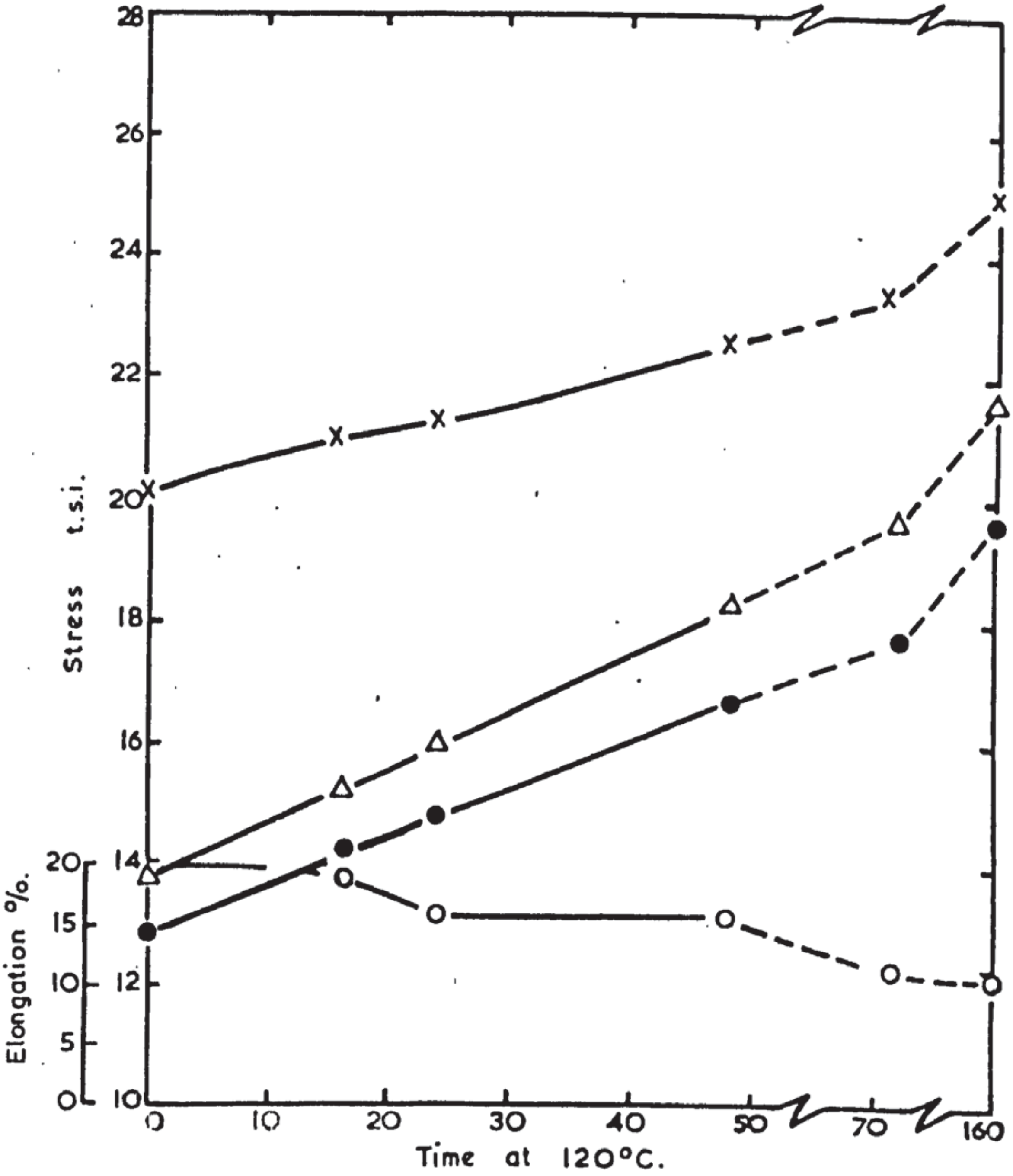
28
26
24
22
20
18
16
14
12
10
Stress t.s.i.
20
15
10
5
0
Elongation %.
0
10
20
30
40
50
70
160
Time at 120°C.

Figure A9

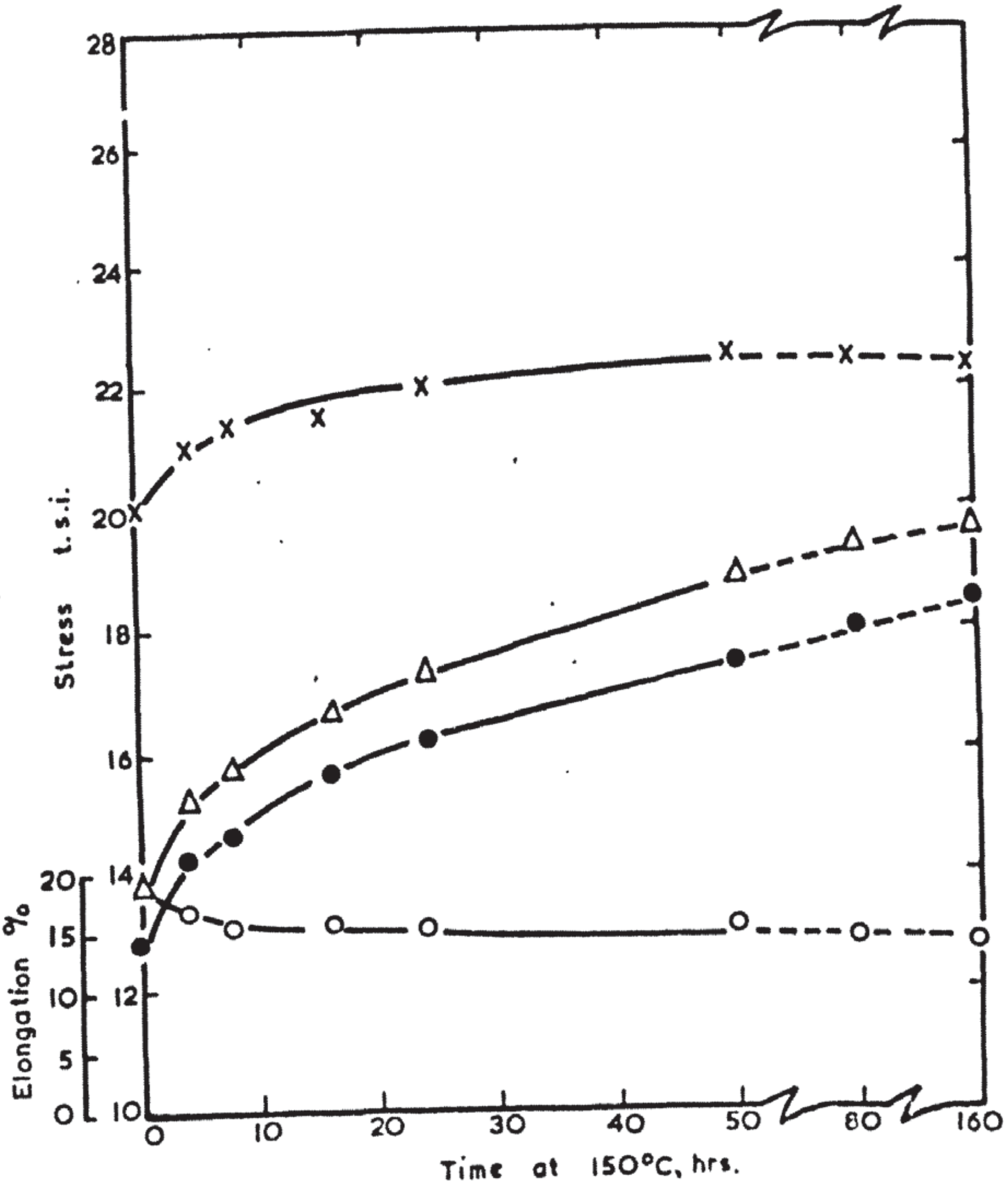
28
26
24
22
20
18
16
14
12
10
Stress t.s.i.
20
15
10
5
0
Elongation %
0
10
20
30
40
50
80
160
Time at 150°C, hrs.

Figure A10

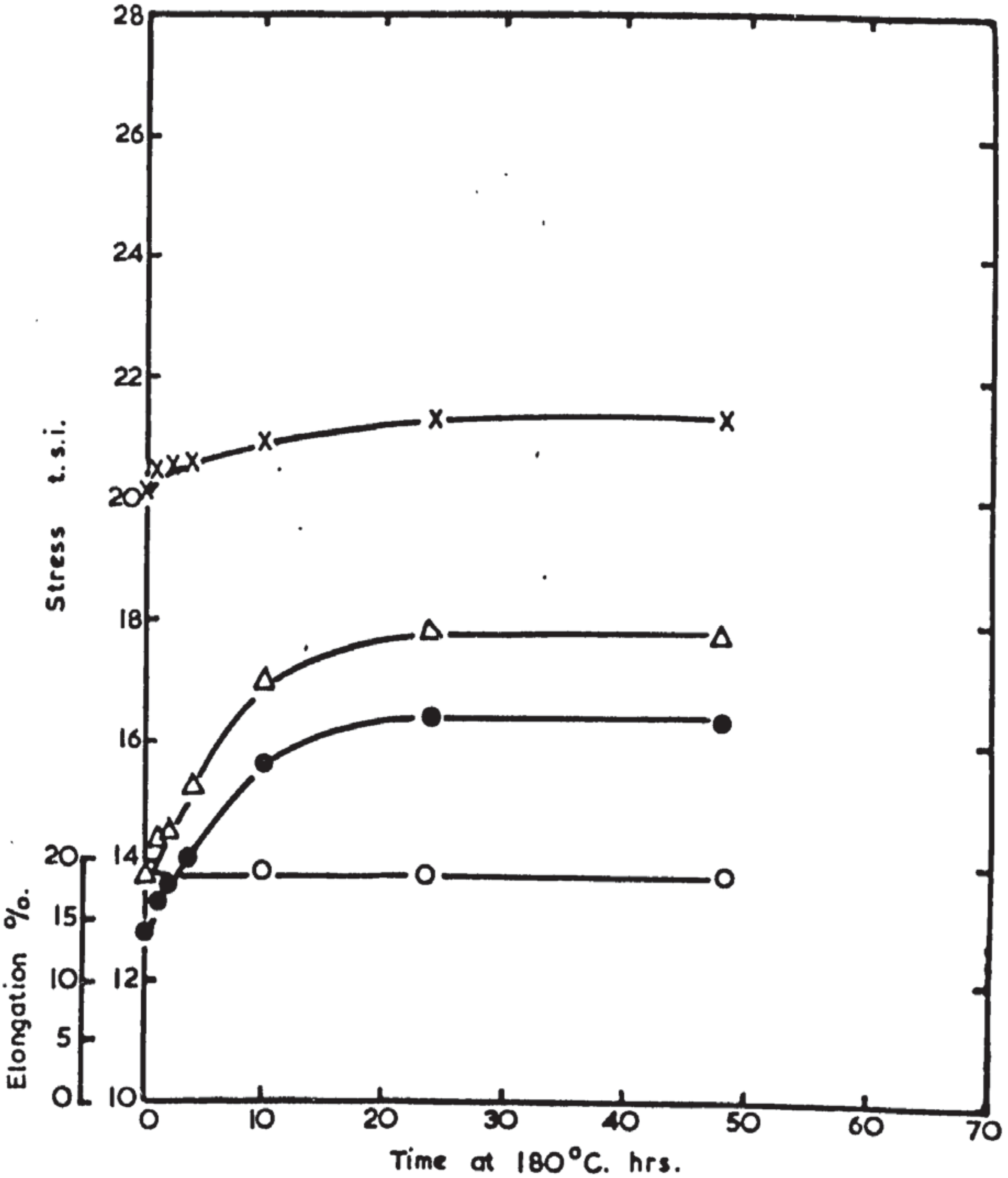

28
26
24
22
20
18
16
14
12
10
Stress t.s.i.
20
15
10
5
0
Elongation %.
0
10
20
30
40
50
60
70
Time at 180°C. hrs.

Figure A11

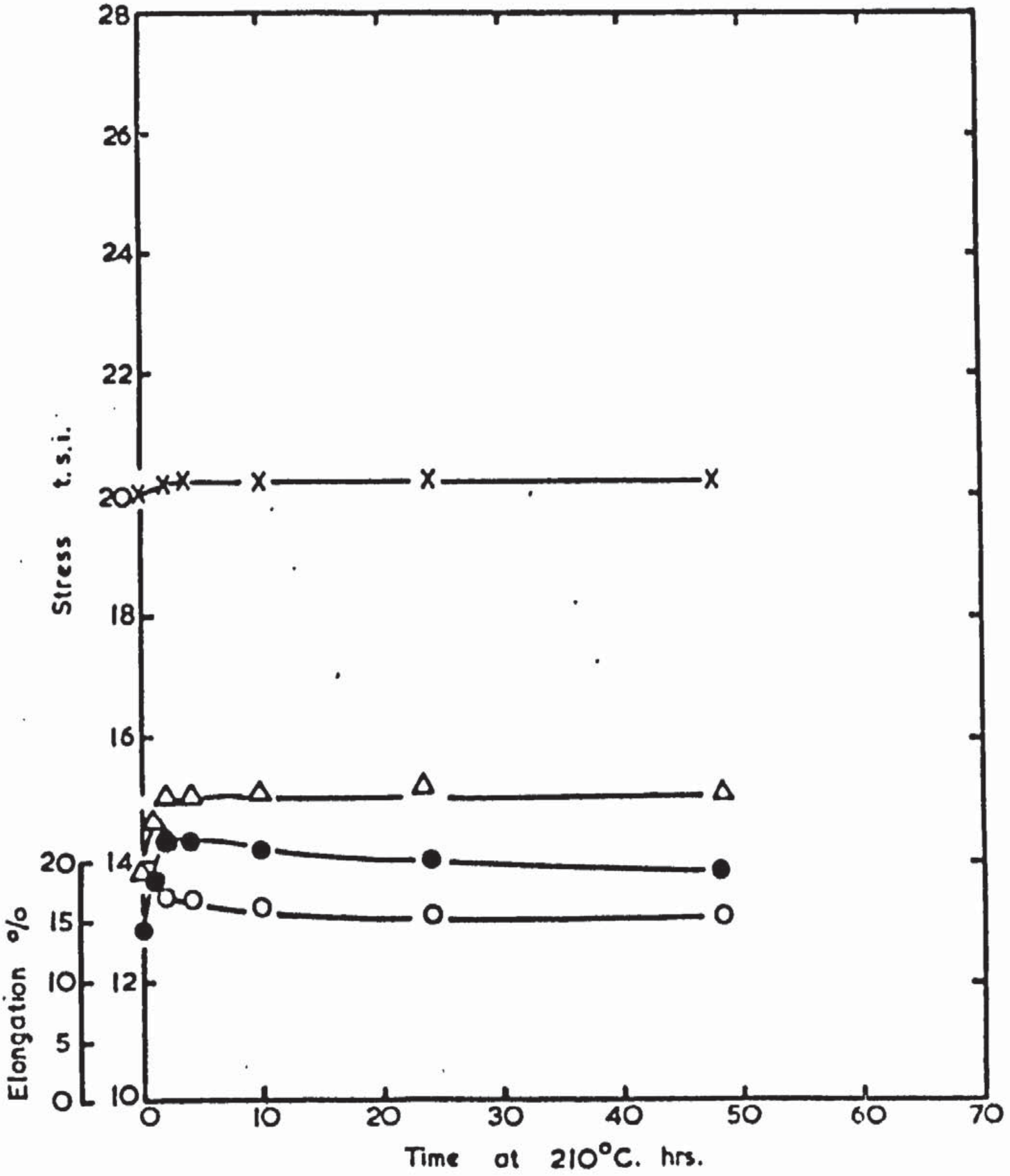
28
26
24
22
20
18
16
14
12
10
Stress t.s.i.
20
15
10
5
0
Elongation %
0
10
20
30
40
50
60
70
Time at 210°C. hrs.

Figure A12